



Surface acoustic wave based flavour sensor system

by

Gurmukh S. Sehra

School of Engineering

University of Warwick

A thesis submitted to the University of Warwick

for the degree of Doctor of Philosophy

September 2004

Contents

Heading	Page
Contents	i
List of Figures	viii
List of Tables	xii
Summary	xiii
Acknowledgements	xiv
Declaration	xv
Selected Abbreviations and Acronyms	xvii
Symbol Reference	xix
CHAPER 1: Introduction	1
1.1 Aims and objectives of the project	1
1.2 The human chemical senses	2
1.2.1 The human taste system	4
1.2.1.1 Taste quality	5
1.2.1.2 Neural taste quality coding	6
1.2.2 Human olfactory system	6
1.2.2.1 Neural code for odour molecules	9
1.2.3 Perception of flavour	9
1.3 Electronic Tongues	11
1.3.1 Concepts of electronic tongues	11
1.3.2 Sensing principles for electronic tongues	12
1.3.3 Potentiometric devices	13
1.3.3.1 Potentiometric taste sensors	15
1.3.4 Voltammetric devices	19
1.3.4.1 Voltammetric electronic tongues	21
1.3.5 Piezoelectric devices	24
1.3.6 Optical devices	26
1.4 Electronic Noses	29
1.4.1 Concept of electronic noses	29
1.4.2 Odour / Gas sensors	30
1.4.2.1 Metal-oxide gas sensors	31
1.4.2.2 Conducting Polymer gas sensors	32

1.4.2.3 Acoustic wave gas sensors	32
1.4.2.4 Field-effect gas sensors	33
1.4.2.5 Electrochemical gas sensors	34
1.4.2.6 Pellistors	34
1.4.2.7 Fibre-optic gas sensors	35
1.4.3 Signal processing & identification in E-nose instrumentation	35
1.4.4 Electronic nose applications	36
1.5 The combination of electronic nose and electronic tongue	37
1.5.1 Commercial electronic noses and tongues	37
1.6 Outline of the thesis	38
1.7 References	40
CHAPTER 2: Acoustic wave modes and devices	47
2.1 Introduction	47
2.2 The piezoelectric effect	47
2.2.1 Piezoelectricity	49
2.3 Acoustic waves	50
2.3.1 Wave propagation	51
2.3.2 Particle displacement, strain and stress	53
2.3.3 Acoustic wave excitation	56
2.3.4 Bulk waves	57
2.3.4.1 Thickness Shear Mode	57
2.3.4.2 Shear-Horizontal Acoustic Plate Mode	58
2.3.5 Surface waves	60
2.3.5.1 Surface Acoustic Waves (Rayleigh SAW)	60
2.3.5.2 Shear horizontal surface acoustic waves	64
2.3.5.3 Love surface acoustic waves	65
2.3.5.4 Flexural plate waves	69
2.4 Detection Mechanisms and performance issues for AW sensing	71
2.4.1 Detection mechanisms	71
2.4.1.1 Mass loading	72
2.4.1.2 Mechanical properties	73
2.4.1.3 Electrical properties	74
2.4.1.4 Thermal effects	74

2.4.2 Performance issues	75
2.4.2.1 Selectivity	75
2.4.2.2 Reversibility	75
2.4.2.3 Sensitivity	76
2.4.2.4 Dynamic range	76
2.4.2.5 Stability, repeatability, reliability & reproducibility	77
2.4.2.6 Response time and environmental effects	78
2.4.3 SAW delay lines and resonators	79
2.5 Conclusions	79
2.6 References	80
CHAPTER 3: Design of SH-SAW liquid sensor	83
3.1 Introduction	83
3.2 Surface acoustic wave mode and substrates for liquid sensor	83
3.3 Design of SH-SAW delay line sensor	87
3.3.1 Delay line transfer function	88
3.3.2 Calculation of the admittances	90
3.3.3 Simplified expressions	94
3.3.4 Design procedure	97
3.4 Operational principle and sensor model	101
3.4.1 Effects of external environment	103
3.4.1.1 Temperature effects	104
3.5 Liquid perturbations	105
3.5.1 Mechanical Perturbations	107
3.5.1.1 Viscous Coupling	107
3.5.1.2 Mass Loading in Liquid	108
3.5.2 Electric perturbations	108
3.5.2.1 Acoustoelectric Interaction	108
3.6 Conclusions	112
3.7 References	114
CHAPTER 4: Device fabrication and measurement systems	116
4.1 Introduction	116
4.2 SH-SAW IDT delay line microsensor fabrication	116
4.2.1 Photolithography techniques	116

4.2.1.1 Basic etching process	117
4.2.1.2 Lift-off process	118
4.2.2 Mask design and generation	120
4.2.3 Wafer preparation	121
4.2.4 Metal selection and deposition	122
4.2.5 Photolithography	124
4.2.6 Wafer dicing and packing	126
4.3 Acoustic wave measurement technology	129
4.3.1 Instrumentation and components	130
4.3.2 Measurement of acoustic wave device frequency response	133
4.3.2.1 Two-port devices	133
4.3.2.2 Real-time measurement and characterisation of acoustic wave devices	134
4.3.2.3 Simultaneous measurement of acoustic wave velocity (phase) and attenuation	135
4.3.2.4 Propagation measurement technique for two-port devices	140
4.3.2.5 Two-port AW devices in oscillator circuits	142
4.3.2.6 Phase-locked loop setup for two-port device measurements	144
4.4 Controlling the sensor environment	145
4.4.1 Temperature effects and control	145
4.4.2 Pressure effects	148
4.4.3 Flow-rate effects	148
4.4.4 Packaging considerations	149
4.5 Conclusions	150
4.6 References	151
CHAPTER 5: SH-SAW device measurement setup, characterisation and experimental results	153
5.1 Introduction	153
5.2 Characterisation of the SH-SAW sensors	153
5.2.1 Measurement of the temperature coefficient	153
5.2.2 Effect of liquid volume loaded on the sensor surface	155

5.2.3 Acoustoelectric interaction for relative permittivity and conductivity	156
5.3 SH-SAW sensors to classify the basic tastes	157
5.3.1 Classification of solutions of basic taste	158
5.3.2 Dilution of the taste solutions to determined the limit of detection	159
5.3.3 Determination of the electrical properties of the taste samples	161
5.4 Use of the SH-SAW sensors with real samples	162
5.4.1 Experiment to discriminate between orange juice and fresh milk	162
5.4.2 Discrimination between full-fat, semi-skimmed and skimmed milk	163
5.4.3 Dilution of full-fat milk using DI water to determine the detection limit	165
5.4.4 Investigation of the freshness of full-fat milk samples	166
5.4.5 Discrimination of fresh, bulging and bacterial loaded milk	167
5.4.6 Analysis of milk samples with a range of bacterial loading	170
5.4.7 Testing of mastitic milk samples	172
5.5 Conclusions	174
5.6 References	176
CHAPTER 6: Combination of the electronic tongue and electronic nose	177
6.1 Introduction	177
6.2 MOS ChemFET sensors	178
6.2.1 Design considerations of ChemFET sensors	178
6.2.1.1 Mode of operation	178
6.2.1.2 ChemFET sensor design	180
6.2.1.3 Deposition of the polymer material	184
6.3 Measurement setup for the combined nose/tongue system	184
6.3.1 Electronic interface for the chemFET sensors [6.4]	184
6.3.2 Measurement setup for the SH-SAW sensors	186
6.3.3 Combined experimental setup	186

6.3.4 Control software	188
6.4 Experiments performed with the combined nose/tongue system	188
6.4.1 Experiment to discriminate between orange juice & milk	189
6.4.2 Discrimination between milks of different fat content	190
6.4.3 Experiments with nose/tongue biased analytes	192
6.5 Conclusions	199
6.6 References	200
CHAPTER 7: High frequency SH-SAW devices	201
7.1 Introduction	201
7.2 Design of the high frequency SH-SAW devices	201
7.2.1 Wired and wireless sensor configurations	202
7.2.1.1 Wired configuration	202
7.2.1.2 Wireless configuration	203
7.2.2 IDT designs	204
7.2.2.1 Uniform single-electrode IDT design	204
7.2.2.2 Double-electrode IDT design	206
7.2.3 Reflector design	208
7.2.3.1 Reflection mechanisms and behaviour in periodic structures	209
7.2.3.2 Reflector grating designs	213
7.2.4 SH-SAW device layouts	214
7.2.4.1 Wired SH-SAW sensor layout	215
7.2.4.2 Wireless SH-SAW sensor layout	215
7.3 Fabrication of the high frequency devices	216
7.3.1 Pattern generation	216
7.3.2 Wafer cleaning	217
7.3.3 Deposition of the grounding layer	218
7.3.4 Photoresist coating	218
7.3.5 Electron beam writing	219
7.3.6 Developing	219
7.3.7 Metallisation and lift-off	219
7.2.8 Removal of grounding layer	219
7.4 Measurement systems	221

7.4.1 Measurement setup for wired sensors	221
7.4.2 Proposed measurement setup for wireless sensors	222
7.5 Micro-fluidic chambers	222
7.5.1 Stainless steel chambers	223
7.5.2 MSL micro-chambers	224
7.5.2.1 Stereolithography	224
7.5.2.2 Microstereolithography	225
7.5.2.3 CAD design and MSL fabrication	227
7.5.2.4 SLA system used	228
7.5.2.5 Flow chamber design	228
7.5.2.6 Disposable chamber	228
7.5.2.7 Parylene coating	229
7.7 Conclusions	229
7.8 References	231
CHAPTER 8: Conclusions and further work	233
8.1 Aims and conclusions	233
8.1.1 Dual-delay line SH-SAW sensors	234
8.1.2 S-parameter characterisation of the SH-SAW devices	235
8.1.3 SH-SAW as liquid sensors (electronic tongue)	235
8.1.4 Combined electronic tongue/nose system	237
8.1.5 High frequency SH-SAW devices	238
8.1.6 Project objectives	239
8.2 Applications of the SH-SAW sensors	239
8.3 Future work	240
APPENDIX A: Software programs	242
APPENDIX B: Cell design details	251
APPENDIX C: High frequency SH-SAW device configurations	257
APPENDIX D: Published papers	263

List of Figures

Heading	Page
Figure 1.1: The tasting process (a) Tongue with different papillae (b) Fungiform papilla on tongue (c) Cross section of a taste bud and taste pore (d) The taste cell with tip just under the pore (e) Membrane at the tip of the taste cell with receptor sites	5
Figure 1.2: The smelling process (a) Olfactory mucosa and olfactory bulb (b) ORN (c) Detailed view of ORN (d) Olfactory receptors (e) Stimulation of OR triggers reactions and hence ion flow (f) Showing the OR is part of the membrane crossing it several times	8
Figure 1.3: Potentiometric ion selective electrode	14
Figure 1.4: Schematic diagram of an ion-selective field effect transistor	14
Figure 1.5: Cross-section (left) and front (right) view of the multichannel electrode	16
Figure 1.6: Experimental setup for the eight-channel electrode system	16
Figure 1.7: Anritsu Corporation taste sensing systems	17
Figure 1.8: Detecting part of the TSFET with lipid/polymer membrane	18
Figure 1.9: Setup of a multi-electrode voltammetric electronic tongue	22
Figure 1.10: (a) Typical QCM sensor schematic (b) Setup for measurement of ionic and polar analytes in water	25
Figure 1.11: (a) SAW delay line sensor configuration (b) SAW resonator (no sensing element)	26
Figure 1.12: Setup of colorimetric electronic tongue and sensing beads in machined wells	27
Figure 1.13: Silicon chip with tiny squares and channels	28
Figure 1.14: A simple schematic of an artificial olfactory system and the mammalian olfactory system	30
Figure 1.15: Structure of a Toguchi-type tin dioxide gas sensor	32
Figure 1.16: Two types of field-effect gas sensors (a) MISFET (n channel) (b) MISCAP	34
Figure 1.17: Basic arrangement of an electrochemical gas sensor	34
Figure 2.1: The piezoelectric effect: mechanical energy transduced into electrical energy	48
Figure 2.2: Particle displacement profiles (a) longitudinal, (b, c) shear uniform plane waves	52
Figure 2.3: Acoustic shear waves in an arbitrary cubic crystal medium	53
Figure 2.4: Equilibrium and deformed states of particles in a solid	54
Figure 2.5: Schematic of a SAW delay line with IDTs metallised on piezoelectric wafer	57
Figure 2.6: (a) One-port SAW resonator (b) Two-port SAW resonator	57
Figure 2.7: Thickness shear mode (TSM) resonator	58
Figure 2.8: Shear-horizontal acoustic plate mode (SH-APM) device	59
Figure 2.9: Rayleigh waves move vertically in the direction normal to the plane of the SAW sensor	61
Figure 2.10: SAW coordinate system showing the propagation vector	62

Figure 2.11: Particle displacement on the sagittal plane for Rayleigh waves	64
Figure 2.12: Shear horizontal surface acoustic waves (SH-SAW) with displacement parallel to the device surface	64
Figure 2.13: Wave generation on a Love wave mode device	66
Figure 2.14: (a) Structure of Love wave device (b) Schematic of Love wave device used for analysis	67
Figure 2.15: A flexural plate wave (FPW) device	70
Figure 3.1: Rayleigh-SAW (R-SAW) and SH-SAW at liquid and piezoelectric substrate interface	84
Figure 3.2: Graphical representation of acoustic wave velocity and particle displacement to rotation angle of LiTaO ₃	86
Figure 3.3: Uniform interdigital transducer delay line arrangement	88
Figure 3.4: Schematic of a SAW delay line with ordinary IDTs	90
Figure 3.5: SAW IDT as a 3-port system	92
Figure 3.6: Typical amplitude response for narrow a frequency range	99
Figure 3.7: Design of SH-SAW dual delay line sensor	101
Figure 3.8: Uniform interdigital transducer delay line arrangement	101
Figure 3.9: Schematic drawing of a dual-delay line SH-SAW microsensor	102
Figure 3.10: Normalized particle displacement u_2 and potential j at the 36YX.LT/water interface	106
Figure 3.11: Velocity shift as a function of the viscosity density product	108
Figure 3.12: Attenuation change and velocity change as a function of relative permittivity	110
Figure 3.13: Attenuation change and velocity shift as a function of relative conductivity	111
Figure 3.14: Permittivity-conductivity chart used to determine the permittivity and conductivity of a sample liquid from the SH-SAW sensor responses	112
Figure 4.1: Basic steps involved in the two lithography processes: etching (left) and lift-off (right)	120
Figure 4.2: (a) Final design of mask plate in L-Edit (b) Photograph of manufactured positive field mask plate	121
Figure 4.3: Fabrication process steps of SH-SAW sensor	126
Figure 4.4: Photograph of wafer with devices patterned (a) before dicing (b) after dicing	127
Figure 4.5: (a) Photograph of single fabricated SH-SAW device (b) Device mounted on a PCB	128
Figure 4.6: Picture of liquid cell with locating pins and slot for electronic nose device	129
Figure 4.7: Photograph of SH-SAW device with the PTFE liquid cell used for experimental setup	129
Figure 4.8: (a) Network analyser setup to measure two-port-device frequency response. (b) Signal generator/VVM combination setup for frequency response measurement	134
Figure 4.9: Signal flow of a two-port network	136
Figure 4.10: Photograph of HP 8753ES vector network analyser setup	138
Figure 4.11: S_{11} measurements of SH-SAW input and output IDTs for a metallised delay-line	139

Figure 4.12: Impedance measurement of IDT (metallised delay-line) using a Smith Chart	139
Figure 4.13: Transmission measurements of a single SH-SAW metallised delay line	140
Figure 4.14: Picture of the signal generator/vector voltmeter setup for liquid experiments (SH-SAW device without cell)	141
Figure 4.15: Two-port SAW delay line-based oscillator loop	143
Figure 4.16: Computer-controlled phase-locked loop configuration for a two-port device measurement	145
Figure 5.1: Temperature characteristics of the SH-SAW on 36YXLT	155
Figure 5.2: Effect of the volume of liquid loading on the attenuation and phase shift	156
Figure 5.3: Velocity shift as a function of relative permittivity	157
Figure 5.4: 3D PCA plot for the four basic taste solutions and DI water as the reference	159
Figure 5.5: 3D PCA plot for the lowest concentrations of the diluted sample solutions	160
Figure 5.6: 2D PCA plot for the dilution testing of the four different taste liquids	160
Figure 5.7: Experimental results for salty (NaCl) and sour (HCl) solutions of different concentrations on the permittivity-conductivity chart	162
Figure 5.8: Principal components analysis of different liquids.	163
Figure 5.9: PCA of different milks showing good discrimination	164
Figure 5.10: Discrimination of different milks using the best combination of pre-processed data	165
Figure 5.11: Effect of milk fat content on attenuation loss of 36YX.LT free delay line	166
Figure 5.12: PCA of milk samples showing the effect of ageing	167
Figure 5.13: PCA plot showing the effects of milk from different points in the oestrus cycle and containing different bacterial loads on the SH-SAW sensors	169
Figure 5.14: PCA plot showing the effects of milk from different points in the oestrus cycle and containing different bacterial loads on the SH-SAW sensors (both freshly prepared samples and frozen samples).	170
Figure 5.15: PCA plot showing the effect of bacterial (<i>S. Uberis</i>) loading in milk on the sensor and its detection limit	171
Figure 5.16: PCA plot showing the effect of bacterial (<i>S. Aureus</i>) loading in milk on the sensor and its detection limit	172
Figure 5.17: PCA plot for the different mastitic milk samples	173
Figure 6.1: Schematic of a sensor and reference with integrated circuitry	180
Figure 6.2: Schematic of a single chemFET device with channel dimensions of $385\ \mu\text{m} \times 10\ \mu\text{m}$	181
Figure 6.3: Schematic drawing of chemFET array device	182
Figure 6.4: Photograph of fabricated 4-element ChemFET sensor	183
Figure 6.5: Close up picture on sensing area	183
Figure 6.6: Photograph of packaged device	184
Figure 6.7: Simplified circuit diagram of constant current electronic hardware	186

Figure 6.8: Photograph of the flavour sensing system with a PTFE sample cell	187
Figure 6.9: Photograph of the experimental setup for the combined electronic nose/tongue measurements	187
Figure 6.10: PCA of liquids with the e-tongue showing excellent linear discrimination	189
Figure 6.11: Response of the poly(9-vinylcarbazole) FET sensor to the different liquids	189
Figure 6.12: Combined PCA plot of different liquids using the e-tongue and e-nose together	190
Figure 6.13: PCA plot of different milks with the e-tongue only	191
Figure 6.14: Transient response of the poly(styrene-co-butadiene)FET sensor to milks of different fat content	191
Figure 6.15: Combined PCA plot of different milks using the e-tongue and e-nose	192
Figure 6.16: PCA plot for the E-tongue data only	194
Figure 6.17: 3-D PCA plot on the attenuation and phase data of the SH-SAW sensor	195
Figure 6.18: Transient responses of the 4 ChemFETs to the each of the samples	196
Figure 6.19: 2-D PCA plot for the $\Delta V_{G_{DS}}$ data from the 4 FETs	197
Figure 6.20: 3-D PCA plot for the $\Delta V_{G_{DS}}$ data from the 4 FETs	197
Figure 6.21: 2-D PCA plot of the combined nose/tongue data	198
Figure 6.22: 3-D PCA of the combined nose/tongue data showing 100% separation	199
Figure 7.1: Wired setup for the dual delay line sensors	202
Figure 7.2: Setup for wireless operation of passive sensors	203
Figure 7.3: Structure of delay line with double electrode IDTs	206
Figure 7.4: Equivalent circuit model for a grating structure	210
Figure 7.5: Incidence and reflection at a strip	211
Figure 7.6: Periodic grating structure	212
Figure 7.7: Bragg reflection	213
Figure 7.8: Bragg condition	213
Figure 7.9: Reflector types	214
Figure 7.10: Layout of wired 433 MHz dual-delay line SH-SAW sensor	215
Figure 7.11: Layout of a wireless 433 MHz dual-delay line SH-SAW sensor with PNR reflectors and the free delay line 2mm shorter	216
Figure 7.12: Final wafer layout for fabrication	217
Figure 7.13: Developed bi-layer of photo-resist producing an 'over-hang'	218
Figure 7.14: Fabrication process steps of high frequency SH-SAW devices	220
Figure 7.15: Photographs of IDT fingers (Test run)	221
Figure 7.16: Stainless steel flow micro chamber	223
Figure 7.17: Schematic of typical SLA setup	225
Figure 7.18: Dynamic mask projection MSL	226
Figure 7.19: MSL chamber for flow measurements	228
Figure 7.20: MSL disposable chamber for static measurements	229

List of Tables

Heading	Page
Table 1.1: Electronic nose and tongue manufactures	38
Table 3.1: Material constants for leaky SAW substrates	85
Table 3.2: SAW at 36YX.LT/water interface	87
Table 3.3: Design parameters for SH-SAW sensor	100
Table 4.1: Chemical etching of metal electrode patterns	118
Table 4.2: Lift-off process	119
Table 5.1 Fisher t values on pre-processed milk data to determine the best separation combination	165
Table 5.2 Approximate cell concentrations obtained for testing the sensitivity of the electronic tongue	171
Table 6.1: ChemFET sensor different gate configurations	182
Table 6.2: Electronic nose/tongue biased analytes	193
Table 7.1: Design parameters for single-electrode IDT SH-SAW delay line sensors	206
Table 7.2: Design parameters for double-electrode IDT SH-SAW delay line sensors	208
Table 7.3: Design parameters of reflector gratings for the reflective delay line devices	214
Table 7.4: E-beam settings used for writing the different feature sizes	219

Summary

In the food and beverage industries, human sensory panels are often employed to measure flavour, however the results depend on subjective judgements and suffer from considerable variability and subjectiveness. Therefore the development of low cost and low power taste and odour sensors with high yield and reproducibility is very desirable. The majority of electronic tongue instruments employ multiple sensor elements requiring several kinds of coating materials, such as artificial lipid membranes, to identify liquid samples. They generally utilise electrochemical techniques with ion selective membranes and suffer from extremely high sensitivity to electrode impedance and are thus very susceptible to surface contamination and fouling. The aim here is to develop liquid sensors with a low cost of fabrication, robustness, micropower operation, durability and, in the future, wireless operation. Novel liquid sensors, based on shear horizontal surface acoustic (SH-SAW) devices without selective membranes have been developed. The SH-SAW devices consist of two delay lines, one shorted (metallised and electrically shielded) and the other free (electrically active). This dual configuration allows the measurement of both the mechanical and acoustoelectric properties of the adjacent liquid analyte and removes common mode effects such as drift/fouling. The approach adopted is based on a generic fingerprint correlated to key physical parameters and does not employ any bio-chemical selective layers, thus ameliorating the problems with electrochemical type sensors and increasing the robustness and lifetime of the sensors.

The taste sensors have been fully characterised in term of the *S*-parameters in air and further characterised in the liquid medium. Initial experiments study the effect of temperature and liquid loading followed by the use of the sensors as taste sensors. All the experiments were performed with the aid of a custom built cell that accommodates the test samples. The sensing system demonstrated the ability to discriminate between four basic tastes without the use of selective membranes, responding to various physical parameters of the liquid – an indirect measure of taste. A detection limit of < 0.1% was achieved. The theory of the electro-acoustic interactions has been used to relate the experimental results to electrical properties of the liquids under test and promising results achieved. Complex samples related to more than a simple basic taste, such as cow's milk, have been analysed. Milks of different fat contents have been classified with a very encouraging sensitivity figure of about 0.1% fat. Promising results were obtained on the milk freshness tests showing possible application of the sensors as milk freshness indicators. The taste sensors presented the ability to discriminate between different levels of sourness (linked to the growth of bacterial infection (somatic cell count)) in milk, with an encouraging detection limit of ca. 10^2 - 10^3 cfu/ml, suggesting their possible application in the dairy industry and also biomedical sensing.

A combined tongue/nose flavour system employing bulk CMOS chemFET odour sensors with the SH-SAW taste sensors has been explored. The bulk CMOS designs use a MOSFET sensing structure with an active polymeric gate material and operate at low temperatures (< 100 °C). The device is based on an array device of four FET sensors with channel lengths of either 10 μm or 5 μm . Composite coated (e.g. poly(ethylene-co-vinyl acetate)) chemFETs were used in the system, and the use of the combined flavour system was justified by performing experiments on different tongue and nose biased samples, where the combination of the sensors contributed to 100 % discrimination of the samples. These results are very encouraging and suggest possible application of the flavour system to analyse complex solutions in the food and beverage industry and for screening of clinical samples.

Acknowledgements

I would like to extend my sincerest thanks to my academic supervisors Dr. Marina Cole and Prof. Julian Gardner for generously allowing me the opportunity of studying in this field, and for their constant guidance and support during my PhD. I would also like to acknowledge the Royal Society, Overseas Research Students Award Scheme (ORS), the Special Studentships Scheme (Warwick University) and the Worshipful Company of Scientific Instrument Makers (WCSIM) for their financial support over the years of this study.

I am also grateful to all of my friends and colleagues for their constant support and encouragement during the course of this study. For practical work associated with my Ph.D. I would particularly like to thank the members of the *Sensors Research Laboratory, School of Engineering, University of Warwick*, including, Mr F. T. Courtney and Mr I. Griffiths for their assistance in mechanical matters and to Dr. J. Covington, I. Leonte and M. Hunt for their assistance in technical matters.

I also like to take this opportunity to thank Dr. Zhang Chui and Mr. Geoff Thomas of *Rutherford Appleton Laboratory, Didcot, UK*. for the fabrication of the devices used in this study.

I would also like thank Prof. Chris Dowson and Mr. Peter Newton of the *Biological Sciences, University of Warwick* for preparing the biological samples. A special thanks Mrs. Jane Emerson of the *Chemistry Department, University of Warwick* for preparing chemical samples using in testing.

Finally I would like to thanks my loving family and friends, for their endless love, encouragement and support which has made my Ph.D. research worthwhile.

Declaration

The work described in this thesis was conducted by the author, except where stated otherwise, in the School of Engineering, University of Warwick between the dates of October 2000 and September 2004. No part of this work has previously been submitted to the University of Warwick or any other academic institution for admission to a higher degree.

Gurmukh S. Sehra, 30th September 2004.

Parts of this work have been presented at international conferences and published in the scientific literature listed below:

1. Journal Papers

- [1] Cole M, Sehra G, Gardner JW and Varadan VK, *Development of smart tongue devices for measurement of liquid properties*, IEEE Sensors Journal, Vol. 4, No. 5, (2004), pp. 543-550.
- [2] Sehra G, Cole M, and Gardner JW, *Miniature tasting system based on dual SH-SAW sensor device: an electronic tongue*, Sensors and Actuators B, 103, (2004), pp. 233-239.

2. Conference Papers

- [1] M. Cole, G. Sehra, J.W. Gardner and V.K. Varadan, *Fabrication and Testing of a Smart Tongue Device for Liquid sensing*, Proc. of IEEE Sensors 2002 Conference, June 12-14, 2002, Orlando, Florida, USA, pp. 237-241.
- [2] Sehra G S, Covington JA, Cole MV, and Gardner JW *Combined electronic nose/tongue for liquid analysis*, Proc. of 9th International Symposium on Olfaction and Electronic Nose, eds A d'Amico and C di Natale, 29 September –2 October 2002, Rome, Italy, pp. 58-63.
- [3] Sehra G, Cole M and Gardner JW, *Miniature taste sensing system based on dual SAW sensor device*, Proc. of 17th European Conference on Solid State Transducers Eurosensors XVII, 21-24 September 2003. Guimaraes, Portugal.

-
- [4] I.I. Leonte, M.S. Hunt, G. Sehra, M. Cole, J.W. Gardner, M. Noh and P.J. Hesketh, *A wireless microsystem for liquid analysis*, Proc. of IEEE Sensors 2004 Conference, October 24-27, 2004, Vienna, Austria, pp. 919-922.
 - [5] I. Leonte, M. Hunt, G. Sehra, M. Cole and J. W. Gardner, *SAW bio-liquid sensors with RF interrogation*, Proc. of IEEE High Frequency Postgraduate Students Colloquium, IEEE catalog no. 04TH8740, 6th and 7th September, 2004 UMIST Manchester, UK, pp. 47-52.
 - [6] J. W. Gardner, M. Cole, C. G. Dowson, P. Newton and G. Sehra, *Smart acoustic sensor for the detection of bacteria in milk*, Proc. of the IASTED International Conference Biomedical Engineering, February 16-18, 2005, Innsbruck, Austria, pp. 539-542.

Selected Abbreviations and Acronyms

TERM	DEFINITION
36YXLT	36° rotated Y-cut X-propagating Lithium Tantalate
AC	Alternating Current
ADC	Analogue to Digital Converter
ANN	Artificial Neural Network
APM	Acoustic Plate Mode
ASIC	Application Specific Integrated Circuit
ASV	Anodic Stripping Voltammetry
BAW	Bulk Acoustic Wave
CAD	Computer Aided Design
CCD	Charged Coupled Device
CMOS	Complementary Metal Oxide Semiconductor
CP	Conducting Polymer
CSV	Cathodic Stripping Voltammetry
CV	Cyclic Voltammetry
DC	Direct Current
DI	Di Ionised
DSP	Digital Signal Processing
EM	Electromagnetic
FET	Field Effect Transistor
FPW	Flexural Plate Wave
FRET	Fluorescent Resonance Energy Transfer
GDS	Graphic Data System
HR	High Resolution
IC	Integrated Circuit
IDT	Indigitated Transducer
IL	Insertion Loss
ISE	Ion Selective Electrode
ISFET	Ion-Selective Field Effect Transistor
LAPV	Large Amplitude Pulse Voltammetry
LSV	Linear Sweep Voltammetry

MECA	Mars Environmental Compatibility Assessment
MISCAP	Metal-Insulator-Semiconductor Capacitor
MISFET	Metal-Insulator-Field Effect Transistor
MOS	Metal Oxide Semiconductor
MOSFET	Metal Oxide Semiconductor Field Effect Transistor
MS	Mass Spectrometry
MSL	MicroStereoLithography
P.C	Personal Computer
PCA	Principal Component Analysis
PCB	Printed Circuit Board
PCR	Polymerase Chain Reaction
PTFE	polytetra- fluoroethene
QCM	Quartz Crystal Microbalance
RF	Radio Frequency
R.H	Relative Humidity
SAPV	Small Amplitude Pulse Voltammetry
SAW	Surface Acoustic Wave
SH-APM	Shear Horizontal Acoustic Plate Mode
SH-SAW	Shear Horizontal Surface Acoustic Wave
SRL	Sensors Research Laboratory
SSBW	Surface Skimming Bulk Wave
STW	Surface Transverse Wave
TCF	Temperature Coefficient of Frequency
TSFET	Taste Sensing Field Effect Transistor
TSM	Thickness Shear Mode
TTS	Triple Transient Signal
UV	Ultra-Violet

Symbol Reference

TERM**DEFINITION**

Chapter 1

Ag	Silver
AgCl	Silver chloride
Al	Aluminium
Au	Gold
C_o	Oxidised concentration
C_r	Reduced concentration
Ca	Calcium
Cu	Copper
E^0	Standard Potential
E^P	Electrode Potential
Fe	Iron
GaAs	Gallium Arsenide
KCl	Potassium chloride
LiNbO ₃	Lithium Niobate
LiTaO ₃	Lithium Tantalate
MSG	Monosodium Glutamate
Na	Sodium
SiO ₂	Silicon dioxide
SnO ₂	Tin oxide
ZnO	Zinc oxide

Chapter 2

ϵ_0	Permittivity of free space
ϵ_r	Relative permittivity
ΔA	Surface area
ΔF	Surface force
l	Wavelength
ρ	Mass density
ω	Angular frequency

v_l	Longitudinal velocity
v_{tr}	Transverse velocity
ν	Poisson's ratio
E_m	Young's modulus
c	Phase velocity of wave
c_{ijkl}	Elastic stiffness constant
D	Electrical displacement
E_k	Component of the electric field
e_{kij}	Piezoelectric constant
G	Lames' constant
k	Wave number
S_{ij}	Strain second-rank tensor
T_{ij}	Mechanical stress second-rank tensor

Chapter 3

a	Attenuation coefficient
K^2	Electromechanical coupling coefficient
y_{12}	Transfer admittance
Y_0	Equivalent characteristic SAW admittance
\bar{v}_n	Amplitude of the equivalent SAW voltage in n^{th} gap
\bar{V}_0	Amplitude of voltage V_0 generated by full aperture gap
G_0	Conductance
C_0	Static capacitance
G_1	Input conductance
S_e	Number of electrodes per electrical period
e_p^T	Effective dielectric constant of substrate
$P_{-s}(\cos \Delta)$	Legendre function of the first kind
t_0	Time delay
A_t	Ratio of triple transient signal to main input signal
y_1, y_2	Source and load admittances
y_{11}, y_{22}	Input and output admittances of IDTs

A_1, A_2	Transfer admittance elements of IDTs
u_1, u_2, u_3	Wave particle displacements
$Y_{11}, Y_{12}, Y_{13}, Y_{23}$	Admittance matrix components of IDTs
a	Width of electrodes
B	Acoustic susceptance
d	Internal distance between IDTs
I_1, I_2	Input and output SAW currents
l	Length of liquid loading
L	Electrical period
N	Number of gaps
T	Temperature
u_1, u_2	Input and output voltages
V	Applied voltage
v_f	Free surface SAW velocity
v_m	Metallised surface SAW velocity
v_t	Velocity of SAWs in IDT area
W	Acoustic aperture

Chapter 4

S_{11}	Reflection coefficient at port 1
S_{22}	Reflection coefficient at port 2
S_{21}	Transmission coefficient from port 1 to port 2
S_{12}	Transmission coefficient from port 2 to port 1
ΔA	Amplitude ratio
Δf	Phase difference
$\Delta a/k$	Attenuation change
$\Delta v/v$	Fractional velocity shift
H_2O	Water
H_2O_2	Hydrogen peroxide
NH_4OH	Ammonium hydroxide
AlN	Aluminium nitride

Chapter 5

n_1, n_2	Number of samples
S_p^2	Pooled estimate of population standard deviation
S	Adjusted standard deviation

Chapter 6

V_{GS}	Gate voltage
V_{DS}	Drain voltage
V_T	Threshold voltage
I_{DS}	Drain current
m_n	Effective surface mobility of electrons
C_O	Gate capacitance per unit area
W	Channel width
L	Channel length

Chapter 7

h	Metallisation ratio
l_t	SAW wavelength in the grating
k_i	Wave number
k_t	Wave number for Bragg condition
R_i	Acoustic impedance
Ar	Argon
Cr	Chromium
Si_3N_4	Silicon Nitride
Ta	Tantalum
Ti	Titanium

CHAPTER 1

Introduction

The purpose of this first chapter is to introduce the aims and objectives of the research followed by the introduction to the human chemical senses (the taste and olfactory systems) and the perception of flavour. The concepts of electronic tongue and electronic nose instruments used to mimic these chemical senses are covered, discussing the technology, current products, applications and limitations. The outline and structure of the thesis is presented at the end of the chapter.

1.1 Aims and objectives of the project

In the food and beverage industries, environmental testing, and other areas, human sensory tests are regularly employed, however the results depend on subjective judgements (variations between panels can be up to 50% in terms of flavour units). Therefore, the development of taste and odour sensors is very desirable. The main problems with electronic tongue and electronic nose devices are the cost of fabrication, the inability to integrate the interface electronics on the sensor itself, and to have devices that operate remotely. Devices with these combined features can result in low cost reproducible sensors, for use in hand held devices and remote sensing in harsh environments. The main work of this project is centred on the design and testing of detection (sensor) part of a piezoelectric (SAW) electronic tongue instrument. Firstly, the different SAW technologies are explored and appropriate technologies for liquid sensing are considered. The base technology in this project is not CMOS compatible,

hence the inability to integrate the electronics; however with the use of ZnO or GaAs it is possible to integrate electronics. The sensors are designed with the ability to detect electrical and mechanical properties of liquids, with a real-time electronic read-out, small size, robustness, and have a low unit cost. Also, the sensors do not have bio-chemical sensitive membranes, making the devices more durable with a longer lifetime. The sensors will be predominately based on shear horizontal surface acoustic wave devices (SH-SAW). Lastly, various high frequency sensors for remote sensing are investigated. The main objectives of the research may be summarised as follows:

- The design and development of novel SAW liquid sensors, employing shear horizontal surface acoustic wave (SH-SAW) delay line configurations. Sensors are fabricated using piezoelectric (LiTaO_3) wafers and do not employ any bio-chemical films.
- The characterisation of the novel SH-SAW sensors without any bio-chemical films in terms of sensitivity, temperature dependence and mass loading. Their response to analyte concentration and the effect of environmental factors (temperature) on the response.
- Ability to classify correctly basic tastes, discriminate different sample liquids and relate the results to the electrical properties of the sample liquids (conductivity).
- Discriminating the ability of the sensors to classify milks of different fat content and bacterial loading.
- Combination of the SH-SAW liquid sensors with novel CMOS compatible gas/vapour sensors, employing field effect transistors (FETs) using bulk CMOS for room temperature operation.
- Modelling, design and development of high frequency (433 MHz to 10 GHz) wireless SH-SAW devices on the piezoelectric wafers (LiTaO_3) and corresponding liquid test cells.

1.2 The human chemical senses

“...We have five senses, but only two that go beyond the boundaries of ourselves. When you look at someone, it’s just bouncing light, or when you hear them, it’s just sound waves, vibrating air, or touch is just nerve endings tingling. Know what smell is?... It’s made up of the molecules of what you’re smelling.” (Angels in America [1.1])

The author of this play overlooked the fact that vision and hearing are also just nerve endings tingling. However, the point that is made is that smell involves taking in molecules of the substance you smell into your body, which is one of the properties of chemical senses that discriminates them from the other senses. Consider a person drinking coffee, they smell it because molecules of coffee in gaseous form enter their nose, and they taste it because coffee molecules in liquid form are stimulating their tongue. Smell and taste have been called molecule detectors because they endow these gas and liquid molecules, with distinctive smells and tastes [1.2, 1.3]. Smell and taste often interact and together termed as flavour. A third sense working alongside smell and taste is the trigeminal sense. Trigeminal nerve endings in the tongue and oral cavity sense, *pungent* chemicals given off by such "hot" spices such as red chilli pepper (capsaicin), black pepper (piperine), mustards and horseradish (isothiocyanates), and onions (diallyl sulfide). They also respond to "cool" spices, such as mint (menthol), and to the chemical "bite" or "sharpness" of ethyl alcohol in tequila and rum. In each of these cases, our trigeminal nerve endings respond to chemical *irritants* rather than to gustatory taste cues per se.

As the stimuli responsible for tasting and smelling are on the brink of being assimilated into the body, these senses are often considered as "gatekeepers," which function (1) to recognise substances that the body requires for survival and hence should be consumed and (2) to detect things that would harm the body and therefore should be rejected. The gatekeeper function of flavour (taste and smell) is served by a large affective, or emotional, component, as things that are bad for us often taste or smell unpleasant, and things that are good for us generally taste and smell pleasant. Furthermore, smelling and tasting is associated with and can trigger memories, which in turn may create emotional reactions.

The taste and smell receptors are constantly exposed not only to chemicals they are designed to sense, but also to irritants (detected by the trigeminal sense), such as bacteria and dirt, and they undergo a cycle of birth, development, and death over a 5 to 7 week period. This process is called **neurogenesis** and is unique to these senses. In the case of vision, hearing and the cutaneous senses, the receptors are safely protected inside organs (eyes, ears and under the skin), however, the receptors of taste and smell are relatively unprotected, hence the need of the renewal mechanism.

In the following subsections taste and olfaction have been considered separately, and it is developed that they often interact. This combined experience, which is known as flavour is also discussed.

1.2.1 The human taste system

The taste system is introduced by describing the anatomy of the tongue and the process of transduction that generates electrical signals from taste stimuli. The tasting process begins with the tongue, when the receptors are stimulated by taste stimuli. The surface of the tongue has many ridges and valleys due to the presence of structures called the papillae, of which there are four kinds: (1) **filiform papillae**, shaped like cones they are found over the entire surface of the tongue, hence its rough appearance; (2) **fungiform papillae**, shaped like mushrooms they are found in the tip and sides of the tongue; (3) **foliate papillae**, are a series of folds along the sides of the tongue; and (4) **circumvallate papillae**, shaped like flat mounds surrounded by a trench and are found at the back of the tongue. All the papillae except the filiform papillae contain **taste buds**, with the entire tongue containing about 10,000 taste buds [1.4]. Figure 1.1 shows the tongue with the different types of papillae, the taste buds, and the taste cells.

A taste bud contains a number of **taste cells**, which have tips protruding into the **taste pore**. Transduction occurs when chemicals contact receptor sites located on the tips of these taste cells. The transduction process involves complex chemical events within the taste cell [1.5] and it occurs when the taste substances affection flows across the membrane of the taste cell. Different types of substances affect the membrane in different ways as shown in Figure 1.1 overleaf. Molecules of bitter and sweet substances bind to receptor sites, which release other substances into the cell, whereas sour substances contain H^+ ions that block channels in the membrane, and salty substances release sodium ions (Na^+) in solution that flow through membrane channels directly into the cell.

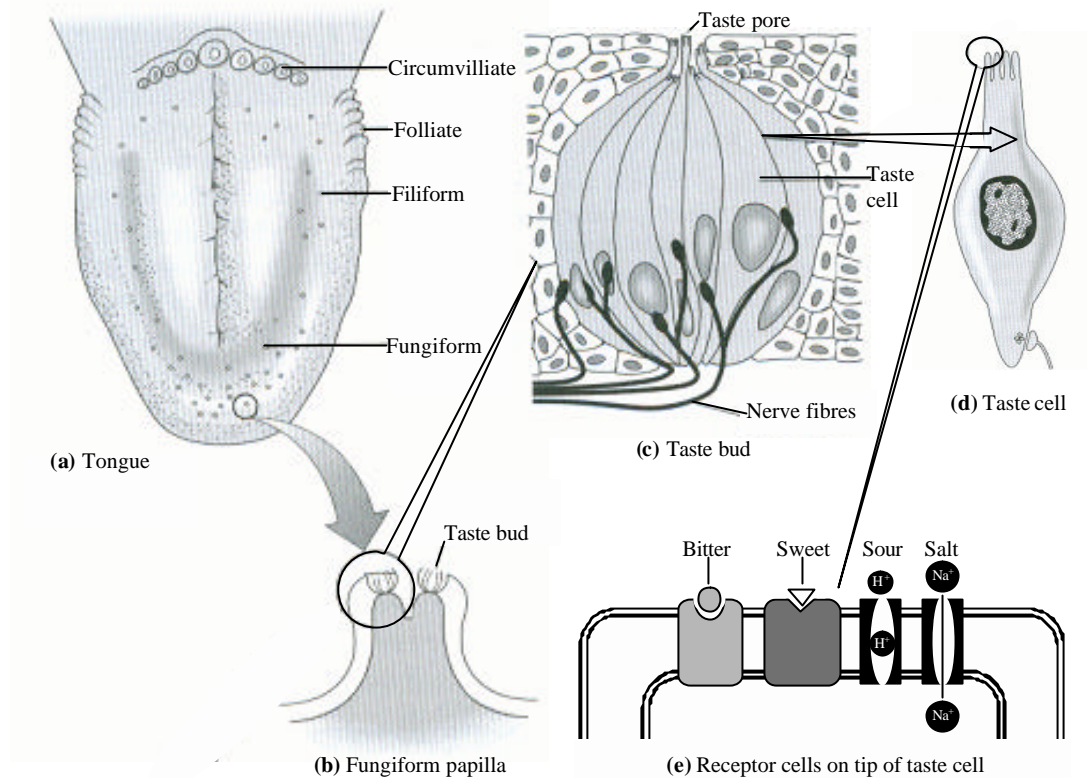


Figure 1.1 The tasting process (a) Tongue with different papillae (b) Fungiform papilla on tongue (c) Cross section of a taste bud and taste pore (d) The taste cell with tip just under the pore (e) Membrane at the tip of the taste cell with receptor sites [1.6]

The electrical signals generated in the taste cells are transmitted from the tongue to the brain. From the tongue they take two paths through the **chorda tympani nerve** (conducts signals from the front and sides of the tongue) and the **glossopharyngeal nerve** (carries signals from the back of the tongue). The signals from the taste receptors in the mouth and the larynx are transmitted in the **vagus nerve**. The nerves connect in the brain stem in the **nucleus of the solitary tract (NST)**, and from there, the signals travel to the thalamus and then to two areas of the frontal lobe – the **insula** and the **frontal operculum cortex** [1.7]. In addition, taste serving nerves also reach the orbital frontal cortex (OFC), which also receives olfactory signals.

1.2.1.1 Taste quality

When considering taste quality, it is simpler than olfaction. In the case of olfaction it has not been possible to fit the many olfactory sensations into a small number of categories or qualities, however, in taste research the taste quality is generally described in terms of four basic taste sensations: salty, sour, sweet, and bitter. Not all researchers

agree with this [1.8, 1.9] and suggest that there is a fifth basic taste called *umami*, which has been described as meaty, brothy, or savory, and is often associated with the flavour-enhancing properties of the chemical monosodium glutamate (MSG) [1.10]. As mentioned earlier there the trigeminal taste sensation is related to *irritants*, however here the main focus is on the four basic taste qualities.

Most of the taste experiences are described on the basis of the four basic taste qualities. Some substances have predominant taste and other substances have a combination of the four tastes. For example, sodium chloride (salty), hydrochloric acid (sour), sucrose (sweet), and quinine (bitter) are compounds with distinct single basic tastes. Other compounds, such as potassium chloride, have substantial salty and bitter components and similarly, sodium nitrate has a combination of salty, sour and bitter components. So their taste sensations can be based on these four taste qualities.

1.2.1.2 Neural taste quality coding

A sensory code is the information contained in the firing of neurons that represents what we perceive. The two ideas about sensory coding can be distinguished as, **specificity coding** that states that specific perceptions are signalled by the activity in specific neurons that are tuned to respond to specific qualities and **distributed coding**, that states, specific perceptions are signalled by the pattern of activity that is distributed across many neurons. There is uncertainty in whether the neural code for taste quality is distributed or specific. The evidence for distributed coding lies in neurons that respond to many substances, in particular substances which have the same across-fibre pattern, and the fact that it is sometimes not possible to tell what substance is present based on the triggering of only one type of neuron. Proof for specific coding is based on the presence of narrowly tuned neurons, the four transduction mechanisms that are specialised for specific molecular characteristics – the selective result of deprivation on sodium-active neurons, and the selective effects of amelioride on salty taste. The neural code for taste quality therefore can be considered as a combination of specific coding to signal a quality and distributed coding to indicate differences in tastes represented by a quality.

1.2.2 Human olfactory system

Odours are generally complex mixtures of molecules that can be identified by the mammalian olfactory system as they travel through air onto the receptor cells of the

nose. The olfactory system can be introduced by describing the anatomy of the receptors that generate the electrical signals from the olfactory stimuli and the central destination of these signals. The transduction occurs in the **olfactory mucosa**, which is the penny-sized region located high in the nasal cavity and contains the olfaction receptors. The olfactory mucosa is located in the roof of the nasal cavity just below the **olfactory bulb**, which is actually an outcropping of the brain.

Looking closely into the olfactory mucosa there is the **olfactory receptor neurons (ORN)**, this is where the transformation of chemicals to electrical signals takes place. The exact site of the transformation is the **olfactory receptor (OR)**, which are found on cilia located at the ends of ORNs. The olfactory receptor is a protein molecule made up of strings of aminoacids that cross the membrane of the ORN seven times. There are many different types of ORs, each made up of different sequences of aminoacids. Using genetic techniques that make use of the fact that ORs are created from instructions coded in genes, it has been recently shown by researchers that there are about 1,000 different kinds of ORs (not all active – about 500 active plus pseudo genes), each of which responds to the same group of odorants [1.11]. Furthermore ORs on a particular ORN are all the same, thus the response of an ORN reflects the properties of the types of receptors that mark its cilia.

The process of olfaction (outlined in Figure 1.2 overleaf) begins by the stimulation of the ORs by contact of the odorants. This occurs by either the flow of the odorants directly to the receptors in the stream of inhaled air or by odorants attaching to molecules called olfactory binding proteins, which transport odorants through the mucosa to the receptors [1.12]. On reaching the ORs the odorants trigger off a series of chemical reactions that lead to the opening of ion channels in the membrane. When the ion channels open, ion flow occurs across the membrane, resulting in an electrical signal in the cilium [1.13]. The signal is then transmitted to the rest of the ORN and into its axon, which being part of the olfactory nerve transmits the signal towards the olfactory bulb of the brain. On reaching the olfactory bulb the ORN axons split out to synapse in small round structures called **glomeruli**, higher level **mitral cells** and the **granular layer**. The input to the glomeruli is such that a particular glomerulus receives signals mainly from one type of ORN.

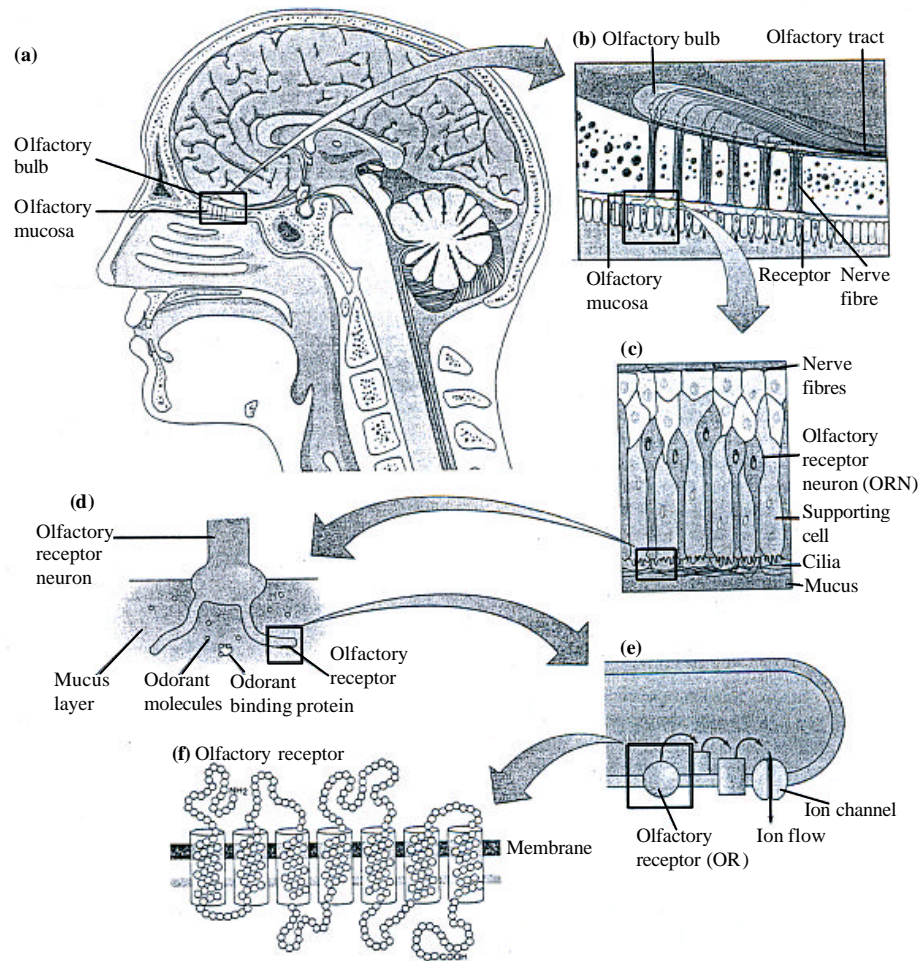


Figure 1.2 The smelling process (a) Olfactory mucosa and olfactory bulb (b) ORN (c) Detailed view of ORN (d) Olfactory receptors (e) Stimulation of OR triggers reactions and hence ion flow (f) Showing the OR is part of the membrane crossing it several times [1.6]

These cells processes and transmit the information to the olfactory cortex which projects it to higher sensory areas of the cerebral cortex which is made of the **primary** and **secondary olfaction cortex**. It is believed that considerable signal averaging occurs (~ 1000 to 1) within the granular layer to improve the signal-to-noise ratio and to amplify the signal, resulting in higher sensitivity and selectivity. Haberly has suggested that the olfactory cortex operates as a content-addressable memory, where a pattern of input signals, from an odour, stimulates a previous memory of that odour [1.14]. The information is stored as a unified sensing experience with memories such as names, places and feelings. The process begins with inhalation of odorous molecules and ends by stimulating the regions of the brain which control thoughts and behaviour.

1.2.2.1 Neural code for odour molecules

Neural code for olfaction poses the question, how does the brain know what odourant molecules are entering the nose? Odour quality may be affected by physical and chemical properties, such chemical reactivity, the electrical charge of the elements in the molecule, and the structure of the molecule, however it is difficult in simple terms to relate these physical and chemical properties and the odours we perceive. The focus has been made on determining what **chemical odorants** cause the triggering of the neurons rather than what **smell** that causes them to fire. Individual ORNs and their glomeruli typically respond to a group of chemicals. Some glomeruli may respond specifically to odorants that share a chemical feature, called an odotope, however the odorants are generally represented by the pattern of response of a number of glomeruli. Single neurons in the orbital frontal cortex (in the secondary olfaction cortex) respond to a number of different odorants.

1.2.3 Perception of flavour

What people usually refer to as “taste” when describing their experience of food (“that tastes good”) is usually a combination of taste, from stimulation of the receptors in the tongue, and smell, from stimulation of the receptors in the olfactory mucosa. This combination of taste and smell, is called flavour. The perception created by the foods is very complex and its not just dealing with one or two different flavours but many flavours contained within a “complex tapestry” [1.15]. The ability to pick particular flavours out of this complex tapestry of flavours is even more amazing when considering the chemical stimuli that create these flavours.

Flavour is the overall impression that is experienced from the combination of nasal and oral stimulation [1.16] and this has been demonstrated by many experiments using both chemical solutions and typical foods. Maxwell Mozell and coworkers [1.17] asked panels to identify common foods with the nostrils open and nostrils pinched shut. The result was that every substance they tested was easier to identify with the nostrils open. This is because when the nostrils are open the odour stimuli from the food reach the olfactory mucosa by following the **retro-nasal route**, from the mouth through the **nasal pharynx**, the passage that connects the oral and nasal cavities. Although closing the nostrils does not close the nasal pharynx, it does prevent vapours from reaching the olfactory receptors by eliminating the circulation of air through this channel. In more recent investigations [1.18] chemicals were applied to the tongues of subjects with the

nostrils open and closed. The results for two chemicals, sodium oleate and ferrous sulphate, showed that the oleate had a strong soapy flavour when nostrils were open but was judged tasteless when they were closed. Similarly, the ferrous sulphate which has a metallic flavour normally was judged tasteless when nostrils were closed. However some compounds are not influenced by olfaction. For example, monosodium glutamate (umami) had about the same flavour with the nostrils open or closed, in this case the sense of taste is predominant. These results indicate that many of the sensations that are called taste, and that are assumed to be caused only by stimulation of the tongue, are greatly influenced by stimulation of olfactory receptors.

It is also considered that trigeminal sense along with the sense of taste and olfaction plays a role in the perception of flavour. Receptors for the trigeminal sense are located in the soft tissues in the back of the throat as well as in other parts of the body and are sensitive to chemically irritant substances, such as those found in hot and spicy foods as described earlier. Furthermore, in beverages and food products, the trigeminal sense also craves mechanical (e.g., crunchiness and texture) and thermal stimulation (e.g., the heat and cold of coffee and cola). These mechanical sensations (e.g. viscosity, hardness and brittleness) are related to what is termed as “mouthfeel” a more subtle quality parameter that also contributes to the perception of flavour.

It has been shown that perceived intensities of binary mixtures of odorants and tastants presented in the mouth come very close to the sum of the perceived intensities of the two presented separately, indicating that there is no significant (note: cross-modality is an interesting field of study and the greatest influence is visual) sensory inhibition between taste and smell.

In the following sections ways of mimicking the human senses of taste and odour using so the so called ‘Electronic Tongue’ and ‘Electronic Nose’ are described. The various types of sensing principles and instruments utilising these sensing techniques, are introduced. In the food and beverage industries and other areas such as environmental testing human sensory tests are often called for. However, human sensory panels have problems such as individual variability, subjectivity, adaptation, infections, harmful exposure to hazardous compounds, mental state and impossibility of on-line monitoring. Therefore the development of taste and odour sensors is very important.

1.3 Electronic tongues

More recently using similar concepts to that of the mature electronic nose technology (see section 1.4), systems for use in the aqueous environment have been developed. These systems are related to the sense of taste in a similar way as the electronic nose to olfaction, thus the terms ‘electronic tongue’ or ‘taste sensor’ are introduced [1.19-1.21]. In certain applications there are advantages in measuring in the aqueous phase rather than in the gaseous phase, as the vapour analysis is an indirect method that relates back to the information about the aqueous phase but contains atmospheric dilutants/interferants. Compounds such as ions and those with low vapour pressure, can only be measured in the aqueous phase, also for many online and inline applications it is only possible to use systems that measure directly in the solution. The electronic tongue system functions by the sensors producing signals that are not necessarily specific to a certain species but a signal outline is produced that can be correlated to particular qualities of the sample. The various measurement principles, different types of electronic tongue devices and their applications are covered in the following sections.

1.3.1 Concepts of electronic tongues

The human taste system covering the aspect of basic taste qualities was previously described. The sense of taste may be presented in two ways with one aspect relating to the five basic tastes of the tongue; sour, salt, bitter, sweet and ‘umami’, as discussed in section 1.21. The other aspect of taste is related to the impression obtained when food enters the mouth. The basic taste is combined with the information from the olfactory receptor cells, when the aroma from the food enters the nasal cavities through the inner passage as seen in section 1.2.4 covering the perception of flavour.

There is a difference in the use of a sensor as a taste sensor or as an electronic tongue. A taste sensor system is used to classify the different basic tastes with the results compared to the human test panels whereas the electronic tongue classifies a quality of a kind of food (drinks, water, beverages etc.), with the results not necessarily compared with human sensations, but with other quality properties of the sample.

The term “electronic tongue” was introduced at the Eurosenors X conference in 1996 [1.20] while the first concepts of taste sensors were published a few years earlier, in 1990 [1.22, 1.23]. The reported devices were based on potentiometric

principles utilising either ion selective lipid membranes or ion selective electrodes. Winquist et al. introduced a voltametric electronic tongue in 1997 [1.21]. Different sensing principles have been used for electronic tongues or taste sensors, such as electrochemical methods like potentiometry or voltammetry, optical techniques, or measurements based on mass sensitive devices.

1.3.2 Sensing principles for electronic tongues

There are several measurement principles that can be used in electronic tongues. The most common ones used are based on electrochemical techniques such as potentiometry, voltammetry, and conductimetry. Both potentiometric and voltammetric techniques use electrochemistry which requires at least two electrodes and an electrolytic solution, with one electrode responding to the target molecule (working electrode) and the second is of constant potential (reference electrode) [1.24].

Potentiometry is a technique, where the surface potential is measured under the flow of no current. The measured potential at the working electrode is used to determine the analytical quantity of interest, such as the concentration of some component in the analyte solution. The potential that develops in the electrochemical cell is the result of the free energy change that would occur if the chemical phenomena were to proceed until the equilibrium condition has been satisfied. Different ion-selective electrodes/membranes (produce a potential that is proportional to the concentration of the analyte) for various recognition properties have been developed. These devices can be used to measure a large number of ionic species.

Voltammetric techniques utilise an electrode potential to drive electrons through an analyte and the resultant current produced is measured. The magnitude of the electric potential determines target redox reaction and whether molecules lose or gain electrons. Voltammetric methods can be used to measure any chemical analytes that are electroactive. This technique offers high sensitivity, a wide linear range, and simple instrumentation and the possibility to measure the conductivity and the amount of ionic compounds in the analyte.

Other measurement methods include optical and mass sensitive techniques and they have certain features that make them suited to electronic tongues. Optical techniques are based on absorption of light at specific wavelengths, from the ultraviolet through the visible to the infrared region. Most compounds have distinct absorption spectra, and by scanning a certain wavelength region, a specific spectrum for the

sample tested can be obtained. The optical techniques offer high reproducibility and good long-term stability.

Mass sensitive devices are based on piezoelectric crystals which operate at a certain resonance frequency such as the quartz crystal resonators. Adsorption of compounds on the surface of the crystal, shifts the resonant frequency of the resonator [1.25]. In the case of the surface acoustic wave (SAW) devices, a surface wave is propagated along the surface of the piezoelectric substrate. Adsorption of a compound in its path causes a change in the properties of the surface wave [1.26]. These devices are simple and provide the possibility to detect a large number of different compounds.

1.3.3 Potentiometric devices

Potentiometric devices employ an ion-selective electrode (ISE), a reference electrode, and a potential measuring device, that measures the interfacial potential at an electrode surface caused by a selective ion exchange reaction. A configuration of the well-known glass pH ISE is illustrated in Figure 1.3. The key to the development of these types of devices is the design of the ion selective membrane, and much research has been done in this area of ionophore-based potentiometric sensors and other improvements [1.27]. The potentiometric sensors use the voltage that is at zero current, typically representative of an equilibrium electrochemical process. These voltages arise because an electrochemical reaction occurs at metal surfaces or at membranes in liquid, solid, or condensed phases. Because the signal is taken for a process at equilibrium, the ultimate signal is less influenced by mass transport characteristics or sensor dimension and provides a reading reflecting the local equilibrium conditions. The generated signal is an electromotive force that is dependent on the activity of the analyte and is described by Nernst's equation given by equation (1.1).

$$E = E^0 + (RT/nF)\ln a \quad (1.1)$$

where E^0 is a constant for the system given by the standard electrode potentials, R is the gas constant, T the temperature, n the number of electrons involved in the reaction, F the Faraday constant and, a is the activity of the measured specie. The potential change is logarithmic in ion activity and ideally at room temperature a 10-fold ion activity change of a monovalent ion would result in a 59.2 mV change in the membrane potential. Response times depend mainly on how fast equilibrium can be established at the sensor interface.

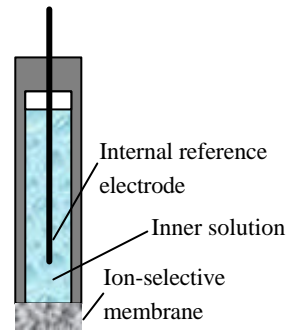


Figure 1.3 Potentiometric ion selective electrode

A common configuration includes the use of a silver-silver chloride electrode as the reference electrode. The electrode is made of a silver wire coated with silver chloride and placed into a solution of chloride ions. A porous plug serves as a voltage bridge to the outer solution. The ion-selective membrane has a similar configuration but an ion-selective membrane is applied to it instead of a voltage bridge. The membrane has to be nonporous, water insoluble, mechanically stable and also have a highly selective affinity for the particular ions. The binding effect of the ions, results in the build up of membrane potential as suggested before by equation (1.1).

Ion-selective field effect transistors (ISFETs) are attractive potentiometric devices, for the use in electronic tongues developed in the early 1970s [1.28]. Figure 1.4 shows a schematic diagram of an ISFET.

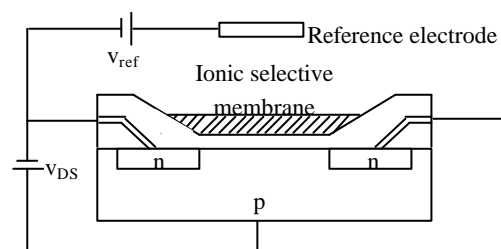


Figure 1.4 Schematic diagram of an ion-selective field effect transistor

In the ISFET the current between the drain and the source (I_{DS}) is dependent on the charge density at the semiconductor, which is controlled by the gate potential, which in turn is determined by the ion interaction with the ion-selective membrane. Here the normal metal gate is replaced with the reference electrode and sample solution. The features that make ISFETs attractive for their use in electronic tongues is their small

size and ability to directly integrate with solid-state electronics and also cheap fabrication at large scale.

The potentiometric devices offer many advantages for use in electronic tongues or taste sensors. There are a large variety of membranes available with different selectivity properties such as various glass membranes and lipid/polymer layers. However, these devices are only limited to measurement of charged species.

1.3.3.1 Potentiometric taste sensors

A significant amount of work has been reported on potentiometric type electronic tongues / taste sensors. One of the first concepts of the potentiometric taste sensors were introduced in 1990 [1.22, 1.23]. The taste sensor was based on a multichannel electrode configuration with transducers composed of lipid membranes immobilised with a polymer. The multichannel taste sensor has global selectivity and the lipid membranes are employed to transform information about substances producing taste into electrical signals and fed into a computer. The idea used to realise the taste sensor was through utilising materials that are similar to biological systems as transduction membranes. As in biological taste reception, the lipids in the biological membranes play an important role [1.29, 1.30]. This multichannel sensor was designed to detect the five basic taste substances. For sour, salty or bitter substances, the lipid is known to be a receptor site, whereas binding proteins act in the case of sweet or umami reception. Studies have reported that lipid membranes can respond to taste substances [1.31-1.34] in the same way as biological taste feeling [1.35, 1.36], and that these lipid membranes also respond to sweet and umami substances. Hence, lipid membranes were used as transducers. However it was seen that these lipid membranes posed weaknesses such as low reproducibility and insufficient information for taste quality recognition hence to overcome these weaknesses a multichannel sensor with polymer immobilised lipid membranes was realised.

Eight different kinds of lipid analogues were used: dioetyl phosphate, cholesterol, oleic acid, decyl alcohol, trioctyl methyl ammonium chloride, oleyl amine, distearyl dimethyl ammonium bromide and trimethyl stearyl ammonium chloride. The lipid membranes were fitted on a multichannel electrode as shown in Figure 1.5. The electrode was made of Ag wire embedded in a basal acrylic board.

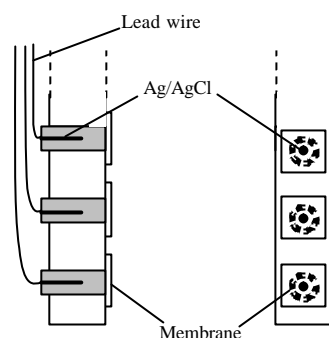


Figure 1.5 Cross-section (left) and front (right) view of the multichannel electrode [1.23]

The membranes were attached to Ag wires and dipped in KCl solution for preparation. The voltage difference between a reference electrode, composed of an Ag/AgCl wire enclosed in a fine glass tube with 100 mM KCl and 1 wt. % Agar, was measured. The five chemicals used for the basic tastes were NaCl for saltiness, HCl for sourness, quinine for bitterness, sucrose for sweetness and monosodium glutamate (MSG) for umami. Figure 1.6 shows their experimental setup. The patterns constructed from the electric potential in the eight lipid membranes were different for the basic tastes, while the pattern closely resembled each other for substances which elicited similar tastes with the lipid membranes showing good reproducibility. The system also showed the ability to distinguish between some kinds of drinks, such as coffees and beer, but could not give information of the taste quality. The responses to substances with the sweet taste were small and the system did not respond well to non-electrolytes, which have little effect on the membrane potential [1.37].

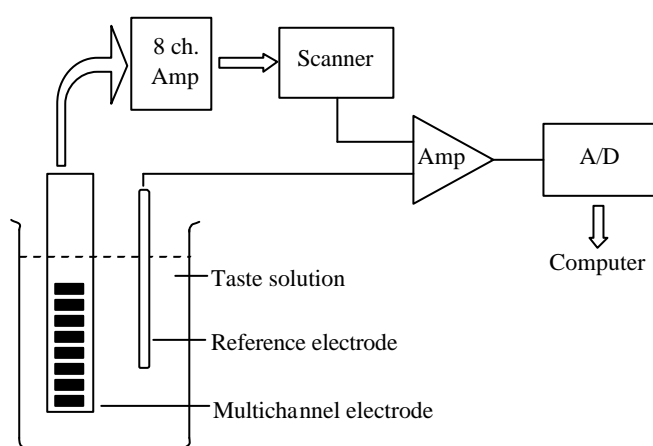


Figure 1.6 Experimental setup for the eight-channel electrode system [1.27]

Further development on these multichannel potentiometric devices has led to a commercialised system [1.38-1.40]. The system incorporates an eight-channel multisensor, placed on a robot arm and controlled by a computer. The test samples are placed in sample holder along with the cleaning solutions and reference solutions. The measurements are performed by dipping the multisensor in the cleaning solutions followed by placing it into the sample solutions. At certain intervals, the multisensor is calibrated by placing it in the reference solution. Figure 1.7 illustrates the commercial Anritsu Corporation SA401 and SA402 systems.

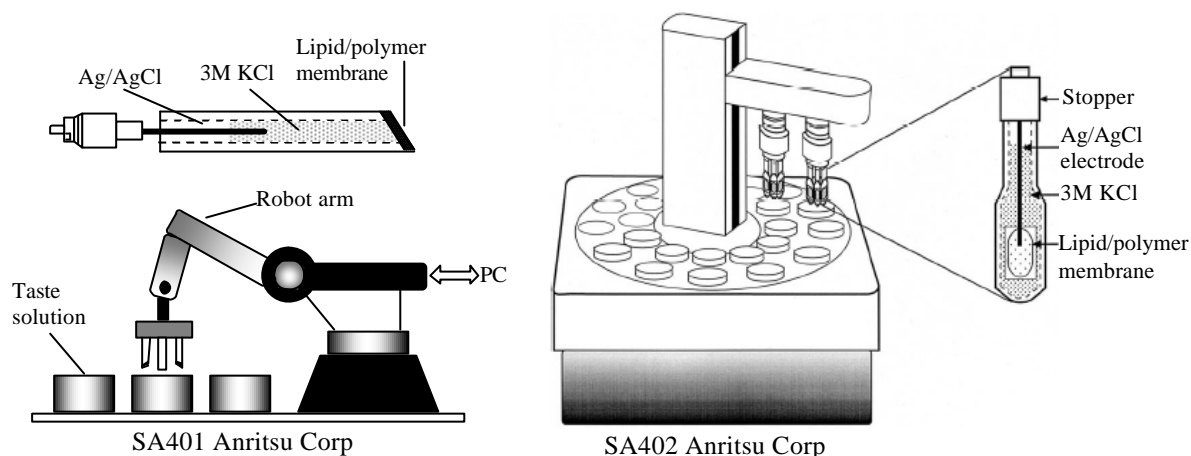


Figure 1.7 Anritsu Corporation taste sensing systems [1.38-1.40]

These taste sensing systems have been used in a number of different applications. They have been mainly used for discrimination and estimation of the taste quality of different commercial drinks, amino acids and other chemical substances with similar and different taste qualities. In one investigation, 33 different brands of beers were studied [1.41], with the samples analysed by both a sensory panel and the taste sensing system. The taste of the different beers was expressed by the sensory panels in terms of the parameters sharp-versus-mild and rich-versus-light. The output from the taste sensor was analysed using principal components analysis (PCA). It was seen that the first principal component corresponded well to the taste parameter rich-versus-light taste, and the second principal component corresponded well to the parameter sharp-versus-mild taste.

In another study the taste system was used to analyse 41 kinds of commercial mineral water [1.42]. A good correlation of the sensor outputs to the hardness of water was determined from the PCA plots and sensors discriminated between the different brands of mineral water.

Other applications involve the monitoring of the fermentation process of soyabean paste [1.37], estimation of the taste of ten brands of coffee from different origins [1.43] and taste variance of milk induced by heat treatment [1.44] and the development of a water quality monitoring system [1.45].

Based on the same principles as the multichannel taste sensor, work in to the development of integrated taste sensors for real-time measurements and miniature size has been researched [1.46]. Figure 1.8 shows a schematic diagram of the taste sensing FET (TSFET), which incorporates a MOSFET as the detecting part. The gate of the MOSFET is coated with lipid/polymer membranes used in the multichannel sensors. Eight MOSFET electrodes with the different lipid/polymer membranes were used and the gate-source voltage measured at constant source-drain current. Hence, the output is given by the V_{GS} the change in membrane potential brought about by the interactions between the membrane and chemical substances.

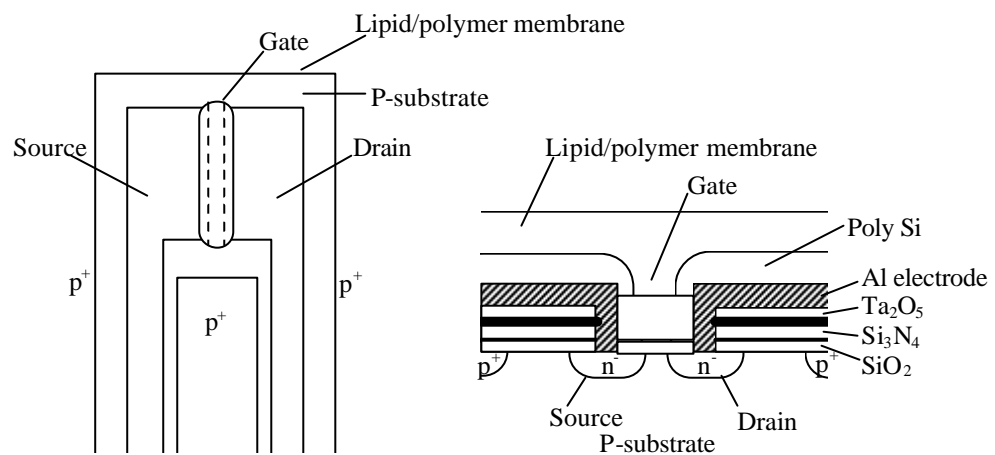


Figure 1.8 Detecting part of the TSFET with lipid/polymer membrane [1.46]

The TSFET has been used for similar applications as the multichannel sensor (such as coffee, canned coffee, beer and sports drink). It was found to give the same characteristics as the conventional taste sensor as the same lipid/polymer membranes were used. However, the stability was found to be poor then the conventional taste sensor. The results were encouraging and work is being done into the fabrication of an integrated taste sensing system.

Another commercially available taste sensing system based on potentiometry is the Astree e-tongue sensor array system. The system employs an array of sensors developed by ALPHA M.O.S. which consist of solid electrochemical electrodes with

the electrode surface covered by a patented coating. Different selectivity is obtained to various taste substances and compounds based on the coating materials. The sensors compose of silicon transistors with organic coatings that govern the sensitivity and selectivity of each individual sensor. Hence the coating development is critical to ensure good repeatability, sensitivity and selectivity. The measurement involves of a potentiometric difference between each coated sensor and an Ag/AgCl reference electrode. The α Astree electronic tongue is equipped with an array of seven different liquid cross-selective sensors. This system has been applied to a number of applications in the food and beverage industry and pharmaceutical / nutraceutical field. It has been used to discriminate substances of basic taste with a detection limit in the range of 1.0×10^{-6} Mol to 5.0×10^{-6} Mol. In another investigation the system has been used to measure the efficiency of a bitterness masking agent in drugs, and to determine its best concentration. The samples having the same concentration of masking agents, the drug formulation and the corresponding placebo were analysed. The effect of increasing the sugar level (of masking agent) showed a convergence in the results of the placebo formulation and the drug formulation and at no difference between the two the bitter taste is effectively masked giving the best concentration of masking agent.

An overview of the potentiometric devices has been given above, although these devices have high sensitivity and selective and used in number of applications they can not be applied to highly sensitive detection of non-electrolytes hence the introduction of other techniques such as voltammetry, which is covered in the following section.

1.3.4 Voltammetric devices

These devices involve the measurement of current at an applied potential. This current is a measure of the concentration of the sample analyte. The reaction occurring at the electrode is a standard redox reaction, with standard potential E^0 . The potential of the electrode, E^P , can be used to establish a relationship between the concentration of the oxidised (C_0) and the reduced form (C_r) of the analyte according to the Nernst relation given in equation (1.1). Substituting for the activity a gives

$$E^P = E^0 + RT / nF (\ln(C_0 / C_r)) \quad (1.2)$$

Thus voltammetry detects materials by oxidising them in solution at a positively polarised "working" electrode. The oxidised material gives up electrons which are collected by the working electrode and generate a current flow through it. The detection

of this current is the basis of the measurement method. Voltammetric techniques offer the possibility to use and combine different analytical principles such as cyclic, stripping, or pulsed voltammetry. Various aspects of information about the analyte can be determined by using these different techniques.

Cyclic voltammetry (CV) is one of the most commonly used electrochemical techniques, and is based on a linear potential waveform; that is, the potential is changed as a linear function of time. The rate of change of potential with time is referred to as the *scan rate*. The simplest technique that uses this waveform is Linear Sweep Voltammetry (LSV). The potential range is scanned starting at the *initial potential* and ending at the *final potential*. CV is an extension of LSV in that the direction of the potential scan is reversed at the end of the first scan (the first *switching potential*), and the potential range is scanned again in the reverse direction. The experiment can be stopped at the *final potential*, or the potential can be scanned past this potential to the second *switching potential*, where the direction of the potential scan is again reversed. The potential can be cycled between the two *switching potentials* for several cycles before the experiment is ended at the *final potential*.

Stripping voltammetry is a very sensitive method for the analysis of trace concentrations of electroactive species in solution. Detection limits for metal ions at sub-ppb concentrations have been reported. The technique consists of three steps. First, metal ions are deposited onto an electrode which is held at a suitable potential. The solution is stirred during this step to maximize the amount of metal deposited. Second, stirring is stopped so that the solution will become quiet. Third, the metal deposits are stripped from the electrode by scanning the potential. The observed current during the stripping step can be related to the amount of the metal in the solution. The stripping step may consist of a positive or a negative potential scan, creating either an anodic or cathodic current respectively. Hence, *Anodic Stripping Voltammetry* (ASV) and *Cathodic Stripping Voltammetry* (CSV) are two specific stripping techniques.

Normally the measurements are performed at a fixed potential, but the use of pulse voltammetry information related to diffusion coefficients of ions can also be determined. It is also possible to obtain further information using working electrodes of different metals types. When using these devices in complex media containing many redox-active species and various ions, the selectivity of the system is normally low for single component analysis. Large amount of complex information is obtained and to extract this multivariate analysis have been employed. Pulse voltammetry is the most

commonly used methods with greater sensitivity and resolution, with the *Large Amplitude Pulse Voltammetry* (LAPV) and *Small Amplitude Pulse Voltammetry* (SAPV) of particular interest.

LAPV involves the electrode being held at a base potential for which there are negligible electrode reactions and after a particular time delay the potential is raised to its final value. This causes current to flow through the electrode, initially sharp and then decays as the electroactive compounds are consumed and until the current remains. The properties of the transient response reflect the amount of diffusion coefficients of both electroactive and charged compounds in the solution. The excitation waveform for LAPV constitutes of successive pulses of gradually changing amplitude between which the base potential is applied.

In SAPV, a slow continuous direct current (DC) scan is applied to the electrode with small amplitude voltage pulses superimposed. This causes a change in the concentration profile of the electroactive species at the surface. The small pulse changes in electrode potential result in small perturbations in the surface concentration. Normally in SAPV the current is sampled twice, once just before pulse application and once at the end of the pulse, with the difference recorded as the output.

Voltammetry is a powerful technique with the ability to be applied to taste sensors/electronic tongues and has the advantage over the potentiometric devices as voltammetric devices can be used for detection of non-electrolytic solutions.

1.3.4.1 Voltammetric electronic tongues

Electronic tongue devices based on voltammetry have been developed and one of the first ones reported used pulse voltammetry (both LAPV and SAPV) [1.21]. These devices consist of a double working electrode (platinum and gold) and were applied to pulse voltammetry. The current and current transient responses were measured using a potentiostat connected to a computer, which was also used for the onset of the pulses, data storage and selection of working electrode (gold or platinum). This electronic tongue was used to discriminate between different types of orange juices, milk and tea [1.47].

Further development to this electronic tongue introduced a configuration with five working electrodes, a reference electrode and an auxiliary electrode of stainless steel. The five working electrodes were made from gold, iridium, palladium, platinum, and rhodium. They were embedded in epoxy resin and placed around the reference

electrode with the ends of all the electrodes exposed. The working and reference electrodes were housed in a plastic tube ending with a stainless steel tube acting as the auxiliary electrode. Each working electrode was essentially connected separately in a three-electrode configuration with the aid of relays. Figure 1.9 shows the setup of the multi-electrode voltammetric electronic tongue configuration.

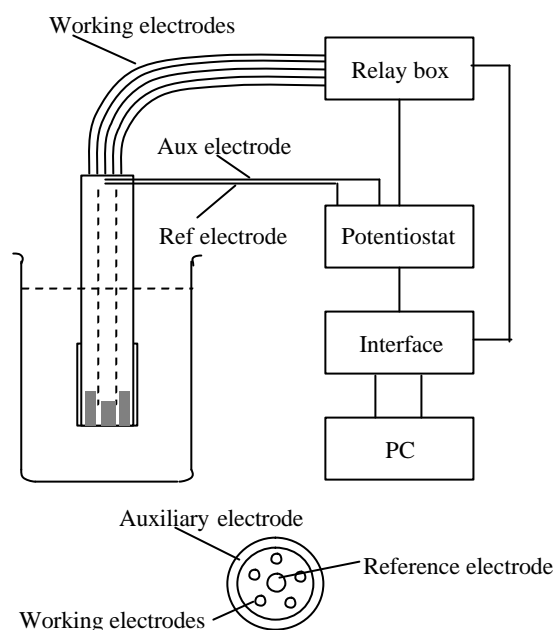


Figure 1.9 Setup of a multi-electrode voltammetric electronic tongue

The different types of pulse voltammetry, LAPV, SAPV and staircase could be applied to this electronic tongue setup. This electronic tongue has been used for a number of applications. In one study it was used to follow the deterioration of milk due to microbial growth when stored at room temperature [1.48]. The results were processed using principal component analysis (PCA) and the deterioration process could be followed. Artificial Neural Networks (ANNs) and projections to latent structure were also used to make models for predictions.

Further work by Winquist et. al. [1.49] reports the combination of the measurements techniques potentiometry, voltammetry, and conductivity. This hybrid electronic tongue was used to classify six different types of fermented milk. Using ion-selective electrodes, pH, carbon dioxide, and chloride ion concentrations were measured. The voltammetric electronic tongue consisted of six working electrodes of different metals (gold, iridium, palladium, platinum, rhenium, and rhodium) and a Ag/AgCl reference electrode. The current transients were measured and the

measurement principle was based on LAPV. The data from the measurements were analysed using multivariate data processing based on PCA and ANN. The separation of the different milks was successfully achieved. Other work with these voltammetric electronic tongues involved the development of a flow system that was used to pump the sample liquids and reference solution [1.50]. The pulse height was measured to determine the responses. The flow system offered advantages of lower baseline drifts due to relative measurements and the ability of injecting calibration samples into the measurement series. The voltammetric tongue has also been applied to monitoring the quality of drinking water [1.51].

Work on voltammetric electronic tongues has also been reported by the Jet Propulsion Laboratory (JPL), California Institute of Technology, and the Chemistry department at Tufts University [1.52]. The investigation was directed to developing a sensor for evaluating water quality, based on electrochemical techniques to detect and identify ions in solution. Cyclic Voltammetry (CV), corrosion measurements, and Anodic Stripping (ASV) methods were used to measure three marker ions Cu, Fe, and Zn that has been done using previous electronic tongue devices. Their system was based on an electrochemical cell developed for the MECA (Mars Environmental Compatibility Assessment) project [1.53], which included of 20 prefabricated ion selective electrodes, a conductivity sensor, a temperature sensor and an oxidation reduction potential sensor. The goal of their work was to develop a water quality sensor for use on the International Space Station Alpha and Martian habitat. The target ions were K^+ (340 mg/L), Ca^{2+} (30 mg/L), Mg^{2+} (50 mg/L) and Cl (200 mg/L) which represent some of the NASA Spacecraft Maximum Contaminant Levels (MCL) for portable water for the space station Alpha. The sensor consists of 3×3 array of working and reference electrodes and a four terminal thermometer arranged on a 45 mm ceramic substrate (alumina). Two different types of working and reference electrodes were fabricated using Pd(12%)/Ag(88%) and Au. The substrate is mounted in a chamber that contains an array of nine Au/Ni plated Cu auxiliary electrodes located above the working electrodes. The system is automated with the flow of the sample liquids into the apparatus to allow on-line measurement.

The approach to detecting the contaminants in water was based on a generic algorithm which has two purposes: to optimise the pattern matching algorithm based on chemometric techniques and to design and select the optimal experimental parameters

that control the conditions in the sample chamber. Using this approach they were able to discriminate between the contaminants in the water at high sensitivity.

Other application area under study is the use of the voltammetric electronic tongue for detection of microbial activity on foodstuff. The studies performed have shown the possibility to follow the growth of mould and bacteria, and also to separate between different strains of molds with a voltammetric electronic tongue [1.54].

Taste sensors based on voltammetric techniques offer high sensitivity and have the advantage over the potentiometric devices as they can be used with non-electrolytic solutions. Combining these different types of sensors can prove to be very useful and applicable in many areas such as the food industry and quality control.

1.3.5 Piezoelectric devices

Piezoelectric materials possess the property to generate an electric field on application of a mechanical force, and distort on application of an electric field. On application of an alternating voltage using an external source to the piezoelectric crystal, it generates a stable oscillation of electric voltage at a particular frequency, known as the resonant frequency. A change in mass of the crystal causes this resonant frequency to shift.

One of the most widely used piezoelectric device, is the quartz crystal microbalance (QCM). Here adsorbent layers on the crystal are employed for chemical sensitivity and selectivity. As the analyte gets adsorbed onto the layer the mass of crystal changes and in turn causes a shift in the frequency. Different chemical compounds can be measured by having chemical adsorbent layers of different affinity properties. Using an array of such devices coated with hydrophilic mono- and dicarbon acids (e.g. hydrophilic poly-carbon acid), organic and inorganic acids, and amines in drinking water have been detected [1.55]. The system used quartz microbalance sensors coated with poly-carbon acid polymer that has capabilities to interact with ionic and polar analytes via hydrogen bonding and salt formation. High signals from the sensors were achieved due to *mass reduction* process on the sensor surface as a result of an ion exchange process of detecting Na, Ca, Cu and Fe cations in water. The sensors in this study were made from AT-cut quartz with gold electrodes. A typical QCM sensor and the experimental setup used in this study are shown in Figure 1.10. Also reported are quartz resonator devices coated with lipid/polymer membranes to measure different taste substances [1.56]. Here the quartz resonator was coated with the same lipid/polymer membrane as that possessed by a potentiometric multichannel taste

sensor discussed in section 1.3.3.1. The oscillation frequency of the coated quartz resonator showed different responses depending on the taste substances and the lipid in the membrane. The responses of the membrane potential and the quartz resonator to taste substances were compared to study the interaction between the membrane and the taste substance.

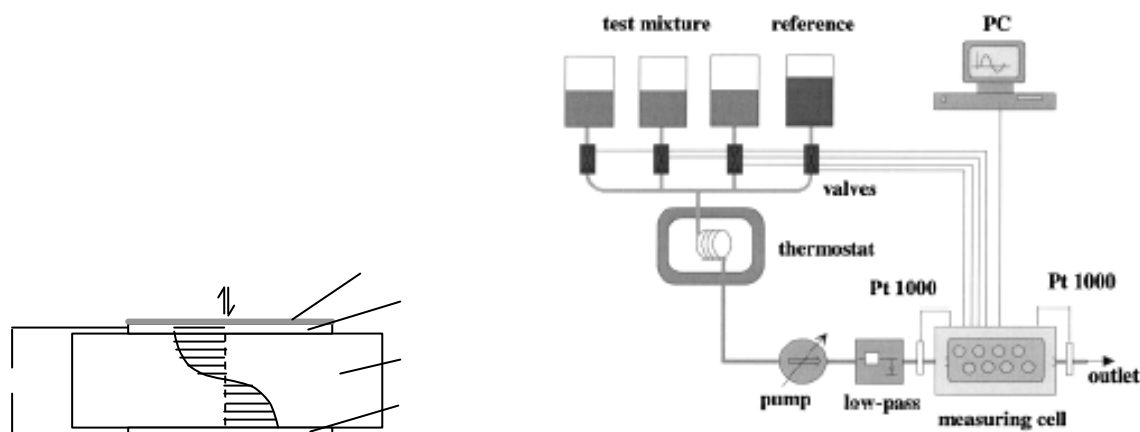


Figure 1.10 (a) Typical QCM sensor schematic (b) Setup for measurement of ionic and polar analytes in water [1.55]

Other devices based on piezoelectric substrates are surface acoustic wave (SAW) devices. For use in aqueous phase the shear horizontal mode (SH-SAW) of the SAW should be used [1.57, 1.58]. The substrates that support this mode of SAW have to be selected, such as the 36° rotated Y-cut X-propagating LiTaO_3 . The SAW devices use an interdigitated transducer (IDT) to launch and receive the acoustic waves, with the sensing part being between the transmitting and receiving IDT. The sensing principle is based on the liquid perturbations that affect the properties of the SAWs propagating on the surface of the device. Common properties measured are the amplitude ratio and phase difference between the sensing and reference signals. These devices can be utilised without any chemical selective membranes/coatings to relate to various mechanical and electrical properties of the analyte. These are small, low cost, robust devices with long life and durability due to absence of any chemical selective membranes. The SAW devices are discussed in more detail in the next chapter as this research project is based in this area of sensors. Schematic drawings of typical SAW delay line sensors and resonators are shown in Figure 1.11.

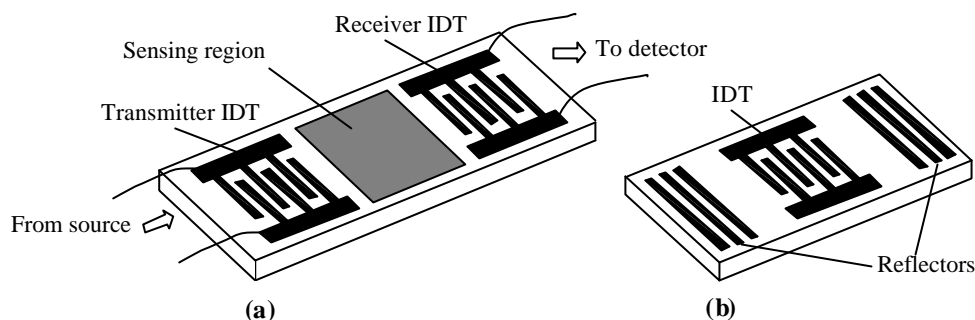


Figure 1.11 (a) SAW delay line sensor configuration (b) SAW resonator (no sensing element)

The shear horizontal surface acoustic wave devices have been applied to a number of applications. In one study the SH-SAW sensors were used to discriminate between orange juices of different origins and manufacture and 11 kinds of fruit juices [1.58]. In another investigation the same sensors by Kondoh et. al. were used to discriminate 17 types of commercial mineral water in terms of their electrical properties (permittivity and conductivity) [1.59] and in another liquid sensing system was applied to measurement of Japanese tea [1.60]. These sensors have no selective coatings however they have been used as biosensors by simple selective coatings of the device sensing area [1.61].

1.3.6 Optical devices

Optical techniques for use in electronic tongue sensors are an attractive alternative approach. This area is developing and research in optical electronic tongue devices has been reported. Work at the University of Texas in Austin [1.62] has been devoted towards the development of micromachined sensor arrays for rapid characterisation of multi-component mixtures in aqueous media. The functionality of the sensor array is based on that of the mammalian tongue and the sensors create specific patterns for different mixtures of analytes.

The sensor arrangement has been done to mimic a mammalian tongue in that, microbeads are arrayed on a silicon chip (about 1 cm²) in a similar fashion to the taste buds on a tongue. Each of the beads are claimed to respond to different analytes like the tongue responds to the basic tastes. This 'optical electronic tongue' has the ability to assay solution content for Ca²⁺, Ce³⁺, H⁺, and fructose using colorimetric indicators that are covalently linked to polyethylene glycol-polystyrene resin beads. The beads are deposited into an array of micromachined etched wells localised on a silicon wafer,

representing taste buds. The micromachined structure is directly interfaced to a charged-coupled-device (CCD) which is used for the simultaneous acquisition of the colorimetric data from the individually addressable beads. A change in colour of the beads on exposure to analytes is examined using simple RGB analyses to determine the colour patterns distinctive to the analytes. Figure 1.12 shows a schematic representation of a single bead in a machined well and the setup of the measurement system [1.62].

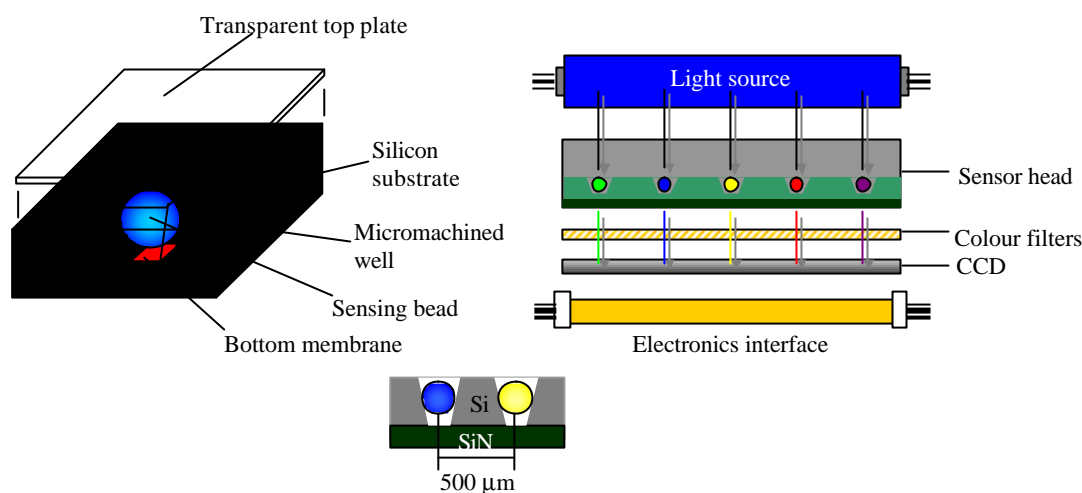


Figure 1.12 Setup of colorimetric electronic tongue and sensing beads in machined wells

The system offers fairly good reproducibility, with bead response and reversibility times in the minutes range and good stability. The response from the sensors is in terms of a colorimetric effect and a fluorescent effect due to the swelling of beads causing a fluorescent resonance energy transfer (FRET). With the use of arrays of different beads unique colour patterns can be used to produce high specificity along with the aid of pattern recognition techniques and learning algorithms. The system can be applied to food, water quality monitoring.

A team of researchers led by Professor David Barrow, at Cardiff University, UK have proposed a low cost miniature electronic tongue design to determine pollution in river water [1.63]. The electronic tongue device uses a technique for separating mixtures known as chromatography, which requires detectors with a large surface area. Conventional column chromatography techniques use columns packed with tiny glass beads that pass liquids or gases. Chemical detectors on these beads sense the presence of other substances in the fluid. The sensor is based on a sieve like structure where millions of tiny pores and channels are etched into a silicon chip creating a huge surface area in a tiny space. This detection end can be placed into rivers and factory

process streams to monitor the mixtures flowing through it. Figure 1.13 shows a picture of the silicon chip with tiny pores (taste chip) as a measurement setup.

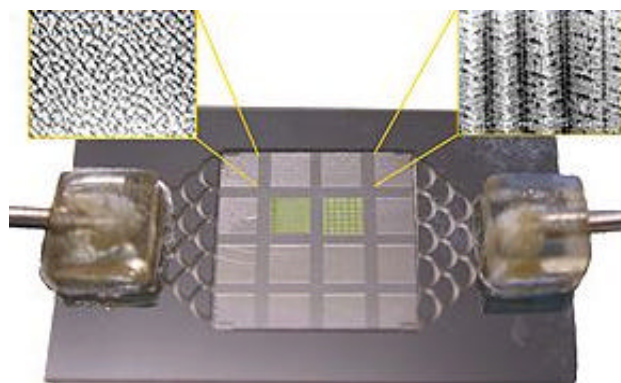


Figure 1.13 Silicon chip with tiny squares and channels [1.70]

Recent work has been reported with efforts into development of a handheld electronic tongue instrument that uses a quad sensor arrangement with ultra thin films deposited on gold interdigitated electrodes [1.64]. High sensitivity was achieved through having ultra thin layers with the sensors produced with Langmuir-Blodgett films [1.65] of 16-mer polyaniline oligomer, polypyrrole, and a ruthenium complex and with self-assembled films of an azobenzene-containing polymer. The output was based on spectroscopic impedance measurements of the transducers. This electronic tongue has been applied to distinguish the four basic tastes in addition to detecting organic contaminants in ultra pure water and identifying different brands of coconut water and suppression of quinine using sucrose was also detected. The ac measurements were performed at various frequencies, with the admittance being treated theoretically with an equivalent circuit representing the sensor immersed in a polyelectrolyte solution. The impedance measurement technique offers the advantages over potentiometric and voltammetric devices such as the no need to treat the solutions to be analysed and no need of a reference electrode. The sensors also offers good stability and fast response times however to achieve good reproducibility and comparable results the films have to be soaked for at least ten minutes before the measurements [1.64].

Having discussed the various types of devices technologies used for electronic tongue instruments and their relative advantages and disadvantages, the next section covers the more developed area of electronic noses. The concept of the electronic noses and various technologies in gas/odour sensors are discussed.

1.4 Electronic Noses

The electronic nose instrument can be considered as a simple and crude replication of the mammalian olfactory system. The human sensor system has until recently been considered the only way to distinguish complex odours such as food and beverages. Not surprisingly, human sensory tests are still called upon for odour discrimination due to its simplicity and discriminating power. More recently, there has been considerable interest and development of the electronic nose instruments to perform these discriminatory tasks. The architecture of the electronic nose can be paralleled to the mammalian olfactory system and segregated into three distinct components: detection, signal processing and identification/recognition. Here a brief history and overview of electronic nose technologies is presented.

1.4.1 Concept of electronic noses

Early research by Hartman in 1954 using an electrochemical sensor can be considered as the first experimental instrument [1.66]. The concept of the odour sensor was introduced by Hartman and Wilkens in 1964 [1.67] followed by arrays of gas sensors in the 1980s, by Stetter [1.68] that could be used to detect complex odours. The term ‘electronic nose’ was first used amongst others, by Persaud et al. in 1982 [1.69], since then, gas sensor technologies, pattern recognition techniques and neural networks have led to the fast development of gas and odour analysis systems.

The electronic nose has been defined by Gardner and Barlett 1994 [1.70] as “an instrument which comprises an array of electronic chemical sensors with partial specificity and an appropriate pattern recognition system, capable of recognising simple or complex odours”. The electronic nose instrument can be divided into an odour delivery system, a detection stage of gas sensors, a number of signal processing steps, and a pattern recognition action to identify the odour. Figure 1.14 gives a schematic of a typical electronic nose instrument and its comparison to the mammalian olfactory system [1.70]. Here the individual sensors i within the electronic nose produce a time-dependent electrical signal $V_{ij}(t)$ in response to an odour j . The response from each sensor is processed and the output represented as $X_{ij}(t)$ and the output from n sensors is a vector given by $X_j = \{X_{1j}, X_{2j}, \dots, X_{nj}\}$. The output of the sensor array is first trained by a pattern recognition (PARC) technique that relates the output from a known odour to a set of descriptors (k classes) held in the knowledge base and then the response from

an unknown odour is tested against the knowledge base and the predicted class membership is given (e.g. Class j as in Figure 1.14)

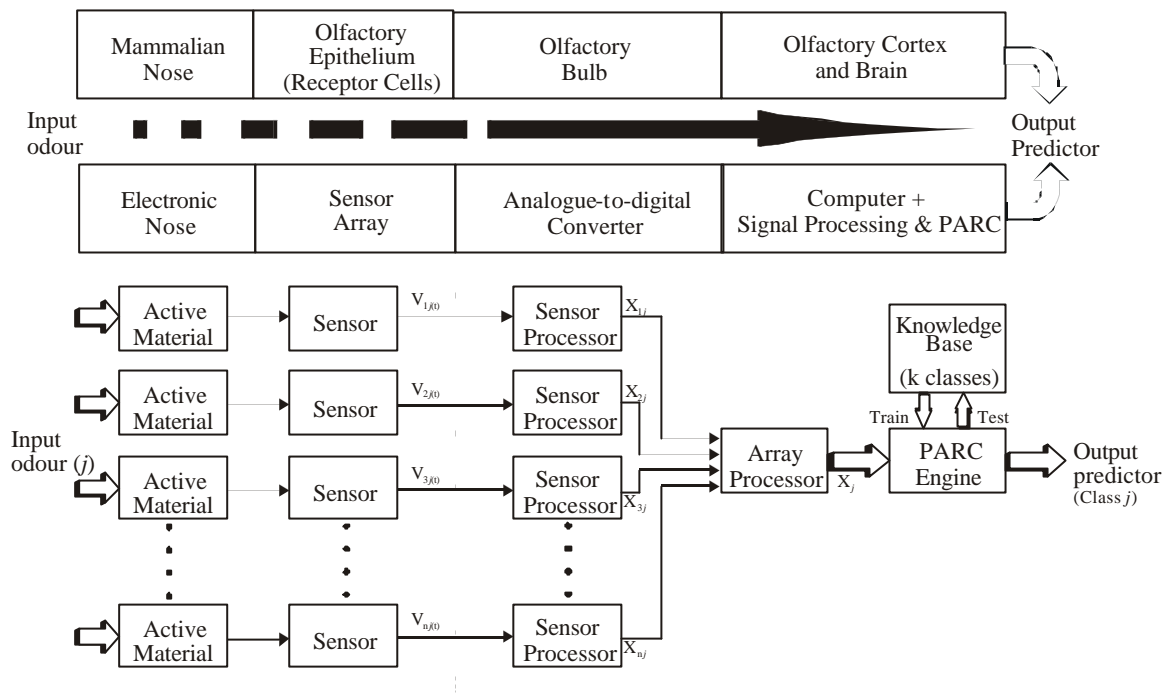


Figure 1.14. A simple schematic of an artificial olfactory system and the mammalian olfactory system [1.70]

1.4.2 Odour / Gas sensors

An odour sensor can be considered as an equivalent of the receptor cell and glomeruli performing the signal measurement role for an electronic nose. Regardless of the sensor output, i.e. an electrical signal, such as resistance, voltage or frequency, or other form depending on the sensor technology, the basic function of the sensor is the same: to convert a chemical input into a useable signal [1.71]. An ideal gas sensor would have a number of generic characteristics independent of any particular sensor technology [1.71]. A clear requirement is that the sensor responds to the input chemical with a wide sensitivity range from low concentrations to the saturation level, of that chemical in any defined environment, without the output itself saturating. In addition, this response would be linear throughout the concentration range. Furthermore, it is necessary that the sensors have an adequate dynamic range and do not saturate in their response in the normal concentration range. Ideally, the sensors should have a linear response to concentration in order to allow the application of linear data processing techniques. In practice, all sensors saturate at some value, at the lowest concentrations the detection limit is determined by the noise, hence it would be desirable for it to be as small as possible.

The sensor response time is another important characteristic. Ideally this would be just a few seconds (<10 s) however, this may not always be possible and for many applications a slower response may be adequate. The recovery time of the sensors following exposure to a sample is also very important as this defines the sampling rate of an instrument consisting of these sensors. The responses from the sensors should be repeatable and return to their initial value once the odour is removed. The common problems encountered with reproducibility of response over time arise from drift in the sensitivity of the sensors and the effects of poisoning. Drift is generally the slow variation in sensitivity, depending on the environmental conditions (e.g. temperature humidity and flow rate) and the ageing effects of the sensor due to slow morphological changes in the sensor material. Sensor poisoning is another problem which is caused by materials that irreversibly bind to the sensing material thus reducing magnitude of response or even total loss of sensitivity. Poisoning can be avoided by careful choice of sensors for particular applications and in the case of biological systems, averaging over a large number of cells that are replaced when poisoned. Careful conditioning of both the sensors and the inputs can minimise these affects.

There are many different gas sensing technologies currently being used in electronic nose instruments as discussed below.

1.4.2.1 Metal-oxide gas sensors [1.72]

These are one of the most widely used and commercially available sensors. These sensors most commonly utilise SnO₂ although many metal oxides show gas sensitivity under suitable conditions. The metal oxide is commonly doped with small amounts of catalytic metal additives such as palladium or platinum and by changing the catalyst material and the operating conditions, sensors for various applications can be developed. The basic construction of the sensors the same (commonly know as the Taguchi-type) comprises of a ceramic tube housing a platinum heater coil. The outside of this tube is coated with sintered metal oxide and the catalytic additives. The sensor effect is a change in conductivity, through an increase in carrier concentration and in potential barrier between grains of the metal-oxide. The general operating temperature range for these devices is between 300 °C and 550 °C depending on the sensing gas.

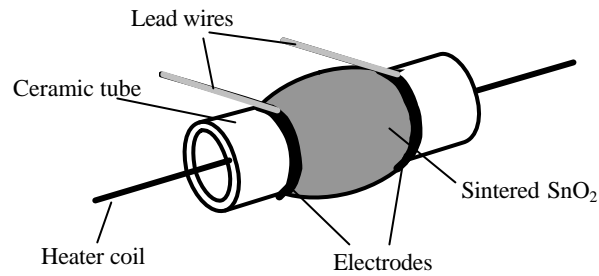


Figure 1.15 Structure of a Toguchi-type tin dioxide gas sensor

1.4.2.2 Conducting Polymer gas sensors [1.73]

These sensors utilise electrically conducting polymers typically in the form of a simple chemoresistor structure. In this the polymer is deposited across the gap between the two electrodes, usually gold, and the dc electrical resistance of the structure monitored. The sensing mechanism is a change in conductance due to exposure to an organic vapour. These sensors demonstrate responses to various organic vapours with the magnitude of the responses varying from polymer to polymer. Further more the devices are small with low power consumption as they operate around room temperature with fast response times and rapid recovery to the baseline when the vapour is removed.

1.4.2.3 Acoustic wave gas sensors [1.74, 1.75]

The sensing effect of acoustic wave gas sensors is the adsorption of molecules on the propagation path of the acoustic waves. There are two main types of acoustic wave gas sensing devices: those based on bulk acoustic waves (BAW) and those on surface acoustic waves (SAW). In both, the basic device consists of a piezoelectric substrate coated with a sorbent material. Binding of the vapour molecules onto the sorbent coating is detected by their effect on the propagation of the acoustic wave causing changes in the wave velocity, hence frequency and amplitude.

BAW devices also known as quartz crystal microbalance (QCM) or thickness shear mode (TSM) are very simple piezoelectric sensors comprising of single quartz crystal typically of about 1 cm in diameter with electrodes (usually gold) evaporated onto the two large faces. When the device is excited at a characteristic resonant frequency the quartz oscillates whereby the particle displacements on the sensor surface are normal to the direction of wave propagation (transverse shear mode). The polymer layer is deposited on the sensor surface and sensing mechanism is a change in the resonant frequency, due to an increase in mass as the vapour gets adsorbed on the

polymer (assuming viscoelastic effects are negligible). A common drawback of these sensors is the sensitivity of the devices to external effects such as temperature, humidity, and flow.

The SAW devices are based on a piezoelectric substrate with interdigitated electrodes (IDT) to launch the surface waves (Rayleigh wave). On excitation the waves are radiated in both directions from IDT structure. These devices are usually operated in two configurations, either as a delay line or as a resonator. In the delay line configuration the second IDT is used to receive the transmitted wave. In the resonator configuration as same transducer (IDT) acts as a transmitter and receiver, with the waves being reflected back to the transducer by a groove or ridge (reflector) formed on the crystal surface. In both cases the propagation of the surface acoustic wave is affected by changes in the properties of the crystal surface (usually coated with polymer film) by predominantly a mass sensitivity (assuming viscoelastic effects are negligible), which is exploited in gas sensing applications. See Figures 1.10 (a) and 1.11 for typical acoustic wave sensor configurations.

1.4.2.4 Field-effect gas sensors [1.76]

These sensors are based on metal-insulator-semiconductor structures in which the metal gate is a catalyst for gas sensing, typically platinum, palladium and iridium. There are two basic configurations: metal insulator-semiconductor field-effect transistor MISFET and metal-insulator-semiconductor capacitor MISCAP. Both configurations operate on the same basic principles, a change in the surface potential at the insulator layer brought about by a change in work function between the gate material and the semiconductor, but they differ in the method of measurement. In the MISFET the surface potential controls the drain current through the work function of the semiconductor whereas in the MISCAP it determines the capacitance of the device. The change in the work function is due to the formation of a hydrogen dipole layer at the metal-insulator interface. All hydrogen containing species will result in a response from these sensors, with production of hydrogen at the catalytic surface of the sensor. The operation temperature of these silicon based sensors is between 100 °C and 250 °C depending on the gas or vapour under test.

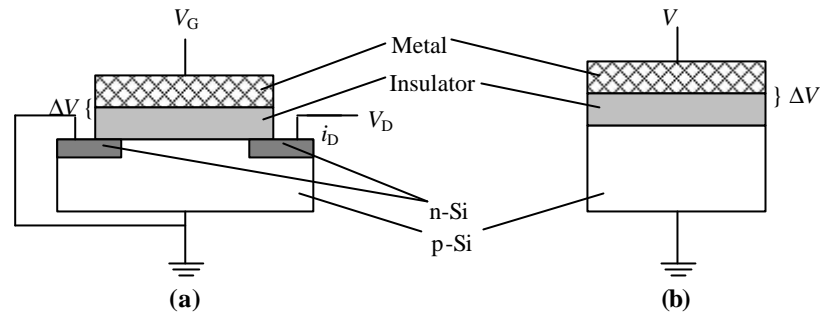


Figure 1.16 Two types of field-effect gas sensors (a) MISFET (n channel) (b) MISCAP

1.4.2.5 Electrochemical gas sensors [1.77]

Electrochemical gas sensors are based on the electrochemical oxidation and reduction of an analyte on the catalytic surface of the sensor. The sensing electrode is typically a metal or other catalyst, combined with carbon coated onto a hydrophobic membrane. The analyte gas diffuses through this membrane and reacts at the boundary between solid electrode, the liquid electrode and the gas. The other two electrodes, the reference and the counter, lie in an electrolytic solution within the body of the device. The electrolytic solution used in these sensors is a concentrated aqueous solution, usually sulphuric acid or potassium hydroxide depending on the sensor chemistry. These sensors normally operate at room temperature and are available for a wide range of redox gases.

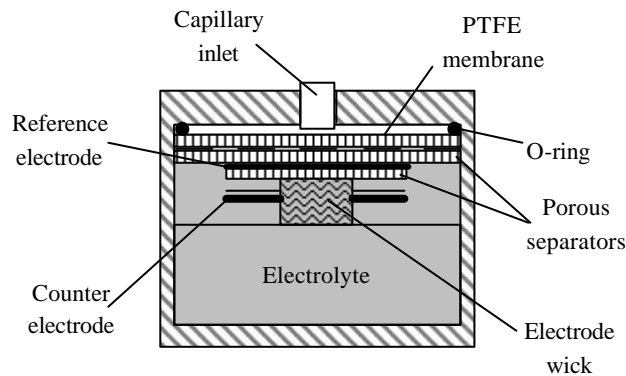


Figure 1.17 Basic arrangement of an electrochemical gas sensor

1.4.2.6 Pellistors [1.78]

These sensors are used for detecting combustible (flammable) gases. The operational principle is the detection of heat released when the combustible gas reacts with oxygen on the surface of a small catalytic bead. The typical pellistor device consists of a fine platinum wire heater coil housed in a bead of porous alumina containing particles of catalytic metals, such as platinum, palladium, or platinum/palladium composites. The

platinum coil serves as a resistive heater to speed up the combustion reaction ($\approx 500^{\circ}\text{C}$) and also as a platinum resistance thermometer to measure the temperature of the catalyst bead. When the combustible gas reacts with oxygen the heat generated and associated rise in bead temperature is detected as a resistance change of the platinum wire.

1.4.2.7 Fibre-optic gas sensors [1.79]

These employ an optical fibre to guide light to and from a chemically sensitive layer. The most common configuration involves the placement of the optical sensing element at the distal end of the fibre. The detection is achieved through measuring optical properties such as optical path length (swelling or refractive index), luminescence, absorption, fluorescence and reflectance. Due to the small diameter of the fibres, large number of fibres can be put together to fabricate miniature sensor arrays. Further more the measurements can be made remote as the fibre allows transmission of light over several kilometres and the devices are not subject to electrical interference. The sensing materials can also be dyed to fluoresce in the presence of certain analytes.

1.4.3 Signal processing and identification in electronic nose instrumentation

The electronic nose instruments include tools that condition the input signal before recognition similar to the olfactory bulb of the human nose [1.80]. These signal processing techniques are used to remove or minimise the effect of noise and baseline drift from the signal. The algorithms most commonly used are difference, averaging, normalising, relative signal, linearisation and autoscaling. These techniques can be customised to the specific sensor or transduction mechanism. For example, the difference measurement is used by many researchers for a response to air followed by a test sample and may remove some of the common additive errors. More recent work, involves the combination of static and dynamic response information to improve the selectivity of the sensors. This signal pre-processing is critical and has a significant effect on the performance of the subsequent pattern analysis systems.

The pre-processed data from the electronic nose instrument is fed into a pattern recognition (PARC) algorithm employed to analyse this information (discrimination and odour identification/classification). The problem of pattern analysis of electronic nose data is closely linked to that of chemometrics or multivariate data analysis [1.81].

There are a large number of PARC algorithms available for electronic nose applications, but to appropriately select one it is necessary to understand the nature of data being analysed. There are two main methods of odour recognition, the common conventional classical statistical parametric PARC techniques and non-parametric (data-driven) methods such as artificial neural networks (ANN) [1.81, 1.82]. The classical statistical PARC is based on application of a probability density function. Recent interest in learning from data has resulted in the development of biologically motivated methodologies, such as artificial neural networks. ANNs are based upon a number of parallel distributed processing elements that store experiential knowledge and make use of it [1.83]. The processing elements represent the biological brain cells or neurones, and their interconnections, the synaptic links. This technique involves a learning or training process to determine the interconnections in the network, known as the synaptic weights. The pattern recognition ability of ANNs is potentially higher than classical PARC methods, due to the parallel signal processing and their ability to deal with non-linear responses. Furthermore, they have greater tolerance to sensor drift and noise, although it is time consuming to optimise the size and shape of the network and to find the best training rule.

1.4.4 Electronic nose applications

The electronic nose has been used in the food industry for assessing various foods, such as freshness of seafood through to maturity of cheese [1.84, 1.85]. In the beverage industry, electronic nose instruments have been used to examine quality of beers and spirits [1.86]. The most lucrative market for electronic nose instruments/gas monitors is in the automotive industry. Here the companies are interested in applications such as the monitoring of air quality in the cabin of the car, but current instruments are bulky and expensive for the mass market. The solution is the development of smart gas sensors, possibly employing CMOS technology, to create small, integrated sensors with a high yield, good repeatability and most importantly at a low cost.

1.5 The combination of electronic nose and electronic tongue

The appreciation of food is based on the collective response of all the five major human senses: vision, tactile, auditory, taste and olfaction. The first impression is given by the appearance of the food, followed by the information of weight and texture when held. When ingested, further information is given by the basic taste and smell.

The sense of flavour is principally the combined effect of the senses of taste and smell. Thus the electronic tongue and electronic nose combination can be regarded as an artificial flavour sensor. Various applications involving the combination of the electronic tongue and electronic nose have been reported. One of the first studies was performed on different types of wines, classified using a taste sensor array with lipid/polymer membranes and an odour sensor array with conducting polymer electrodes [1.87]. Further studies have been done to see the effect of aging of wines, and more detailed studies of wines based on investigating the results from different sensor systems. Here, an electronic nose based on eight quartz microbalance (QCM) sensors using different metalloporphyrins layers and an electronic tongue based on six porphyrin-based electrodes were used [1.88]. The combination has also been used to classify different fruit juices, with the electronic nose based on ten MOSFET devices and an electronic tongue based on the pulse voltammetry technique [1.89].

1.5.1 Commercial electronic noses and tongues

There are several research groups and small companies involved in the development of electronic nose and tongue instruments. Research at university combined, with the many practical applications, has led to improvement in both sensor technologies and pattern recognition techniques. These instruments should not be confused with sensors or sensor systems that detect only simple single gases or vapours; e-noses are designed to measure and quantify chemical signals from complex odours, where there may be over a thousand different chemical components.

There are a number of different sensor technologies available for both the electronic nose and electronic tongue as described earlier, and no two instruments are based on exactly the same technology. Some commercial instruments are listed in Table 1.1.

Table 1.1 Electronic nose and tongue manufactures

Company	Sensor type		Product name
	E-Nose	E-Tongue	
Agilent Technologies	MS	—	4400
Alpha M.O.S	MOS, CP, SAW MS and MS-EN	Potentiometric	Fox, Centauri, Gemini Kronos and Prometheus Astree (E- Tongue)
Anritsu Corporation	—	Potentiometric	SA401, SA402
Applied Sensor	MOSFET, MOS, QCM 4 × MOS, 8 × QCM	—	3320, 3310
Bloodhound Sensors	CP	—	BH114
Cyrano Sciences Inc.	CP	—	Cyranose 320
Daimler Chrysler Aerospace	QCM, SAW, MOS	—	SAM system
Electronic Sensor Technology	SAW	—	zNose
Element	MOS	—	FreshSense
EnviroNics Industry	IMCELL	—	MGD-1
Forschungszentrum Karlsruhe	MOS, SAW	—	Sagas
HKR Sensorysysteme	QCM, MS	—	QMB6
Lennartz Electronic	QCM, MOS, electrochemical	—	MosesII
Marconi Applied Technologies	CP, MOS, QCM	—	e-Nose 5000
Microsensor System	SAW	—	Prosat
Osmetech	CP	—	OMA
Quartz Technology	QCM	—	QTS-1
Smart Nose	MS	—	Smartnose-300
Z Nose	GC, SAW	—	Z Nose

CP – conducting polymer, MOS – metal-oxide semiconductor, MOSFET – metal-oxide semiconductor field-effect transistor, MS – Mass spectrometry, QCM – quartz-crystal microbalance, SAW – surface acoustic wave

1.6 Outline of the thesis

The first chapter reviewed the mammalian flavour system, different electronic nose/tongue technologies and instruments and their applications. The aims and objectives of this thesis have also been presented.

Chapter 2 reviews in more detail many of the background technologies used in the project. This includes the basic properties of bulk and surface acoustic waves and their application in chemical and biological sensing. Furthermore the fundamentals of liquid sensing are discussed along with the sensing mechanisms.

Chapters 3 and 4 describe the design and development of novel SH-SAW liquid sensors. This includes the operational principle, design rules and concepts that should be followed to produce a working design. Chapter 4 discusses the fabrication of the devices followed post processing to realise the sensors. Also covered are the various measurement systems and the performance issues.

The SH-SAW devices as liquid sensors is described in chapter 5. The experimental setups and details of the all the experimental conditions and analytes used are also presented.

Chapter 6 describes the combined electronic nose and electronic tongue “flavour” system detailing the design and measurement setup of the gas/vapour sensors used in the system along with the experimental setup used to carry out the combined measurements. The combined results are presented and discussed.

Chapter 7 introduces the high frequency wired and wireless SAW devices. It details the design and fabrication of both configurations. The chapter also briefly discusses the proposed measurement system for the wireless system. The designs of liquid chambers for these new devices are detailed along with miniature microstereolithography (MSL) chambers.

Chapter 8 concludes the thesis by discussing the results and how these have fulfilled the aims of the project. Lastly in further work, the latest developments from the research are presented and possible advancements for liquid sensing and specific applications proposed.

1.7 References

- [1.1] Tony Kushner, *Angels in America*, (1992), p. 17
- [1.2] W. S. Cain, R. A. Atkinson, R. J. Herrnstein, G. Lindzey, and R. D. Luce (Eds.), *Olfaction, Stevens' handbook of experimental psychology: Vol 1. Perception and motivation*, Wiley New York (1988), pp. 409-459.
- [1.3] J. S. Kauer, T. E. Finger and W. C. Silver (Eds.), *Coding in the olfactory system, Neurobiology of taste and smell*, Wiley New York (1987), pp. 205-231.
- [1.4] L. M. Bartoshuk, J. W. King and L. A. Riggs (Eds.), *The chemical senses, Experimental psychology*, Holt, Rinehart and Winston, New York (1971 3rd Ed.)
- [1.5] M. A. Hoon, E. Alder, J. Lindemeier, J. F. Battey, N. J. P. Ryba, and C. S. Zuker, Putative mammalian taste receptors: A class of taste-specific GPCRs with distinct topographic selectivity, *Cell*, 96 (1999), pp. 541-551.
- [1.6] E. B. Goldstein, *Sensation and Perception*, Wadsworth Group (2002 6th Ed.), pp. 479-488.
- [1.7] T. E. Finger and W. L. Silver (Eds.), *Gustatory nuclei and pathways in the central nervous system, Neurobiology of taste and smell*, Wiley New York (1987), pp. 331-353.
- [1.8] B. Halpern, G. K. Beauchamp and L. Bartoshuck (Eds.), *Psychophysics of taste, Tasting and smelling*, Handbook of perception and cognition, Academic Press, San Diego, CA, (1997 2nd Ed.), pp. 72-123.
- [1.9] S. S. Schiffman and R. P. Erickson; S, A, Simon and S. D. Roper (Eds.), *Psychophysics: Insights into transduction mechanisms and neural coding, Mechanisms of taste transduction*, CRC Press, Boca Raton, FL (1993), pp. 395-424.
- [1.10] T. R. Scott, T. E. Finger and W. L. Silver (Eds.), *Coding in the gustatory system, Neurobiology of taste and smell*, Wiley New York (1987), pp. 355-378.
- [1.11] R. Axel, The molecular logic of smell, *Scientific American* 273, (1995), pp. 154-159.
- [1.12] J. Pevsner, V. Hou, A. M. Snowman, and S. H. Snyder, Odorant-binding protein: Characterisation of ligand binding, *Journal of Biological Chemistry*, 265, (1990), pp. 6118-6125.

- [1.13] S. Firestein; D. P. Corey and S. D. Roper (Eds.), *Physiology of transduction in the single olfactory sensory neuron*, *Sensory transduction*, Rockefeller University Press, New York (1992), pp. 61-71.
- [1.14] J.W. Gardner and P. N. Bartlett, *Electronic Noses: Principles and Applications*, Oxford University Press (1999), pp. 36-42.
- [1.15] R. Reichl, *Dining in New York*, New York Times (1994).
- [1.16] H. Lawless and E. B. Goldstein (Ed.), *Black-well handbook of perception*, Blackwell, Oxford UK (2001), pp. 601-635.
- [1.17] M. M. Mozell, B. P. Smith, P. E. Smith, R. L. Sullivan, and P. Swender, Nasal chemoreception in flavour identification, *Archives of Otolaryngology*, 90, (1969), 131-137.
- [1.18] T. P. Hettinger, W. E. Myers, and M. E. Frank, Role of olfaction in perception of nontraditional “taste” stimuli, *Chemical Senses*, 15 (1990), pp. 755-760.
- [1.19] K. Toko, Taste sensor with global selectivity, *Materials Science and Engineering*, C4, (1996), pp. 69-82.
- [1.20] A. Legin, A. Rudinitskaya, Y. Vlasov, C. Di Natale, F. Davide, A. D’Amico, Tasting of beverages using an electronic tongue based on potentiometric sensor array, *Technical digest of Eurosenors X*, Leuven, Belgium (1996), pp. 427-430.
- [1.21] F. Winqvist, P. Wide, I. Lundström, An electronic tongue based on voltammetry, *Anal. Chimica. Acta.*, (1997), pp. 21-31.
- [1.22] K. Toko, K. Hayashi, M. Yamanaka, K. Yamafuji, Multichannel taste sensor with lipid membranes, *Technical digest 9th sensors symposium*, Tokyo (1990), pp. 193-196.
- [1.23] K. Hayashi, M. Yamanaka, K. Toko, K. Yamafuji, Multichannel taste sensor using lipid membranes, *Sensors and Actuators B2*, (1990), pp. 205-213.
- [1.24] A. J. Bard, L. R. Faulkner: *Electrochemical Methods – Fundamentals and Applications*, John Wiley & Sons, Inc. (1980).
- [1.25] R. Lucklum, P. Hauptmann, The quartz crystal microbalance – Mass sensitivity, viscoelasticity and acoustic amplification, *Sensors and Actuators B70*, (2000), pp. 30-36.
- [1.26] T. Yamazaki, J. Kondoh, Y. Matsui, S. Shiokawa, Estimation of components in mixture solutions of electrolytes using a liquid flow system with SH-SAW sensor, *Sensors and Actuators A83*, (2000), pp. 34-39.

- [1.27] S. Yao, M. Wang, and M. Madou, A pH electrode based on melt-oxidised iridium oxide, *Journal of the Electrochemical Society*, 148, (2001), pp. H29-H36.
- [1.28] P. Bergveld, The ISFET, *IEEE Transactions on Biomedical Engineering BME*, 19, (1970).
- [1.29] K. Kuihara, K. Yoshii, and M. Kashiwayanagi, Transduction mechanisms in chemoreception, *Comp. Biochem. Physiol.*, 85A (1986), pp. 1-22.
- [1.30] M. Miyake, N. Kamo, K. Kurihara, and Y. Kobatake, Physicochemical studies of taste reception, *Biochim. Biophys. Acta*, 436 (1976) pp. 856-862.
- [1.31] K. Toko, M. Tsukiji, S. Iiyama, and K. Yamafuji, Self-sustained oscillations of electric potential in a model membrane, *Biophys. Chem.*, 23 (1986), pp.201-210.
- [1.32] K. Hayashi, K. Yamafuji, K. Toko, N. Ozaki, T. Yoshida, S. Iiyama, and N. Nakashima, Effect of taste substances on electric characteristics of a lipid cast membrane with a single pore, *Sensors and Actuators*, 16 (1989) pp. 25-42.
- [1.33] S. Iiyama, K. Toko, K. Hayashi, and K. Yamafuji, Effect of sweet substances on electric characteristics of a dioleoylphosphate membrane, *Agric. Biol. Chem.*, 53 (1989), pp. 675-681.
- [1.34] K. Toko, K. Hayashi, S. Iiyama, K. Yamafuji, Taste sensing system utilising dynamic properties of phase transition in synthesised lipids, *Tech. Digest, 4th Int. Conf. Solid-state Sensors and Actuators* (Transducers 1987), Tokyo, Japan, June 2-5 (1987), pp. 793-796.
- [1.35] S. Iiyama, K. Toko, and K. Yamafuji, Effect of bitter substances on a model membrane system of taste reception, *Agri. Biol. Chem.*, 50 (1986), pp. 2709-2714.
- [1.36] K. Hayashi, Y. Matsuki, K. Toko, T. Murata, Ke. Yamafuji, and Ka. Yamafuji, Sensing of 'umami' taste and synergistic effects with synthetic lipid membranes, *Sensors Mater.*, 1 (1989), pp. 321-334.
- [1.37] K. Toko, *Biomimetic Sensor Technology*, Cambridge University Press (2000).
- [1.38] Taste Sensing System SA401, Anritsu Corporation, Japan.
- [1.39] K. Toko, A taste sensor, *Meas. Sci. Technol.*, 9 (1998), pp. 1919-1936.
- [1.40] K. Toko, Taste sensor, *Sensors and Actuators B 64*, (2000), pp. 205-215.
- [1.41] K. Toko, Electronic Tongue, *Biosensors and Bioelectronics*, 13 (1998), pp. 701-709.

- [1.42] K. Toko; H. Baltes, W. Göpel, J. Hesse (Eds.) *Electronic sensing of tastes, Sensors Update 3*, Wiley-VCH, Weinheim (1998), pp. 131-160.
- [1.43] T. Fukunaga, K. Toko, S. Mori, Y. Nakabayashi, M. Kanda, Quantification of taste of coffee using a sensor with global selectivity, *Sensors and Materials* 8(1) (1996), pp. 47-56.
- [1.44] T. Iyota, T. Matsuno, K. Toko, K. Yamafuji, Y. Mizota, T. Yoshihara, T. Doi, R. Watanabe, Study of heat effect on the taste of milk using a taste sensor, *Technical Digest of the 13th Sensor Symposium*, (June 1995), pp. 245-248.
- [1.45] T. Taniguchi, Y. Naito, N. Maeda, Y. Sato, H. Ikezaki, Development of a monitoring system for water quality using a taste sensor, *Sensors and Materials* 11(7) (1999), 437-446.
- [1.46] K. Toko, R. Yasuda, S. Ezaki, T. Fujiyoshi, Taste sensing FET (TSFET), *Trans. IEE Jpn.* 118-E (1998), pp. 1-5.
- [1.47] P. Ivarsson, S. Holmin, N. Höjer, C. Krantz-Rülcker, F. Winqvist, Discrimination of tea by means of a voltammetric electronic tongue and different applied waveforms, *Sensors and Actuators B* 76 (2001), pp. 449-454.
- [1.48] F. Winqvist, C. Krantz-Rülcker, P. Wide, I. Lundström, Monitoring of milk freshness by an electronic tongue based on voltammetry, *Measurement Science and Technology* 9 (1998), pp. 1937-1946.
- [1.49] F. Winqvist, S. Holmin, C. Krantz-Rülcker, P. Wide, I. Lundström, A hybrid electronic tongue, *Analytica. Chimica. Acta.* 406 (2000), 147-157.
- [1.50] F. Winqvist, S. Holmin, C. Krantz-Rülcker, I. Lundström, Flow injection analysis applied to a voltammetric electronic tongue, *Int. Jour. Food Microbiology.*
- [1.51] C. Krantz-Rülcker, M. Stenberg, F. Winqvist, I. Lundström, Electronic tongues for environmental monitoring based on sensor arrays and pattern recognition: a review, *Analytica. Chimica. Acta.* 426 (2001), pp. 217-226.
- [1.52] M. G. Buehler, G. M. Kuhlman, and D. Keymeulen, Advanced electronic tongue concept, *IEEE Aerospace Conference Proceedings*, 1 (2002).
- [1.53] S. J. West, X. Wen, R. Geis, J. Herdan, T. Gillette, M. H. Hecht, W. Schubert, S. Grannan, S. P. Kounaves, Electrochemistry on Mars, *American Laboratory* 31 (20), (Oct 1999), p. 48.
- [1.54] C. Söderström, Electronic tongue detects mold, Linköping University, Sweden (2003);

URL:http://www.innovationsreport.com/reports/process_engineering/report-18594.html

- [1.55] R. Borngräber, J. Hartmann, R. Lucklum, S. Rösler, P. Hauptmann, Detection of ionic compounds in water with a new polycarbon acid coated quartz crystal resonator, *Sensors and Actuators B65*, (2000), pp. 273-276.
- [1.56] S. Ezaki, S. Iiyama, Detection of interactions between lipid/polymer membranes and taste substances by quartz resonators, *Sensors and Materials* 13(2), (2001), pp. 119-127.
- [1.57] J. Kondoh, K. Saito, S. Shiokawa, H. Suzuki, Simultaneous measurement of liquid properties using multichannel shear horizontal surface acoustic wave microsensor, *Japanese Journal of Applied Physics* vol. 35, Part 1, No. 5B, 1996, pp. 3093-3096.
- [1.58] J. Kondoh and S. Shiokawa, New application of shear horizontal surface acoustic wave sensors to identifying fruit juices, *Japanese Journal of Applied Physics* Vol. 33, Part 1, No. 5B, 1994, pp. 3095-3099.
- [1.59] J. Kondoh, M. Nakamura, Y. Matsui, S. Shiokawa, Shear horizontal surface acoustic wave microsensor system for water identification, *Proceedings of the Second International Symposium on Microstructures and Microfabricated Systems* (1995).
- [1.60] J. Kondoh, T. Muramatsu, T. Nakanishi, S. Shiokawa, Development of surface acoustic wave liquid sensing system for Japanese tea measurements, *IEEE frequency control symposium*, (2001).
- [1.61] J. Kondoh, Y. Matsui, and S. Shiokawa, New biosensor using shear horizontal surface acoustic wave device, *Jpn. J. Appl. Phys.* 32 (1993), pp. 2376-2379.
- [1.62] J. J. Lavigne, S. Savoy, M. B. Clevenger, J. E. Ritchie, B. McDoniel, S-J. Yoo, E. V. Anslyn, J. T. McDevitt, J. B. Shear, D. Neikirk, Solution-based analysis of multiple analytes by a sensor array: toward the development of an “Electronic Tongue”, *Jour. Am. Chem. Soc.* 120 (1998), 6249-6430.
- [1.63] D. Barrow, Cardiff University UK, 2002, Electronic tongue to taste pollution, URL: <http://news.bbc.co.uk/1/hi/sci/tech/1911259.stm>
- [1.64] A. Riul, D. S. dos Santos, K. Wohnrath, R. Di Tommazo, C. P. L. F. Carvalho, F. J. Fonseca, O. N. Oliveira, D. M. Taylor, and L. H. C. Mattoso, Artificial taste sensor: Efficient combination of sensors made from Langmuir-Blodgett

- films of conducting polymers and Ruthenium complexes and self-assembled films of an Azobenzene-containing polymer, *Langmuir* 18 (2002), pp. 239-245.
- [1.65] G. G. Roberts, *Langmuir-Blodgett Films*, Plenum Press New York (1st Ed. 1990)
- [1.66] J. D. Hartman, A possible objective method for the rapid estimation of flavours in vegetables, *Proc. Am. Soc. Hort. Sci.*, 64 (1954), pp. 335.
- [1.67] W. F. Wilkens and J. D. Hartman, An electronic analog for the olfactory processes, *Ann. NY Acad Sci.*, 118 (1964), pp. 608.
- [1.68] S. Zaromb and J. R. Stetter, Theoretical basis for identification and measurement of air contaminants using an array of sensors having partially overlapping sensitivities, *Sensors and Actuators*, 6 (1984), pp. 225-243.
- [1.69] K. C. Persaud and G. H. Dodd, Analysis of discrimination mechanisms in the mammalian olfactory system using a model nose, *Nature* 299 (1982), pp. 352-355.
- [1.70] J. W. Gardner, P. N. Bartlett, A brief history of electronic noses, *Sensors and Actuators B*, 18-19, (1994), pp. 211-220.
- [1.71] J. W. Gardner and P. N. Bartlett, *Electronic Noses: Principles and Applications*, Oxford University Press (1999), pp. 67-110.
- [1.72] P. T. Moseley, A. M. Stoneham and D. E. Williams, Oxide semiconductors: patterns of gas response behaviour depending on material type. In *Techniques and mechanisms of gas sensing*, (ed. P. T. Moseley, J. O. W. Morris and D. E. Williams), (1991), Adam Hilger, Bristol, pp. 108-138.
- [1.73] P. N. Bartlett and J. W. Gardner, Odour sensors for an electronic nose, In *Sensors and Sensory Systems for electronic noses*, (ed. J. W. Gardner and P. N. Bartlett) NATO ASI Series, Vol. 212, (1992), pp. 31-51.
- [1.74] J. W. Grate, S. J. Martin and R. M. White, Acoustic wave microsensors: Part 1 & 2, *Anal. Chem.*, 65 (1993), 940A-948A & 987A-996A.
- [1.75] Campbell, C., *Surface acoustic wave devices and their signal processing applications*, Academic Press (1989), Boston, USA.
- [1.76] I. Lundström, Hydrogen sensitive MOS structures, *Sensors and Actuators*, 1, (1981), pp. 403-426.
- [1.77] B. S. Hobbs, A. D. S. Tantrum and R. Chan-Henry, *Liquid electrolyte fuel cells*, in *Techniques and mechanisms in gas sensing* (ed. P. T. Moseley, J. O. W. Morris and D. E. Williams), (1991), Adam Hilger, Bristol, pp. 161-188.

- [1.78] E. Jones, The pellistor catalytic gas detector, In *Techniques and mechanisms of gas sensing*, ((ed. P. T. Moseley, J. O. W. Morris and D. E. Williams), (1991), Adam Hilger, Bristol, pp. 17-31.
- [1.79] T. A. Dickinson, D. R. Walt, J. White and J. S. Kauer, A chemical-detecting system based on a cross-reactive optical sensor, *Nature*, 382, (1996), pp. 697-700.
- [1.80] J. W. Gardner and P. N. Bartlett, *Electronic Noses: Principles and Applications*, Oxford University Press (1999), pp. 117-138.
- [1.81] T.C. Pearce, S.S. Schiffman, H.T. Nagle and J.W. Gardner: *Handbook of Machine Olfaction Electronic Nose Technology*, Wiley-VCH (2003), pp. 133-161.
- [1.82] S. Haykin, *Neural Networks: A comprehensive foundation*, Macmillan Publishing Company, New York (1994).
- [1.83] J.W. Gardner, E.L. Hines, M. Wilkinson, The application of neural networks to an electronic nose, *Meas. Sci. Technol.*, 1, (1990), pp. 446-451.
- [1.84] R. Olafsson, E. Martinsdottir, G. Olafdottir, S. I. Sigfusson and J. W. Gardner, Monitoring the fish freshness using tin oxide sensors, In *Sensors and Sensory Systems for electronic noses*, (ed. J. W. Gardner and P. N. Bartlett) (1992), pp. 257-272.
- [1.85] K. C. Persaud and P. J. Travers, *Arrays of broad specificity films for sensing volatile chemicals, in handbook of biosensors and electronic noses: medicine, food and the environment* (ed. E. Kress-Rogers), CRC Press, Ohio, pp. 563-592.
- [1.86] T. C. Pearce J. W. Gardner, S. Freil, P. N. Bartlett and N. Blair, Electronic nose for monitoring the flavours of beers, *Analyst*, 118 (1993), pp. 371-377.
- [1.87] S. Baldacci, T. Matsuno, K. Toko, R. Stella, D. De Rossi, Discrimination of wine using taste and smell sensors, *Sensors and Materials* 10(3), (1998), pp. 185-200.
- [1.88] C. Di Natale, R. Paolesse, A. Macagnano, A. Mantini, A. D'Amico, M. Ubigli, A. Legin, L. Lvova, A. Rudinitskaya, Y. Vlasov, Application of a combined artificial olfaction and taste system to the quantification of relevant compounds in red wine, *Sensors and Actuators B69*, (2000), pp. 243-347.
- [1.89] F. Winquist, P. Wide, I. Lundström, The combination of an electronic tongue and an electronic nose, *Sensors and Actuators B69*, (2000), pp. 243-347.

CHAPTER 2

Acoustic wave modes and devices

2.1 Introduction

Chapter 1 covered the various electronic tongue sensor technologies and devices. The research in this project is based on surface acoustic wave devices for liquid sensing and hence this chapter introduces the properties, excitation, propagation and detection of the various acoustic wave modes in piezoelectric materials. The different types of elastic waves are discussed under the main branches of bulk acoustic waves and surface acoustic waves. Acoustic devices employing these different wave modes for a variety of sensing applications are also covered, along with the performance issues of acoustic wave devices in general.

2.2 The piezoelectric effect

A discussion relating to acoustic wave devices in sensor technology or otherwise should begin with the description of the phenomenon known as *piezoelectricity*. Although it appears that piezoelectricity was observed before the incredible work of Pierre and Jacques Curie in the 1880s, they have been credited with the discovery of piezoelectricity. They observed, while performing experiments on various crystals, that on application of pressure these crystals would electrically polarise. These electrical effects were recorded on an electrometer connected using tin foil electrodes [2.1]. Following the work of the Curie brothers, the term piezoelectricity was actually introduced by Hankel a year later [2.2, 2.3]. Lippman [2.4] at the same time predicted

the piezoelectric effect on thermodynamic grounds while the Curie brothers verified that the application of electrical energy can result in crystal mechanical deformation. Lord Kelvin [2.5] was also responsible for a theory of piezoelectricity based on thermodynamic concepts. Voigt [2.6] contributed by developing a theory involving elastic vectors and elastic tensors and published a book on properties and theory of piezoelectricity. In 1885, Lord Rayleigh [2.7] confirmed the existence of elastic vibrations on the surface of solid materials.

The piezoelectric effect can be demonstrated by applying either a compressive or tensile stress to the opposite faces of a piezoelectric crystal. Figure 2.1 shows the effect when two equal and opposite forces (generating a tensile stresses) are applied to a piezoelectric crystal. The tensile stress results in the deformation of the crystal lattice and causes separation of the centres of gravity of positive and negative charges¹. This effect results in electrical charge appearing on the surface of the electrodes. Removal of the compressive or tensile force, releases the strain in the crystal lattice causing the flow of charge and hence current, and returning the potential difference between the electrodes to zero.

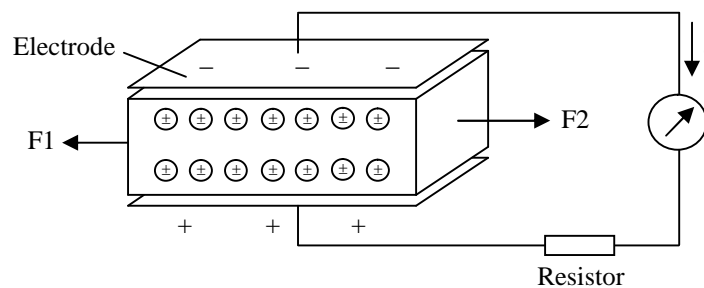


Figure 2.1 The piezoelectric effect: mechanical energy transduced into electrical energy

On application of a sinusoidal stress, alternating between tensile and compressive forces, to opposite crystal faces; a sinusoidal piezoelectric voltage is produced between the electrodes. In this case, electrical energy is produced from mechanical energy. In contrast when an external voltage is applied to the electrodes, the crystal lattice will deform by an amount proportional to the applied voltage. In this case electrical energy is transformed into mechanical potential energy [2.8].

¹ This effect does not occur in crystalline silicon because its lattice structure is centro-symmetric.

There are three important properties of piezoelectric transducers that justify their use for sensing applications [2.9].

1. Good coupling between the electric circuitry and mechanical properties of the crystal to ensure a frequency match between the mechanical acoustic wave and the electrical frequency; a distortion free interface with low dissipation.
2. The anisotropic nature of the piezoelectric crystals allows for different angles of cut with respect to the crystallographic axis, which, therefore, allows the use of crystals to produce various acoustic wave modes at a range of frequencies.
3. Possibility to vary either the mode of the acoustic wave such as from compressional to shear, or the angle of propagation.

2.2.1 Piezoelectricity

In a solid medium, the mechanical forces are addressed by the components of the stress field T_{ij} and the mechanical deformations are described by the components of the strain field S_{ij} . In the case of non-piezoelectric elastic solids, the mechanical stress and strain, for small static deformations are related according to the Hooke's Law [2.10]

$$\mathbf{T}_{ij} = \mathbf{c}_{ijkl} \mathbf{S}_{kl} \quad (2.1)$$

where T_{ij} are the mechanical stress second-rank tensor components (N/m^2), S_{kl} are the strain second-rank tensor components (no dimensions), and c_{ijkl} is the elastic stiffness constant (N/m^2) represented by a fourth-rank tensor.

In the case of the piezoelectric materials the coupling between strain and electrical polarisation gives rise to mechanical deformation and vice versa upon application of an electric field. Thus giving a mechanical stress represented by

$$\mathbf{T}_{ij} = \mathbf{c}_{ijkl}^E \mathbf{S}_{kl} - \mathbf{e}_{kij} \mathbf{E}_k \quad (2.2)$$

where e_{kij} is the piezoelectric constant (C/m^2), E_k is the k th component of the electric field, and c_{ijkl}^E is measured either under a zero or a constant electric field.

The electrical displacement \mathbf{D} in non-piezoelectric materials, is related to the applied electric field according to

$$\mathbf{D} = \epsilon_r \epsilon_0 \mathbf{E} \quad (2.3)$$

where ϵ_r is the relative permittivity and ϵ_0 is the permittivity of free space. In the case of the piezoelectric materials the displacement relationship is extended to

$$D_i = e_{ikl} S_{kl} + \varepsilon_{ik}^S E_k \quad (2.4)$$

with ε_{ik}^S measured at constant or zero strain.

Equations (2.2) and (2.4) are known as the *piezoelectric constitutive relations*.

2.3 Acoustic waves

The research development in the acoustic sensor field has increased significantly since the early 1960s and has shown a lot of diversity. The basic detection principle of a change of physical property follows from the transduction mechanism of an acoustic device, which involves the conversion of signals from the physical (acoustic wave) domain to the electrical domain. Small perturbations affecting the acoustic wave manifest themselves as large-scale changes when converted to the electromagnetic (EM) domain because of the enormous difference in their velocities (5 orders of magnitude less)[2.11].

Acoustic wave devices offer a rugged and relatively inexpensive means for the development of wide-range of sensing applications. An attractive feature of acoustic sensors is that they respond directly to physical and chemical parameters, including surface mass, stress, strain, liquid density, viscosity, permittivity, and conductivity [2.12]. Furthermore, the anisotropic nature of the piezoelectric crystals allows for various crystal cuts and orientation, with each cut providing different properties. Also depending on the orientation and crystal cut, various acoustic waves with different acoustic wave modes can be constructed, which may be application suited and specific. Other advantageous attributes include very low internal loss, uniform internal density, and elastic constants [2.13]. These properties allow the design of different sensors and optimise them to meet the needs of specific sensing applications, leading to their increasing role in chemical and physical sensing [2.14].

Acoustic wave devices are described by the mode of wave propagation through or on the surface of the piezoelectric substrate. Acoustic waves are distinguished primarily by their velocities and particle displacement directions with many combinations possible. These depend on the properties of the piezoelectric material (such as crystal cut) and the boundary conditions. The transducer of each device provides the electric field necessary to displace the substrate and thus form an acoustic wave. Transverse, or shear, waves have particle displacements that are normal to the direction of wave propagation and which can be polarised so that the particles

displacements are either parallel to or normal to the sensing surface. Shear horizontal wave motion signifies transverse displacements polarised parallel to the sensing surface whereas shear vertical motion indicates transverse displacements normal to the surface.

A wave propagating through the substrate is called a bulk wave. The most commonly used acoustic wave (BAW) devices are the thickness shear mode (TSM) resonator and the shear-horizontal acoustic plate mode (SH-APM) sensor. On the other hand if the wave propagates on the surface of the substrate, it is known as a surface wave. The most widely used surface acoustic wave devices are the surface acoustic wave (Rayleigh SAW) sensor and the shear-horizontal surface acoustic wave (SH-SAW) sensor, also sometimes known as the surface transverse wave (STW) sensor.

All acoustic wave devices can be considered as sensors as they are sensitive to perturbations of many different parameters. Any change in the characteristics of the path over which the acoustic wave propagates will result in a change in the output. All the sensors can operate in the gaseous or vacuum environments, but only a subset of them function efficiently in the aqueous phase. The TSM, SH-APM, and SH-SAW devices all generate waves that are primarily in the shear horizontal mode. The shear wave does not radiate energy into liquids, hence suitable for operation in liquid environment without excessive damping. Conversely, the Rayleigh SAW mode has a surface-normal particle displacement that radiates compression waves into the liquid, thus causing excessive damping.

Other acoustic waves that are promising for sensors include the flexural plate wave (FPW), Love wave, surface skimming bulk wave (SSBW), and Lamb wave. The various acoustic waves and devices employed for sensor applications are discussed in this section, focusing primarily on bulk wave sensors: Thickness shear mode (TSM), acoustic plate mode (APM) and surface acoustic wave sensors: Rayleigh surface acoustic waves, shear horizontal surface acoustic waves (SH-SAW), Love wave mode, and flexural plate wave (FPW).

2.3.1 Wave propagation

The most general type of acoustic wave is the *bulk wave* that propagates in a homogeneous medium with no boundaries (i.e. an infinite medium). They are categorised into *longitudinal* and *transverse (shear)* waves, depending on the polarisation and direction on propagation of the vibrating atoms within the medium [2.15]. Figure 2.2 shows the particle displacement profiles for the two types of bulk

waves. In the case of the longitudinal waves, the particles vibrate in the direction of propagation (x-direction in Figure 2.2) whereas for the transverse waves, the particles vibrate in a plane normal to the direction of propagation (y- and z-directions in Figure 2.2)

On introduction of boundary conditions to the propagation medium it is no longer an infinite material, and hence, the nature of the waves. Different types of acoustic waves are supported in a finite/semi-infinite medium depending on the boundary conditions. On introduction of a single plane boundary, a semi-infinite solid is formed that permits *surface elastic/acoustic waves* to propagate along that single boundary. Adding a second boundary parallel to the first forms a plate, and permits the propagation of *plate waves*. All these waves are useful for sensor applications but the *surface acoustic waves* (SAWs) are of great interest here; these waves are guided along the surface with its amplitude decaying exponentially away from the surface into the medium and potentially offer better sensitivity and CMOS integration with piezoelectric substrates such as ZnO.

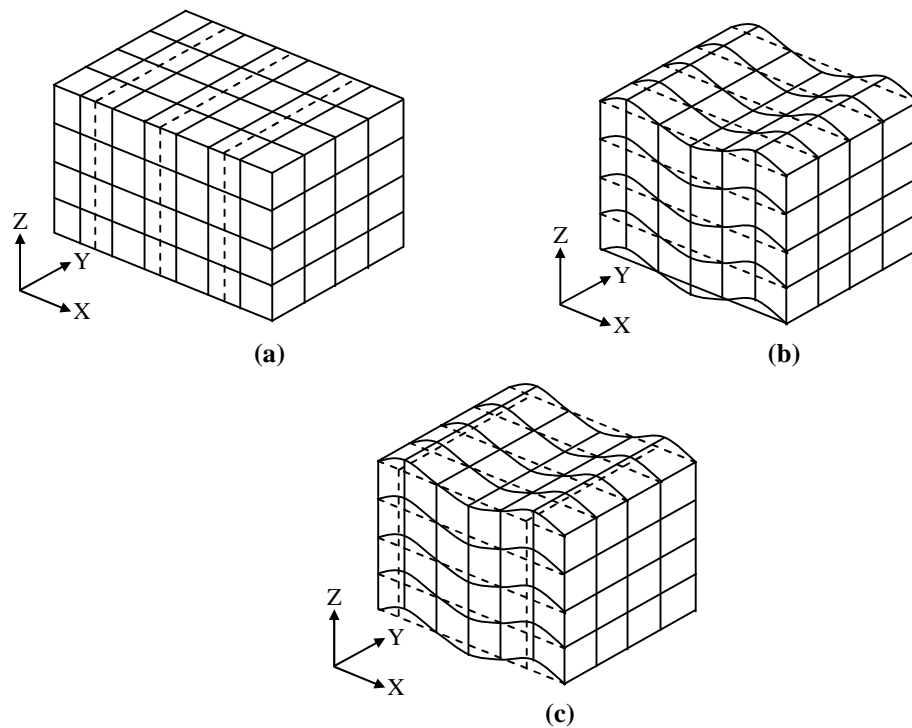


Figure 2.2 Particle displacement profiles (a) longitudinal, (b, c) shear uniform plane waves

Figure 2.3 illustrates a visualisation of the concept of shear wave propagation. It presents the propagation of a shear wave in an arbitrary cubic crystal medium. The

wave can be described in terms of both its propagation and polarisation directions. With reference to the x, y, z coordinate system the polarised SAWs are associated with a corresponding polarisation, as illustrated in the figure.

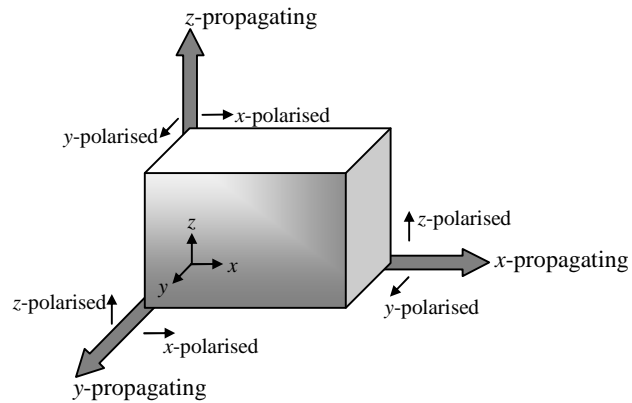


Figure 2.3 Acoustic shear waves in an arbitrary cubic crystal medium

2.3.2 Particle displacement, strain and stress

An acoustic wave in a solid is a result of a deformation of the solid material. This deformation occurs as a result of atoms moving out of their equilibrium positions, which introduces internal restoring forces that return the material back to equilibrium [2.15]. Assuming that the deformation is dependent on time, then these restoring forces together with the inertia of the particles, result in the net effect of propagating wave motion, with each atom oscillating about its equilibrium position. The material is referred to as being *elastic* with the associated waves known as *elastic* or *acoustic waves*. Figure 2.4 shows an arbitrary solid with both steady and deformed states of particles (equilibrium \bullet and deformed \circ).

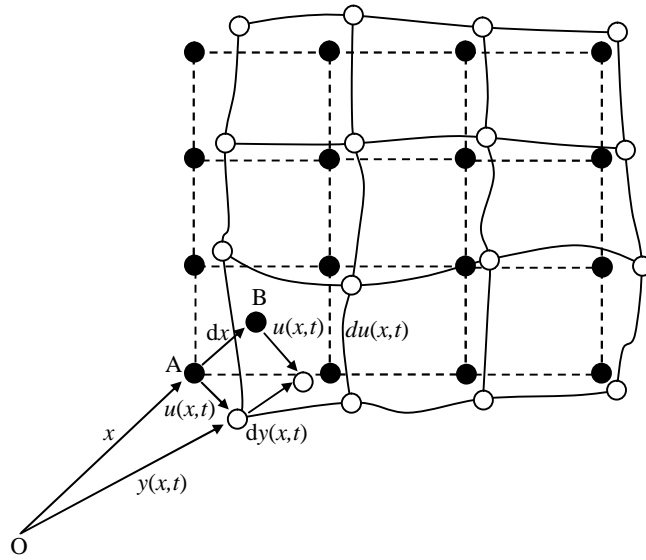


Figure 2.4 Equilibrium and deformed states of particles in a solid

Each particle is associated with an equilibrium (position) vector \mathbf{x} and a corresponding displaced position vector $\mathbf{y}(x,t)$ after deformation which is time-variant and a function of \mathbf{x} (the equilibrium state). These continuous displaced position vectors can be used to determine the displacement of the particle at point \mathbf{x} through the expression

$$\mathbf{u}(x,t) = \mathbf{y}(x,t) - \mathbf{x} \quad (2.5)$$

where $\mathbf{u}(x,t)$ is a continuous variable describing the vibrational motion of all particles within the medium.

The deformation or *strain* of a material occurs only on relative displacement of the medium particles. If the particles maintain their relative position there is no deformation as in the case of rigid translations and rotations, as long as these occur at a constant velocity (accelerations causes strain). From figure 2.4 a measure of strain between two particles can be approximated. Consider particles A and B, that lie on the position vector \mathbf{x} and $\mathbf{x} + d\mathbf{x}$, respectively, then the deformation or strain between these two points after the application of a force can be written as

$$\Delta' = d\mathbf{y}^2(x,t) - (d\mathbf{x})^2 \quad (2.6)$$

$$\Delta'(x,t) = 2\mathbf{S}_{ij}(x,t)d\mathbf{x}_i d\mathbf{x}_j \quad (2.7)$$

where $\mathbf{S}_{ij}(x,t)$ is the second-order strain tensor given by

$$S_{ij}(x,t) = \frac{1}{2} \left[\frac{\partial u_i}{\partial x_j} + \frac{\partial u_j}{\partial x_i} + \frac{\partial u_k}{\partial x_i} \frac{\partial u_k}{\partial x_j} \right] \quad (2.8)$$

where the subscripts i , j and k correspond to x , y and z .

In the case of rigid materials, the deformation gradient as expressed by equation (2.8) must be kept small to avoid permanent damage to the material. Therefore the last term in the equation (2.8) is assumed to be negligible and the strain-displacement tensor can be expressed as

$$S_{ij}(x,t) = \frac{1}{2} \left[\frac{\partial u_i(x,t)}{\partial x_j} + \frac{\partial u_j(x,t)}{\partial x_i} \right] \quad (2.9)$$

When the particles in a medium oscillate acoustically about the equilibrium positions, elastic restoring forces (*stresses*), develop between adjacent particles. In the case of a freely vibrating body, these are the only forces present. On the other hand if the vibration is influenced by external forces, two types of excitation forces (*body and surface forces*) must be considered. Body forces affect the internal particles of the body directly, whereas surface forces are applied to material boundaries to generate acoustic vibration. The excitation applied by the surface forces does not have a direct influence on the particles of the body, but it is transmitted to them through elastic restoring forces (stresses), acting between the adjacent particles. These stresses between particles in a vibrating medium are defined by considering the material particles as volume elements, with reference to some orthogonal coordinate system [2.15]. Consider a small surface area ΔA on an arbitrary solid body with a unit normal \mathbf{n} , to which is applied a surface force $\Delta \mathbf{F}$ with uniform components ΔF_i . Then the surface ΔA can be expressed as a function of its surface components ΔA_j and the unit normal components n_j

$$\Delta A_j = n_j \cdot \Delta A \quad (2.10)$$

with the subscript j taking a value of 1, 2 or 3.

The stress tensor, T_{ij} , can now be related to the applied surface force and area by

$$T_{ij} = \frac{\Delta F_i}{\Delta A_j} \quad (2.11)$$

again with i and j taking values of 1, 2 or 3.

Furthermore, considering the stress tensor T_{ij} to be time-dependent and acting upon a unit cube, we can extend the stress analysis to determine dynamic equations of motion by summing the acting forces. Therefore,

$$\frac{\partial \mathbf{T}_{ij}}{\partial \mathbf{x}_j} + \rho \mathbf{F}_i = \rho \frac{\partial^2 \mathbf{u}_i}{\partial t^2} \quad (2.12)$$

where ρ is the mass density, \mathbf{F}_i are the forces acting on the body per unit mass, and \mathbf{u}_i represents the components of particle displacement along the i -direction.

2.3.3 Acoustic wave excitation

Acoustic waves propagating on the surface of piezoelectric wafers provide means of implementing a variety of signal-processing devices at frequencies ranging from several MHz to a few GHz. An interdigital transducer (IDT) is the vital cornerstone of SAW device technology. The IDTs convert electrical energy into mechanical energy, and vice versa, for the generation and detection of the SAWs.

The IDT is made up of two metal comb-shaped electrodes deposited on the surface of the piezoelectric substrate. On application of a voltage to the IDT, an electric field is created which introduces dynamic strains in the piezoelectric substrate releasing the mechanical acoustic waves with velocity v . When an alternating voltage (AC) $V(t)$ [$V_0 \exp(j\omega t)$] is applied to the electrodes, the wave induced by the finger pair travels along the piezoelectric substrate in both directions. Constructive interference and in-phase stress is achieved by ensuring that the distance d between two neighbouring electrode fingers is equal to half the elastic wavelength λ .

$$d = \lambda/2 \quad (2.13)$$

The related frequency is known as the *synchronous frequency*, f_0 , given by

$$f_0 = v/\lambda \quad (2.14)$$

at this frequency, the efficiency of the transducer in converting the electrical energy to mechanical acoustical energy, or vice versa, is maximised. The SAW devices fall into two major categories: the nondispersive delay line devices (2-port) and the SAW resonators (1-port or 2-port) as shown in figure 2.5). The SAW delay lines are equipped with input and output IDTs to utilise the SAWs. One of the IDTs acts as the device input and is connected to the electrical source while the other connected to a detector. The source IDT sets up an electric field in the substrate that launches a SAW by means of the piezoelectric effect, and the receiving transducer converts the acoustic wave to an electrical signal.

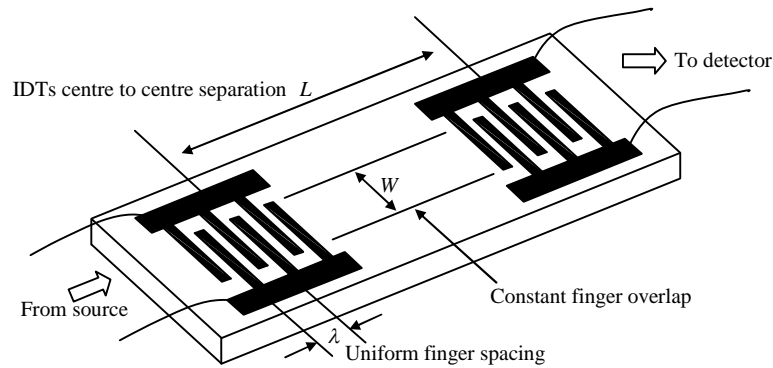


Figure 2.5 Schematic of a SAW delay line with IDTs metallised on piezoelectric wafer

The SAW resonators are equipped with reflectors on either side of the IDT to utilise energy-trapping by the SAW. The SAW resonator is constructed with either one or two ports. A one-port SAW resonator (Figure 2.3 a) has a single IDT with reflecting arrays on either side of it, resulting in efficient reflection. After having been generated by the IDT, a SAW is trapped between the two reflectors, giving a high-Q resonance. A two-port resonator (Figure 2.3 b) has a pair of IDTs flanked by a pair of reflectors, resulting in a similar high-Q resonance to a one-port resonator.

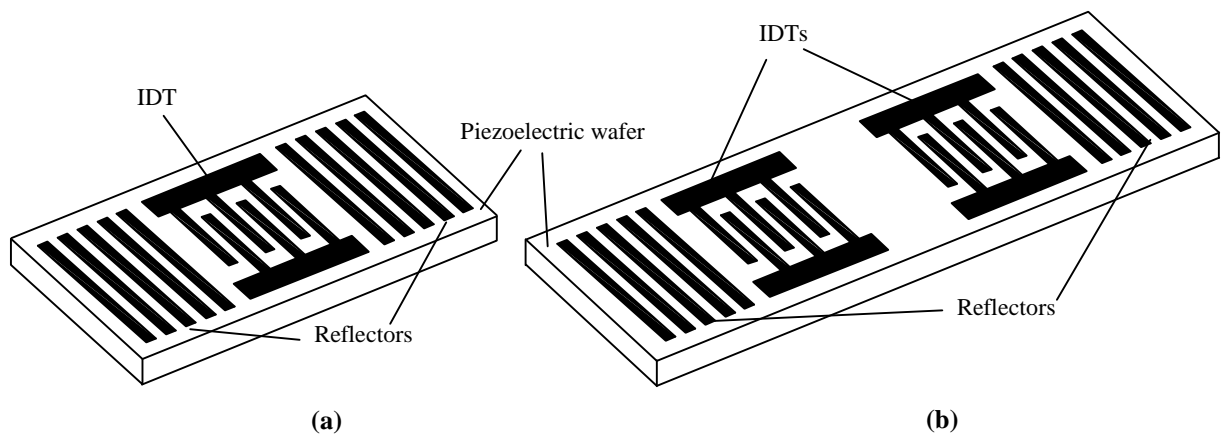


Figure 2.6 (a) One-port SAW resonator **(b)** Two-port SAW resonator

2.3.4 Bulk waves

2.3.4.1 Thickness Shear Mode

The TSM, also widely referred to as a quartz crystal microbalance (QCM), is the most widely known and simplest acoustic wave device. The TSM resonator consists of a thin disk of AT-cut quartz with parallel circular electrodes patterned on both sides. Figure 2.7 illustrates a schematic of the TSM resonator device. Shear deformation of the

crystal results on application of a voltage between the electrodes. These devices are known as resonators because the crystal resonates when electromechanical standing waves are created. There is maximum displacement at the crystal faces, making the device sensitive to surface interactions.

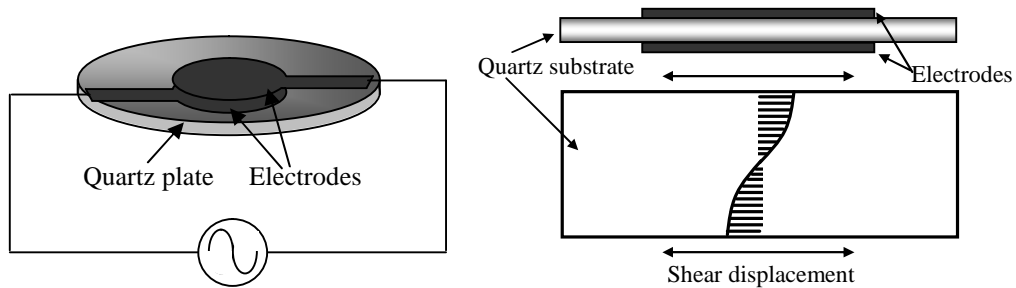


Figure 2.7 Thickness shear mode (TSM) resonator

These devices were originally used to measure metal deposition rates in vacuum systems where they were commonly used in an oscillator circuit [2.16]. The oscillation frequency tracks the crystal resonance and indicates mass accumulation on the device surface. The TSM devices offer simplicity of manufacture, robustness, temperature stability, and good sensitivity to additional mass deposited on the crystal surface [2.17]. The TSM resonator also has the capability of liquid sensing due to the presence of its shear wave propagation component. One disadvantage of these devices is their low mass sensitivity, but this can be improved by increasing the operating frequency. Making the devices very thin, increases the operating frequency and thus the mass sensitivity, but thinning the sensors beyond the normal range results in fragile devices that are difficult to manufacture and handle. Recent work involves the development of high frequency TSM resonators using piezoelectric films and bulk silicon micromachining techniques [2.18].

2.3.4.2 Shear-Horizontal Acoustic Plate Mode

These devices use thin piezoelectric substrates (plate), typically of a few acoustic wavelengths that functions as an acoustic waveguide confining the energy between the upper and lower surfaces of the plate as shown in Figure 2.8. The generated waves propagate in the bulk of the substrate at angles to the surface and reflect off the plate surfaces as they travel between the IDTs. As a result both surfaces of the plate undergo displacement, so detection can occur on either side (wave displacement has antinodes on both the top and lower surface of the substrate). This can be advantageous, as the

side patterned with the IDTs can be isolated from conducting fluids or gases (relatively simpler to isolate than if sensing surface and transducers on the same side), while the other side can be used as the sensing surface. In these devices the operation frequency is determined by the thickness of the plate and the IDT finger-spacing.

The main applications of the SH-APM devices are in liquid (biosensor) sensing, due to the absence of a surface-normal component of wave displacement. These devices also offer an advantage of using the back surface of the plate as the sensing active area and in this way isolating the IDTs from the liquid media and avoiding potential problem of chemical attack. Applications towards biosensor implementation have been reported. One particular application involves detection of microgram-per-litre levels of mercury, which is adequate for safe drinking water act compliance testing [2.19]. The particle motion in these waves is transverse relative to the direction of propagation with displacements at the surface almost in-plane. Although these devices are more sensitive to mass loading than the TSM resonator they are less sensitive than surface wave sensors due to the following two reasons. Firstly, as the sensitivity to mass loading and other perturbations are directly related to the thickness of the substrate, with sensitivity increasing as the device is thinned. However the minimum thickness is limited by manufacturing processes. Secondly, the energy of the wave is not maximised at the surface, reducing the sensitivity.

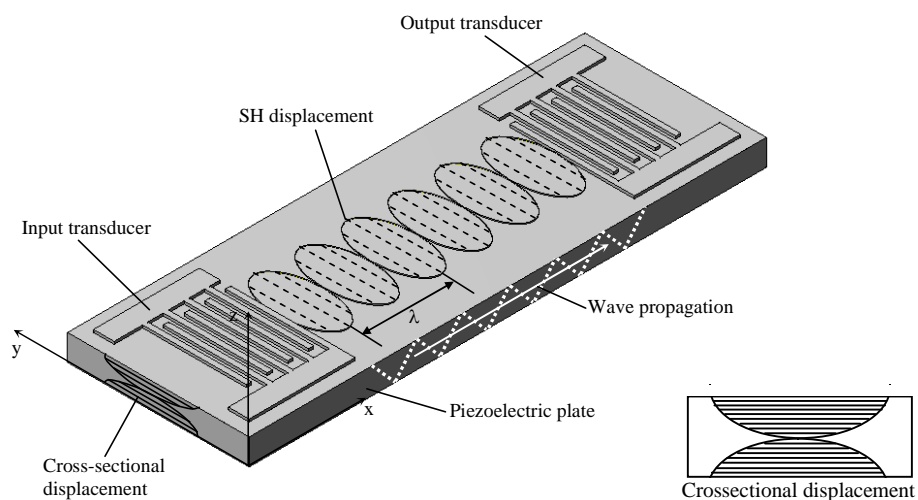


Figure 2.8 Shear-horizontal acoustic plate mode (SH-APM) device

2.3.5 Surface waves

2.3.5.1 Surface Acoustic Waves (Rayleigh SAW)

Surface acoustic waves were first described by Lord Rayleigh and from the applications point of view the Rayleigh wave has become the most widely known and used SAW [2.20]. A perfect analogy to represent a Rayleigh wave is ripples formed on calm water by a physical disturbance. Such a disturbance was first described by White and Voltmer [2.21] in a quartz crystal using an IDT. Figure 2.9 illustrates the propagation of a Rayleigh SAW in a quartz substrate through deformation of the substrate on application of a RF signal to the IDT.

The Rayleigh wave has both surface-normal component and a surface-parallel component with respect to the propagation direction and hence can couple with a medium in contact with the device's surface. This coupling strongly affects the amplitude and velocity of the wave. The waves have two particle displacement components in the sagittal plane. The surface particle displacement associated with these waves is elliptical in form and can be thought as a combination of shear and longitudinal displacements. The associated electric field moves in the same direction. The SAW energy is concentrated close to the surface of the piezoelectric wafer and is of a few wavelengths thick [2.22]. Due to the strong effect on the amplitude and velocity of the wave the SAW sensors have the ability to directly sense mass and mechanical properties.

The surface motion also allows the devices to be used as microactuators. The Rayleigh wave has a velocity that is approximately 5 orders of magnitude less than the corresponding electromagnetic wave, making the Rayleigh surface wave amongst the slowest to propagate in solids. The wave amplitudes are typically ~ 1 nm and the wavelengths vary from 1 to 100 μm [2.23]. The Rayleigh waves have virtually all their acoustic energy confined within one wavelength of the surface, thus making the SAW sensors have the highest sensitivity compared to other acoustic sensors reviewed. The SAW sensors operate in a typical frequency range of 25 to 500 MHz. One disadvantage of these devices is that they are not suitable for liquid applications due to the Rayleigh waves being surface-normal waves and result in compressional waves into the liquid causing heavy attenuation of the surface wave.

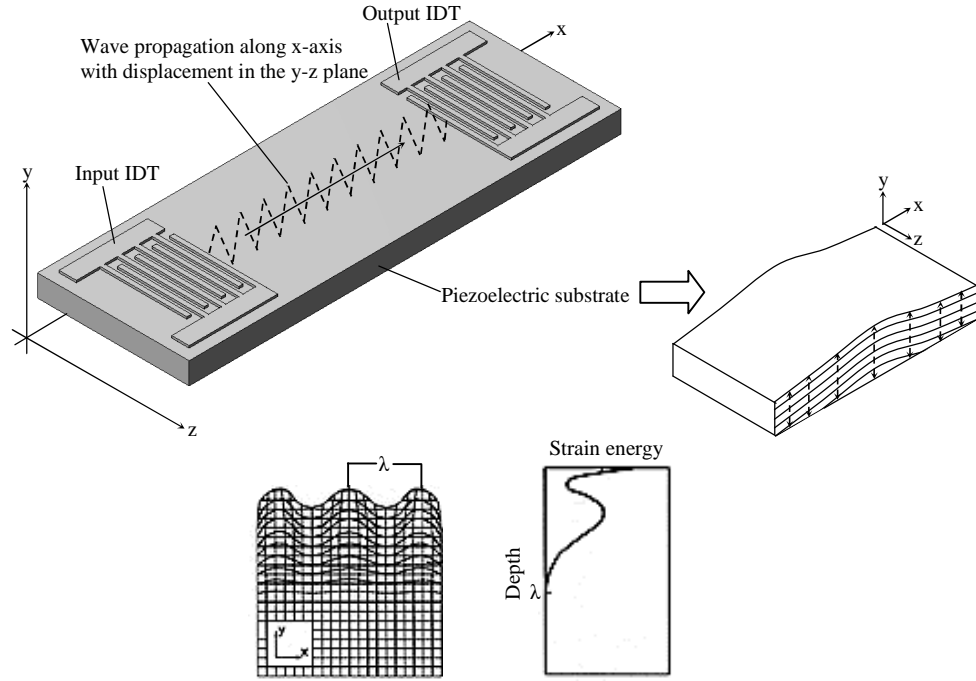


Figure 2.9 Rayleigh waves move vertically in the direction normal to the plane of the SAW sensor (top); Deformation field due to SAW propagation and the associated distribution of potential energy confined to one wavelength (bottom)

Uniform plane wave propagation in a piezoelectric solid

To approximate the acoustic wave propagation, the wave equation for a piezoelectric medium has to be considered [2.15]

$$\rho \ddot{u}_i = T_{ij,j} \quad (2.15)$$

where ρ is the mass density, u_i is the particle displacement and i and j are equal to 1, 2 or 3. (Note: in tensor notation the two dots over a symbol denotes $\partial / \partial t^2$ and a subscript (e.g. i) preceded by a comma denotes $\partial / \partial x_i$).

The strain-mechanical displacement relation is given by

$$c_{ijkl} S_{kl} = c_{ijkl} u_{l,k} \quad (2.16)$$

Assuming no intrinsic charge in the material, then the electrical displacement is

$$D_{j,j} = 0 \quad (2.17)$$

The wavelength of the elastic waves is much smaller than that of electromagnetic waves and hence the validity of the quasi-static approximation, thereby the magnetic effects generated by the electric field can be neglected [2.15].

$$E_k = -\phi_{,k} \quad (2.18)$$

where ϕ is the electric potential associated with the acoustic wave.

Equations (2.15) to (2.18) and the piezoelectric constitutive equations (2.2) and (2.4) present the acoustic wave propagation and substitution gives

$$\rho \ddot{\mathbf{u}}_i = \mathbf{c}_{ijkl}^E \mathbf{u}_{l,jk} + \mathbf{e}_{kij} \phi_{,jk} \quad (2.19)$$

$$0 = \mathbf{e}_{jkl} \mathbf{u}_{l,jk} - \varepsilon_{jk}^S \phi_{,jk} \quad (2.20)$$

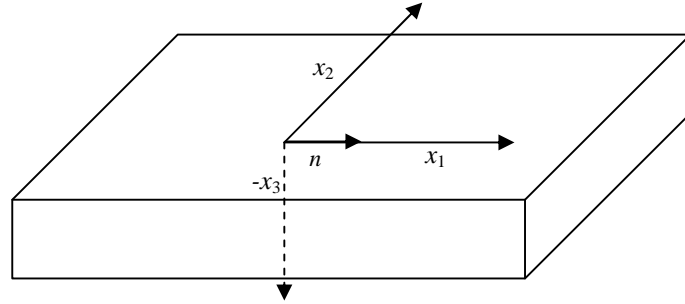


Figure 2.10 SAW coordinate system showing the propagation vector

Consider the geometry for the problem of SAW wave propagation shown in Figure 2.10, with a traction-free surface ($x_3 = 0$) and an infinitely deep solid from free space. The traction free boundary conditions are [2.20, 2.24]

$$T_{i3} = 0 \text{ for } x_3 = 0 \quad \text{where } i \text{ is equal to } 1, 2 \text{ or } 3. \quad (2.21)$$

The solutions of the coupled wave equations (2.19) and (2.20) have to satisfy the mechanical boundary conditions of Equation (2.21). Here of interest are the solutions of surface acoustic waves that propagate parallel to the surface with a phase velocity of v and decaying displacement and potential with distance away from the surface ($x_3 > 0$). The direction of propagation can be taken as the x_1 -axis, and the (x_1, x_3) plane can be defined as the sagittal plane.

The elastic constants (\mathbf{c}_{ijkl}), the piezoelectric constants (\mathbf{e}_{ijk}), and the dielectric constants (ε_{ij}) can be substituted by \mathbf{c}'_{ijkl} , \mathbf{e}'_{ijk} and ε'_{ij} . These primed parameters refer to a rotated coordinate system through the Euler transformation matrix [2.15]. The solutions of Equations (2.19) and (2.20) under the boundary conditions are of the form of running waves. The surface wave solution is the form of a linear combination of partial waves of the form [2.15]

$$\mathbf{u}_i = A_i \exp(-kx_3) \exp \left[-j\omega \left(t - \frac{x_1}{V_R} \right) \right] \quad (2.22)$$

$$\phi = B \exp(-kx_3) \exp\left[-j\omega\left(t - \frac{x_1}{V_R}\right)\right] \text{ and } x > 0 \quad (2.23)$$

where ω is the angular frequency of the electrical signal, k is the wave number, given by $2\pi/\lambda$, where λ is the wavelength given by $2\pi v/\omega$.

The solutions generated when there are three particle displacement components, are called *generalised Rayleigh waves*. Other boundary conditions (electrical and mechanical) and crystal symmetry impose further constraints on the partial wave solutions. Since the Rayleigh waves have no variation in the x_2 -direction, the displacement vectors have no components in the x_2 -direction and the solution is given as follows [2.24].

Assume displacements u_1 and u_3 to be of the form $A \exp(-bx_3) \exp[jk(x_1 - ct)]$ and $B \exp(-bx_3) \exp[jk(x_1 - ct)]$, and u_2 equal to zero, with the elastic half-space that exists for x_3 being equal to or less than zero, B and A are unknown amplitudes, k is the wave number for propagation along the boundary (x_1 -axis) and c is the phase velocity of the wave. Physical consideration requires b to be complex with a positive real part. By substituting these displacements into Navier-Stokes equation gives [2.24]

$$\nabla \cdot \boldsymbol{\tau} - \rho \frac{\partial^2 \mathbf{u}}{\partial t^2} = 0 \quad (2.24)$$

and by the use of the generalised Hooke's law for anisotropic elastic solids, two homogeneous equations in A and B are achieved. For a nontrivial solution, the determinant of the coefficient matrix cancels out, giving two roots for b in terms of the longitudinal and transverse velocities. Substituting these roots of b in the homogeneous equations for A and B gives the amplitude ratios, and hence a general displacement solution as given by equation (2.24) [2.24]. These displacements are shown overleaf in Figure 2.11. Here u_3 is in phase quadrature with u_1 , and the motion of each particle is an ellipse. Due to the change in sign of u_1 at a depth of about 0.2 wavelengths, the ellipse is described in different directions above and below this point and at the surface, the motion is retrograde, whereas lower down it is prograde.

$$\begin{aligned} u_1 &= [A_1 \exp(-b_1 x_3) + A_2 \exp(-b_2 x_3)] \exp[jk(x_1 - ct)] \\ u_3 &= (-b_1 / jk) A_1 \exp(-b_1 x_3) + (jk / b_2) A_2 \exp(-b_2 x_3) \exp[jk(x_1 - ct)] \end{aligned} \quad (2.25)$$

where $b_1 = k(1 - c^2/v_l^2)^{1/2}$ and $b_2 = k(1 - c^2/v_{tr}^2)^{1/2}$ with the longitudinal and transverse velocities, v_l and v_{tr} , are given by

$$v_l = \sqrt{\frac{\lambda + 2G}{\rho}}$$

$$v_{tr} = \sqrt{\frac{G}{\rho}}$$

where G is the Lames' constants given by $E_m / 2(1 + \nu)$ and λ is given by $\nu E_m / [(1 + \nu)(1 - 2\nu)]$ with ν being the Poisson's ratio and E_m being the Young's modulus.

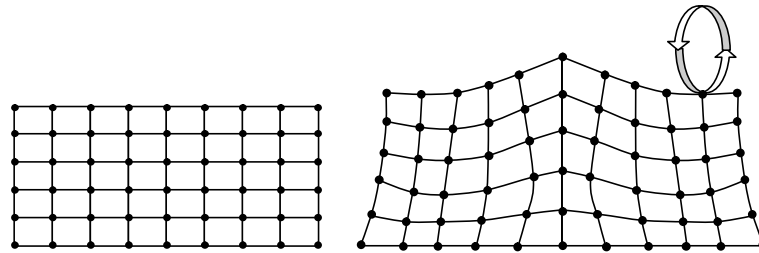


Figure 2.11 Particle displacement on the sagittal plane for Rayleigh waves

2.3.5.2 Shear horizontal surface acoustic waves

The use of a different crystal cut of a substrate can yield a shear horizontal surface acoustic wave (SH-SAW) instead of a vertical Rayleigh wave [2.25]. The SH waves have particle displacements that are transverse to the direction of propagation and parallel to the plane of the surface. Certain substrate crystals support this mode of acoustic waves and have different properties such as the SAW velocity that influence the frequency of operation. These acoustic waves have shown considerable promise in their application of microsensors in the liquid media [2.26, 2.27]. They show greater sensitivity to mass-loading, viscosity, conductivity, and permittivity of the adjacent liquid. Figure 2.12 illustrates the propagation of a SH surface acoustic wave.

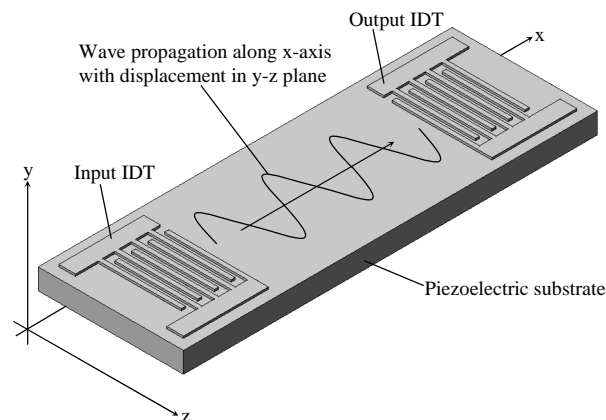


Figure 2.12 Shear horizontal surface acoustic waves (SH-SAW) with displacement parallel to the device surface

Propagation of shear horizontal and acoustic plate modes

As mentioned earlier these modes of acoustic waves have their energy confined between the upper and lower surfaces of a substrate, hence confining the waves to travel between an input and output IDT (reflector). SH modes may be thought of as those waves with a superposition of SH plane waves, which are multiply reflected at an angle between the upper and lower surface of the substrate plate. These boundary surfaces impose a transverse resonance condition, resulting in each SH mode having a displacement maximum at the surfaces, with sinusoidal variation between the surfaces.

The solution is simply a plane shear wave having parallel propagation to the surface, with its amplitude independent of x_3 (see Figure 2.10) within the material. The phase velocity is represented by v_t and the particle displacement associated with the n th order SH mode (propagating in the x -direction) has only an x_2 -component and is given by [2.15, 2.28]

$$u_2 = u_0 \left[\frac{n\pi}{b} \left(x_2 + \frac{b}{2} \right) \right] \exp[j(\omega t - \beta_n x_1)] \quad (2.26)$$

where b is the thickness of the substrate, u_2 is the particle displacement at the surface, n is the transversal modal index (0,1,2,3...) and t is time. The exponential term in the equation describes the propagation of the displacement profile down the length of the waveguide in the x_1 direction with angular frequency ω and wave number β_n which is given by

$$\beta_n = \sqrt{\left(\frac{\omega}{v_0} \right)^2 - \left(\frac{n\pi}{b} \right)^2} \quad (2.27)$$

with v_0 being the unperturbed propagation velocity of the lowest-order mode.

2.3.5.3 Love surface acoustic waves

Love waves can be considered as SAWs propagating in a waveguide material that is deposited on a substrate with different acoustic properties and infinite thickness compared to the waveguide material [2.29]. The Love waves are transverse and introduce only shear stresses. The displacement vector of the volume element is perpendicular to the propagation x -direction and is oriented in the direction of the z -axis (see Figure 2.13). The Love waves are surface waves and hence their energy is localised to the guiding layer and part of the underlying substrate close to the interface. The amplitude of the love waves decreases exponentially with depth (the wave

displacement has an antinode at the surface of the guiding layer and decays into the substrate) [2.30]. In comparison, SH-SAWs are limited by high noise levels and background interference from reflection off the lower surface. The guiding layer (usually SiO_2) as its name suggests confines and guides the wave in itself over the top of the device and hence circumvents the disadvantages (usually reduced sensitivity at the interface) associated with a similar SH device [2.31].

The geometry and polarisation associated with a Love wave is shown in Figure 2.11. The shear acoustic velocity in the guiding layer has to be smaller than the velocity in the underlying substrate for the existence of the Love wave and the larger the difference in velocities the larger the guiding effect [2.32]. The basic principle of generation is the same as that for the SH-SAWs. The only difference would be the fact that the Love wave mode would be the same SH-SAW mode travelling in a layer that was deposited on top of the IDTs. The particle displacements of these waves are transverse to the wave-propagation direction, that is, parallel to the plane of the surface-guiding layer. SAW devices that employ this wave mode have also shown great promise to liquid phase sensing [2.33, 2.34].

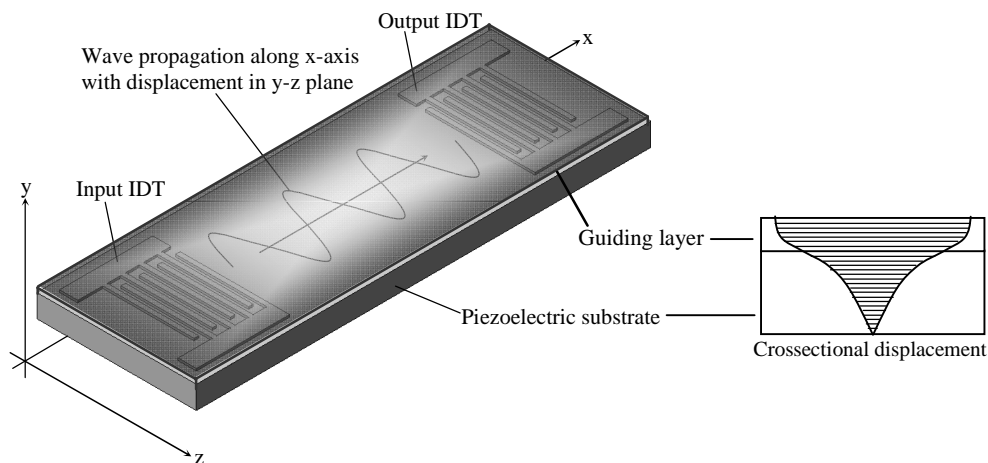


Figure 2.13 Wave generation on a Love wave mode device

Similar to the SH-APM devices in Love wave devices the waves generated by the IDTs are coupled into the guiding layer and propagate in the waveguide reflecting at angles to the surface. Again the frequency of operation is determined by the thickness of the guiding layer and the IDT finger-spacing [2.35]. These devices are mainly used for liquid-sensing and offer the advantage of using the same surface of the device as the sensing active area.

Love wave propagation

Seismology was first explained and established by Love in 1911, he showed that there could be no SH surface wave on the free surface of a homogeneous elastic half-space [2.29], and thus his model could not explain the seismology measurements. However he showed that the waves involved were SH waves, confined to a superficial layer of an elastic half-space and the layer having a different set of properties from the rest of the half-space. Using his proposed theory the Love waves are considered as SAWs that propagate along a waveguide material deposited on a substrate of another material, with different acoustic properties and an infinite thickness relative to the waveguide material. These are transverse waves and introduce only shear stresses. The displacement vector of the volume element is perpendicular to the direction of propagation $0-x_1$ and is oriented in the direction of the $0-x_2$ axis (see figure 2.14). Being surface waves the propagating energy is located in the layer and in part of the substrate close to the interface, with its amplitude decreasing with depth.

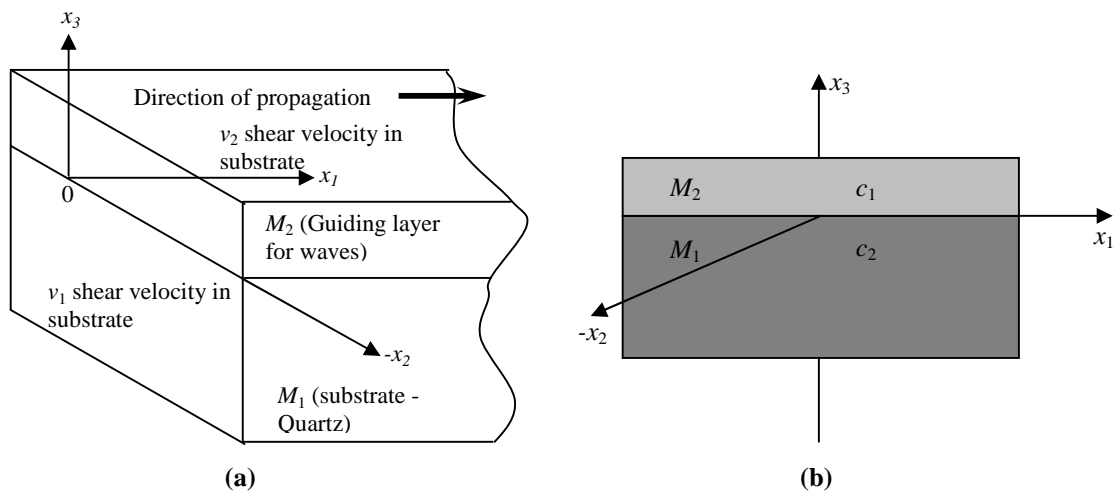


Figure 2.14 (a) Structure of Love wave device (b) Schematic of Love wave device used for analysis

The origin of the coordinate system is taken at the interface with $0-x_1$ axis oriented in the direction of propagation and the $0-x_3$ axis oriented vertically upwards. The plane $x_3 = h$ represents the free boundary of the layer. Assuming the displacements are oriented along the x_2 -axis and are independent of x_1 , then a monochromatic progressive wave of frequency ω propagating along the x_1 -axis can be considered.

The density, shear modulus and the displacement vector of the volume elements of the substrate and the layer are represented by the symbols ρ_1, G_1, u_1 and

ρ_2, G_2, u_2 respectively; the phase velocity and wave number of the transverse waves in the substrate and layer represented by v_{T1}, k_1 (equal to ω/v_{T1}) and v_{T2}, k_2 (equal to ω/v_{T2}) respectively; and finally the v_l and k_l (equal to ω/v_l) the velocity and wave number of the Love wave, whose existence is assumed. The solutions of the propagation Equations (2.25) can now be written as

$$\begin{aligned} u_{1 \times 2} &= A \exp(j\omega t - jkx_1 + \alpha_1 x_3) \\ u_{2 \times 2} &= (B_1 + B_2) \exp(j\omega t - jkx_1 + \alpha_2 x_3) \end{aligned} \quad (2.28)$$

where

$$\alpha_1 = -k\sqrt{1 - v_l^2 / v_{T1}^2} \quad \text{and} \quad \alpha_2 = -k\sqrt{1 - v_l^2 / v_{T2}^2} \quad (2.29)$$

It has been shown that the above equation satisfies the Naviers Equation (2.24) in both media and that $u_3 \rightarrow 0$ as $x_3 \rightarrow -\infty$ [2.24]. The constants A, B_1 , and B_2 are determined by the boundary conditions that only require the tangential stresses σ_{23} cancel out in the plane $x_3 = h$ but also that they are continuous as well as the displacements $u_{1 \times 2}$ and $u_{2 \times 2}$ in the plane $x_3 = 0$ [2.30, 2.10].

The first of these conditions gives

$$B_1 \exp(-\alpha_2 h) - B_2 \exp(+\alpha_2 h) = 0 \quad (2.30)$$

and the other two conditions lead to

$$A = B_1 + B_2 \quad \text{and} \quad \alpha_1 G_1 A = \alpha_2 G_2 (B_1 - B_2) \quad (2.31)$$

This system of three linear equations gives a solution different from zero if

$$\tan(\alpha_2 h) = \frac{G_1 \alpha_1}{G_2 \alpha_2} \quad (2.32)$$

The roots of this equation have a real value when $k_1 < k < k_2$, that is, when $v_{l2} < v_l < v_{l1}$. This implies that the condition of existence of Love waves is that the propagation velocity of transverse waves in the layer must be smaller than the propagation velocity of the transverse waves in the substrate.

From Equation (2.30) it can be deduced that there are infinite modes owing to the periodicity and the tangential function; when v_l tends to v_{l1} , $\tan(\alpha_2 h)$ tends toward the value of $n\pi$ (with n being 1, 2...), and for the first mode, the wavelength becomes infinite compared to thickness. The particle displacements during the propagation of Love waves can be obtained using Equation (2.31) as

$$u_{1 \times 2} = A \exp(\alpha_1 x_3) \exp[j(\omega t - kx_1)]$$

$$u_{2 \times 2} = A \frac{\cos[\alpha_2(h - x_3)]}{\cos \alpha_2 h} \exp[j(\omega t - kx_1)] \quad (2.33)$$

where A is the propagation constant determined by the excitation signal. It can be seen from the Equation in (2.33) that the displacement amplitude $u_{1 \times 2}$ decreases exponentially in the substrate and also that the different modes $u_{2 \times 2}$ correspond to 0, 1, 2... nodal planes in the layer. The displacement is also dependent on the frequency and it is noticed that the energy is entirely established in the substrate at very low frequencies and the Love wave propagates at velocity v_{l1} as if the waveguide layer does not exist. On the other hand, at very high frequencies the acoustic energy is concentrated in the layer and the velocity of the Love wave tends towards v_{l2} , the wavelength being very small with respect to the thickness of the layer. There is thus a similarity between the SH-SAW and Love wave modes in terms of displacement, and relationships for change in velocity and frequency shift can be determined using the perturbation theory (discussed in chapter 3).

2.3.5.4 Flexural plate waves

In a flexural plate wave (FPW) device, an acoustic wave is excited in a thinned membrane. As with the other acoustic wave devices discussed the FPW devices also sense quantities that cause its phase velocity to change. An interesting feature of the FPW device is that it can be designed so that its phase velocity is lower than that of most liquids, which lie in the range from 900 to about 1500 ms^{-1} . On operation in a liquid, a slow mode of propagation exists in which there is no radiation from the plate, making the FPW devices function well in the liquid environment, and hence appropriate for biosensing and chemical sensing in liquids. The mass per unit area of the thin plate is significantly increased on mass-loading (due to adsorption of chemical vapour molecules on the plate). This decreases the phase velocity of the propagating waves. Other forms of mass loading that can be measured is fluid loading on the FPW devices, this again decreases the phase velocity of the ultrasonic waves. As the density of the fluid increases the velocity decreases and similar effects seen as molecules (protein, cells, bacteria etc.) adhere to the surface of the plate. An opposite effect occurs when the tension in the plate is increased, increasing the phase velocity.

The FPW devices typically consist of a silicon wafer, with a membrane layer (such as silicon nitride, silicon dioxide, oxy-nitride, aluminium nitride and diamond) and the piezoelectric material (zinc oxide) is sputtered on the dielectric membrane surface. The IDTs are patterned on top of the piezoelectric material and the membrane is released by performing a backside etch of the silicon wafer. The membrane motion can be normal to the surface or can propagate a shear wave like in the SH-SAW devices [2.36]. Any perturbation of the surface changes the propagating wave velocity and damps the acoustic vibration.

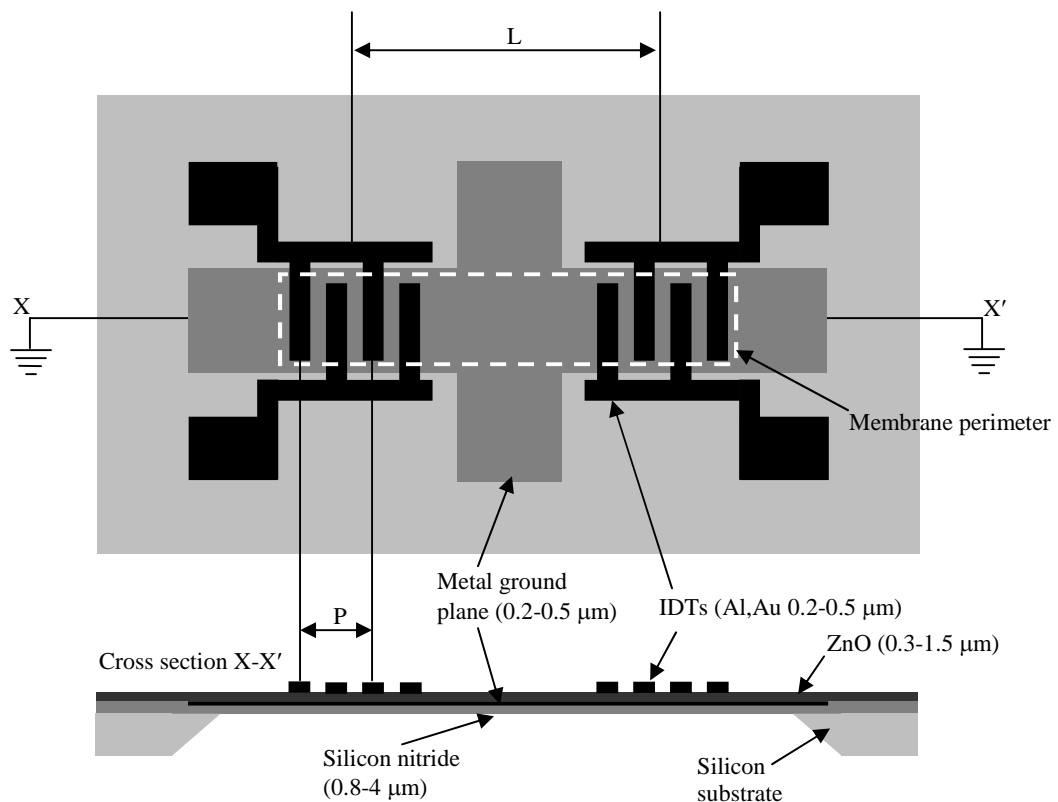


Figure 2.15 A flexural plate wave (FPW) device

The detection sensitivity is not based on frequency of operation like the other acoustic devices, but instead on the relative magnitude of the perturbation to a parameter of the membrane. In the case of mass, the sensitivity is the ratio of the added mass to the membrane mass. Since very thin (low mass) membranes can be fabricated, very high detection sensitivities can be achieved, higher than other acoustic sensor modes. Other advantages include low operating frequencies hence simple and cheaper electronics to drive and detect the sensor signals; based on a silicon wafer allows the possibility of integrating the electronics and large scale sensor system integration with low cost

fabrication and packaging; for biosensing the fluid is in contact with the backside of the device which provides a natural barrier to the electrodes and electronics on the other side of the devices (promising technology). The drawback of the FPW devices is that the membrane technology has not been fully developed and it is difficult to develop low stress membranes with good acoustic characteristics. Also the membranes being very thin tend to be fragile; hence advances to make them more robust are required.

2.4 Detection mechanisms and performance issues for AW sensing

In the preceding sections we have described the propagation of different acoustic wave modes and the operating principles of various acoustic wave devices that can be used as sensors of various physiochemical phenomena in surrounding media. This section describes the extension of these capabilities to the detection and performance in sensing of various analytes.

2.4.1 Detection mechanisms

The detection of chemical analytes can be based on changes in one or more of the physical characteristics of a thin film or layer in contact with the sensor surface. Some of the basic film properties that can be used for detection include mass/area, elastic stiffness (modulus), viscoelasticity, viscosity, electrical conductivity, and permittivity. In addition, changes in extrinsic variables such as temperature and pressure can also produce a sensor response, by either directly affecting the acoustic wave or via changes in the film's intrinsic properties. All the detection mechanisms are not of practical significance to all types of sensors and there can be several mechanisms operating simultaneously to affect a response. Thus the range of detection mechanisms is a two way system that leads to a high degree of versatility and a broad range of potential analytes, but can also make interpretation of sensor responses difficult in certain cases. The development of equivalent circuit models has assisted in the evaluation of sensor responses and has provided relative importance of a given transduction mechanism for a specific sensor application. These transduction mechanisms employed in analytical applications involve changes in the velocity and/or the amplitude of the acoustic waves. The wave velocity is generally the preferred measurement, however wave attenuation sometimes provides an additional indicator of a particular interaction and, importantly, aids in distinguishing one sort of perturbation from another [2.37, 2.38].

In majority of the cases, the relevant perturbation mechanism can depend on the nature of the analyte in contact with the acoustic sensor. The various detection mechanisms are discussed in the following sections followed by the performance issues.

2.4.1.1 Mass loading

This is the most commonly used detection mechanism, based on the change of wave velocity (or, equivalently, oscillation frequency) by the addition or removal of mass at the sensor surface. Simple mass loading perturbs the wave velocity without producing attenuation effects, distinguishing it from other detection mechanisms discussed in the following sections. As this effect is accessible to all acoustic wave modes a vast majority of analytical applications utilise changes in mass loading.

Surface mass changes can result from physical sorption or chemical reactions between analyte and coating, and can be used for sensing applications in both liquid and gas phases. The absolute mass sensitivity of a sensor (uncoated) depends on the type of piezoelectric wafer, operating frequency, device dimensions and the acoustic mode utilised, with a linear dependence predicted in all cases. This allows a very general description of the working relationship between mass-loading and frequency shift, Δf_m , for acoustic wave devices given as

$$\Delta f_m = -KS_m \Delta m_A \quad (2.34)$$

where S_m is a device specific constant and depends on the factors mentioned above, K is a geometric factor for the fraction of the sensing device area being perturbed, and Δm_A is the change in mass/area on the device surface. K can be a simple fraction of the centre to centre spacing between IDTs (the sensing area) that is coated with a uniform chemically selective layer or exposed to the analyte, or it can be a complex function that relates some non-uniform coating geometry with the distribution of acoustic energy for resonators.

The majority of the acoustic wave sensors for chemical and biological sensing, use coatings that physically or chemically interact with the analytes and hence cause a change in mass. Therefore, this sensing mechanism offers a great amount of freedom in the selection of suitable sorptive or reactive coating materials. However, the challenge in employing this detection mechanism is to impart selectivity.

2.4.1.2 Mechanical properties

Interaction with an analyte can result in a change of mechanical properties of a sensing surface (coated/uncoated). An increase in mass loading produces a decrease in frequency without affecting the attenuation, as mentioned before. Conversely, changing the mechanical properties of a sensing surface can produce changes in both frequency and the attenuation of the acoustic wave. Furthermore, these changes can either increase or decrease either or both of the acoustic wave propagation parameters.

The mechanical properties of a thin film coating can be considered as either elastic or viscous in nature. In most of the cases, these two properties are so interdependent and are therefore considered together as *viscoelastic* properties. In the instance where mechanical effects are adequately treated as purely elastic, the frequency of a SAW device is perturbed by modulus changes according to

$$\Delta f_e = S_e f_0^2 \Delta \left(\frac{4h\mu}{v^2} \left(\frac{\lambda + \mu}{\lambda + 2\mu} \right) \right) \quad (2.35)$$

where S_e is a constant related to the substrate material, h is the thickness of the coating, v is the surface wave velocity, and μ and λ are the shear modulus and Lamé constant of the coating, respectively. Note that in equation (2.35) there is a Δ outside of the brackets, indicating that a change in the entire term is used in computing the elastic perturbation. This is convenient because it applies to either the deposition of the elastic material or changes in the elastic moduli and/or thickness of already present film on the device surface.

Organic polymers comprise of the most common type of coating used with acoustic wave sensors due to their ability to sorb vapours and liquids, reversibly. The majority of the work reports on the use of polymer coating for SAW sensing, the polymer's elastic modulus has been considered small enough for modulus effects to be neglected; most of these studies did not, however, consider viscoelastic effects at all. The relative importance of the mass-loading and viscoelastic contributions to the observed acoustic sensor response is an issue that is yet to be resolved. Furthermore, capitalising on these effects to improve chemical selectivity and detection sensitivity requires further characterisation of sensor response, in terms of both velocity and attenuation changes (requires real and imaginary parts (complex) to separate out mass loading and viscoelastic).

The response as a result of a Newtonian liquid loading on to the quartz surface is a more complex than a solid mass layer involving a frequency shift and a broadening

of the resonance. This indicates both energy storage and energy dissipation. The frequency shift of the perturbed wave was predicted by Kanazawa and Gordon as follows [2.39]:

$$\Delta f_s = -\frac{f_s^{3/2}}{N} \left(\frac{\rho\eta}{\pi\mu_q\rho_q} \right)^{1/2} \quad (2.36)$$

where ρ and η are the density and viscosity of the liquid, μ_q and ρ_q are the shear stiffness and mass density of the quartz and N is the mode index (integer). In a liquid the shear mode oscillation of the crystal surface entrains the liquid and the liquid motion has an exponential decay into the liquid of $\exp(-x_3/\delta)$ where x_3 is the coordinate normal to the surface and $\delta = (\eta/\pi f_s \rho)^{1/2}$ is the decay or the shear wave penetration depth [2.40].

2.4.1.3 Electrical properties

The acoustic wave sensors are based on piezoelectric substrates, which have an associated electric field accompanying the propagating wave as it propagates through the substrate. This electric field interacts with mobile charge carriers in the analyte or sensing surface/coating and this affects both the acoustic velocity and attenuation. This detection mechanism can advantageously be employed in chemical sensor design although careful choice of piezoelectric material has to be made. The attenuation and velocity of surface acoustic waves depend on the square of the electromechanical coupling coefficient of the substrate, which varies by orders of magnitude from one material to another.

Increase in conductivity of the sensing surface due to analyte (polar) interaction, causes a decrease in frequency and the conductivity change enhances frequency shifts due to increased mass or decreased modulus. To isolate the conductivity effects from mass and mechanical effects, the device can be metallised which shorts out the electric field and prevents its interaction with the analyte. This can be used as a reference device and the signal compared to the sensing device that has no metallisation, and the resulting difference in frequency shifts depends only on conductivity changes.

2.4.1.4 Thermal effects

The velocity of acoustic waves in piezoelectric material is very sensitive to changes in temperature. Due to this effect, temperature control/compensation measures have to be

considered and for most chemical sensing applications substrates with small temperature coefficients such as ST-quartz for SAW sensors and AT-quartz for TSM sensors are chosen. There are cases where the temperature sensitivity of acoustic wave devices is of potential, but thus far undemonstrated, value.

The temperature sensitivity of the acoustic velocity allows the possibility of enthalpimetric measurements. As in the case with the acoustoelectric effects discussed above, maximum temperature sensitivity would be obtained with careful choice of the substrate. Substrates with high temperature coefficients such as YZ-LiNbO₃ (80 ppm/°C) would be a good choice SAW temperature sensors. Furthermore, minimising the thermal mass of the AW device and any coating film, relative to the active sensing area, enhances the sensitivity.

The piezoelectric materials such as LiTaO₃ also demonstrate a pyroelectric effect, whereby a temperature gradient reduces the normal polarisation state of the crystal which induces charge to flow off its surface and creating a voltage [2.41, 2.42]. This property can be used to measure the heat produced by chemical reactions at a sensor surface, with the most common application being the detection of biological species via enzyme-catalyzed reactions [2.43, 2.44] that generate considerable amounts of heat (up to 100 kcal/mole [2.45]).

2.4.2 Performance issues

In the development of a sensor for a given application, various factors affecting the performance have to be considered. Among these are sensitivity, selectivity, reversibility, response time, dynamic range, stability, reliability, and environmental effects (e.g. temperature). Some of these issues dictate the choice of substrate and/or acoustic mode, optimal operating conditions and selection of the coating materials for specific bio-sensing.

2.4.2.1 Selectivity

Selectivity refers to the ability of a sensor to discriminate between the analyte of interest and possible interferences. For acoustic wave chemical sensing this characteristic is determined in most cases by the properties of the coating material. Selectivity for single analytes is very difficult to obtain but can be realised with some biologically-based coatings. However, a good amount of selectivity can be achieved in

many cases if the nature and number of potential interferants is known. The issue of selectivity applies to most monitoring systems and should not be considered a limitation unique to the present, or any other, sensor technology. However this is only a constraint that is application specific, as if a broader range of analytes are to be measured it is not really an issue.

2.4.2.2 Reversibility

Reversibility is the ability of a sensor to return to its original baseline condition, after exposure to an analyte. More particularly, the coating-analyte interaction is considered to be reversible if removal of the analyte results in complete desorption from the coating/sensor, with no permanent physical or chemical change having occurred. The reversibility of these interactions obviously depends on the relative strength of the interactions, and on the kinetics and thermodynamics of them. In the case of uncoated sensors the reversibility is easier as there is no interaction between the analyte and a selective coating and the sensor surface can easily be cleaned to the baseline.

2.4.2.3 Sensitivity

Sensitivity for a reversible sensor is defined as the change in sensor output signal obtained for a change in concentration of an analyte. The sensitivity of a reversible acoustic wave sensor can be expressed in terms of (frequency change) / (concentration change), e.g., Hz/M (M=mol/L), Hz/(μ g/L), or even ppm/ppm (normalised frequency change / concentration). In the case of an irreversible sensor, the sensitivity is more appropriately expressed by frequency change / integrated exposure, e.g., Hz/M-min.

The overall sensitivity of an acoustic wave sensor system depends on the individual device, the selective coating (if coated) and also in some cases the supporting hardware. The overall sensitivity is different from the mass sensitivity of the device although it takes it into account plus many other factors. For an acoustic wave sensor of a given acoustic mode, the sensitivity to an analyte is determined by the amount of coating/sensing area (thickness and/or available surface area) and the strength of analyte-coating/sensing surface interaction.

2.4.2.4 *Dynamic range*

The dynamic range is the concentration range over which the range outputs a continuously changing response. A linear dynamic range corresponds to the region where there is a linear proportionality relation maintained between the concentration and sensor response. The dynamic range is bounded by the limit of detection (LOD) at the lower end and by the saturation effects at the upper end (saturation limit). Analyte concentrations below the LOD give no detectable response (indistinguishable from noise), while concentrations at the saturation limit or above all give the same output.

The LOD depends on the inherent sensitivity of the device itself, as well the kinetics and thermodynamics of analyte-coating/sensing surface interaction and quantity of (thickness and/or surface area) coating/sensing area available. The LOD also depends on the system noise level as is expressed in terms of the ratio (response when analyte is present)/(noise level when there is no analyte present). The LOD is expressed in units of concentration (e.g. M, $\mu\text{g/L}$, or ppm).

2.4.2.5 *Stability, repeatability, reliability and reproducibility*

Stability is related to four important concepts: short and long term effects, noise, and drift. The short term effects are rapid compared to the typical time interval over which the sensor response occurs, while the long term effects are slow over the time scale. Noise represents a positive and negative fluctuation about an unchanging average value (over a long time scale), while drift refers to a unidirectional change in the signal that causes the average value to change monotonically (not necessarily linearly though) with time. In the short term, the goals are minimal noise and short-term drift. Noise has a detrimental effect on the LOD and on the accuracy of the response. The short term drift is often associated with short term systematic changes in ambient conditions such as temperature, pressure, and relative humidity that can exceed noise, hence the drift dictating the LOD. The noise can be partly compensated by averaging several consecutive data points, but this is more difficult for short-term drift.

Long term aging of the sensor system such as the device, coating, and the electronic circuitry, results in drift and may require frequent recalibration, particularly in the case where the physiochemical properties of the coating change. Long term baseline drifts resulting from e.g. slow temperature variations or “burn in” of a device and circuitry, can be compensated for using baseline subtraction techniques. Some of

the short and long term effects can be corrected by performing differential measurements using dual-device configurations (a sensing and reference device), provided the drifts are comparable for the two devices.

Repeatability is the degree to which an individual sensor repeatedly yields that same signal for the same analyte concentrate under the same operating conditions. Reliability is the same as repeatability, except that the responses are obtained under a variety of ambient conditions expected for a particular sensor application and period of time. Reproducibility is often confused with reliability and repeatability; it actually gives the extent to which two nominally identical sensors (fabricated under same set of procedures, but at different times or different facilities) produce the same output to a particular stimulus. A high reproducibility rate suggests that a single sensor from a large batch can be used to obtain calibration data for all other sensors in that batch. Such reproducibility is difficult to attain due to practical issues such as variability in fabrication and packaging.

2.4.2.6 Response time and environmental effects

The response time of the sensors should be appropriate for the intended application of the sensors. The response time depends on various properties of sensor systems such as analyte deliver systems, and on the properties of the device itself such as coatings and sorption/reaction kinetics. The rates of adsorption and desorption determine response times for coated sensors that utilise a flat, impermeable surface or a sufficiently thin coating with high diffusivity that permeation is comparatively rapid. In the case of reactive coatings, reaction rates can be affected by reagent surface area: small particle sizes and/or highly porous supports that maximise area/volume ratio produce a larger response in a shorter time – as long as the rate of delivery of analyte to the device is not a limiting factor.

Of all the environmental factors, temperature is the most significant, affecting sensor performance. The sensor temperature, and surrounding changes, can affect the response in a number of ways. As discussed earlier the effect on temperature on the acoustic wave devices can be minimised by appropriately choosing the piezoelectric substrates. Again temperature-drift compensation can be minimised using dual-device configuration, although this may not be completely successful due to difficulty of precisely matching thermal stress effects for the sensing and reference devices (these issues are further discussed in chapter 4).

2.4.3 SAW delay lines and resonators

Previously when looking at the excitation of acoustic waves the two main types of transducer setups were introduced on the piezoelectric substrates to form the SAW delay lines and SAW resonators. Following that, the various types of SAW devices related to different applications, measurement mechanisms and performance criteria were introduced. All the different types of devices discussed in the previous sections can be fabricated in the form of SAW delay line or SAW resonator configurations and applied to a number of sensing applications including chemical (liquid) applications having selective coatings or without.

Selecting an appropriate type of SAW for sensing purposes mainly depends on the application. Although there are the relative merits with the use of a particular type of device fabricated on a certain substrate, it may not be possible for it to be used for certain applications.

Most chemical and biological sensors are coated with selective layers making the devices highly selective to a particular analyte or species, however they are affected by aging effects making the devices less robust. On the other hand uncoated devices based on physical rather the chemical parameters, are more robust and durable to aging effects although to the expense of lower selectivity. Again this can put this down to an application oriented choice of devices.

2.5 Conclusions

In this chapter background to the basic principles governing acoustic waves and SAW devices has been covered. The basic equations that describe the propagation of different types of wave in elastic solids have been presented along with expressions for particle displacements. Particular emphasis has been directed to Rayleigh, SH modes and Love wave modes and it has been established that SH-SAW modes are most suited to liquid sensing. Also covered in this chapter are the various detection mechanisms and performance criteria for SAW sensors and the different types of SAW devices compared. The material here will help understand the SAW sensor design and application of this study in other chapters.

2.6 References

- [2.1] J. Curie and P. Curie, *Bull. Soc. Fr. Mineral.* 3, 90 (1880).
- [2.2] W.G. Hankel, *Abh. Sächs*, 12 (1881), p. 547.
- [2.3] W.G. Hankel, *Ber. Sächs*, 33 (1881), p. 52.
- [2.4] G. Lippman, *An. Chim. Phys. Ser. 5*, 24 (1881), p.145.
- [2.5] Lord Kelvin, *Phil. Mag.*, 36 (1893), pp. 331, 342, 384, 453.
- [2.6] W. Voight, *Abh. Götl*, 36 (1890), p. 1.
- [2.7] Lord Rayleigh, *Proc. London Math. Soc.*, 17 (1885).
- [2.8] C. Campbell, *Surface Acoustic Wave Devices and their Signal Processing Applications*, Academic Press, London, (1998).
- [2.9] D. P. Morgan, *Surface-Wave Devices for Signal Processing*, Elsevier, Netherlands, (1978).
- [2.10] A. J. Slobodnik, Surface acoustic waves and materials, *Proc. IEEE*, 64, (1976), pp. 581-595.
- [2.11] V. K. Varadan and V. V. Varadan, IDT, SAW and MEMS sensors for measuring deflection, acceleration and ice detection of aircraft, *SPIE*, 3046, (1997), pp. 209-219.
- [2.12] J.W. Grate, S. J. Martin and R.M. White, Acoustic wave microsensors, *Part I, Analytical Chem.*, 65, pp. 987-996.
- [2.13] R. Bechmann, A. D. Ballato, and T. J. Lukaszek, Higher order temperature coefficients of the elastic stiffness and compliances of alpha-quartz, *Pro. IRE*, (1962).
- [2.14] J.W. Grate, S. J. Martin and R.M. White, Acoustic wave microsensors, Part I, *Analytical Chem.*, 65, pp. 987-996.
- [2.15] B. A. Auld, *Acoustic Fields and Waves in Solids*, John Wiley and Sons I (1973a), New York.
- [2.16] D. S. Ballantine et al., *Acoustic Wave Sensors – Theory, Design, and Physio-Chemical Applications*, Academic Press (1997), pp. 36-42.
- [2.17] M. Schweyer et al., A Novel Monolithic Piezoelectric Sensor, *Proc. Ultrasonics Symposium*, Vol. 1, (1997), pp. 371-374.
- [2.18] S. Martin, Gas Sensing with Acoustic Devices, *Proc. Ultrasonics Symposium*, Vol. 1, (1996), pp. 423-434.

- [2.19] M. Schweyer et al., An Acoustic Plate Sensor for Aqueous Mercury, *Proc. Ultrasonics Symposium*, Vol. 1, (1996), pp. 355-358.
- [2.20] I. A. Viktorov, *Rayleigh and Lamb Waves: Physical Theory and Applications*, Plenum Press, New York (1967).
- [2.21] R. W. White and F. W. Voltmer, Direct piezoelectric coupling to surface elastic waves, *Appl. Phys. Lett.*, 7, pp. 314-316.
- [2.22] D. P. Morgan, *Surface-Wave Devices for Signal Processing*, Elsevier, Netherlands, (1978).
- [2.23] H. Wohltjen, Surface Acoustic Wave Microsensors, *Transducers*, (1987).
- [2.24] V. V. Varadan and V. K. Varadan, *Elastic wave propagation and scattering*, Engineering Science and Mechanics, Pennsylvania State University, USA.
- [2.25] N. Nakamura, M. Kazumi and H. Shimizu, SH-type and Rayleigh-type surface waves on rotated Y-cut LiTaO₃, *Proc. IEEE Ultrasonics Symp.*, 2, (1987), pp. 819-822.
- [2.26] G. Kovacs and A. Venema, Theoretical comparison of sensitivities of acoustic shear wave modes for (bio)chemical sensing in liquids, *Appl. Phys. Lett.*, 61, (1992), pp. 639-641.
- [2.27] S. Shiokawa and T. Moriizumi, Design of SAW sensor in liquid, *Proceedings of the 8th Symposium on Ultrasonic Electronics*, (July 1987), Tokyo.
- [2.28] B. A. Auld, *Acoustic Fields and Waves in Solids II*, John Wiley and Sons (1973), New York.
- [2.29] A. E. H. Love, *Theory of Elasticity*, Cambridge University Press (1934), England.
- [2.30] W. M. Ewing, W. S. Jardetsky and F. Press, *Elastic Waves in Layered Media*, McGraw-Hill (1957), New York.
- [2.31] E. Gizeli, N. J. Goddard, C. R. Lowe, and A. C. Stevenson, A love plate biosensor utilising a polymer layer, *Sensors and Actuators A*, 6, (1992), pp. 131-137.
- [2.32] J. Du et al., A study of love wave acoustic sensors, *Sensors and Actuators A*, 56, (1996), pp. 211-219.
- [2.33] R. Haueis et al., A love wave based oscillator for sensing in fluids, *Proceedings of the 5th International Meeting of Chemical Sensors*, Rome, Italy, 1, (1994), pp. 126-129.

- [2.34] M. Hoummady, D. Hauden, and F. Bastien, Shear horizontal wave sensors for analysis of physical parameters of liquids and their mixtures, *Proc. IEEE Ultrasonics Symp.*, 1, (1991), pp. 303-306.
- [2.35] P. Tournios and C. Lardat, Love wave dispersive delay lines for wide band pulse compression, *Trans. Sonics Ultrasonics*, SU-16, (1969), pp. 107-117.
- [2.36] D. S. Ballantine et al., *Acoustic Wave Sensors – Theory, Design, and Physio-Chemical Applications*, Academic Press (1997), pp. 111-119.
- [2.37] S. J. Martin, G. C. Frye, *Appl. Phys. Lett.* 57, (1990), pp. 1867.
- [2.38] A. J. Ricco, S. J. Martin, *Sensors and Actuators B* 10, (1993), p. 123.
- [2.39] K. K. Kanazawa and J. G. Gordon II, *Anal. Chim. Acta* 175, (1985), p. 99.
- [2.40] D. S. Ballantine et al., *Acoustic Wave Sensors – Theory, Design, and Physio-Chemical Applications*, Academic Press (1997), p. 56.
- [2.41] N. J. Zemel, in *Solid-State Chemical Sensors*, J. Janata, J. R. Huber, (Eds), Academic Press, (1985), Orlando, FL, 163-207.
- [2.42] L. D. Polla, R. M. White, S. R. Muller, *IEEE Electron. Dev. Lett.* EDL-7(4), (1986), p. 254.
- [2.43] R. E. Dessy, L. Burgess, L. Arney, J. Petersen, in *Chemical Sensors and Microinstrumentation*, ACS Symp. Series No. 403, R. W. Murray, R. E. Dessy, W. R. Heineman, J. Janata, R. W. Seitz (Eds), *Amer. Chem. Soc.*, Washington D. C., (1989), p.143.
- [2.44] G. G. Guilbault, B. Danielsson, C. F. Mandenuis, K. Mosbach, *Anal. Chem.*, 55, (1983), p. 1582.
- [2.45] K. Mosbach, B. Danielsson, *Anal. Chem.*, 53, 1981, 83A.

CHAPTER 3

Design of SH-SAW liquid sensor

3.1 Introduction

From the previous chapter it can be seen that SAW based devices are suitable for sensing applications in both gaseous and liquid environments. They offer many attractive features such as small size, robustness and high sensitivity. This chapter discusses the choice of SAW propagating mode and hence the suitable piezoelectric substrate for the liquid microsensor. The operating principle and the sensor model based on the perturbation theory which in turn can be related to the mechanical and acousto-electric properties of an analyte are discussed and detailed sensor design is presented.

3.2 Surface acoustic wave mode and substrates for liquid sensor

When using acoustic devices as sensors, the sensitivity can theoretically be raised by increasing the frequency. SAW device frequency can now be chosen to be higher than 1 GHz, while quartz oscillator frequency is usually below a few tens of MHz. This high operating frequency ability of the SAW devices make them well suited for high sensitivity chemical sensing applications. Here liquid sensing is of interest and as previously discussed the appropriate mode of SAWs has to be selected for this application.

As a SAW propagates on the piezoelectric crystal surface, it is influenced by physical and chemical changes at the surface and/or an adjacent medium. The sensors

in this study are designed for the liquid phase and hence the appropriate substrate and SAW propagation mode had to be chosen. When a piezoelectric substrate generated Rayleigh SAWs is in contact with liquid, the Rayleigh SAWs radiate longitudinal waves which result in high propagation losses. These Rayleigh SAWs have two components of particle displacement, one parallel to the surface along the direction of the wave propagation, and the other normal to the surface (as described in Chapter 2). Displacements normal to the surface generate compressional waves, which dissipate the wave energy in the liquid. This mode conversion caused by the surface vertical displacement of the SAWs, was studied by Campbell and Jones [3.1]. Thus there was a need to find other types of propagation modes that do not experience the propagation loss mentioned above for liquid sensing applications. Thus the requirements for a potential liquid sensing SAW mode can be listed as below

- Large surface shear horizontal displacement
- Propagation power confined at the surface
- Large electromechanical coupling coefficient
- Low temperature coefficient

The anticipated modes are shear horizontally polarised shear waves (SH waves) [3.2]. In 1977, Prof. Nakamura et al. [3.3], Tohoku University, reported that the SAW on 36° rotated Y-cut X-propagating LiTaO₃ is a leaky type SH mode. In 1987, Prof. Shiokawa et al. [3.4] proposed a liquid-phase sensor based on 36YX LiTaO₃. Figure 3.1 shows propagation of Rayleigh-SAW and the SH-SAW at the liquid and piezoelectric surface interface.

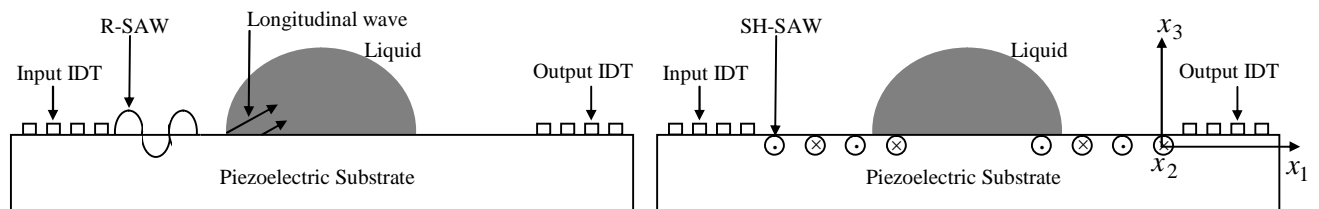


Figure 3.1 Rayleigh-SAW (R-SAW) and SH-SAW at liquid and piezoelectric substrate interface

From the Figure 3.1 above it can be seen that the Rayleigh wave generates longitudinal waves into the liquid and thus it will be highly attenuated. Conversely, the SH-SAW

can propagate at liquid/solid interface and therefore the SH-SAW can be utilised for a liquid-phase sensor.

Examining the results reported for leaky SAW mode without liquid loading, on different substrates it was established that LiNbO_3 and LiTaO_3 satisfy these requirements. Shiokawa et al. performed computations to verify the suitability of these crystals. The computations were based on the method reported by Campbell and Jones [3.1] using material constants from Nakagawa et al. [3.5] and Smith and Welsh [3.6] for LiNbO_3 and LiTaO_3 , respectively. They took into consideration the influence of liquid viscosity, as SH displacement at the surface drives shear fluid movement by viscosity coupling, which eventually results in the additional increment of the propagation loss. From these computations they determined that for LiTaO_3 the SH displacement is dominant and the propagation loss is minimum at a rotation angle of 36° . The electromechanical coupling constant at that angle is also large. Although the results for LiNbO_3 demonstrated a higher electromechanical coupling constant than LiTaO_3 , the propagation losses were also higher. Table 3.1 presents some of the material constants for LiNbO_3 and LiTaO_3 leaky SAW substrates (Note: v_1 , v_2 and v_3 are particle velocities of the leaky SAWs at $x_3 = 0$ (see Figure 3.1) and P is the powerflow density).

Table 3.1 Material constants for leaky SAW substrates [3.5]

Air/Solid LSAW			Liquid/Solid LSAW					
Material	Electrical Boundary	Phase velocity (ms^{-1})	Attenuation constant (dB/λ)	Phase velocity (ms^{-1})	Attenuation constant (dB/λ)	$\frac{v_1}{\sqrt{P}}$	$\frac{v_2}{\sqrt{P}}$	$\frac{v_3}{\sqrt{P}}$
36 LiTaO_3	OPEN	4172	3.8×10^{-5}	4125	2.6×10^{-3}	0.08	1.92	0.14
	SHORT	4077	1.6×10^{-4}	4077	6.9×10^{-3}	0.13	2.29	0.24
41 LiNbO_3	OPEN	4772	1.7×10^{-4}	4587	5.8×10^{-2}	0.04	2.21	0.59
	SHORT	4403	1.7×10^{-2}	4401	1.6×10^{-1}	0.11	2.61	1.00
64 LiNbO_3	OPEN	4712	4.7×10^{-1}	4573	7.7×10^{-2}	0.42	2.22	0.66
	SHORT	4475	2.5×10^{-4}	4475	1.1×10^{-1}	0.31	2.38	0.86
						$\times \sqrt{\omega} \times 10^{-6} \left[\frac{\text{ms}^{-1}}{\sqrt{\text{watts}/\text{m}}} \right]$		

Figure 3.2 (a) overleaf shows the relationship of the LiTaO_3 rotation angle and the velocity of the SH-SAW on a free and metallised surface with water loading and the normalised particle displacements on free (b) and metallised (c) surfaces (u_1 and u_2 are

the in-plane components of displacement and u_3 is the surface-normal component of displacement.

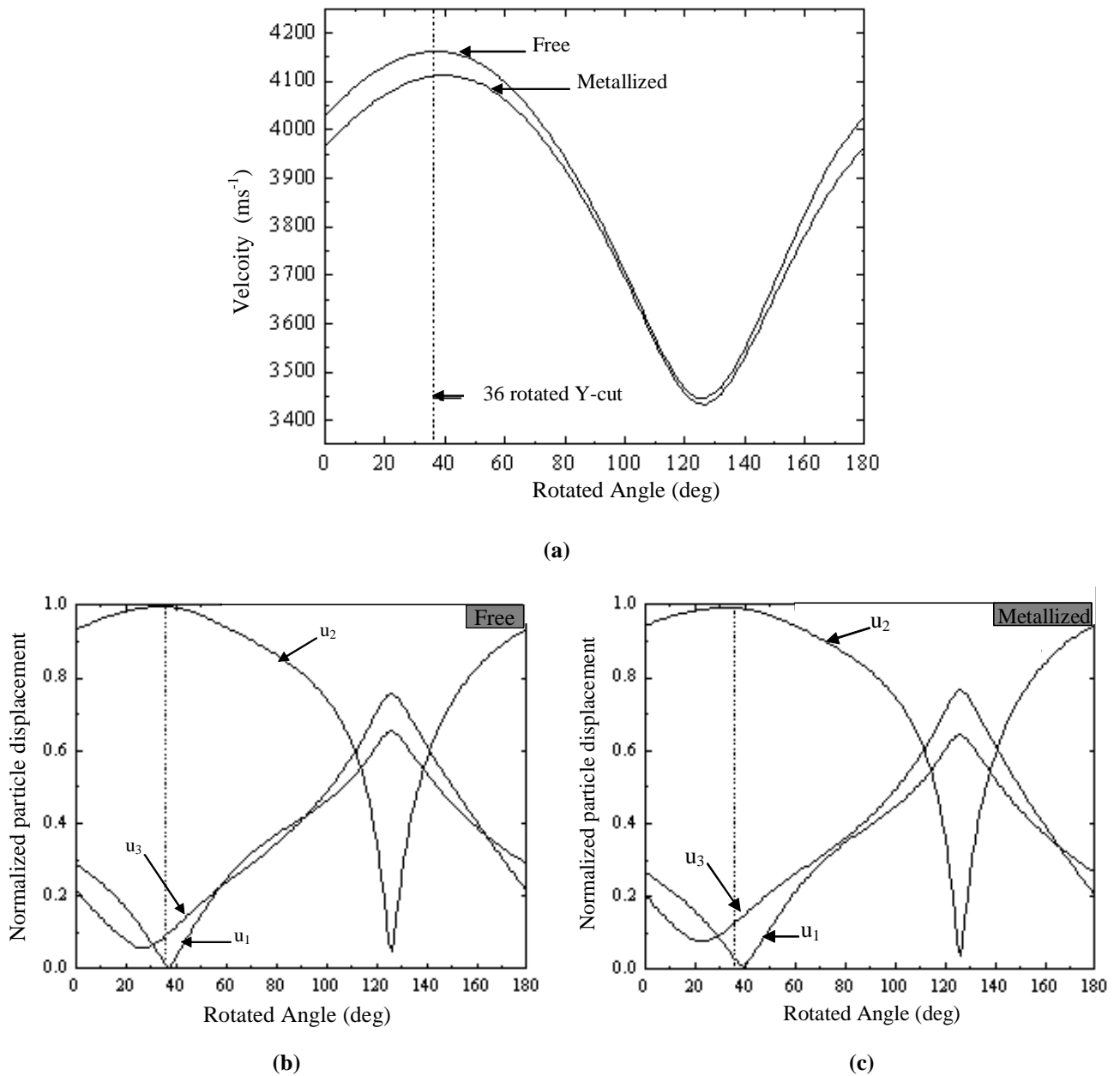


Figure 3.2 Graphical representation of acoustic wave velocity and particle displacement to rotation angle of LiTaO₃

From figures 3.2 it can be seen that 36 rotated Y-cut X-propagating LiTaO₃ has a large electromechanical coupling coefficient given by $K^2 = 2 \left(\frac{V_{free} - V_{met}}{V_{free}} \right)$ (even with water loading) and that the main particle displacement of it is u_2 . Table 3.2 overleaf gives the values for the velocity at the 36YX.LT/water interface.

Table 3.2 SAW at 36YX.LT/water interface

Surface	Velocity (m/s)	$u_1:u_2:u_3$
Free	4161.5	0.011:1:0.093
Metallised	4110.8	0.03:1:0.13

From the results it was concluded that the propagating wave on the 36YX.LT is a leaky type SH-SAW and it can be utilised for a liquid phase sensor. In the case of LiNbO₃ the propagation losses are much higher in liquids although it has a higher electromechanical coupling constant and at the same time also suffers from a very high temperature coefficient (≈ 80 ppm/°C) [3.7].

Based on the above analysis the decision was made that the liquid sensors for this project and application are going to be designed 36° rotated Y cut X propagating LiTaO₃ substrate. The next step was to decide on the type of SAW device for the sensor. After carefully considering the advantages and disadvantages of both the delay line and resonant device configurations (as summarised in Table 2.1) it was decided to opt for the simple delay line configuration.

In the following section the SH-SAW sensor design is discussed with the main component in the design being the IDT.

3.3 Design of SH-SAW delay line sensor

SAW delay lines are frequently used as piezoelectric elements in sensors. The basic arrangement as discussed in Chapter 2 consists of two bidirectional interdigitated transducers (IDTs), with the sensing region in between the IDTs. The ends of the piezoelectric substrate are usually covered with an acoustic absorber or cut at an angle to reduce SAW reflections. There is no specific design procedure for IDT microsensors based on SAW delay lines. Although substantial work has been done on delay line designs for filtering and signal-processing applications, the requirements are essentially different from those for commercial non-SAW oscillator-based sensors. The SAW device used as a microsensor should not only have the appropriate frequency-transfer characteristics, but its physical dimensions should also allow for miniaturisation and possible remote-sensing of a variety of physical and chemical media.

There are two main structures of the SAW delay line depending on whether its is used in an oscillator circuit or a vector voltmeter configuration. In the case when the phase or amplitude of the output is to be measured by means of a vector voltmeter, the

delay line must have a broader bandwidth. Conversely if it is to be used in an oscillator circuit, the bandwidth should be narrow enough to eliminate undesired modes. However in both cases, for correct sensor operation the delay line requires careful design [3.8].

3.3.1 Delay line transfer function

Basic principle of operation of the SH-SAW sensor in single free delay line configuration is shown in Figure 3.3. In this input and output IDTs are connected to the source and the load with admittances y_1 and y_2 , respectively. The first design principles and considerations are identical to those used for Rayleigh SAWs, i.e. design of the IDTs for the generation and detection of SH-SAWs uses the delay line configuration often employed for SAW filters [3.9].



Figure 3.3 Uniform interdigital transducer delay line arrangement

From Figure 3.3 the voltage transfer function of the delay line, u_2/V , can be determined and is given by

$$\frac{u_2}{V} = \frac{y_1 y_{12}}{y_{12}^2 - (y_1 + y_{11})(y_2 + y_{22})} \quad (3.1)$$

where y_1 and y_2 are the source and load admittances, y_{11} and y_{22} are the input admittances of the transmitter and receiver IDT, respectively, and y_{12} is the transfer admittance.

However usually the voltage ratio is measured hence

$$A_{12} = \frac{u_2}{u_2'} \quad (3.2)$$

where u_2' is the output voltage for the case when the source and load are directly connected. In this case we have

$$\frac{u_2'}{V} = \frac{y_1}{y_1 + y_2} \quad (3.3)$$

Then from equations (3.1) and (3.3) we obtain

$$A_{12} = \frac{(y_1 + y_2)y_{12}}{y_{12}^2 - (y_1 + y_{11})(y_2 + y_{22})} \quad (3.4)$$

Equation (3.4) can be expressed in the form

$$A_{12} = |A_{12}| \exp(j\phi) \quad (3.5)$$

where $|A_{12}|$ is the ratio of the amplitudes and ϕ is the phase angle. The insertion loss IL (in dB) and group time delay are defined as

$$IL = -20 \log |A_{12}| \quad (3.6)$$

$$\tau = -\frac{d\phi}{d\omega} \quad (3.7)$$

The variations of the group time delay are a measure of the non-linearity of the phase response ϕ .

The term y_{12}^2 in the denominator of Equation (3.4) represents what is known as a triple transient signal (TTS). The TTS is due to multiple SAW reflections between bidirectional input and output IDTs. This is associated with regenerative effects caused by current flow in the IDTs. Some of the SAW power received by the output IDT is reradiated into piezoelectric substrate. This portion from the output IDT that arrives back at the input can lead to further regeneration of a SAW wave. As a result, the main voltage signal induced in the output IDT is corrupted by additional voltages due to these multiple SAW reflections. The path differences between the main and the doubly reflected SAW signals result in amplitude and phase ripples across the SAW passband, at a ripple frequency $f_r = 1/2\tau_0$, where τ_0 is the time for the SAW propagation between the input and output IDT phase centres. This triple transient interference causes power-loss issues and can be addressed by the use of double electrode IDTs which are covered in chapter 7. The ratio of the TTS voltage to the main signal can be calculated from the expression [3.10].

$$A_{tt} = \frac{y_{12}^2}{(y_1 + y_{11})(y_2 + y_{22})} \quad (3.8)$$

from this the suppression S_{tt} (in dB) of the triple transient signal can be calculated as

$$A_{tt} = -20 \log |A_{tt}| \quad (3.9)$$

This suppression figure should be high enough to compensate for and eliminate distortions of the delay line transfer function. Next the admittances of the IDTs have to be calculated.

3.3.2 Calculation of the admittances

To work out the above responses (amplitude ratio, phase and triple transient) we need to know the individual admittances y_{11} , y_{22} , and y_{12} (y_1 and y_2 are know from the external measuring system). The possibility of admittance matrix calculation of a surface acoustic wave IDT based on the impulse response method was first demonstrated by Mitchell and Reilly [3.11]. However, their input admittance calculations were limited to the unapodised IDTs. To characterise an apodised IDT, its input admittance should be known. However, calculations of the admittance based on the equivalent circuit model are complicated and time consuming [3.12, 3.13]. Therefore, simpler and more efficient methods of calculation that have been reported were used [3.14, 3.15].

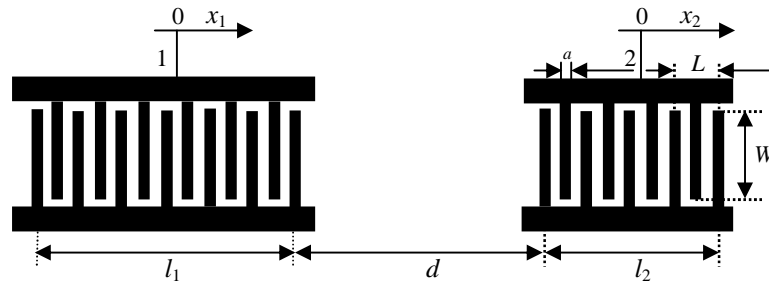


Figure 3.4 Schematic of a SAW delay line with ordinary IDTs

To derive an expression for the transfer admittance y_{12} it is assumed that the two different IDTs have the same aperture W (see Figure 3.4). Following the procedure by DeVries [3.10], the following expression for the transfer admittance y_{12} is obtained.

$$y_{12} = 2Y_0 A_1 A_2 \exp(-jk_f d) \quad (3.10)$$

where

$$A_1 = \left[\frac{Y_{12} Y_{13} - Y_{23} (Y_0 + Y_{11})}{(Y_0 + Y_{11})^2 - (Y_{12})^2} \right]_1 \quad (3.11)$$

$$A_2 = \left[\frac{Y_{12} Y_{13} - Y_{23} (Y_0 + Y_{11})}{(Y_0 + Y_{11})^2 - (Y_{12})^2} \right]_2 \quad (3.12)$$

Y_0 is an equivalent characteristic SAW admittance, A_1 and A_2 are the transfer admittance elements of IDT1 and IDT2, respectively, in which Y_{11}, Y_{12}, Y_{13} and Y_{23} are admittance matrix components of the IDTs, $k_f = \omega / v_f$, where v_f is the SAW velocity in the area between the IDTs, and d is the internal distance between the IDTs. The admittance matrix components can be determined by considering a SAW IDT as a 3-port system as shown in Figure 3.5. To derive the admittance matrix, it is assumed that there are no reflections and no propagation and ohmic losses, and that the SAW sources are located in the gaps between the IDT electrodes. Thus as in Figure 3.5 we have acoustic ports 1 and 2 of the IDT placed at the centres of the first ($x = -1/2$) and the last gap ($x = 1/2$), with the length of the IDT equal to l . If a voltage V_3 is applied to the electrical port 3, then, outside the IDT, the equivalent voltage V^- and V^+ of the SAW propagating in the negative and positive direction along the x -axis respectively, can be written as

$$V^- = \sum_{n=1}^N v_n \exp[jk(x - x_n)] \quad \text{for } x \leq -1/2 \quad (3.13)$$

and

$$V^+ = \sum_{n=1}^N v_n \exp[-jk(x - x_n)] \quad \text{for } x \geq 1/2 \quad (3.14)$$

where N is the number of gaps, $v_n = \pm \bar{v}_n$ and \bar{v}_n is the amplitude of the equivalent SAW voltage generated by the source in the n th gap, $k = 2\pi/\lambda$, λ being the SAW wavelength, and x_n is the n th gap centre position on the x -axis.

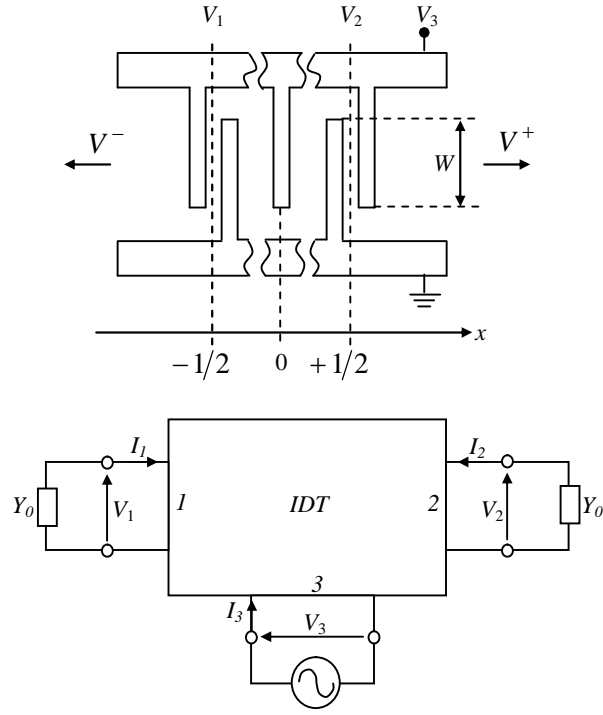


Figure 3.5 SAW IDT as a 3-port system

Expressions for the voltages V_1 and V_2 can be obtained from equations (3.13) and (3.14) respectively. As $V_1 = V^-$ for $x = -1/2$ and $V_2 = V^+$ for $x = 1/2$, then

$$V_1 = \sum_{n=4}^N v_n \exp(-jkx_n) \exp(-jkl/2) \quad (3.15)$$

$$V_2 = \sum_{n=1}^N v_n \exp(jkx_n) \exp(-jkl/2) \quad (3.16)$$

Normalising the voltages v_n to \bar{V}_0 (the amplitude of voltage V_0 generated by the full aperture gap W), transforms the above expressions to

$$V_1 = \bar{V}_0 H \exp(-jkl/2) \quad (3.17)$$

$$V_2 = \bar{V}_0 H^* \exp(-jkl/2), \quad (3.18)$$

$$\text{where } H = \sum_{n=1}^N a_n \exp(-jkx_n) \quad (3.19)$$

$a_n = v_n / \bar{V}_0$ and H^* is the complex conjugate of H (the expression of H (equation (3.19)) is a well known formula for frequency response of transversal filters.

The equivalent SAW currents can be determined according to the following equations

$$I_1 = Y_{11}V_1 + Y_{12}V_2 + Y_{13}V_3 \quad (3.20)$$

$$I_2 = Y_{12}V_1 + Y_{11}V_2 + Y_{23}V_3 \quad (3.21)$$

$$I_3 = Y_{13}V_1 + Y_{23}V_2 + Y_{33}V_3 \quad (3.22)$$

where I_1 and I_2 are the equivalent SAW currents at the acoustic ports 1 and 2, respectively and the voltages V_1 and V_2 are given by equations (3.17) and (3.18). I_3 and V_3 are the current and voltage at the electrical port 3, and $Y_{11}, Y_{12}, Y_{13}, Y_{23}$ and Y_{33} are the admittance matrix components. Assuming that an ideal voltage is applied to electrical port 3 and that acoustical ports 1 and 2 are loaded by an equivalent characteristic admittance Y_0 it can be confirmed that current I_2 is flowing towards port 2.

When $V_3 = 0$, the electrical port 3 is short circuited (as in Figure 3.6) and the IDT is equivalent to a uniform lossless transmission line of length l . $V_2 = V_1 \exp(-jkl)$ and the SAW incident on port 1 is represented by a voltage source $2V_1$ with an internal impedance of $1/Y_0$. Voltages and currents at ports 1 and 2 will then satisfy the following conditions: $V_1 = I_1/Y_0$ and $V_2 = -I_2/Y_0$. Then from equations (3.20) and (3.21) the following expressions can be derived

$$Y_{11} = -jY_0 / \tan(kl) \quad (3.23)$$

$$Y_{12} = -jY_0 / \sin(kl) \quad (3.24)$$

If $V_3 \neq 0$, then $V_1 = -I_1/Y_0, V_2 = -I_2/Y_0$ and equations (3.20) and (3.21) give

$$Y_{13} = -\frac{V_1(Y_0 + Y_{11})}{V_3} - \frac{Y_{12}V_2}{V_3} \quad (3.25)$$

$$Y_{23} = -\frac{Y_{12}V_1}{V_3} - \frac{V_2(Y_0 + Y_{11})}{V_3} \quad (3.26)$$

Now referring back to Figure 3.4

$$y_{12} = G_0 H(\omega) \quad (3.27)$$

where G_0 is a conductance given by

$$G_0 = 2Y_0(\bar{V}_0 / \bar{V}_3)^2 \quad (3.28)$$

and

$$H(\omega) = H_1^*(\omega) H_2(\omega) \exp\{-j[k_t(l_1 + l_2)/2 + k_f d]\} \quad (3.29)$$

$$H_1^*(\omega) = \sum_{n=1}^{M_1} a_{1n} \exp(jk_t x_{1n}) \quad (3.30)$$

$$H_2(\omega) = \sum_{n=1}^{M_2} a_{2n} \exp(-jk_t x_{2n}) \quad (3.31)$$

Here M_1, M_2 are the number of gaps, a_{1n} and a_{2n} are the transversal filter coefficients, and x_{1n} and x_{2n} are the gap positions along the x_1 and x_2 axes of IDT1 and IDT2, respectively. $k_f = \omega/v_f$ and $k_t = \omega/v_t$, where v_f is the SAW velocity in the area between the IDTs, and v_t the velocity in the area of the IDTs.

3.3.3 Simplified expressions

For a complete description of the IDT, G_0, C_0, Y_0 , and \bar{V}_0/\bar{V}_3 also have to be known, where C_0 is the static capacitance of the IDT. Using Engan's [3.16] infinite array approximation, an expression for the unapodised IDT input conductance G_1 at resonance frequency and for the static capacitance C_0 can be derived. This expression for G_1 can be written as

$$G_1 = \omega_0 W (\varepsilon_0 + \varepsilon_p^T) F(s) K^2 N_s^2 \quad (3.32)$$

where

$$F(s) = \left[\frac{\sin \pi s}{P_{-s}(\cos \Delta)} \right]^2 R_s \quad (3.33)$$

here $s = 1/S_e$, where S_e is the number of electrodes per electrical period. $\Delta = \pi a/L$, where a is the width of the electrodes and L is the period. $P_{-s}(\cos \Delta)$ is the Legendre function of the first kind. K^2 is the electromechanical coupling coefficient for SAW, $\omega_0 = 2\pi f_0$, f_0 being the resonance frequency, W is the aperture length, ε_0 is the dielectric constant of vacuum, ε_p^T is the effective dielectric constant of the substrate, R_s is a constant coefficient which depends on s and N_s is the number of gaps for which $a_n \neq 0$. For the two most popular cases, single and double electrode IDTs, $s = 1/2$ and $s = 1/4$, respectively. For $s = 1/2$, $R_s = 1/2$ and $N_s = N$, while for $s = 1/4$, $R_s = 1/4$ and $N_s = N/2$.

At resonance, for the unapodised IDTs, G_1 is also given by

$$G_1 = G_0 N_s^2 \quad (3.34)$$

comparing equations (3.32) and (3.34) gives

$$G_0 = 2\pi f_0 W(\varepsilon_0 + \varepsilon_p^T) F(s) K^2 \quad (3.35)$$

Further more using equations (3.28) and (3.35) an expression for Y_0 and \bar{V}_0/\bar{V}_3 can be obtained. Since Y_0 is not dependent on K and s

$$Y_0 = \left[\omega_0 W(\varepsilon_0 + \varepsilon_p^T) \right] / 2 \quad (3.36)$$

and

$$(\bar{V}_0/\bar{V}_3)^2 = F(s) K^2 \quad (3.37)$$

The static capacitance C_0 as derived by Engan [3.16] for the unapodised IDTs can be approximately applied to the apodised transducers. For $s=1/2$ and $s=1/4$ it can be written as

$$C_0 = W(\varepsilon_0 + \varepsilon_p^T) \sin \pi s \frac{P_{-s}(\cos \Delta)}{P_{-s}(-\cos \Delta)} R_s \sum_{n=1}^N abs(a_n) \quad (3.38)$$

The Legendre function $P_{-s}(\pm \cos \Delta)$ can be calculated from the expansion [3.17]

$$P_{-s}(\pm \cos \Delta) = \sum_{m=0}^{\infty} p_m, \quad (3.39)$$

where $p_0 = 1$ and

$$p_m = \frac{(m-1+s)(m-s)(1 \pm \cos \Delta)}{2m^2} p_{m-1} \quad (3.40)$$

Therefore assuming the IDTs have a constant period L , and that the widths of gaps and of electrodes are equal to a ($a=L/4$) (see figure 3.4), the expression for the conductance G_0 can be written as

$$G_0 = 2.2549 f_0 W(\varepsilon_0 + \varepsilon_p^T) K^2 \quad (3.41)$$

the static capacitance C_0 of a single full-aperture overlap for a single electrode IDT ($s=1/2$) can be calculated from the expression

$$C_0 = W(\varepsilon_0 + \varepsilon_p^T) \quad (3.42)$$

The velocity v_t in the area of IDTs is given by [3.18]

$$v_t = \frac{v_f}{[1 + 0.85(v_f - v_m)/v_m]} \quad (3.43)$$

where v_f and v_m are the SAW velocities for the free and metallised surface, respectively.

In this expression the influence of the mass of the electrodes is not taken into account.

The resonance centre frequency can be written as

$$f_0 = v_t / (4a) \quad (3.44)$$

For simple IDTs the following expressions for admittances y_{11} , y_{22} and y_{12} can be obtained

$$y_{11} = G_1 + j(B_1 + \omega C_{01}) \quad (3.45)$$

with

$$G_1 = G_0 N_1^2 (\sin(X_1) / X_1)^2 \quad (3.46)$$

$$B_1 = G_0 N_1^2 [\sin(2X_1) - 2X_1] / (2X_1^2) \quad (3.47)$$

$$C_{01} = N_1 C_0 \quad (3.48)$$

$$y_{22} = G_2 + j(B_2 + \omega C_{02}) \quad (3.49)$$

with

$$G_2 = G_0 N_2^2 (\sin(X_2) / X_2)^2 \quad (3.50)$$

$$B_2 = G_0 N_2^2 [\sin(2X_2) - 2X_2] / (2X_2^2) \quad (3.51)$$

$$C_{02} = N_2 C_0 \quad (3.52)$$

$$y_{12} = G_0 N_1 N_2 \sin X_1 / X_1 \sin X_2 / X_2 \exp(-j\omega\tau_0) \quad (3.53)$$

where

$$X_1 = \pi N_1 (f - f_0) / 2f_0 \quad (3.54)$$

$$X_2 = \pi N_2 (f - f_0) / 2f_0 \quad (3.55)$$

$$\tau_0 = \frac{l_1 + l_2}{2v_t} + \frac{d}{v_f} \quad (3.56)$$

N_1 and N_2 are the number of gaps with non zero overlaps (gaps for which the nearest electrodes are connected to the opposite bus bars). For example in Figure 3.4, $N_1 = 12$ and $N_2 = 8$. τ_0 is the time delay between the centres of the IDTs.

For $f = f_0$, from equations (3.44)-(3.55) the following expressions can be obtained:

$$y_{11}(\omega_0) = G_0 N_1^2 + j\omega_0 C_{01} \quad (3.57)$$

$$y_{22}(\omega_0) = G_0 N_2^2 + j\omega_0 C_{02} \quad (3.58)$$

$$y_{12}(\omega_0) = G_0 N_1 N_2 \exp(-j\omega_0\tau_0) \quad (3.59)$$

3.3.4 Design procedure

To obtain amplitude and phase responses without the presence of unwanted ripples, the levels of spurious signals should be sufficiently low [3.10]. The main sources of these signals are acoustic reflections of the SAWs from the edges of the piezoelectric substrate, feedthrough and the triple transient signal (TTS). The acoustic reflections are minimised using angled edges of the piezoelectric substrate and by using acoustic absorbers. The feedthrough signals can be reduced by proper shielding and making the separation distance d (see Figure 3.4) large enough. In the case of the ordinary bi-directional IDTs, the TTS can be lowered by making the TTS suppression S_{tt} high enough. Since for high S_{tt} , the insertion loss IL is also high, it means that the input and output IDTs are strongly unmatched, hence the input admittances y_{11} and y_{22} can be omitted in preliminary calculation of A_{tt} from expression (3.8) giving

$$A_{tt} \approx y_{12}^2 / y_1 y_2 \quad (3.60)$$

At the centre frequency f_0 , equations (3.58) and (3.59) give,

$$G_0 N_1 N_2 = \sqrt{|A_{tt} y_1 y_2|} \quad (3.61)$$

now using equation (3.60) W , N_1 and N_2 can be estimated. G_0 can be expressed in the form

$$G_0 = G_p W / \lambda_t \quad (3.62)$$

$$\text{where } \lambda_t = 4a \quad (3.63)$$

is the wavelength in the area of the IDTs, and

$$G_p = 2.2549 v_t (\epsilon_0 + \epsilon_p^T) K^2 \quad (3.64)$$

therefore equation (3.60) becomes

$$G_p N_1 N_2 W / \lambda_t = \sqrt{|A_{tt} y_1 y_2|} \quad (3.65)$$

The minimum value of the acoustic aperture W is limited by the diffraction effects, therefore usually chosen as $W / \lambda_t \geq 20$. In the case of identical input and output IDTs

$N_1 = N_2 = N$, then

$$N^2 = \frac{\sqrt{|A_{tt} y_1 y_2|}}{G_p W / \lambda_t} \quad (3.66)$$

For the preliminary values of W and N the input admittances of the IDTs, and the accurate values of A_{12} and A_{tt} can be calculated from equations (3.4) and (3.8),

respectively. Using these various equations and specifications of the chosen piezoelectric substrate the delay line sensors were designed.

A delay line consisting of two identical IDTs, was designed on the 36° rotated X propagating Y cut Lithium Tantalate substrate for a centre frequency $f_0 = 61\text{MHz}$, for operation in a $50\ \Omega$ phase-measuring system. The amplitude and phase ripples were considered to lie under 1° , and since the output voltage of a delay line is the sum of the voltages of the main signal and the TTS, we can estimate $|A_{tt}|$ from the following expression

$$|A_{tt}| < \tan(\Delta\phi) \quad (3.67)$$

Thus having $\Delta\phi \leq 1^\circ$ we get $|A_{tt}| < 0.017$. During the design it was assumed that $|A_{tt}| = 0.015$ (which is equivalent to $S_{tt} = 40\ \text{dB}$), hence giving $\Delta\phi = 0.6^\circ$. For $36^\circ\text{YX LiTaO}_3$ $v_f = 4161\ \text{ms}^{-1}$, $v_m = 4110\ \text{ms}^{-1}$, and $K^2 = 0.027$, $\varepsilon_p^T = 51.7$. Using equation (3.42) $v_t = 4118\ \text{ms}^{-1}$, and from equation (3.63) $G_p = 0.12\ \mu\text{S}$. Since the period is given by $\lambda_t = v_t / f_0$, then we have $\lambda_t = 67.5\ \mu\text{m}$ and $a = 16.88\ \mu\text{m}$. The aperture W was chosen to be $2\ \text{mm}$ (greater than $20\lambda_t$). The external measuring system is $50\ \Omega$ hence giving $y_1 = y_2 = 0.02\ \text{S}$, then from equation (3.65) $N \approx 26$. After exact calculations, $N = 27$ was chosen (56 electrodes). For a given distance d we can calculate the time delay τ_0 from equation (3.55). The distance d was chosen as $5.6\ \text{mm}$ so as to have an overall standard die size of the delay line of $10\ \text{mm}$ in length. Using equations (3.4) and (3.6) the insertion losses $\text{IL}(f_0)$ was calculated to be approximately $15\ \text{dB}$. Figure 3.6 below shows the amplitude versus frequency response of the designed delay line.

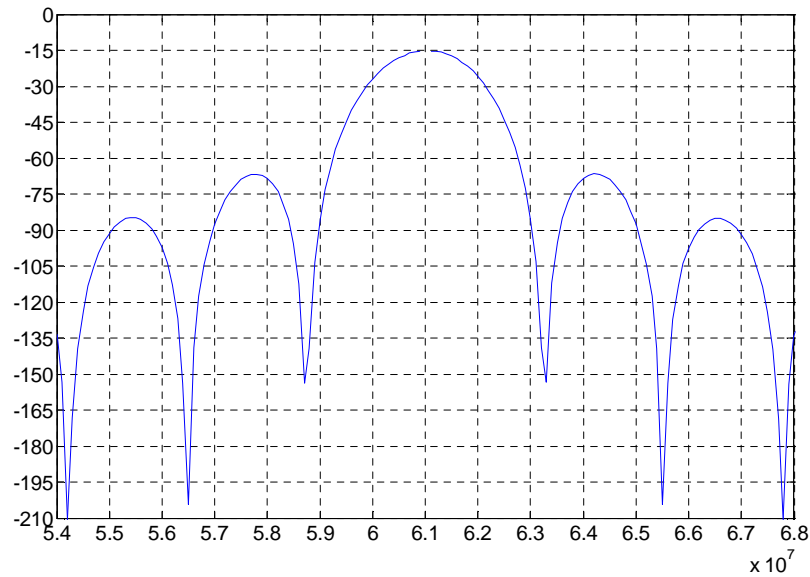


Figure 3.6 Typical amplitude response for a narrow frequency range

Having considered the IDT and delay line design the next step was to finalise the sensor design, in relation to its application. Having chosen the appropriate substrate for liquid sensing, effect from the surrounding environment is also needed to be considered and then design to minimise these effects. Another requirement was to design the liquid sensor so as to make simultaneous measurements of both the electrical (acousto-electric) and mechanical (acoustic) properties of the sample liquids under test. This is achieved through a dual delay line configuration, one shorted (metallised and electrically shielded) and the other left free (electrically active). This way, apart from mass loading and viscosity (shorted delay line), it is possible to monitor additionally the permittivity and conductivity (free delay line) of the liquid under test, parameters that can be related to taste properties, such as sweetness and saltiness. Furthermore, the approach adopted is based on a generic fingerprint correlated to key physical parameters and so does not employ a bio-chemical selective layer. This in turn increases the lifetime and durability of the resultant devices, albeit with a loss of specificity. The various design parameters are listed in Table 3.3 overleaf.

Table 3.3 Design parameters for SH-SAW sensor

Parameter	Value on LiTaO ₃
Free SAW velocity (v_f)	4161.5 ms ⁻¹
Metallised SAW velocity (v_m)	4110.8 ms ⁻¹
SAW velocity in IDT area (v_l)	4118.3 ms ⁻¹
Centre frequency (f_0)	61 MHz
Wavelength (λ_l)	67.5 μ m
Width of IDT fingers (a)	16.875 μ m
IDT length ($l_1 = l_2$)	1870 μ m
Distance between IDTs (d)	5626 μ m
Acoustic aperture (W)	2000 μ m
Number of gaps ($N_1 = N_2$)	27
Time delay τ_0 for distance d	$\approx 1.8 \mu$ s
Area of free surface ($l \times w$)	2 \times 1.5 mm ²
Overall size of device ($l \times w$)	10 \times 7.5mm ²

The drawing of the complete device, with the dual delay line and the various dimensions is shown in Figure 3.7 overleaf. It shows the metallised and electrically shorted delay line and the free delay line that has an opening in the metallization layer through to the piezoelectric substrate. The material chosen for the metallisation is gold. Gold was chosen in preference to aluminium as it is more chemically inert does not oxidise and has higher conductivity. More details about the fabrication and processing of these devices is discussed in Chapter 4 along with the packaging, realisation and test procedure of the devices.

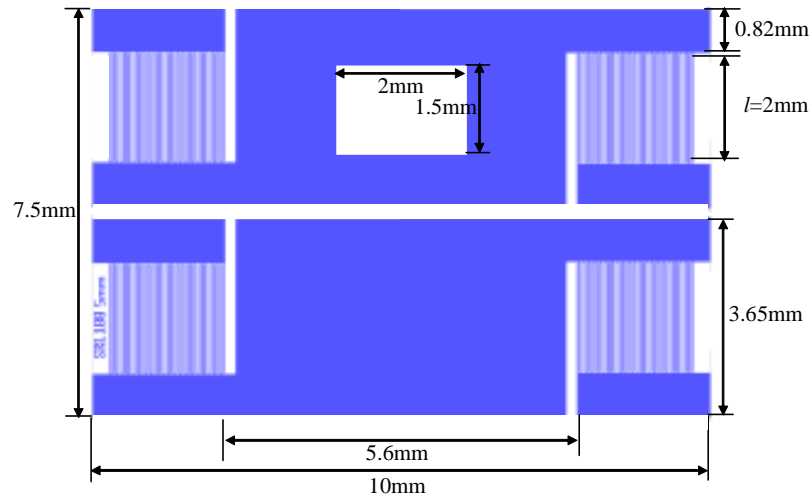


Figure 3.7 Design of SH-SAW dual delay line sensor

3.4 Operational principle and sensor model

The basic principle of operation of the liquid SH-SAW sensor in single free delay line configuration is shown in Figure 3.7. It is basically the same setup as shown earlier in Figure 3.3 only that here we have the sample liquid under test in the sensing area. In this input and output IDTs are connected as before to the source and the load with admittances y_1 and y_2 , respectively.

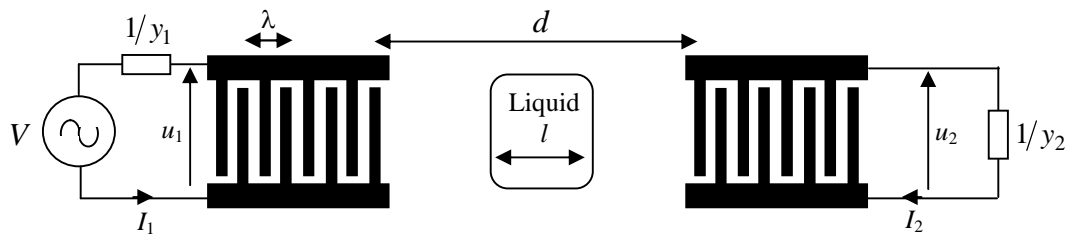


Figure 3.8 Uniform interdigital transducer delay line arrangement

The sensors consists of two adjacent delay lines, with a thin layer of metal between the two IDTs on one delay line, representing an electrical short and the other delay line with a free non metallised surface area as shown in Figure 3.9 overleaf.

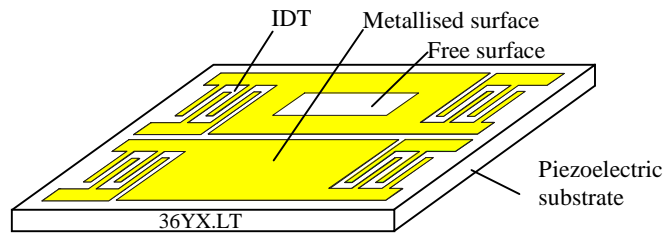


Figure 3.9 Schematic drawing of a dual-delay line SH-SAW microsensor

The basic operating principle utilised in the liquid sensing devices is that perturbations that affect SH-SAW propagation on a metallised and electrically shorted surface are associated with the mechanical properties of the adjacent liquid, while SH-SAW propagating on a free surface are associated with both the mechanical and electrical properties of the adjacent liquid [3.19]. The common environmental interactions are elicited from both delay lines and can be removed by comparison between the two signals. The design is made considering analysis and prediction of the sensor response, which requires for the sensor effect to be accounted for in the device response. The sensor effect can be incorporated into the device unperturbed transfer function, to allow for the variations of delay time (related to phase shift) and attenuation [3.20].

Applying a voltage V across the two bus bars of the transmitter IDT, which are connected to identical finger pairs, results in a current I_1 entering the electrodes. The current is determined by the static capacitance C_0 of the electrodes and the input admittance $G(\omega) + jB(\omega)$ (where G and B are the real and imaginary parts). The input conductance $G(\omega)$ and acoustic susceptance $B(\omega)$ can be approximated using equations (3.32) and (3.47).

Then as in equation (3.45) the input admittance of the transmitter IDT (IDT1) can be rewritten in terms of frequency as below

$$y_{11}(\omega) = G_1(\omega) + jB_1(\omega) + j\omega C_{01} \quad (3.68)$$

As mentioned before and according to the design we have reciprocity, hence the input admittance of the receiver IDT, $y_{22}(\omega)$ is equal to that of the transmitter IDT $y_{11}(\omega)$. Therefore the complex unperturbed admittance transfer function for transmitter to receiver can be approximated as [3.17]

$$y_{12}(\omega) \approx G(\omega)\alpha \exp(-j\omega\tau_0) \quad (3.69)$$

where τ_0 is the delay time of the acoustic wave between the two transducers which can be determined using equation (3.56), α an attenuation coefficient which from comparing equations (3.59) and (3.69) at the centre frequency can be determined as $\alpha = N_1 N_2$ (N_1 and N_2 being the number of non-zero overlaps i.e. gaps for which the nearest electrodes are connected to the opposite bus bars) for the acoustic waves.

The sensor effect, due to the presence of a liquid which causes a variation of the delay time and the attenuation of the SH wave, has to be included in this admittance transfer function as an additional phase shift and attenuation. Therefore the perturbed admittance transfer function for the liquid sensor can be written as

$$y_{12}(\omega) \approx G(\omega)\alpha \exp(-j\omega\tau_0) \exp(j2\pi\delta l/\lambda) \exp(-al) \quad (3.70)$$

where $\delta = \Delta v/v$ the fractional velocity change of the SH-SAW due to the sensing effect, l the length of the liquid contact area and a the attenuation of the SH-SAW due to the sensor effect along the region of liquid contact l . Thus for the dual delay line configuration the admittance transfer functions can be presented as:

$$y_{m12}(\omega) \approx G_m(\omega)\alpha_m \exp(-j\omega\tau_0) \exp(j2\pi\delta_m l/\lambda) \exp(-a_m l) \quad (3.71)$$

$$y_{f12}(\omega) \approx G_f(\omega)\alpha_f \exp(-j\omega\tau_0) \exp(j2\pi\delta_f l/\lambda) \exp(-a_f l) \quad (3.72)$$

where the subscripts s and f represent the shorted delay line and free delay line, respectively. In the case of the conductance $G_m(\omega)$ and $G_f(\omega)$, due to identical delay lines all the parameters affecting their values are the same hence they would be equal. In terms of the voltage the transfer function can be represented as in equations (3.1-3.7), and from these equations the expressions for the measurement of attenuation and phase shift can be written as

$$\text{Attenuation } A \text{ [dB]} = -20 \log(|A_{12}|)$$

$$\text{Phase } \Delta\phi \text{ [deg]} = \arg(|A_{12}|)$$

where A_{12} is given by equation (3.4).

3.4.1 Effects of external environment

Acoustic-wave devices are sensitive to a large number of different physical parameters. These include temperature, pressure, acceleration, stress, and the adjacent medium's density, viscoelastic properties, electrical permittivity and electrical conductivity. Indeed, it is this range of measurand sensitivities that make acoustic wave devices attractive for a wide range of different sensing applications [3.21]. However since the

usual interested is in exploiting only one of these sensitivities for a particular application, all other responses become undesirable interferences. Thus, it is essential that the sensor environment be carefully controlled to eliminate the effects of sensor cross-sensitivities [3.21], and a difference and ratiometric principle adopted to remove common mode effects. The following section discusses one of the most common interference; the effect of temperature.

3.4.1.1 Temperature effects

Temperature has a direct effect on the operation of all acoustic-wave devices. A change in temperature produces a change in the density of the substrate (a direct effect of change in the length of the substrate), which in turn causes a change in velocity of the SH-SAW. For simplicity reasons, let us ignore the temperature dependence of the Young's modulus. Since the change in wave velocity, along with the attenuation, is parameter most commonly used in SAW sensors applications, there will be a temperature-dependent component associated with the sensor output signal. While efforts to identify substrates that have low temperature coefficient have produced a significant reduction of temperature sensitivities, no substrate with negligible temperature coefficients that support SH-SAW are available in practice. Furthermore physical properties of coating materials are often temperature dependent. Also, the liquid under test and the packaging material of the SAW sensor generally have different expansion coefficients than the device, which compounds the problem.

Assuming a linear thermal expansion in the substrate then the acoustic path length d and the sensing length in liquid l will vary according to the linear relationship

$$d = d_0(1 + \kappa\Delta T) \quad (3.73)$$

where, d_0 is the length at a reference temperature T_0 , ΔT is the change in temperature given by $(T - T_0)$, κ the expansion coefficient and d the length at actual temperature T .

A positive change in length Δd will cause an increase in the delay time by $\Delta\tau_0$. Thus, the total delay time becomes $\tau_0 + \Delta\tau_0$. Similarly the sensing length l will also change due to the change in temperature to $l + \Delta l$.

Substituting these changes in the expressions for the delay line admittances, equations (3.71) and (3.72) we get

$$A_{m12}(\omega) = G_m(\omega)\alpha_m \exp(-j\omega(\tau_0 + \Delta\tau_0)) \exp(j2\pi\delta_m(l + \Delta l)/\lambda) \exp(-a_m(l + \Delta l)) \quad (3.74)$$

$$A_{f12}(\omega) = G_f(\omega)\alpha_f \exp(-j\omega(\tau_0 + \Delta\tau_0)) \exp(j2\pi\delta_f(l + \Delta l)/\lambda) \exp(-a_f(l + \Delta l)) \quad (3.75)$$

From the above equations it can be seen that both delay lines are affected by the changes in the temperature. The actual sensing effect or perturbation due to the liquid contact could be determined by taking the ratio of the sensing line (i.e. shorted delay line) to that of the reference (i.e. free delay line), eliminating the effect of temperature and other common external effects.

$$\frac{A_{m12}}{A_{f12}} = \frac{\alpha_m}{\alpha_f} \exp\left(2\pi j(\delta_m - \delta_f)\left(\frac{l}{\lambda} + \frac{\Delta l}{\lambda}\right)\right) \exp(-(a_m - a_f)(l + \Delta l)) \quad (3.76)$$

Furthermore, by subtraction of the signals between the free and shorted lines, the signal that corresponds to the electrical properties can be determined from the free line which senses both the electrical and mechanical properties.

3.5 Liquid perturbations

When the crystal surface is metallised and electrically shorted, the potential becomes zero at the surface. In such case, the particle displacement, u_2 (See figure 3.2), interacts with the liquid. Conversely, when the surface is opened (free), both u_2 and the potential φ , interact with the liquid. The interaction between u_2 and the liquid is called a mechanical interaction/perturbation and that between φ and the liquid is called an acoustoelectric interaction/perturbation. Figure 3.10 overleaf shows the normalised particle displacement and potential at the 36YX.LT and water interface. The subscripts m and f represent a metallised and free surface. [3.22, 3.23]

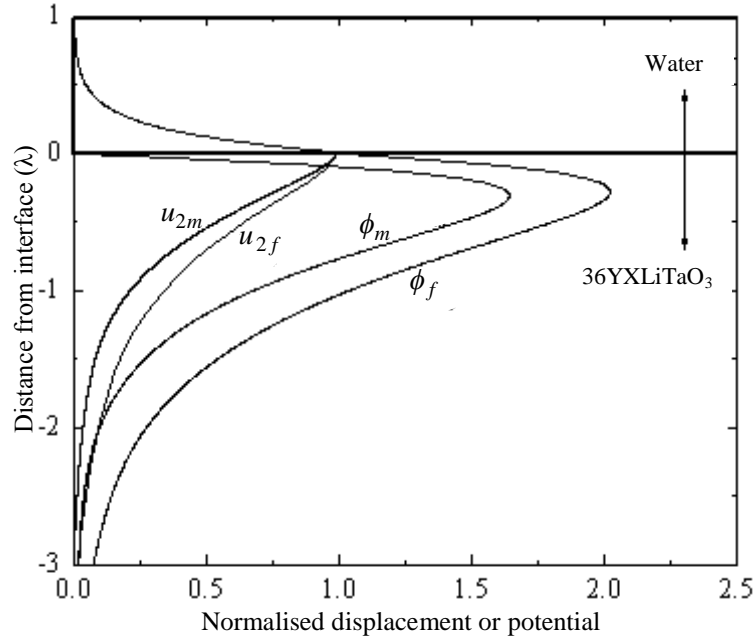


Figure 3.10 Normalized particle displacement u_2 and potential ϕ at the 36YX.LT/water interface

SH-SAWs propagating on a metal are perturbed by the mechanical properties of the adjacent liquid [3.23]. The changes in the SH-SAWs can be derived from Auld's [3.24] perturbation theory for gases, which can be extended to the liquid phase. The perturbation formula for a liquid sensor is given by

$$\frac{\Delta\beta}{k} = -\frac{j\nu}{4\omega P} (v_p^* \cdot Z' \cdot v_p + v_p \cdot Z^* \cdot v_p^*) \quad (3.77)$$

Where, k is the wave number, ν the phase velocity, ω the angular frequency, P the flow per unit width, v_p the particle velocity vector, and Z the acoustic metal surface impedance. Also, $'$ indicates a perturbed quantity $*$ indicates a complex conjugate.

$\Delta\beta$ is the perturbation of the complex propagation constant β . β is defined in terms of k and the attenuation α as

$$\beta = k - j\alpha \quad (3.78)$$

From equation (3.78), $\Delta\beta$ is given by

$$\frac{\Delta\beta}{k} = -\frac{\Delta\nu}{\nu} - j\frac{\Delta\alpha}{k} \quad (3.79)$$

From equations (3.77) and (3.79), the change in the complex propagation constant can be decomposed into the changes of the velocity and the attenuation as

$$\frac{\Delta\nu}{\nu} = -\frac{\nu}{4\omega P} (v_p^* \cdot Z_i' \cdot v_p - v_p \cdot Z_i \cdot v_p^*), \quad (3.80)$$

$$\frac{\Delta\alpha}{k} = -\frac{v}{4\omega P} (v_p^* \cdot Z_r' \cdot v_p + v_p \cdot Z_r \cdot v_p^*). \quad (3.81)$$

Where, the subscripts r and i represent the real and imaginary parts of Z .

3.5.1 Mechanical perturbations

3.5.1.1 Viscous coupling

Assuming that a Newtonian fluid with a viscosity of η and density ρ_l is loaded on the metallised surface, substitution of the surface acoustic impedance Z into equations (3.80) and (3.81) gives,

$$\frac{\Delta v}{v} = -\frac{v v_{pc}^2}{4\omega P} \left(\sqrt{\frac{\omega \eta' \rho_l'}{2}} - \sqrt{\frac{\omega \eta \rho_l}{2}} \right) \quad (3.82)$$

$$\frac{\Delta\alpha}{k} = \frac{v v_{pc}^2}{4\omega P} \left(\sqrt{\frac{\omega \eta' \rho_l'}{2}} + \sqrt{\frac{\omega \eta \rho_l}{2}} \right) \quad (3.83)$$

Where, v_{pc} is the particle velocity component of the shear horizontal mode, η and ρ_l are the viscosity and density of the reference liquid (distilled water with $\eta = 0.001 \text{ kgm}^{-1}\text{s}^{-1}$ and $\rho_l = 1000 \text{ kgm}^{-3}$), η' and ρ' are the viscosity and density of the sample liquid.

Rearranging equations (3.82) and (3.83) gives

$$\frac{\Delta v}{v} = -C \left(\sqrt{\eta' \rho_l'} - \sqrt{\eta \rho_l} \right) \quad (3.84)$$

$$\frac{\Delta\alpha}{k} = C \left(\sqrt{\eta' \rho_l'} + \sqrt{\eta \rho_l} \right) \quad (3.85)$$

$$\text{where } C = \frac{v v_{pc}^2}{4\omega P} \cdot \frac{\sqrt{\omega}}{\sqrt{2}} \quad (3.86)$$

in which $\frac{v_{pc}}{\sqrt{P}} = \sqrt{\omega} (2.26 \times 10^{-6})$, $v = 4110.8 \text{ ms}^{-1}$ and $\omega = 2\pi f$. Substituting the values into equation (4.8) gives $C = 9.3 \times 10^{-9} \sqrt{f}$. The velocity shift as a function of the viscosity density product can now be plotted.

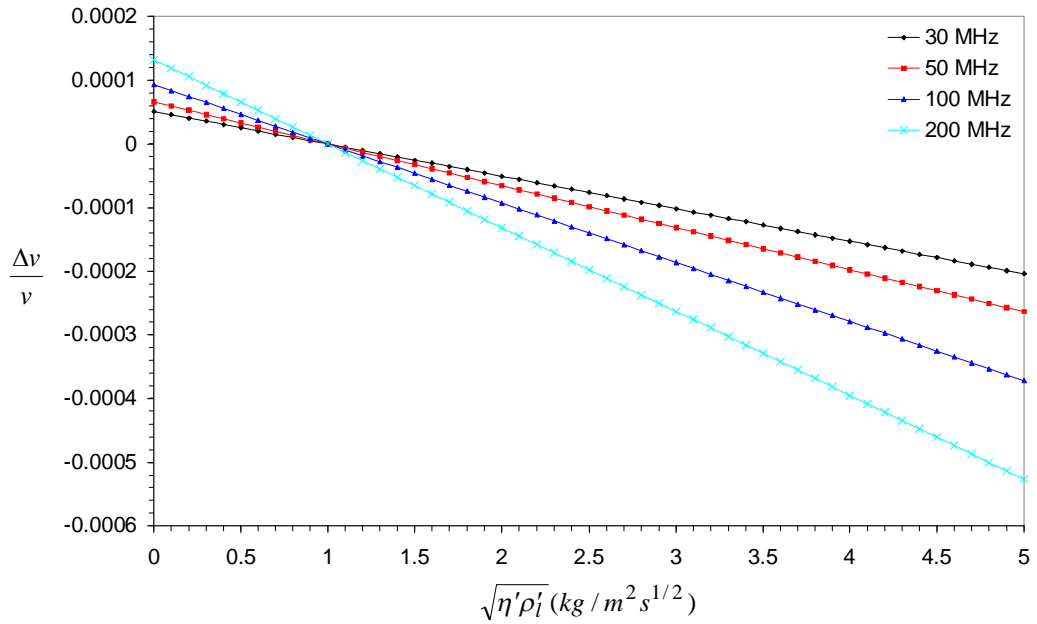


Figure 3.11 Velocity shift as a function of the viscosity density product

3.5.1.2 Mass loading in liquid

Considering an isotropic thin film of thickness h and density ρ , uniformly loading the metallised surface in a liquid and that the liquid properties do not change before and after perturbation, the velocity shift and attenuation change can be obtained as,

$$\frac{\Delta v}{v} = -\frac{vhv_{pc}^2}{4P} \left(\rho' - \frac{\mu'}{v^2} \right), \quad (3.87)$$

$$\frac{\Delta \alpha}{k} = 0. \quad (3.88)$$

where μ' is the Lamè constant of the film. Equations (3.87) and (3.88) correspond to the Auld's equations for the gas phase [3.24].

3.5.2 Electric perturbations

3.5.2.1 Acoustoelectric interaction

The SH-SAW wave that propagates on the surface of LiTaO₃/LiNbO₃ substrates has an associated electric field that propagates several micrometers into a liquid. This electrical interaction (also known as the acousto-electric interaction) with the liquid affects the velocity and/or attenuation of SH-SAW propagation and it is utilised in sensing the dielectric properties of the liquids [3.24]. It has also been claimed that the high electromechanical coupling coefficients (~5 %) of LiTaO₃/LiNbO₃ materials is a

characteristic which enables SH-SAW sensors fabricated on these substrates to exhibit some specificity in detecting the electrical properties of an adjacent liquid [3.23].

When the surface is electrically shorted, the piezoelectric potential becomes zero and thus only horizontally polarised shear displacement waves interact with the fluid. In this case, mechanical properties including the viscosity and density will be detected. On the other hand, the piezoelectric potential at the free surface extends to the liquid and subsequently measures additionally the complex dielectric properties, such as relative permittivity and conductivity [3.25]. If the conductivity of an unperturbed (or reference) liquid is equal to zero, its electrical properties are given by

$$\varepsilon_l = \varepsilon_r \varepsilon_0 \quad (3.89)$$

Here, ε_l and ε_0 are the permittivity of the unperturbed liquid and that of the free space, and ε_r is the relative permittivity of the unperturbed liquid. After perturbation, ε_l changes to the complex permittivity ε_l' expressed by

$$\varepsilon_l' = \varepsilon_r' \varepsilon_0 - j \frac{\sigma'}{\omega} \quad (3.90)$$

Here, σ is the conductivity. By employing the perturbation theory proposed by Auld [3.25], the following acousto-electric interaction (electrical) relationships for changes in velocity and attenuation of the SH-wave in the presence of a liquid are achieved:

$$\frac{\Delta v}{v} = -\frac{K_s^2}{2} \frac{(\sigma'/\omega)^2 + \varepsilon_0(\varepsilon_r' - \varepsilon_r)(\varepsilon_r' \varepsilon_0 + \varepsilon_p^T)}{(\sigma'/\omega)^2 + (\varepsilon_r' \varepsilon_0 + \varepsilon_p^T)^2} \quad (3.91)$$

$$\frac{\Delta \alpha}{k} = \frac{K_s^2}{2} \frac{(\sigma'/\omega)(\varepsilon_r \varepsilon_0 + \varepsilon_p^T)}{(\sigma'/\omega)^2 + (\varepsilon_r' \varepsilon_0 + \varepsilon_p^T)^2} \quad (3.92)$$

Here, K_s^2 is the electromechanical coupling coefficient when the unperturbed liquid is loaded in the free surface, k is the wave number, ε_p^T is the effective permittivity of the SAW crystal, ε_r is the permittivity of the reference liquid (distilled water), ε_r' and σ' are the permittivity and conductivity (related to loss) of the measurand. If the conductivity of the reference liquid is not zero ($\varepsilon_l = \varepsilon_r \varepsilon_0 - j(\sigma/\omega)$), equations (3.91) and (3.92) are equivalent to a parallel shift of the origin. Using equations (3.91) and (3.92) the velocity shift and attenuation can be plotted as a function of relative permittivity and conductivity.

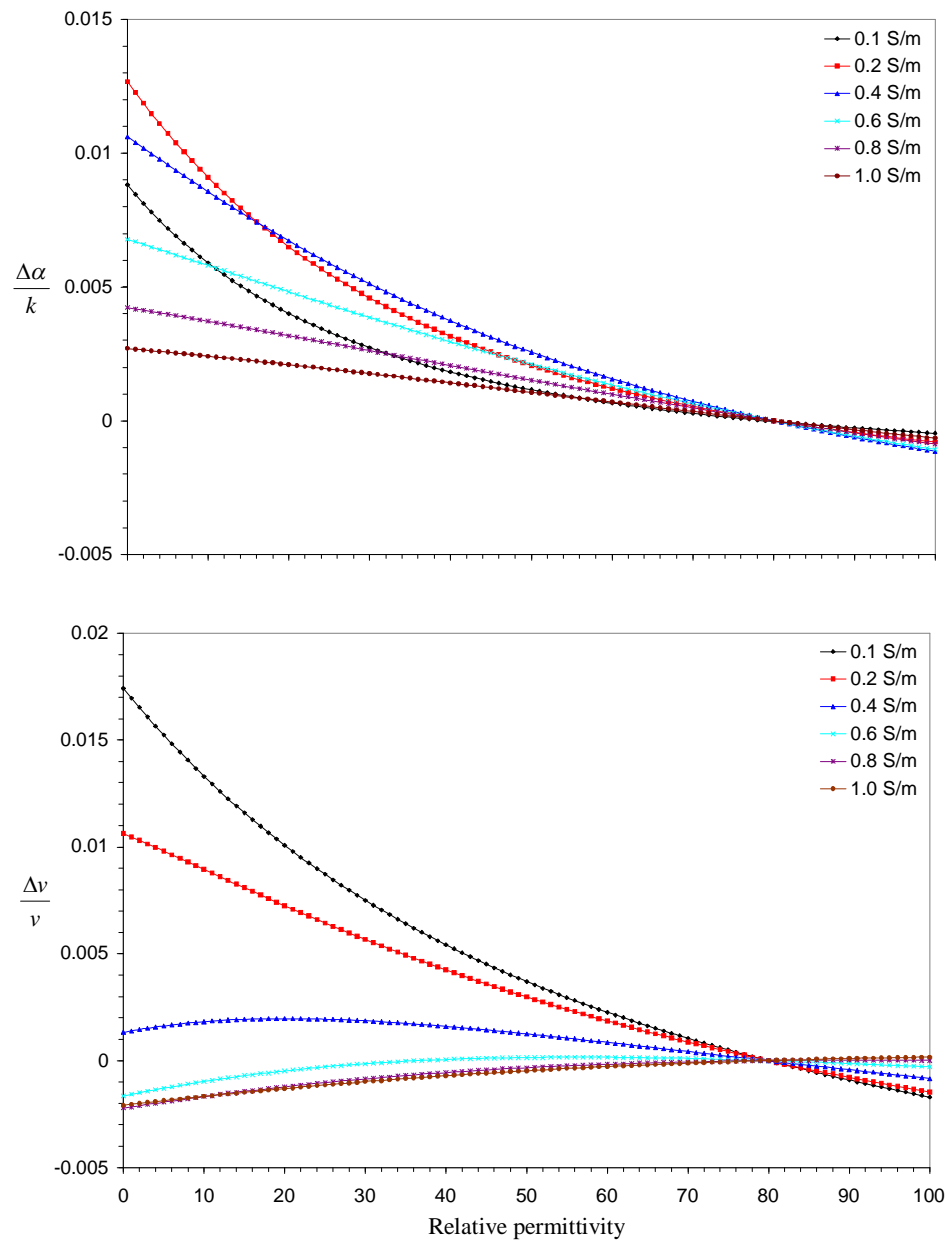


Figure 3.12 Attenuation change and velocity change as a function of relative permittivity (61 MHz)

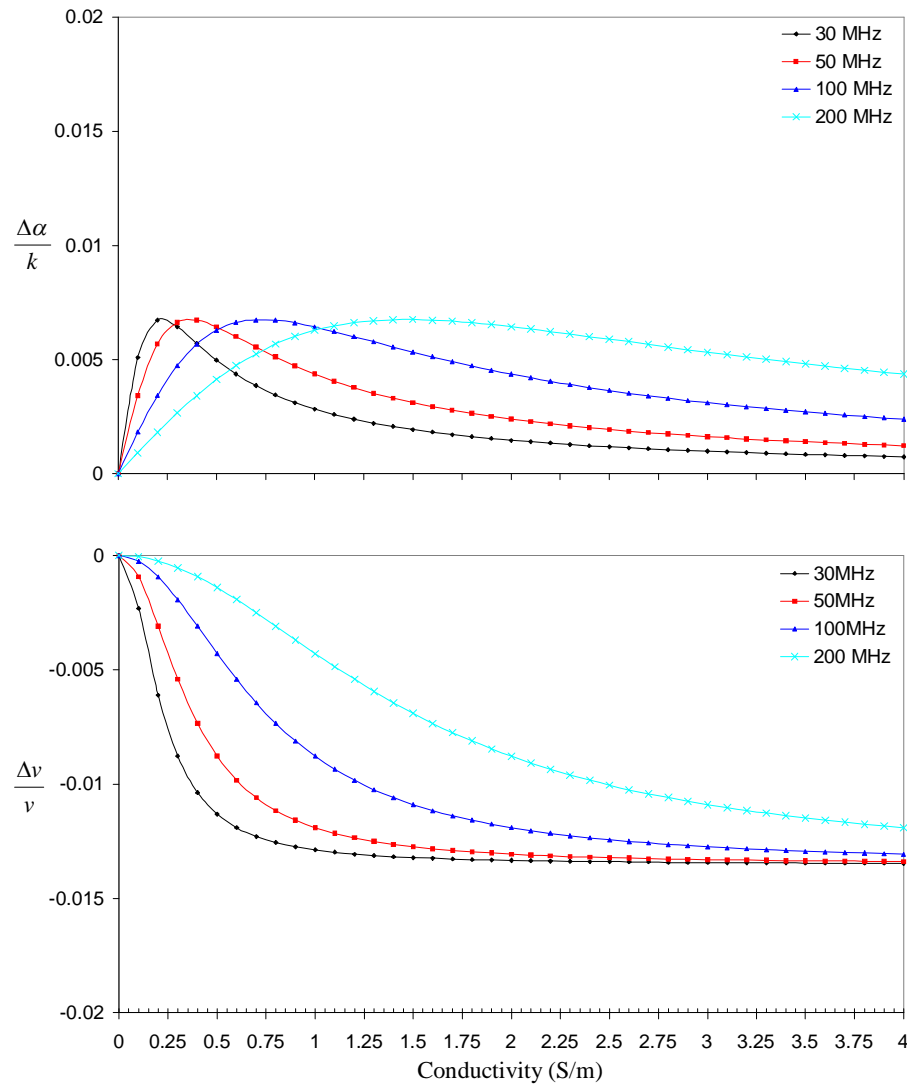


Figure 3.13 Attenuation change and velocity shift as a function of relative conductivity

From equations (4.13) and (4.14) circle formulae can be determined and by eliminating the conductivity and permittivity of the measurand from these formulae we can draw a permittivity-conductivity chart [3.25].

$$\left[\frac{\Delta v}{v} + \frac{K_s^2}{4} \frac{\varepsilon_0(2\varepsilon_r' - \varepsilon_r) + \varepsilon_P^T}{\varepsilon_r'\varepsilon_0 + \varepsilon_P^T} \right]^2 + \left[\frac{\Delta\alpha}{k} \right]^2 = \left[\frac{K_s^2}{4} \frac{\varepsilon_r\varepsilon_0 + \varepsilon_P^T}{\varepsilon_r'\varepsilon_0 + \varepsilon_P^T} \right]^2 \quad (3.93)$$

$$\left[\frac{\Delta v}{v} + \frac{K_s^2}{2} \right]^2 + \left[\frac{\Delta\alpha}{k} - \frac{K_s^2}{4} \frac{\varepsilon_r\varepsilon_0 + \varepsilon_P^T}{\sigma'/\omega} \right]^2 = \left[\frac{K_s^2}{4} \frac{\varepsilon_r\varepsilon_0 + \varepsilon_P^T}{\sigma'/\omega} \right]^2 \quad (3.94)$$

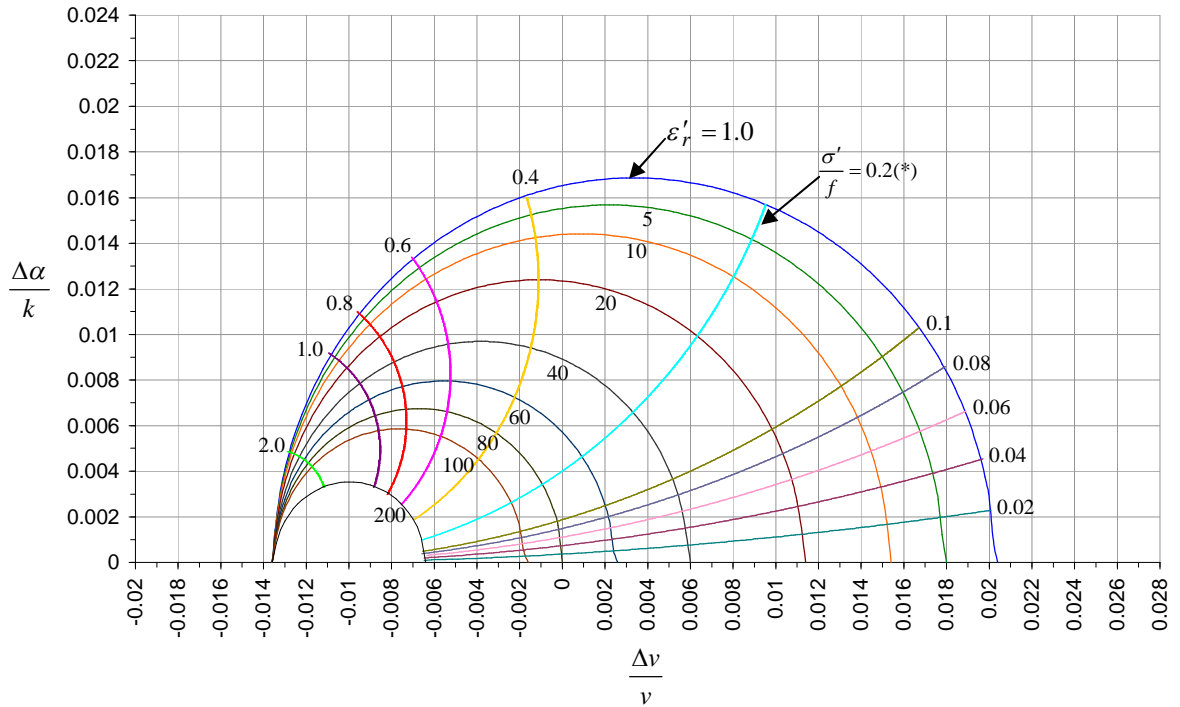


Figure 3.14 Permittivity-conductivity chart used to determine the permittivity and conductivity of a sample liquid from the SH-SAW sensor responses. (*: 1×10^{-8} (S/m)/Hz)

Thus the changes in the velocity of SH-SAW on the two delay lines can be concluded to be functions of several parameters, some of them being common for both lines:

$$\left(\frac{\Delta v}{v}\right)_{free} = f(\varepsilon, \sigma, \eta, \rho, T) \quad (3.95)$$

$$\left(\frac{\Delta v}{v}\right)_{shorted} = f(\eta, \rho, T) \quad (3.96)$$

where, ε , σ , η , ρ are the permittivity, conductivity, viscosity and density of the liquid under test and T the temperature common to both delay lines. It is these physical parameters that are being used to measure indirectly “taste” in the so-called electronic tongue.

3.6 Conclusions

This chapter covered the design of the IDT delay line sensors having discussed the requirements and choice of the substrate based on the sensing application. A detailed theoretical design of the sensor transducers is presented with the both theoretical and practical frequency responses. The various design details of the sensor along with the dimensions have been presented. The basic operational principle and sensor effect for

the dual delay line sensors has been discussed and the perturbation theory covered to relate the sensor outputs to the mechanical and acousto-electric properties of the sample under test. The next chapter details the fabrication the sensors followed by the realisation and characterisation of the sensors.

3.7 References

- [3.1] J. Campbell and W. Jones, Propagation of Surface Waves at the Boundary between a Piezoelectric crystal and a fluid medium, *IEEE Transactions on Sonics and Ultrasonics*, Vol. SU-17, No.2 (1970), pp. 71-76.
- [3.2] H. Wohltjen, *Transducers, Technical Digest* (1987), p. 471.
- [3.3] K. Nakamura, M. Kazumi, H. Shimizu, *IEEE Ultrasonic Symposium Proceedings* (1977), p. 819.
- [3.4] S. Shiokawa and T. Moriizumi, Design of SAW sensor in Liquid, *Japanese Journal of Applied Physics*, Vol. 27, Supplement 27-1 (1988), pp. 142-144.
- [3.5] M. Nakagawa, K. Yamanouchi, K. Shibayama, *Japanese Journal Applied Physics*, Vol. 44 (1973), p. 3969.
- [3.6] R. T. Smith and F. S. Welsh, *Japanese Journal Applied Physics*, Vol. 42 (1971), p. 2219.
- [3.7] D.S. Ballantine, R.M. White, S.J. Martin, A.J. Ricco, E.T. Zellers, G.C. Frye, H. Wohltjen, *Acoustic Wave Sensors Theory, Design, and Physico-chemical Applications*, Academic Press (1997), pp. 238-239.
- [3.8] Waldemar Soluch, Design of SAW delay lines for sensors, *Sensors and Actuators A* 67 (1998), pp. 60-64.
- [3.9] G. L. Matthaei, D. Y. Wong, B. P O'Shaughnessy, Simplification for the analysis of interdigital surface-wave devices, *IEEE Transactions on Sonics and Ultrasonics*, SU-22 (1975), p. 105.
- [3.10] A. J. DeVries, Surface wave bandpass filters, in: H. Mathews (Ed.), *Surface Wave Filters*, John Wiley, New York (1977), p. 263.
- [3.11] R. F. Mitchell and N. H. C. Reilly, Equivalence of δ -function and equivalent-circuit models for interdigital acoustic-surface wave transducers, *Electron Lett.*, Vol. 8 (1972), pp. 329-331.
- [3.12] R. H. Tancrell and M. G. Holland, Acoustic surface wave filters, *Proceedings of IEEE*, Vol. 59 (1971), pp. 393-409.
- [3.13] A. J. Vigil, B. P. Abbot, and D. C. Malocha, A study of the effects of apodized structure geometries on SAW filter parameters, *Proceedings of IEEE Ultrasonics Symposium* (1987), pp. 139-144.

- [3.14] W. R. Mader and H.R. Stocker, Extended impulse model for the design of precise SAW filters on quartz, *Proceedings of the IEEE Ultrasonics symposium* (1982), pp. 29-34.
- [3.15] P. J. Naglowski, Fast computation of finger-length-weighted SAW transducer dynamic admittance, *Electron letters*, Vol. 24 (1988), pp. 1494-1496.
- [3.16] H. Engan, Surface acoustic wave multielectrode transducers, *IEEE Transactions on Sonics and Ultrasonics*, Vol. SU-22 (1975), pp. 395-401.
- [3.17] D. P. Morgan, *Surface wave devices for signal processing*, Elsevier, Amsterdam Netherlands (1985), p. 335.
- [3.18] K. Blotekjer, K. A. Ingebrigsten, H. Skeie, Acoustic surface waves in piezoelectric materials with periodic metal strips on the surface, *IEEE Transactions on Electron Devices*, ED-20 (1973), p. 1139.
- [3.19] J. Kondoh, K. Saito, S. Shiokawa and H. Suzuki, Simultaneous Measurements of Liquid Properties Using Shear Horizontal Surface Acoustic Wave Sensors, *Jpn. J. Appl. Phys.* Vol. 35, Part 1, No. 5B (1996), pp. 3093-309.
- [3.20] M. Cole, G. Sehra, J.W. Gardner, and V.K. Varadan, Development of smart tongue devices for measurement of liquid properties, *IEEE Sensors Journal*, Vol. 4, No. 5 (Oct 2004), pp. 543-550.
- [3.21] D.S. Ballantine, R.M. White, S.J. Martin, A.J. Ricco, E.T. Zellers, G.C. Frye, H. Wohltjen, *Acoustic Wave Sensors Theory, Design, and Physico-chemical Applications*, Academic Press (1997), p. 375.
- [3.22] J. Kondoh and S. Shiokawa, New Application of Shear Horizontal Surface Acoustic Wave Sensors to Identifying Fruit Juices, *Jpn. J. Appl. Phys.* Vol. 33, Part 1, No. 5B (1994), pp. 3095-3099.
- [3.23] J. Kondoh, K. Saito, S. Shiokawa and H. Suzuki, Simultaneous measurements of liquid properties using multichannel shear horizontal surface acoustic wave microsensor," *Jpn. J. Appl. Phys.* Vol. 35, Part 1, No. 5B (1996), pp. 3093-3096.
- [3.24] B.A. Auld, *Acoustic Fields and Waves in Solids*, Volume II, John Wiley and Sons, Inc (1973), pp. 271-332.
- [3.25] Vijay K. Varadan and Julian W. Gardner, "Smart Tongue and Nose," Part of the *SPIE Conference on Smart Electronics and MEMS Newport Beach*, California, SPIE Vol. 3673 (1999), pp. 67-75.

CHAPTER 4

Device fabrication and characterisation

4.1 Introduction

In this chapter the details of the various fabrication techniques are presented. The steps required to fabricate the interdigital transducer (IDT) and the two processes that are commonly used to define the IDTs and their relative merits and choice are covered. Post processing to realise the devices, such as dicing of the wafer up to mounting the individual devices in packages are also addressed here. Finally the various measurement setups that could be used are discussed along with performance issues.

4.2 SH-SAW IDT delay line microsensor fabrication

4.2.1 Photolithography techniques

The two commonly used photolithography techniques used to define the patterns for the IDT structures are an *etch process* and a *lift-off process* [4.1]. Both these methods are suitable for the fabrication of SH-SAW IDT delay line sensors, but the ultimate choice of either the etching or the lift-off process mainly depends on the minimum feature size (resolution and accuracy) of the patterned structure required. Although the etching process is relatively easy to realise and acceptable resolution is achievable, it is more susceptible to electrical shorts between features than that of the lift-off process. This can be a major problem, especially for minimum feature sizes approaching 1–2 μm , where the influence of contaminants becomes more significant [4.2]. However, for

larger minimum feature sizes, of $5\mu\text{m}$ or greater, it is recognised that the etching process is acceptable and comparable in terms of device fabrication yield and quality to that of the lift-off process. Nevertheless, it is dependant on the fabrication process and the lift-off techniques has the potential problem of leaving “wings”. Both processes are explained in more detail in the following sections.

4.2.1.1 Basic etching process

Aqueous chemical etching has been used for decades to define metal electrode patterns on substrates surfaces, and is still a widely used technique. The standard wet etch process begins with the metallisation of the clean wafers, followed by cleaning of the metallised wafer and deposition of a positive/negative photoresist (depending on the polarity of the mask). The wafers are given a solvent clean (commonly acetone and isopropanol) to remove any possible loose surface contaminants that could have appeared during storage since the initial wafer-cleaning procedure. The wafer is then thoroughly rinsed in deionised water followed by a bake in the oven to remove moisture. Following this the clean metallised wafers are coated with a positive/negative photoresist and the wafer baked to remove any excess solvents from the photoresist. After cooling to room temperature the photoresist is exposed to UV light through a mask with appropriate polarity. A mask aligner is used to align the mask plate to the photoresist coated wafer. (Details of mask polarity and appropriate photoresist are given in the next section).

This is followed by the development of the photoresist, which is very critical as over or under development, results in degradation of the fabricated features. After development, a ‘soft’ post bake of the photoresist is performed; at this stage the pattern should be successfully transferred to the wafer. The chemical wet-etching of the unwanted metal is then performed with etchant solution that must be chosen appropriately such that it attacks the metal but not the substrate or the photoresist. Some surface wave substrates are chemically reactive and impose limitations on the chemical etchants that can be used. The etching time (rate of etching) is extremely critical because undercutting of the structure walls can occur if prolonged times are employed. The temperature, concentration, and agitation of the etchant solutions and the thickness of the metal layers are important factors that have a significant influence

on the etching times. The main advantages and disadvantages of chemical etching are summarised in Table 4.1.

Table 4.1 Chemical etching of metal electrode patterns [4.3]

Advantages
1. Simplicity and low cost
2. Compatible with mass production
3. Metal deposition methods can be used which produce highly adherent films (e.g. sputtering)
Disadvantages
1. Difficult to optimise process parameters when a small number of substrates are to be processed
2. Chemical etchants must be compatible with substrates
3. Post-baking can produce dimensional changes
4. Loss of resolution due to ragged edges, lateral etching, and a tendency to undercut
5. Low yield for line widths under $5\mu\text{m}$ (shorts being a dominant fault at these line widths) and for repetitive type patterns, however depends on laboratory and expertise

4.2.1.2 Lift-off process

As with the etching process, the lift-off process begins with the initial cleaning of the wafer which is followed by the deposition of photoresist (positive/negative). The cleaning process is similar to that used for the etching process. After the photoresist coated wafers have been baked and cooled they are ready to be exposed using the mask aligner. To improve lift-off capability, the wafer is normally immersed in chlorobenzene at room temperature for a period that depends on the intensity of the UV exposure lamp.

Chlorobenzene modifies the surface of the photoresist by developing a characteristic 'lip' in the developed pattern, which ensures that the material (metal) deposited on the substrate, arrives at near normal incidence. This creates a discontinuity at the edges of the patterned photoresist when a metal is evaporated on the surface of the wafer; thus, unwanted metal is subsequently removed more easily. If any continuity between the material (metal) deposited occurs the lift-off will not take place, or relatively violent techniques such as ultrasonic agitation have to be used. The wafer is then baked to remove any excess solvents and allowed to cool before being developed with care to prevent under or overdeveloping.

After inspecting the transfer of the pattern on the photoresist – edges of the patterned photoresist should be well defined and sharp to facilitate the lift-off process, the wafer is metallised using a metal evaporation or sputtering technique. After the metallisation the unwanted metal is removed by removing the photoresist by immersing the wafers in an acetone bath at room temperature. Table 4.2 summarises the advantages and disadvantages of the lift-off technique. The two photolithography techniques are summarised in Figure 4.1.

Table 4.2 Lift-off process [4.3]

Advantages

-
1. High resolution and precise dimensional control (~ 10 to 100 nm)*
 2. Compatible with chemically reactive substrates, and substrates with rough surfaces
 3. Compatible with any deposited metals or combination of metals, and with non-metals
 4. Electrical shorts improbable
 5. Excellent repeatability and photolithography processing independent of resolution
-

Disadvantages

-
1. Extra care required to achieve vertical sidewalls in photoresist
 2. Substrate cannot be heated during deposition
 3. Deposition material must arrive at normal incidence to the substrate
 4. Substrates must be extremely clean to ensure good film adhesion
-

*For the high resolution features typically 1 μm and less a direct write to the photoresist using an E-beam writer has to be performed rather than contact lithography using a photomask

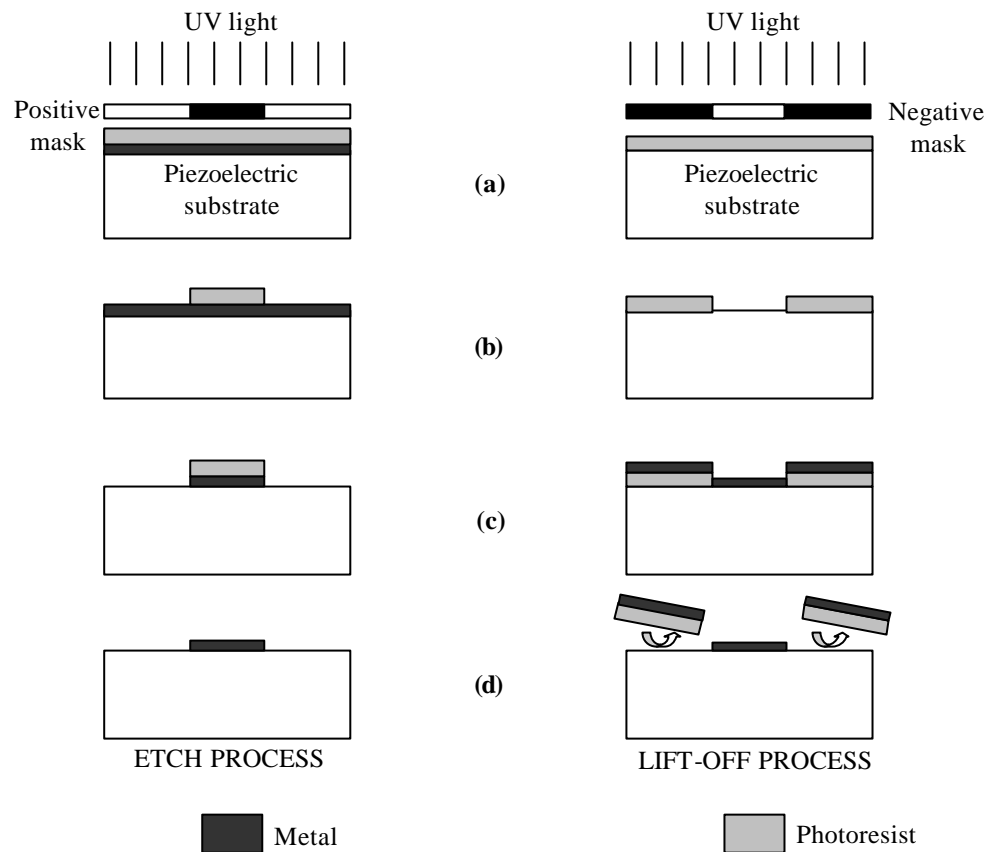


Figure 4.1 Basic steps involved in the two lithography processes: etching (left) and lift-off (right) [4.4]

As mentioned earlier in this section, the choice of either a lift-off or etch process mainly depends on the minimum feature size required. As the minimum feature size in the first design is $17\ \mu\text{m}$ which is greater than the minimum acceptable size in the etch process (of about $5\ \mu\text{m}$) and due to this simplicity the wet etch process was chosen over the lift-off. Furthermore chemical etching is preferred for the fabrication of simple metal pattern (as is the case here) on relatively inert substrates, such as LiTaO_3 and LiNbO_3 . A detailed description of the fabrication process used for the SH-SAW sensors is given in the following sections from the mask generation to having a patterned wafer ready to be diced.

4.2.2 Mask design and generation

Having the exact dimensions of the devices from calculations in Chapter 3, the SH-SAW sensors were designed using a computer-aided design (CAD) system. The layout was prepared at a wafer level using L-Edit layout software (Tanner Tools Inc.) and the

electronic design files exported into a standard GDS II format that offers compatibility with an electron-beam (E-beam) writer. The E-beam writer is used for the process of E-beam lithography that writes the layout generated using L-Edit, onto a square, low-expansion glass plate. 3" LiTaO₃ wafers were used hence a 4" glass mask plate was required.

The mask plate was manufactured according to the specifications, by Compugraphics International Ltd. A positive field, 4" square mask plate (1.5 mm thick) on white crown flint glass (soda Lime) with a coating of anti-reflective chrome was manufactured. The minimum feature size was determined by the IDT design (17 μm) and hence a 1 μm resolution for the mask was sufficient. The writing chrome side was specified to be down. The master mask was made to these specifications and used for the photolithography details of which are covered in the following sections. Figures 4.2 (a) and (b) show the final design from the L-Edit program and the actual manufactured mask plate, respectively.

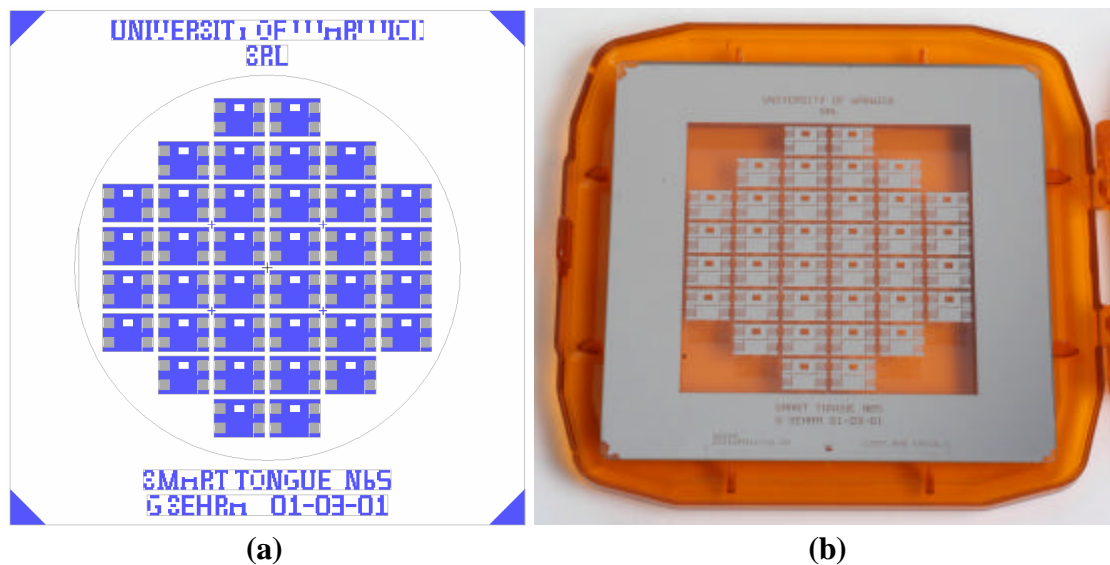


Figure 4.2 (a) Final design of mask plate in L-Edit (b) Photograph of manufactured positive field mask plate

4.2.3 Wafer preparation

As described in the previous chapter the wafers chosen for the sensors are 36° rotated Y-cut X-propagating lithium tantalate (36XYLT). Effective cleaning of these wafers was an essential requirement in order to obtain good adhesion and a uniform coating of the metallic film used to make the IDTs. All the cleaning processes were performed in a

fume cupboard (in a clean room) to allow the safe and fast removal of any possible harmful fumes produced during the cleaning process as suggested by Campbell [4.5].

The wafers were initially cleaned of any surface contaminants, such as dust, grease, or any other soluble organic particles, by immersion in trichloroethylene at 60°C for 10 minutes, followed by an acetone bath at 60°C for 10 minutes. The wafers were then rinsed with methanol and finally with deionised water. A slow evaporation of the solvents was allowed in a fume cupboard rather than drying using filtered nitrogen to minimise further surface contaminants. More cleaning was then undertaken to remove more stubborn contaminants. The wafers were then immersed in a mixture of three parts of deionised water (3H₂O), one part ammonium hydroxide (NH₄OH) and one part of 30% unstabilised hydrogen peroxide (H₂O₂) at 75°C for 10 minutes. This mixture was handled with care as it harmful, and the hydrogen peroxide was added last to minimise reaction side effects. After this the wafers were thoroughly rinsed in deionised water and dried using compressed filtered (0.2 µm filtration) nitrogen.

4.2.4 Metal selection and deposition

Next step involves the deposition of a metal layer from which the IDT structures are to be formed. Before the deposition the choice of metal to be deposited had to be made. The two ‘metallisations’ commonly used to fabricate transducers for SAW devices are gold-on-chromium and aluminium. Both these metallisations have advantages and disadvantages and a trade off has to be made. Gold is normally chosen for chemical detection applications because of its inertness and resistance to corrosion. However, the inertness of Au is at the expense of it not adhering to the piezoelectric wafers, and therefore requiring a seeding layer normally that of chromium. The electropositive nature of Cr allows it to form strong bonds with the oxide surfaces, while alloying between the Cr and Au chemically binds the two metal layers tightly together. However care must be taken not to expose the freshly deposited Cr layer to oxygen (air) before the Au is deposited, as chromium oxide layer will form instantaneously, preventing adhesion of the Au to the Cr. Furthermore, at elevated temperatures ($\geq 300^{\circ}\text{C}$), Cr and Au interdiffuse causing the conductivity of the Au layer to decrease significantly, eventually, rendering the metallisation too resistive for use. This problem can partially be circumvented by substituting titanium or tantalum for Cr as the adhesion layer, although Ti is more difficult to deposit.

Aluminium has the advantage that it adheres well to commonly used piezoelectric substrates, easy to deposit, is only 17% less conductive, less expensive, and is far less dense than gold. The lower density is significant because reflections of the acoustic waves from the gold IDT fingers in delay-line devices can cause appreciable pass band ripples in the IDT frequency response. However, the main disadvantage of using Al is that it oxidises relatively easily (surface oxide) which can be a major problem for liquid/chemical sensing applications. This problem is sometimes addressed, particularly for (non-sensor) commercial applications of SAW devices, by passivating the Al with a relatively impermeable layer of a material such as SiO_2 , Si_3N_4 or AlN .

The choice of metallisation was made based on the application of the sensor, because of oxidation issues, Au/Cr was chosen over Al. The deposition of the metals can be accomplished in one of several ways. The simplest is by thermal evaporation in a high-vacuum system (base pressure $<1 \times 10^{-6}$ Torr). Au and Al are held in a tungsten basket or filament and when heated they melt and evaporate. Cr sublimates from the solid when heated. Ti and Ta cannot be deposited thermally, that is why they are not normally used to replace Cr, and usually used in conjunction with platinum layers.

Electron-beam-induced evaporation, in which a stream of electrons is emitted from a hot filament and accelerated into the target metal to be deposited, is another means to deposit Al, Au, Cr, Ti and most other metals, again in a high-vacuum system. However the added complexity of the e-beam systems makes them considerably more expensive than comparable thermal deposition apparatus.

Another method of deposition (almost all metals), and a large number of metal oxides and other dielectrics as well, is sputtering. An inert-gas (often Ar) plasma is formed in contact with a target of the material to be deposited; excitation is provided by a DC or RF electric field. Magnetron sputtering utilises a strong magnetic field to limit the trajectories of the electrons associated with the plasma, preventing electron bombardment of the sample being coated; the magnetron also lowers the impedance of the sputtering structure. Energetic species in the plasma knock atoms loose from the target material; the dislodged atoms become part of the plasma and deposit onto nearby surfaces. Because of the high gas pressure (a significant fraction of 1 Torr), sputtering typically results in conformal coverage (over/around steps, edges, etc.), in contrast to the other two evaporation techniques which result in line-of-sight coverage.

LiTaO₃ exhibits a pyroelectric effect and so sparking can occur on the two faces of the wafer when exposed to a large temperature gradient. Hence to minimise this effect a conformal coating of Cr/Au was employed. This was done using a commercial CVC 601 dc sputtering system the clean LiTaO₃ wafers were deposited with 20 nm of Cr followed by 120 nm of Au on both sides of the wafer. The complete metallisation (short circuiting) of the wafer provides a path for even spread of the charge and prevents sparking from point to point, due to the pyroelectric effect. The thickness uniformity of the metal layers across the profile of the wafer is very important to ensure consistent behaviour from device to device.

4.2.5 Photolithography

Having decided on the photolithography technique to be used in section 4.2.1 (etch process chosen) the appropriate photoresist was selected to match the mask polarity. Since the mask manufactured was of positive (clear) field a positive photoresist that becomes more soluble when exposed to light, had to be chosen. The positive (clear) field mask which is opaque at the regions where metal is to be retained was used with Hoechst AZ5214E (28% PGMEA) positive photoresist. The wafers are first immersed in an acetone bath at 60°C for 10 minutes and then rinsed in isopropanol to remove any possible loose surface contaminants that could have appeared during storage since the initial wafer-cleaning procedure. Next the wafers are thoroughly rinsed in a deionised water bath for 5 minutes, followed by an oven bake at 75°C for 10 minutes to remove any moisture from the surface of the wafer. The clean metallised wafer is then coated with the photoresist using a Headway Research Inc.® spinner at 4500 rpm for 45-60 seconds, producing a thin film ($\approx 1.2\mu\text{m}$) over one side of the wafer. The wafer was then ‘soft’ baked in an oven at 90°C for 5 minutes (gradually ramping up the temperature to 90°C to avoid any sudden thermal shock).

Following the soft bake and cooling the wafers were exposed to ultraviolet (UV) light via the photo-mask using a double mask aligner (Karl Suss MA-6 system). The wafers were exposed for 1.5 seconds defining the geometry of the device structures on the wafers. The photoresist was then chemically developed by immersing the wafer in a developer (1:4 mixture of AZ-400K[®] and DI water) for 45 seconds, so that the regions exposed to light were removed leaving exposed areas of metal. During this process great care was taken to ensure no under or overdeveloping and an immersion

style was adapted, where the wafer was slowly agitated during the developing process at 10 second intervals, followed by a deionised water rinse and a close inspection under the microscope. Following the development a post bake was performed at 90°C for 30 minutes, which assists in hardening and formation of sharp features of the photoresist.

The wafer was then allowed to cool to room temperature for approximately 15 minutes and the device pattern successfully transferred onto the wafer. The chemical wet-etch of the Au and Cr was then performed using standard commercial ISO gold and chromium etchants at room temperature for approximately 45 seconds. The etching time is extremely critical because undercutting of the structure walls can occur as a result of prolonged etching. Therefore the etching as with the developing of the photoresist was performed at 10 second intervals, followed by a deionised water rinse and close inspection under the microscope.

Having successfully transferred the device patterns onto the metallised wafer through the etching process the wafer was ready to be diced. Figure 4.3 shows the fabrication steps.

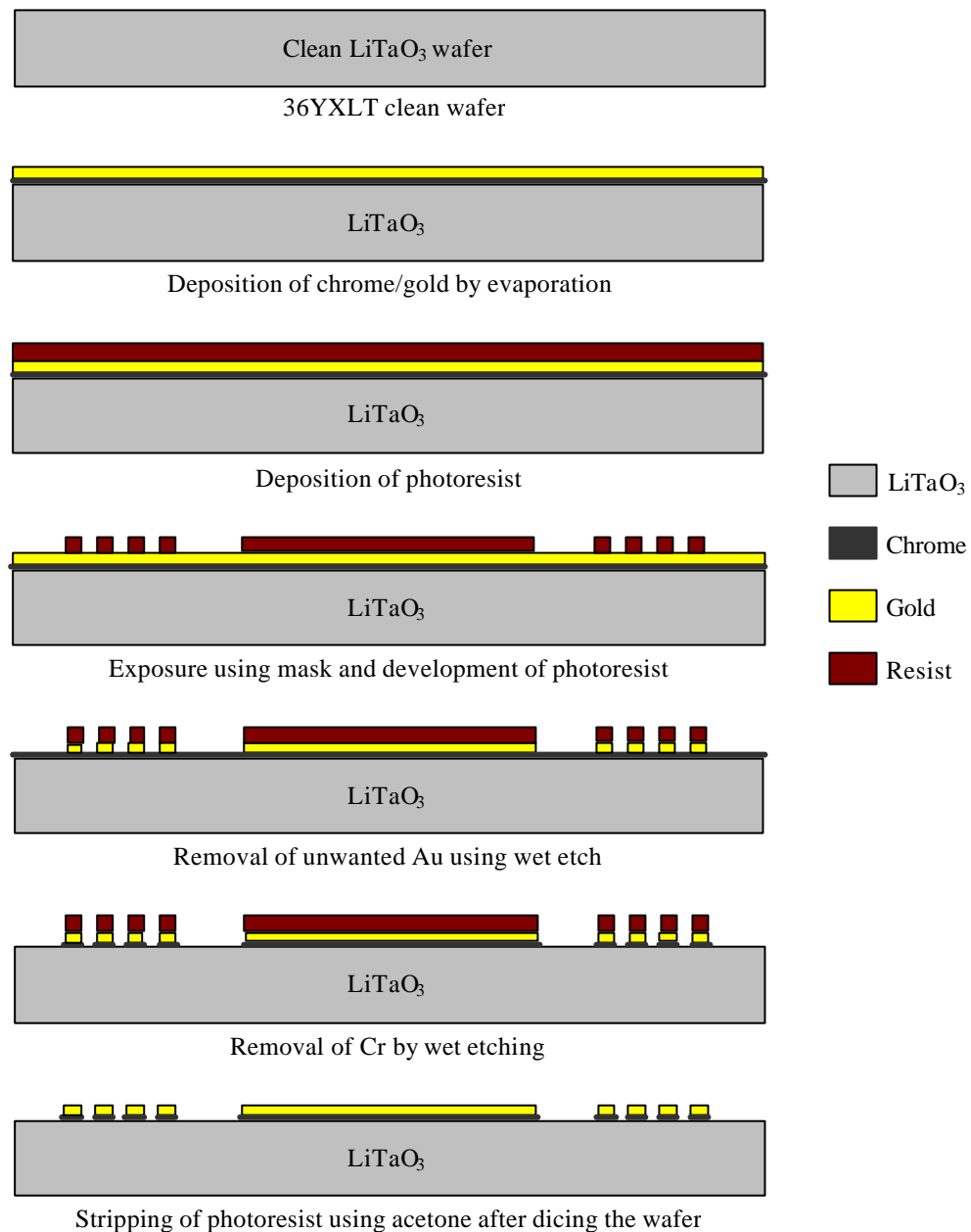


Figure 4.3 Wet-etching fabrication process steps of SH-SAW sensor

4.2.6 Wafer dicing and packing

A picture of the processed wafer with the device structures pattern in the gold (photoresist still on) is shown in Figure 4.4. The photoresist was not removed as it protects the delicately patterned IDT structures from debris damage while cutting.

The wafer was diced using a saw (Sola Basic Tempres model 602) with a diamond-coated blade at high speed of approximately 30,000 rpm. When laying out the mask plate design with the individual devices, enough clearance between each device and surrounding devices was left in order to allow for blade thickness and not lose any

devices. $500\ \mu\text{m}$ gap was left between the individual devices and a $100\ \text{mm}$ thermocarbon blade was chosen. During the dicing the diamond coated blade is impregnated with a stream of cooling deionised water. The wafer is stuck down on a sticky tape (trimmed to size) to hold the wafer. The wafer was loaded onto the appropriate side of chuck plate which has two sides (the side with the larger circles is for 3" and 4" wafers and side with the smaller circles for 2" wafers and pieces of wafers). As the wafers are very brittle a test cut was performed and it was decided to cut through the wafer in steps of $100\ \mu\text{m}$ through the thickness of the wafer ($500\ \mu\text{m}$). The individual device edges parallel to the IDT fingers were kept rough to minimise the normal reflections of the edges back into the transducer. After dicing the whole wafer the individual devices were easily peeled off the tape for use.

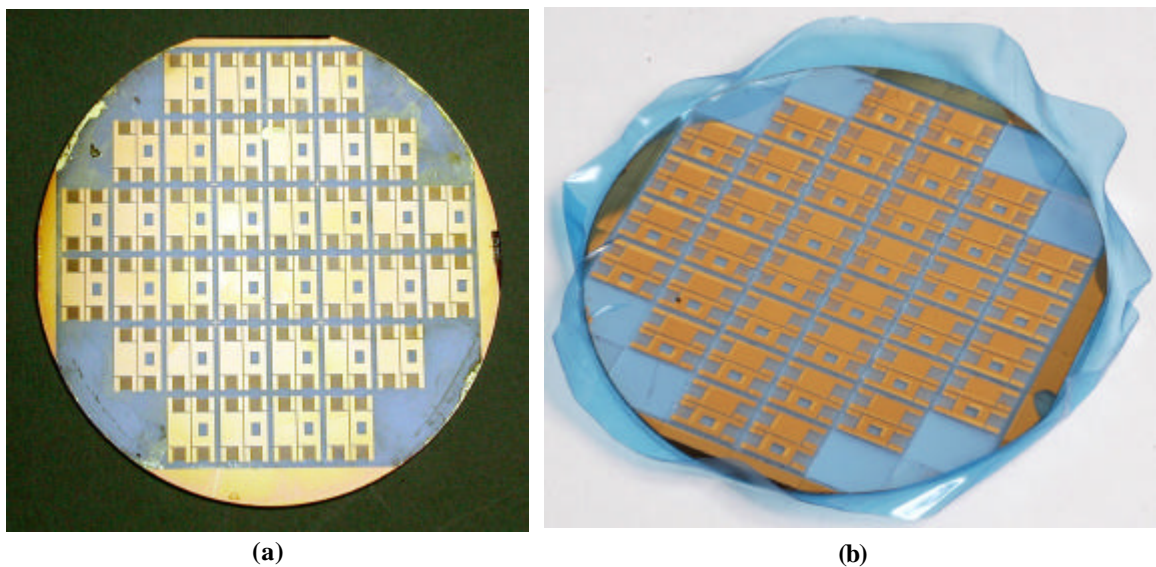
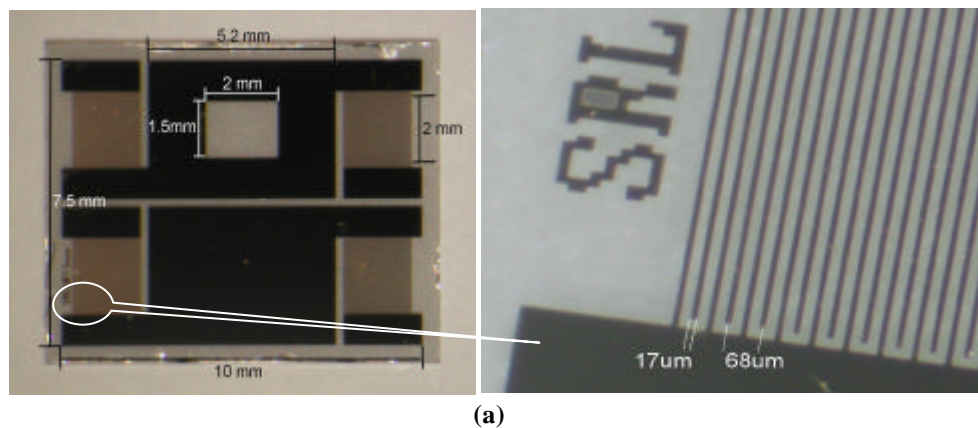


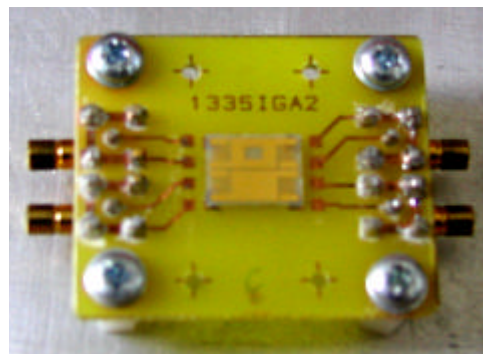
Figure 4.4 Photograph of wafer with devices patterned (a) before dicing (b) after dicing

The individual devices were mounted on a custom designed PCB and the contact pads wire bonded to the RF connector pads on the PCB using an ultrasonic wedge bonder. The PCB was designed to accommodate the SH-SAW sensor, 4 RF (SMA or SMB) connectors (an input and output for each delay line) and guiding holes for the chamber that holds the liquid in the sensing area. Alignment marks for the sensor and guiding holes were located on the PCB and the device was mounted onto pins at each of its corners to prevent contact with the PCB. The device was glued to these pins only at one end to minimise the influence of bending stresses as a result of expansion due to temperature variations, which would cause strain-related perturbation of the AW. This

problem is discussed in more detail in Section 4.4.4. Mounting on to the pins also minimise coupling of any bulk waves propagating through the thickness of the substrate, into the PCB. This method of mounting the devices also made it easier to reuse the PCBs because the pins the devices are glued to could be pushed out and replaced by new ones. After mounting the device on the PCB, the pads of the IDTs are wire bonded (gold wire) to the connection pads for the RF connectors. This was performed with the aid of an ultrasonic wedge bonder (Kulicke and Soffa Model 4126). Figure 4.5(a) shows a photograph of the fabricated SH-SAW device and Figure 4.5(b) shows the device mounted on the PCB. The sensor on the PCB as a unit, were placed onto an aluminium block for ease of handling and support during external connection to the PCB with cables (see Figure 4.7).



(a)



(b)

Figure 4.5(a) Photograph of single fabricated dual-delay line 60MHz SH-SAW device **(b)** Device mounted on a PCB without liquid cell

The liquid cell (chamber) was designed to hold a small volume of the sample liquid over the sensing area of the SH-SAW device. It was designed using a computer aided design program (AutoCAD) and machined out of polytetra-fluoroethene (PTFE). It was made such that only a very small area (with walls ≈ 1 mm thick) around the central well

that holds the sample liquid came into physical contact with the SH-SAW sensor. The liquid cell dimensions were 32 mm in length by 20 mm wide with a central reservoir of $6.8 \times 2.5 \times 8.0 \text{ mm}^3$ and a volume of approximately 136 μl . Full dimension details are of the cell are given in Appendix B. The liquid cell was positioned accurately over the sensing area between the IDTs with the aid of guiding pins that fit into holes in the PCB as shown in Figure 4.6. The cell rests on the device without any sealant. This enables easy removal of the cell to clean the device and yet holds the liquid without leakage. Furthermore the liquid chamber was designed to accommodate for an electronic nose device that fits on the top of the chamber to sample the headspace of the liquid under test. Details of the electronic nose device used and the experimental details are covered in chapter 6.



Figure 4.6 Picture of PTFE liquid cell with locating pins and central slot for liquid fill

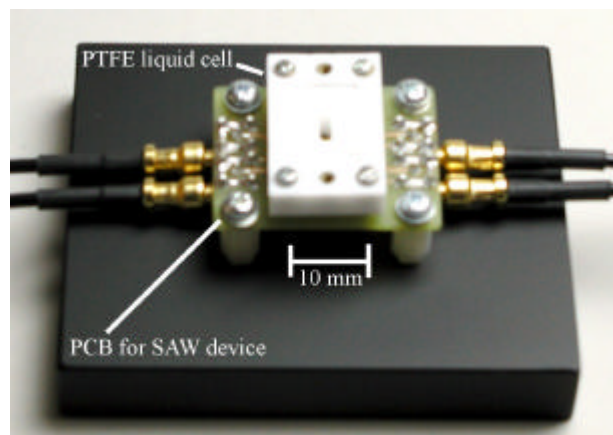


Figure 4.7 Photograph of SH-SAW device with the PTFE liquid cell used for experimental work

4.3 Acoustic wave measurement technology

Having designed the SH-SAW delay line devices, the external measurement systems required to transmit and receive signals from the devices and extract information about the samples under test, had to be explored. This section outlines the instrumentation

and measurement aspects of typical IDT-SAW sensors and the different measurement techniques available along with comparisons between them.

4.3.1 Instrumentation and components

Acoustic wave (AW) sensors convert a physical or chemical property of interest into a suitable signal for measurement. Eventually the measured sensor information must be processed to be presented to the user in a sensible and meaningful manner. This is the role of the instrumentation. Before embarking on descriptions of how various acoustic-wave devices are connected to instruments necessary to make basic measurements, an introduction to some of the components and instrumentation used to perform measurements on these systems are introduced.

Active/Passive devices

Active devices require an input of power commonly via low-level voltages (5-24 Volts), to achieve their specified function, with the consequence that their output RF power level can exceed RF input power. Conversely, passive devices cause some transformation of the signal input without use of any external power source, so that the power is always less than or equal to the input power. The components are specified as either active or passive (noting that the addition of electronic control instrumentation, e.g. a motor drive to set the value of a variable attenuator, is not considered grounds for calling a component active). In the following descriptions the active/passive identification has been made only for circuit components having an input and output, not for measurement instruments (e.g. network analyser), the output in which is a visual indication or computer bus-compatible signal.

Amplifier (active)

The amplitude of the output signal from an amplifier is equal to the gain multiplied by the amplitude of the input signal. The gain may be non-inverting (positive) or inverting (negative). When the amplifier is operating in *saturation*, its output power level and/or amplitude remains constant for small variations in the input signal. Thus, in saturation, the greater the amplitude of the input signal, the smaller the gain. The amplifier bandwidth is the range of frequencies over which the gain is at least $1/\sqrt{2}$ of its specified value. Typically, the gain bandwidth product is approximately a constant for

any given amplifier circuit, thus amplifiers with larger bandwidth tend to have a lower gain.

Attenuator (passive)

This can be considered as the opposite of an amplifier, it diminishes the amplitude of an input signal by a specified fraction.

Directional coupler (passive)

This device has three or more ports and passes the majority of an input signal straight through to the device's output while splitting off a small, specified fraction of the signal to send to another device (e.g. a frequency counter). The device is directional because any power returning to the output (split-off port) from the external circuit is diverted either to another output port or to an internal load where it is dissipated.

Filter (passive)

This is a device that allows the passage of only a particular range of frequencies. A bandpass filter allows a specified band of frequencies (its bandwidth is often expressed as a percentage of the centre of the pass band); a notch filter removes a narrow band of frequencies; high-pass and low-pass filters pass signals higher or lower than a specified cut-off frequency, respectively.

Frequency counter

Measures frequency by counting the number of cycles (uses an clock) in an accurately know time period. The accuracy of the counter's internal time base is critical, making temperature-controlled acoustic wave devices a common internal timing element of these instruments. Greater the required accuracy longer the counter must sample the signal. Interpolation techniques are commonly employed allowing the counters to record frequencies to accuracies of 0.1% of the reciprocal of the sampling rate, e.g., a one-second sampling time can give resolution of 0.001 Hz.

Impedance-matching network (passive)

This is an interconnected arrangement of components, the most important of which is an inductor (often tunable), that matches the impedance of device (e.g. one transducer of an AW sensor) to the impedance of the instrument (e.g. an amplifier) to which it is to

be connected. This impedance matching maximises the power transfer by minimising the reflection.

Network analyser

This is an instrument that provides a controlled-amplitude signal to the input of a test device or circuit over a range of frequencies, then records and displays the output of the device/circuit in terms of its magnitude and phase relative to the input as a function of frequency. The network analyser is the most powerful single tool for the characterisation of the AW devices. Some of the important features found in most of the models include a wide range of display options, the ability to simultaneously measure both reflected and transmitted power, and the capability of Fourier transform frequency-domain responses into the time domain.

Phase shifter (passive)

This device shifts the phase of the output signal by a specified (knob or voltage-selectable) number of degrees relative to its input. These devices function over a specified frequency range and heavy attenuation of the signal typically occurs outside this range.

RF detector (passive)

This device converts the RF signal into a DC signal of magnitude proportional to the RF power.

Synthesized oscillator (signal generator)

This is an instrument that digitally synthesizes a controlled-amplitude, controlled-frequency signal. The source is typically computer controllable, allowing a sweep (in discrete steps) of frequency.

Vector voltmeter

A vector voltmeter is a fully automatic tuned receiver that makes RF voltage (amplitude) and phase measurements between two signals (one signal serves as a reference), simpler. Typically, the phase difference as well as the ratio, difference, or individual values of the amplitudes of the two signals can be output in analog, digital, or visual display form. By using a combination of a synthesized source and a vector

voltmeter to measure frequency dependent responses, an ersatz equivalent of a network analyser can be constructed.

4.3.2 Measurement of acoustic wave device frequency response

The measurement of the frequency response of an AW device is important for several reasons. The response of acoustic-wave sensor to an external perturbation (e.g. in chemical sensing), can be better understood when the device's frequency response is known in prior. The frequency response measurement is also very important in designing a stable and accurate measuring system for a particular device. Finally, the change in frequency response of a device that results from some significant modification of its "surface environment," such as the immersion of the surface in a liquid or deposition of a polymer layer, can provide more information about the effect of that modification, in terms of the physical properties of the contacting layer or phase, than measurement of, say, oscillation frequency alone.

The frequency response of a device can be defined by the magnitude and phase of its "output signal" as a function of the frequency of a (constant amplitude) input signal¹. The nature of the output signal varies from device to device (e.g. single port resonators and 2-port delay lines) and accordingly, the instrumentation used to make the measurements, vary. The measurement methods described here are focused on two port delay line devices.

4.3.2.1 Two-port devices

As discussed in chapter 2 the two-port devices include all delay line (such as SAW, FPW and APM) devices and the two-port resonator variations of these devices. For all these delay lines, the transmitted signal S_{12} (between the input and output port) is the most important, although reflected signals (S_{11} and S_{22}) can be of considerable help in diagnosing IDT problems or in matching IDT impedance. The network analyser is the instrument of choice to measure the frequency response of these devices; the setup is depicted in Figure 4.8(a). The frequency response can also be measured using a

¹ Another way of expressing the response data, chosen for ease of mathematical manipulation, is in terms of real and imaginary components of a vector in phase space. For such a response vector, expressed as $S = a + jb$, the magnitude is given by $S = (a^2 + b^2)^{1/2}$ and its phase angle is $\mathbf{f} = \tan^{-1}(b/a)$.

synthesized oscillator (signal generator) and vector voltmeter combination as shown in Figure 4.8(b).

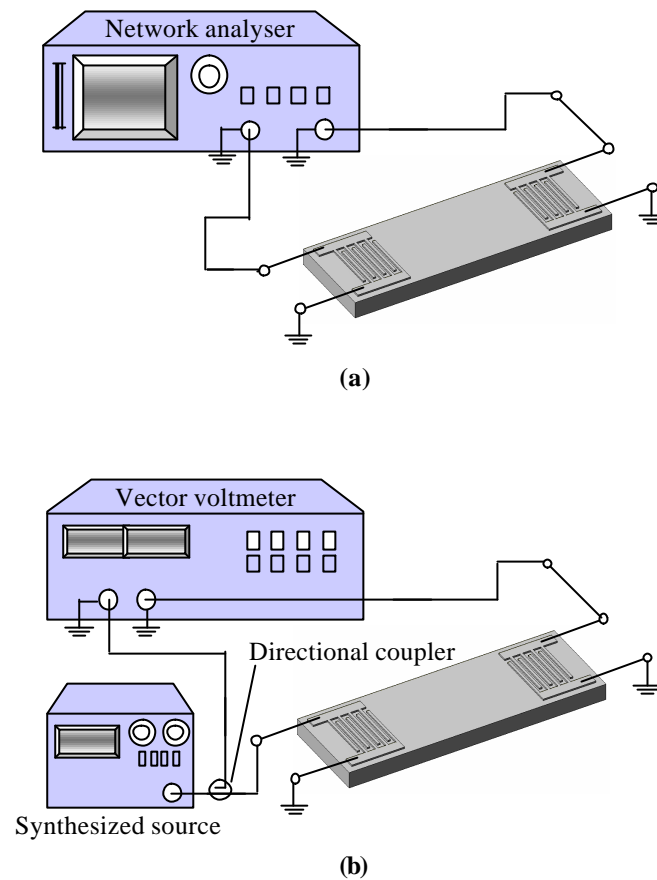


Figure 4.8(a) Network analyser setup to measure two-port-device frequency response. **(b)** Signal generator/VVM combination setup for frequency response measurement

4.3.2.2 Real-time measurement and characterisation of acoustic wave devices

The most complete and unambiguous characterisation of acoustic wave device response is always obtained from a complete frequency response spectrum, including all four S parameters. Furthermore there are cases, particularly for fairly complex interactions such as between the AW and a surface film or a liquid, in which the nature of the response might not be understood without this important tool. However there are several reasons that reflect on not performing an entire frequency response measurement as a routine measurement, to monitor the real-time responses of an AW sensor. First, the amount of time required to obtain and store a frequency response is in the range of one to several minutes, depending on the frequency resolution and noise level desired; this should be compared to a fraction of one second to obtain, for example, the oscillation frequency and insertion loss from a SAW delay line. Secondly,

the accuracy with which the centre of the frequency-response peak can be determined is limited by the resolution of the network analyser, unless curve fitting is used; even then the asymmetry of typical response peaks, as well as other variables, makes it difficult to match the fraction-of-one-hertz accuracy possible with carefully designed oscillator circuit. Finally, the expense, complexity, lack of portability, need for highly qualified personnel make the network analyser (synthesized source/vector voltmeter) impractical for practical field applications.

4.3.2.3 Simultaneous measurement of acoustic wave velocity (phase) and attenuation

The network analyser is not ideal for field use or even certain laboratory measurements of real-time perturbations (due to reasons explained above), however, in many cases, it is very important to measure both the velocity and attenuation simultaneously using a network analyser. The majority of the acoustic wave sensor research reported relies heavily on measurements of velocity perturbations (typically through frequency shifts for an oscillator circuit). This approach is sufficient if it is known in advance that all perturbations will affect AW velocity alone (perturbations relating to mass changes and purely elastic changes in mechanical properties). By measuring the attenuation changes a clear indication as to whether it is being affected can be achieved, providing a clear picture of whether it is safe to interpret a response in terms of a mass change alone. These measurements require the use of a network analyser, vector voltmeter, one or two RF detectors, or the analogue output from the automatic gain control (AGC) circuit of an AGC amplifier.

Network analyser setup used for RF characterisation of the SH-SAW devices

A vector network analyser (HP8753ES) was used to measure the various reflection and transmission parameters associated with the SH-SAW devices. After appropriate calibration of the network analyser the measurements can be performed. The measurements are expressed in terms of the S parameters which describe the signal flow within the network. The S parameters are defined as ratios and are represented by $S_{in/out}$, with the subscripts referring to the input and output signal, respectively. Figure 5.1 below shows the energy flow in a two-port network [4.7].

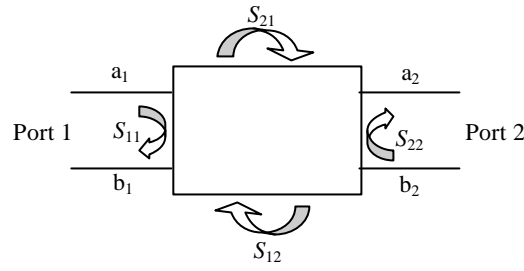


Figure 4.9 Signal flow of a two-port network

In Figure 4.9 above a_1 is the input microwave signal from analyser port 1 into the system, b_1 is the reflected microwave signal from the system into port 1 of the analyser, a_2 is the input microwave signal into the system from analyser port 2 and b_2 is the reflected microwave signal from the system into port 2 of the analyser [4.8].

The S parameters are given by

$$S_{11} = \left. \frac{b_1}{a_1} \right|_{a_2=0} = \Gamma_1 \text{ reflection coefficient at port 1 with } a_2 = 0 \quad (4.1)$$

$$S_{22} = \left. \frac{b_2}{a_2} \right|_{a_1=0} = \Gamma_2 \text{ reflection coefficient at port 2 with } a_1 = 0 \quad (4.2)$$

$$S_{21} = \left. \frac{b_2}{a_1} \right|_{a_2=0} = T_{21} \text{ transmission coefficient from port 1 to port 2 with } a_2 = 0 \quad (4.3)$$

$$S_{12} = \left. \frac{b_1}{a_2} \right|_{a_1=0} = T_{12} \text{ transmission coefficient from port 2 to port 1 with } a_1 = 0 \quad (4.4)$$

Calibration of any measurement is essential in order to ensure the accuracy of the system. Errors in systems may be random or systematic. The systematic errors are the most significant source of measurement uncertainty and being repeatable however can be measured using the network analyser and the correction term computed from the measurements. Conversely, the random errors are not repeatable and are caused by factors such as changes in temperature (predictive so not totally random), noise, and other surrounding environment factors. The process of calibration involves the connection of a series of known standards to the system and the systematic effects are determined as the difference between the measurand and the known response of the standards. The frequency response is the vector sum of all the test setup variations in magnitude and phase and the frequency, which includes all the signal-separation devices, such as test setup and cabling. The measurement system is calibrated using the

full two-port calibration technique. The four standards that are commonly used are the shielded open circuit, short circuit, load, and through (port 1 and port 2 of the network analyser connected together). The full two-port calibration method provides full correction of directivity, source match, reflection and transmission-signal path, frequency response, load match, and isolation for S_{11} , S_{12} , S_{21} , and S_{22} . It involves reflection, transmission and isolation measurements.

For the reflection measurement (S_{11} , S_{22}), the open, short and load standards are connected to each port in turn and the frequency response measured. These six measurements result in the calculation of the reflection error coefficients for both ports. For the transmission measurement, the two ports are connected together and the following measurements performed, forward through transmission (S_{21} - frequency response), forward through match (S_{21} -load), reverse through transmission (S_{12} - frequency response), and reverse through match (S_{12} - load). These four measurements defined by equations (4.1) to (4.4) are used to compute the transmission error coefficients. The forward and reverse isolation-error coefficients are computed from measurements with loads connected to the two ports and S_{21} and S_{12} noise floor level measured. The reference results are saved and the systematic errors removed.

Figure 4.10 shows a picture of the network analyser setup used to characterise the SH-SAW devices. The setup was used for reflection, transmission and impedance measurements. The vector network analyser shown is the HP 8753ES model by Agilent technologies. It has a frequency range of 30 MHz to 3 GHz with 50 ohm 3.5 mm SMA type connectors on the test leads (More details on the network analyser can be attained from the user manual [4.9]).

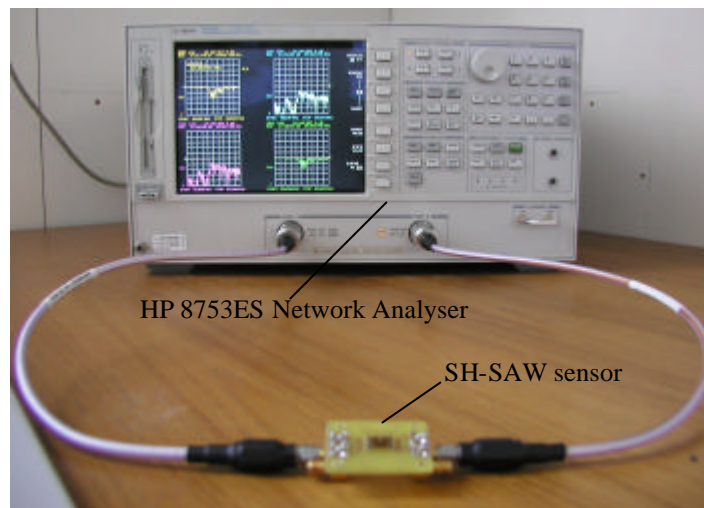


Figure 4.10 Photograph of HP 8753ES vector network analyser setup

The S parameters were measured after a full two port calibration consisting of reflection, transmission and isolation (omitted) of the network analyser in the appropriate frequency range of 10-100 MHz (known from theoretical design). The calibration was performed using an open circuit, short circuit and 50 Ω load terminations for the reflection parameters and a through for the transmission. The following sections give typical S parameter measurement results of the devices.

Reflection measurements (S_{11}, S_{22})

The setup shown in Figure 4.10 was used to perform the reflection measurements (S_{11}, S_{22}) to determine the impedance mismatch between the 50 Ω source and the load (SH-SAW device). The reflection coefficients were plotted in terms of both the log magnitude and on a Smith chart as shown in Figures 4.11 and 4.12 overleaf. It can be seen from the plots that the resonant frequency for that particular device was 60.5 MHz with a return loss of approximately -26 dB ($S_{11} \sim 0.05$ with 0 being perfectly matched). This shows that the input port of the device was not perfectly matched to the 50 Ω source but allowed the majority (95%) of the power through without reflection. The impedance of the input port was also measured using the Smith chart format of the network analyser and is given in Figure 4.12. The Smith chart shows an impedance of approximately 51.4 Ω at the resonant frequency of 60.5 MHz which is close to the theoretical and source impedances.

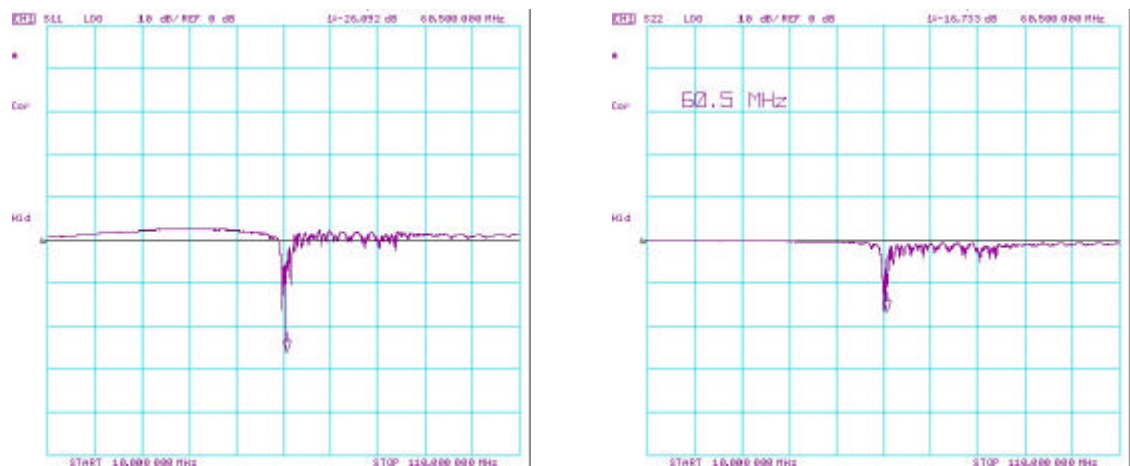


Figure 4.11 S_{11} (left) and S_{22} (right) measurements of SH-SAW input and output IDTs for a metallised delay-line

From the measurements it can be seen there is a slight mismatch in the impedances, but since there is negligible reflection of power it was decided not to implement any matching circuitry. In the case of large mismatches and heavy loss of power it is essential to compensate by constructing simple external impedance matching circuitry.

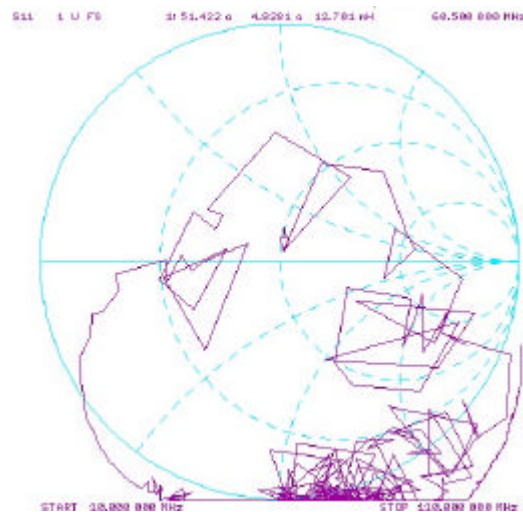


Figure 4.12 Impedance measurement of IDT (metallised delay-line) using a Smith Chart

Transmission measurements (S_{21} , S_{12})

The forward and reverse insertion losses were measured using the same setup over the same frequency range. Figure 4.13 shows the log magnitude of the transmission coefficients. The insertion losses varied between 10 to 15 dB for the devices which is close range to the theoretical value of 15dB. From these measurements the transmission

frequency (frequency with minimum insertion loss) of the delay lines was achieved which was used for single frequency measurements using the signal generator/vector voltmeter setup.

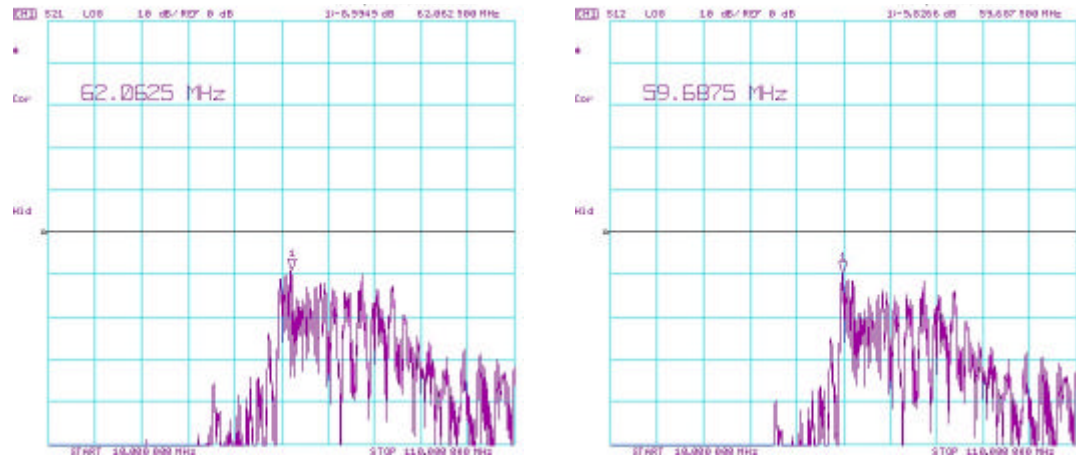


Figure 4.13 Forward S_{21} (left) and reverse S_{12} (right) transmission measurements of a single SH-SAW metallised delay line

4.3.2.4 Propagation measurement technique for two-port devices

In the propagation measurement technique, a fixed frequency signal is input to one IDT using an external RF source (oscillator or signal generator), while a vector voltmeter is used to monitor the changes in AW amplitude and phase shift between the transducers as illustrated in Figure 4.8(b). At constant frequency, the changes in the wave velocity are proportional to changes in phase according to

$$\frac{\Delta v}{v_0} = \frac{\Delta \mathbf{f}}{\mathbf{f}_0} \quad (4.5)$$

where $\mathbf{f}_0 = 2\mathbf{p}N_1 + \mathbf{f}_r$, \mathbf{f}_r being the phase difference (in radians) displayed by the vector voltmeter; $\Delta \mathbf{f}$ is the change in \mathbf{f}_r as a result of a perturbation and N_1 is the centre to centre IDT spacing expressed in terms of acoustic wavelengths. Although with this method the small phase shifts cannot be measured with great accuracy, the measurements are not subject to mode hopping that can afflict an AW oscillator circuit under certain circumstances. This is fortunate as sudden, large shifts in phase ($> 2\mathbf{p}$ radians) are likely to result in additive errors of factors $\pm 2n\mathbf{p}$ ($n = \text{integer}$) in the measurement of $\Delta \mathbf{f}$ (phase is measured to $\pm \mathbf{p}$). Perturbation measurements are best made when the region underlying the IDTs is *not* at all perturbed, so that the fixed-

frequency source continues to match the frequency of least insertion loss of the IDTs as the perturbation progresses.

Thus the perturbation (propagation) measurements are made when

1. The highest accuracy is not necessary.
2. A substantial perturbation only to the region between the IDTs is anticipated.
3. Such a large perturbation is anticipated that it would be difficult to distinguish between a mode hop and the perturbation itself (e.g. a transition from a dry surface to one covered with a liquid).
4. Such a large insertion loss is anticipated over the course of the measurement that it is not possible to set up and maintain a stable oscillator circuit.

Signal generator / vector voltmeter setup for liquid measurements

After having performed S parameter characterisation of the SH-SAW devices using the network analyser the necessary information (mainly the transmission frequency) to drive the devices using the signal generator/vector voltmeter is attained. (This information could also be achieved by sweeping a range of frequencies from the signal generator to the device and response measured by the vector voltmeter however it is easier in terms of visual display and more accurate if a network analyser is employed).

Figure 4.14 shows a picture of the signal generator/vector voltmeter setup with the SH-SAW device connected. This setup was used to perform the propagation measurements of the SH-SAW devices with different liquid loading on the sensing surface.

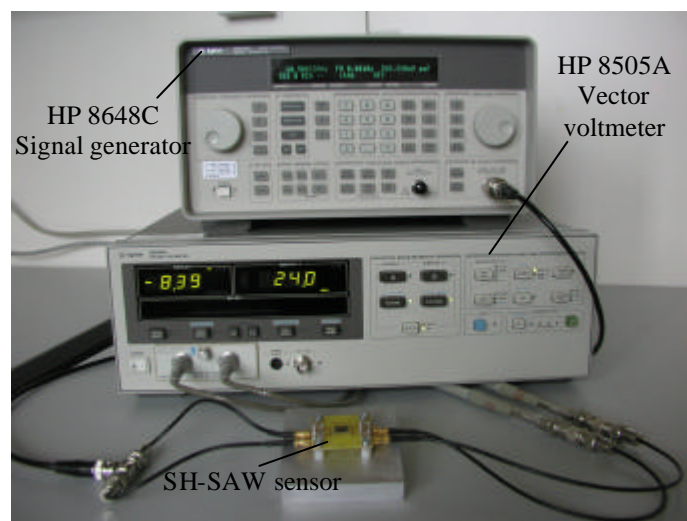


Figure 4.14 Picture of the signal generator/vector voltmeter setup for liquid experiments (SH-SAW device without cell)

The set-up comprised a signal generator (HP 8648C), the dual delay line SH-SAW sensor and a vector voltmeter (HP 8505A). The experimental procedure for SH-SAW devices involves the measurement of both the phase velocity and attenuation of the SH-SAW signals propagating on the delay lines of the sensor. Using this setup, an electrical signal is fed from the signal generator to the input IDTs of either one at a time or both delay lines simultaneously. The amplitude ratio ΔA and phase difference Δf between the input and output signals of each delay line (when signal fed to only one delay line and used as the reference) and between the output signals (when signal fed to input IDTs of both delay line simultaneously) of the sensing and reference delay lines were monitored by the vector voltmeter. The fractional velocity shift $\Delta v/v$ and attenuation change $\Delta a/k$ of the SH-SAW can be derived from the phase difference and the amplitude ratio, respectively [4.10]. By substituting these experiments results into the approximate equations of the perturbation theory presented in chapter 3, the liquid properties are obtained. The vector voltmeter was controlled via the PC using a GPIB interface using Labview software, which also stores the results displayed on the vector voltmeter (the program is given in Appendix A)

The SH-SAW sensor was mounted on a custom made PCB (as described earlier) and supported on an aluminium block. To provide the sensors a stable environment they were placed in a commercial Dri-Bloc™ (DB-2D) heater ($\pm 0.1^\circ\text{C}$) and covered to maintain a constant temperature while performing the experiments. The details of the experiments performed with the various liquid and results obtained are presented in chapter 5.

4.3.2.5 Two-port AW devices in oscillator circuits

SAW delay-line-based devices in an oscillator loop are a useful system to make real-time measurements. The main components in the oscillator circuit are the SAW delay line and an amplifier. The SAW delay line device provides a feedback path for the amplifier. For stable oscillation to occur, i.e., for the signal to add coherently to itself after having traversed the loop, the signal must return to its starting point having equal amplitude and being shifted in phase by an integral multiple of 2π radians. Although it is clear that under these conditions oscillation will occur, the initial source of the signal that starts the oscillation is not as obvious. The answer lies in ever-present noise, small

in amplitude that is invariably picked up and amplified by the amplifier/SAW device combination.

Figure 4.15 shows a schematic representation of a SAW delay-line based oscillator circuit with necessary components required.

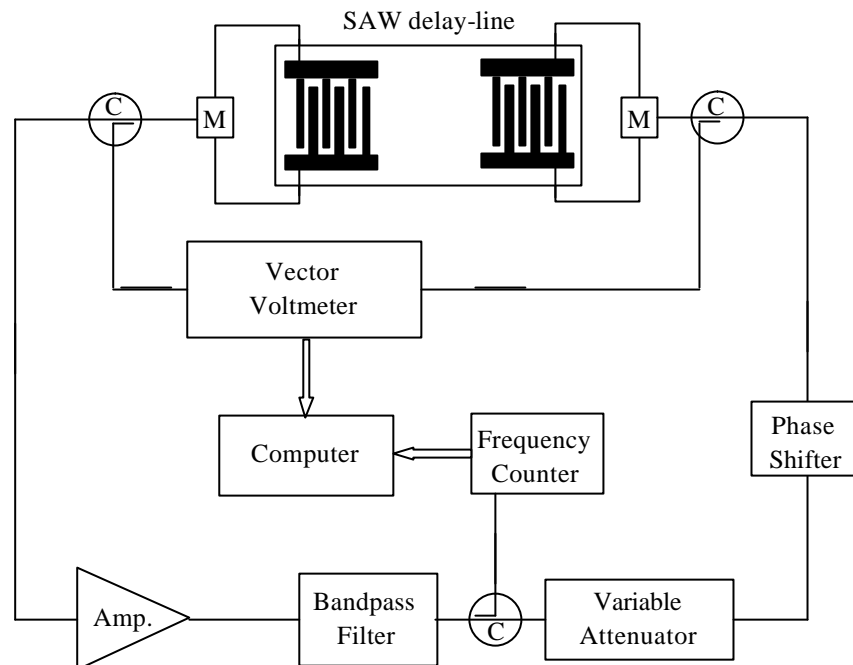


Figure 4.15 Two-port SAW delay line-based oscillator loop

The components include an amplifier, which depending on its gain and a variety of factors pertaining to the device, its coating (if device coated) and their application, may need to be cascaded with more than one amplifier; a band-pass filter to prevent spurious oscillation at unwanted frequencies; one or more variable attenuators to adjust the total gain of the circuit; a tuneable phase shifter to adjust the round-trip phase shift of the circuit; directional couplers to send fractions of the loop signal to measurement instrumentation; a frequency counter; a vector voltmeter or other means to determine insertion loss by comparing the SAW device input and output amplitudes; an impedance-matching network for each IDT; and a computer for data acquisition.

The setup shown in Figure 4.9 can be rearranged but the arrangement shown has proven to yield the highest stability [4.11]. For example, placing the bandpass filter immediately after the amplifier removes any amplifier-generated harmonics that might confuse the frequency counter. Although stable oscillation can be achieved without the use of impedance matching networks for the IDTs, impedance matching eliminates 10-

20 dB of insertion loss, requiring less amplifier gain. The phase shifter is important because it allows the phase response to be moved along the frequency axis, permitting a zero-phase point to be made to coincide precisely with the frequency of minimum insertion loss. Similarly, adjusting the attenuator allows shifting of the insertion loss down and eventually leaving one unique frequency where the gain of the amplifier is sufficient for oscillation and the round-trip phase shift is simultaneously zero. The vector voltmeter is not necessary for stable loop oscillation, but it makes it possible to measure the attenuation. The vector voltmeter can be eliminated, by replacing it with a pair of RF detectors (one for each IDT), the DC signals from which indicate the magnitudes of the input and output signals; or by a single RF detector at the device output if it is known with certainty that the amplifier driving the device is in saturation (constant power output) at all times; or by using the analogue output from an automatic gain control (AGC) amplifier used to drive the device.

4.3.2.6 Phase-locked loop setup for two-port device measurements

This setup can be considered as a hybrid of the oscillator circuit and the propagation measurement systems. The setup is shown in Figure 4.9, which closely resembles that used for propagation measurements. As the name suggests the phase is locked or maintained at a constant value. This is done by initially recording the phase difference between the two IDTs (before perturbation) and when a perturbation affects the phase difference, the frequency of the signal from the source is adjusted to return the phase to its initial value. In this way, the source frequency is constantly returned to the extent dictated by the perturbation, and the phase difference between the two transducers remains “locked.”

The setup shown in Figure 4.16 uses a computer to monitor the phase difference, compute the frequency required to maintain the phase at its initial value, and then send an appropriate signal to the synthesized source. Thus this system is known as a computer-controlled phase-locked loop [4.12]. For the appropriate algorithm to calculate setting of the new frequency, the phase slope (change in phase per unit change in frequency) must be predetermined, before any perturbation. In practice, the phase slope might also vary to some extent as a function of the changes in the AW device surface, its coating (if coated), and the environment. Thus it is helpful to create an iterative computer program that adjusts the source frequency in progressively smaller

steps to fine tune the phase difference, and also to redetermine the phase slope when three to four iterations fail to properly tune the phase.

As with oscillator circuits, this measurement setup, is best suited to perturbations that occur in the substrate areas under the IDTs and the rest of the path length. This is because constant retuning of the source frequency to track the perturbation eventually leads to detuning relative to the point of minimum insertion loss of the IDTs. The main advantage of the computer-controlled phase-locked loop configuration is that it is rugged because of the fixed-frequency perturbation measurement system that allows functionality even during large changes in attenuation.

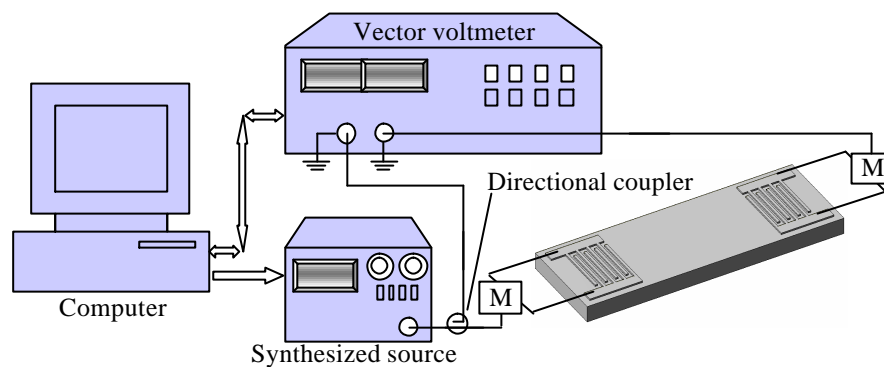


Figure 4.16 Computer-controlled phase-locked loop configuration for a two-port device measurement

4.4 Controlling the sensor environment

Acoustic wave devices are sensitive to a large number of physical and chemical parameters. These include parameters such as temperature, pressure, acceleration, stress, and the adjacent medium's density, viscoelastic properties, and electrical conductivity. Owing to these wide range of measurand sensitivities makes the acoustic wave devices attractive for a wide variety of sensor applications. However, since only one of these measurands is of interest to be exploited for a particular application, all the other responses become undesirable interferences. Thus, it is essential that the sensor environment is carefully controlled to eliminate the effect of sensor cross-sensitivities. In the following sections the common unwanted effects and ways to minimise them are discussed.

4.4.1 Temperature effects and control

A temperature change produces a change in dimension which in turn results in a change in density, hence changing the velocity of any propagating acoustic wave. Since

velocity is the most commonly used fundamental AW response, there would be a temperature dependent component in the sensor output. Efforts into discovering piezoelectric materials with low temperature coefficients have yielded a significant reduction of temperature sensitivity. The physical properties of the chemically (bio-chemical) sensitive coating materials are also temperature dependent. The devices used in this project have no chemically selective coatings hence overcoming this problem. However, the packaging material would normally have a different temperature coefficient from that of the device substrate creating the problem. Also, the temperature of the analytes (liquid/gas) will affect the response and has to be kept constant.

The main methods to minimise the effects of temperature on AW sensors are: (1) selection of low-temperature-coefficient materials; (2) incorporation of a temperature sensor and compensation circuitry or software; and (3) active control of the sensor temperature. Although several low temperature-coefficient materials have been characterised for AW applications, not all can be used for liquid sensing as is the case here. (See chapter 3 for choice of substrate) Quartz substrates of ST and AT cuts provide nominal zero temperature coefficients near room temperature for SAW devices and TSM resonator devices.

To place this problem of temperature drift into perspective, the piezoelectric wafer in question has to be considered. 36YXLT has a temperature coefficient of approximately 32 ppm/°C near 30°C, thus at 30°C a 60-MHz SH-SAW delay line device would experience a resonant frequency shift of about 1.92 kHz/°C. Depending on the design of either rest of the oscillator circuitry or measurement instrumentation, a short-term frequency “noise” of less than 20 Hz can be assumed, which suggests that the temperature must be controlled to $\pm 0.01^\circ\text{C}$ if the temperature drift is not to exceed the frequency noise. This is a very challenging requirement, particularly for portable instrumentation. However the need for stringent temperature control can be somewhat relaxed by either employing a second SAW device as a temperature reference (as discussed in chapter 3), or by correcting SAW data (frequency/attenuation) numerically using data from a nearby temperature sensor [4.13]. By the using a reference delay line device and comparing the outputs between the two delay lines it is possible to reduce the magnitude of the observed temperature drift by a factor of 10 or better. This would change the temperature sensitivity to about 190 Hz/°C, which would still demand temperature control of about $\pm 0.1^\circ\text{C}$ to eliminate temperature effects. Thus,

considerable attention to temperature control is essential unless the anticipated signals are so large that they make the temperature drift insignificant. In the next chapter the temperature characterisation of the SH-SAW devices is presented.

The temperature variations can also produce drift due to strain created in the SAW device by the packaging that has a different coefficient of expansion to that of the substrate material. Mounting the SAW device rigidly onto a material that expands at a different rate with temperature, would result in strain in the SAW device and causing a perturbation. This is discussed in more detail in Section 4.4.4.

In the case of coated SAW devices, the problem of temperature variation is compounded when the coating materials have different temperature coefficients of expansion to those of the substrate material. In the case of most organic coatings the temperature coefficient of expansion is larger (near room temperature) than that of the quartz and ceramic substrates. This makes the AW velocity dependence on temperature greater (many times greater in some cases) for a device that is coated with such a film than for an uncoated device. More severe perturbations occur when a polymeric material used as a coating undergoes a significant viscoelastic or phase change near the operating temperature, such as glass-to-rubber transition, melting, or a long-chain-related relaxation. Also, at a temperature where the density and sound velocity in the film are such that the film thickness corresponds to an integral multiple of one-quarter of the acoustic wavelength in the film, resonant energy transfer occurs, resulting in a major perturbation of the AW velocity and attenuation. Furthermore, the sensitivity of the coatings to the analyte are temperature dependent and so is the partition coefficient between analyte in the ambient gas or liquid phase and that sorbed by the coating (typically an exponential dependence on absolute temperature). Thus the sensitivity of the coated device will always have some temperature dependence [4.14]. These issues are not discussed in details as the devices used here do not have a coating.

Clearly, temperature has a significant effect on the performance of AW devices. To achieve highest levels of sensor performance, the practical devices would thus require incorporation of temperature sensing and compensation circuitry, active control of device temperature and to some extent a choice of low-temperature-coefficient substrate materials. Here the choice of substrate, based on the application and the design of a dual delay line helps the temperature problem, and the anticipated attenuation and velocity perturbations due to liquid loadings are considerably larger

than that caused by a controlled temperature drift. Furthermore, the devices have no coating hence avoiding temperature related problems mentioned above.

4.4.2 Pressure effects

Ambient pressure can affect the response from AW devices mainly in the following two ways: it can cause a hydrostatic compression of the device, which causes small perturbations in the AW velocity and length of the AW path and it can affect the density of the fluid medium in contact with the device. The sensitivity of the AW devices to hydrostatic pressure changes is very slight (e.g. 0.1 ppm/atmosphere variation in wave velocity for a quartz SAW substrate) and so it can be neglected in most applications. However, changes in the density of the fluid medium in contact with the AW device surface caused by pressure variations can result in significant changes in the wave amplitude and velocity (more so in the case of gases as liquids are highly incompressible) [4.15]. AW devices which have primarily in-plane (e.g. shear horizontal) wave displacements are less affected than those having longitudinal or shear vertical displacement components. As with temperature effects, the pressure-related changes to the output can be compensated for by use of a reference sensor and signal subtraction.

The ambient pressure can also indirectly affect the base line signal of an AW sensor. One way is through its affect on the rate at which heat is dissipated from the device, which in turn affects the device temperature, hence the AW velocity. However this effect is small as the power dissipation in the devices is typically in the mW range and also because majority of the heat transfer is via conduction. The pressure also affects adsorption, desorption, and condensation on coated devices. A high pressure change can perturb the stable concentration of sorbed species (e.g. water) on the sensor surface. Although this implies a pressure-related transient, it is actually due to a change in partial pressure of sorbed species in the contacting vapour phase.

4.4.3 Flow-rate effects

These effects are mainly a concern for vapour sensing applications, where it is often necessary to flow the vapours to be monitored over the AW sensors. The air-flow rate can affect both the sensor base line signal and the apparent response time of the sensor. The baseline signal is affected due to the air flow over the device that can cause cooling and hence a small shift in device temperature and hence wave velocity. This is not

really a problem at low flow rates or if it is kept constant. To control the effect of the flow rates on the apparent response time, the cell that contains the sensor has to be carefully designed, as its finite volume affects the flow rate through it and hence the response time. The type of flow (laminar or turbulent) which again depends on the flow rates and cell geometries also has an affect on the apparent response time. Since the flow rate effects are mainly concerns for the vapour phase sensing it is not discussed here in detail as the work in this project is in the liquid phase and flow rate effects are not an issue.

4.4.4 Packaging considerations

All AW sensor devices have to be packaged in order to be used, and the best packaging method is highly dependent on the application intended for the sensor. The sensor package performs several critical functions including: provides a mechanical mounting point for the device; provides an electrical interface to the device; provides access to the measurands; and provides a heat sink and/or temperature-controlled platform for the sensor. Optimisation of the package for one of these criteria can adversely affect one of the other concerns. Thus the design of the package requires almost as much effort as the design of the AW sensor itself with the packaging considered at earliest stages of the device development.

With AW chemical sensors, the package often defines the volume of the cell that holds the analyte around the device. As discussed earlier, it is appropriate to minimise the dead volume of the cell for improved sensor response times. Furthermore the package material should be able to withstand the operating environment of the sensor which of course is the case with the cell itself. Here the cell was made of PTFE, as discussed earlier, which is in contact with the liquid analyte. PTFE has high chemical inertness, large temperature range (-50°C to 260°C), outstanding “antistick” characteristics (easily cleanable) and non contaminating properties making it very suited to application in aqueous solution.

The package also plays an important part in thermal management of the sensor device. The package should allow discharge of the heat generated by the sensor; hence a package material with good thermal conductivity would help. Here the sensor is mounted on aluminium pins close to the transducers, which help in this thermal grounding.

The physical attachment of the device depends on a number of factors, including the nature of the acoustic mode and the sort of environment with which the device is to interact. One aspect often neglected during packaging is the thermally-induced stresses that can be imposed on the acoustic device as a result of thermal expansion coefficient mismatch between the sensor and package. Hence, as mentioned earlier, the use of packaging materials with similar expansion coefficients is effective. However this can be difficult and costly, therefore “single-point” sensor mounting schemes that fix only a single edge or corner of the device can overcome thermal stresses. This method of single-point mounting was performed here.

Although more care is taken when mounting devices that have acoustic modes causing motion on both faces of the substrate, it was decided to prevent direct contact of the device to the mounting PCB to prevent coupling of any bulk waves into the PCB. The PCB package was carefully designed to allow alignment of the devices/cell, tracks widths and spacing appropriately designed to maintain the impedance.

4.5 Conclusions

This chapter describes the fabrication details for the SH-SAW sensors namely; mask generation, metal selection and deposition, photolithography technique, up to final wafer dicing and single device mounting. After careful consideration of all the issues, the wafers were fabricated using a well developed single mask wet-etch process with gold as the metallisation layer. Also discussed are the various measurement systems for two-port devices detailing all the various instruments and measurement setups, along with the advantages and disadvantages of these setups.

The network analyser setup used to do the RF characterisation of the SH-SAW devices is described and the characterisation procedure of in terms of the S parameters has been presented. The characterisation results showed good correlation to the anticipated theoretical design such as the resonant frequency of around 61 MHz, input impedance of transducers almost equal to 50 Ω and insertion losses of approximately 10-15 dB. Following this characterisation the signal generator/vector voltmeter setup used for experiments with liquid analytes is introduced. Finally, the sensor environment and its control are discussed signifying the importance of shielding the unwanted external effects. The next chapter details the characterisation of the fabricated devices followed by various experiments with different analytes.

4.6 References

- [4.1] M. Hatzakis, Canavello, B. J and Shaw, J. M, Single-step optical lift-off process, *IBM Journal of Res. Develop.*(1980), pp. 452-460.
- [4.2] M. J. Vellekoop, *A smart Lamb-wave sensor system for the determination of fluid properties*, PhD Thesis, Delft University, The Netherlands (1994).
- [4.3] A. A. Oliner, *Acoustic Surface Waves*, Springer-Verlag Berlin Heidelberg New York (1978), pp. 316-324.
- [4.4] J. W. Gardner, V. K. Varadan and O. O. Awadelkarim, *Microsensors MEMS and Smart Devices*, Wiley (2001), pp. 345-358.
- [4.5] C. Campbell, *Surface Acoustic Wave Devices and their Signal Processing Applications*, Academic Press, New York (1998).
- [4.6] I. D. Avramov, Analysis and design aspects of SAW-delay-line-stabilised oscillators, *Proceedings of the 2nd Int. Conf. on Frequency Synthesis and Control*, London (April 1989), pp. 36-40.
- [4.7] J. W. Gardner, V. K. Varadan, O. O. Awadelkarim, *Microsensors MEMS and Smart Devices*, John Wiley and Sons Ltd (2001), pp. 337-346.
- [4.8] Hewlett Packard, Test and Measurement application note 95-1 – S parameter techniques for faster more accurate network design, URL: <http://www.hp.com/go/tmappnotes>
- [4.9] Agilent Technologies, User's guide for Network Analysers 8753ET and 8753ES, part number 08753-90472 (July 2000).
- [4.10] J. Kondoh, and S. Shiokawa, New application of shear horizontal surface acoustic wave sensors to identifying fruit juices, *Jpn. J. Appl. Phys.* Vol. 33 Part 1 No. 5B (1994) pp. 3095-3099.
- [4.11] D.S. Ballantine, R.M. White, S.J. Martin, A.J. Ricco, E.T. Zellers, G.C. Frye, H. Wohltjen, *Acoustic Wave Sensors Theory, Design, and Physico-chemical Applications*, Academic Press (1997).
- [4.12] A. J. Ricco and S. J. Martin, Multiple frequency SAW devices for chemical sensing and material characterization, *Sensors and Actuators*, B10 (1993), pp. 123-131.
- [4.13] J. F. Alder, C. G. Fox, A. R. M. Przybylko, N. D. D Rezgui and R. D. Snook, *Analyst* 114 (1989), p. 1163.

-
- [4.14] H. Wohltjen, D. S. Ballantine and Jr. N. L. Jarvis, *Chemical Sensors and Microinstrumentation*, *ACS Symposium*, Series 403, ACS: Washington, DC (1989), pp. 157-175.
- [4.15] H. Wohltjen and R. E. Dessy, Surface acoustic wave probe for chemical analysis I. Introduction and Instrument Design, *Analytic Chemistry*, Vol. 51 (9) (1979), pp. 1458-1475.

CHAPTER 5

SH-SAW characterisation and experimental results

5.1 Introduction

In the previous chapter the various measurement techniques were explored and the setup used for the RF characterisation of the SH-SAW sensors detailed. This chapter, presents the experimental procedures and details of all the experiments performed using the SH-SAW devices as liquid sensors. The initial characterisation of the sensors such as effect of temperature is described followed by the use of the sensors as an electronic tongue to discriminate between different liquid samples.

5.2 Characterisation of the SH-SAW sensors

The measurement systems used for the RF characterisation of the SH-SAW devices were described and the characterisation results were presented in chapter 4. From this RF characterisation the essential parameters to operate the SH-SAW devices as sensors in the liquid media using the signal generator/vector voltmeter setup (detailed in chapter 4) were obtained. The following sections describe the procedures for experiments performed with the SH-SAW sensors in different liquid analytes, using the signal generator/vector voltmeter setup.

5.2.1 Measurement of the temperature coefficient

The measurement of the temperature coefficient of the SH-SAW device substrate with a liquid loaded on the surface is important for evaluating the detection limit. The

temperature coefficient of frequency (TCF) was measured with the SH-SAW sensor and the signal generator/vector voltmeter setup. The sensor was loaded with chilled distilled de-ionised (DI) water at approximately 10°C by injecting approximately 60µl of it into the liquid cell using a micro-pipette (Gilson Pipetman P200). The temperature of the DI water was monitored using a thermocouple wire with a digital output of the temperature value. The temperature was increased through ambient up to about 60°C with the aid of a commercial Dri-Bloc™ (DB-2D) heater.

The readings from the vector voltmeter were carefully taken at regular intervals of temperature increment. The shift in phase as a result of temperature change measured using the vector voltmeter for each delay line was related to the velocity shift and hence a frequency shift as shown below.

$$\frac{\Delta f}{f} = \frac{\Delta v}{v} = \frac{l}{d} \frac{\Delta f}{f} \quad (5.1)$$

where Δf is the phase shift in degrees, v is the phase velocity of the SAW, f is the operating frequency, l is the length of liquid in contact with sensing area and d is the acoustic path length between the input and output IDTs (as described in chapter 3). The phase shift between the two delay lines was also measured and related to the frequency shift according the following relationship.

$$\frac{v\Delta f}{2fl} = \frac{\Delta v}{v} = \frac{l}{d} \frac{\Delta f}{f} \quad (5.2)$$

Figure 5.1 shows the experimental results with the frequency shift on both the shorted and free delay lines and the differential frequency shift. The TCF computed from the results to be approximately -30 ppm/°C on each delay line; however that of the differential frequency reduced to only -0.2 ppm/°C. Therefore, the temperature effect is dramatically reduced by detecting the differential signals.

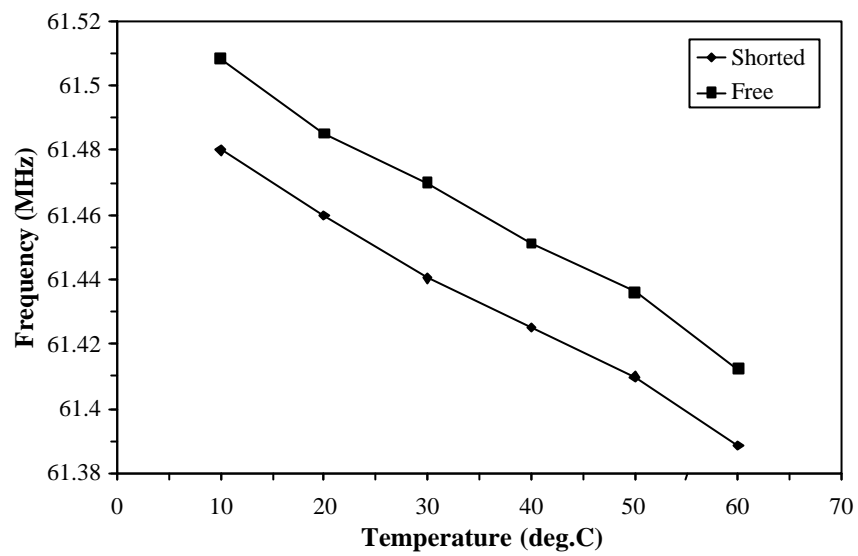


Figure 5.1 Temperature characteristics of the SH-SAW on 36YXLT (note that slopes are almost identical)

5.2.2 Effect of liquid volume loaded on the sensor surface

Using the same vector voltmeter setup with the SH-SAW devices controlled at a steady temperature of $30 \pm 0.1^\circ\text{C}$, DI water was loaded into the liquid cell in increments of $10\mu\text{l}$ between each measurement, using a micro-pipette. The phase shift and attenuation between the input and output of each delay line was measured and the results are displayed in Figure 5.2.

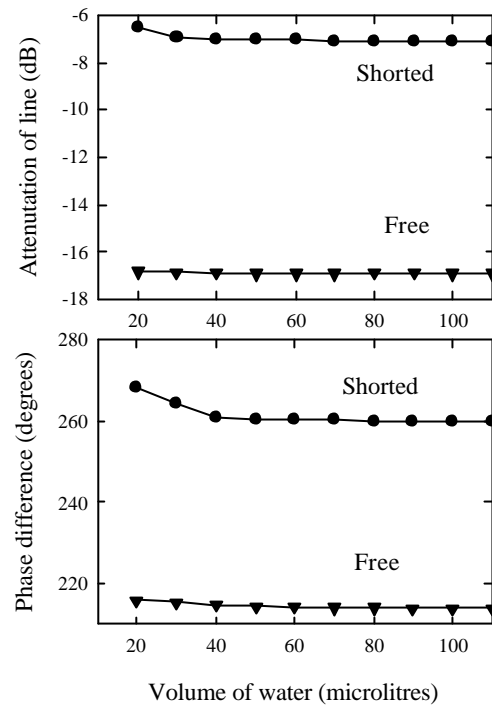


Figure 5.2 Effect of the volume of liquid loading on the attenuation and phase shift

From the results it was seen that above 40 μl the amount (volume) of liquid loaded on the surface of the sensor has negligible mass loading effect on output signals from the sensors; so immediate liquid evaporation should not affect the readings.

5.2.3 Acoustoelectric interaction for relative permittivity

The sensors were used to measure the electrical properties (conductivity and permittivity) of solutions and the approximate perturbation theory used to compare the results. The same signal generator/vector voltmeter setup was used, with the input IDTs of each delay line fed with the operating frequency signal from the signal generator and amplitude ratio and phase difference between the output IDTs of the two delay lines monitored using the vector voltmeter. The fractional velocity shift $\Delta v/v$ and attenuation change $\Delta a/k$ of the SH-SAW is determined from the phase difference Δf and amplitude ratio A_f/A_s (subscripts f and s represent the free and shorted delay line, respectively) according to equations (5.3) and (5.4)

$$\frac{\Delta v}{v} = \frac{v\Delta f}{2fl} \quad (5.3)$$

$$\frac{\Delta a}{k} = -\frac{v \ln(A_f/A_s)}{2pfl} \quad (5.4)$$

where Δf is the phase shift in degrees and A_f/A_s the amplitude ratio between the free and shorted delay lines, f is the operating frequency, v the phase velocity of the SAW, l is the sensing (or interaction) length between the waves and liquid.

Using the same arrangement as the other experiments and temperature controlled at approximately 25°C measurements were performed on solutions with known permittivity values (values at 25°C [5.1]). Figure 5.3 below shows the plot fitted to the perturbation solution (see chapter 3) and the experimental results using non-conductive organic solutions of known permittivity values.

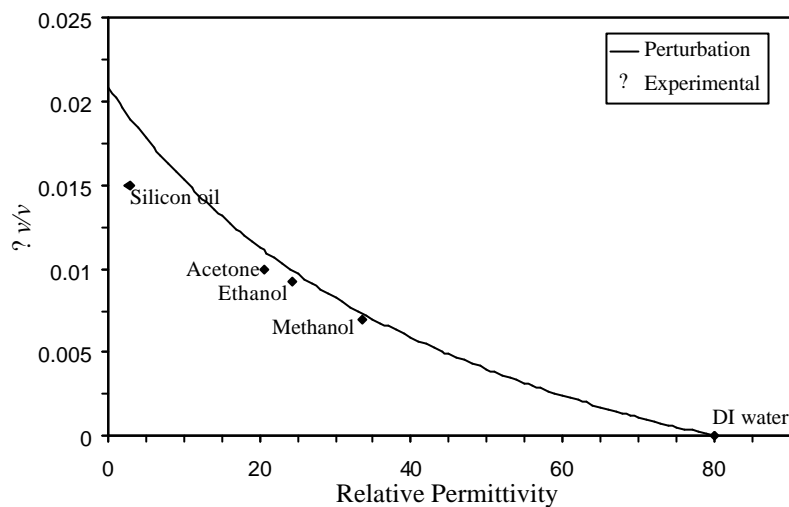


Figure 5.3 Velocity shift as a function of relative permittivity at 60 MHz

Having characterised the sensors in terms of temperature effect, effect of liquid loading and the ability to determine the properties of the liquids using the approximate perturbation theory, the sensors were employed as taste sensors (electronic tongue). The next section details the experiments performed with the SH-SAW sensors being used to discriminate between the basic tastes, in a “quasi” electronic or smart tongue.

5.3 SH-SAW sensors to classify the basic tastes

Chapter 1 covered the sense of taste and the concept of the basic taste. Here the SH-SAW sensing system is employed to classify the four basic tastes of sour, salt, bitter, and sweet that originate from the different chemosensory receptors on the tongue called the papillae (see chapter 1 for details). The compounds with distinct single basic tastes used to represent the typical ground tastes are sodium chloride (salty), hydrochloric acid (sour), sucrose (sweet), and quinine (bitter).

5.3.1 Classification of solutions of basic taste

Aqueous solutions of NaCl, HCl, and sucrose with 0.1 M concentration and a quinine solution of 1.3×10^{-4} M were prepared in distilled deionised (DI) water at the Chemistry Department, University of Warwick. Distilled DI water was used as the reference liquid and the setup temperature regulated at $30 \pm 0.1^\circ\text{C}$ using a commercial Dri-Bloc™ (DB-2D) heater. The devices were setup inside the heater and the temperature allowed to settle for approximately 10 minutes before the introduction of distilled DI water (60 μl) into the liquid cell with the aid of the micro-pipette (Gilson Ppetman P200). After stabilisation the readings from the vector voltmeter were recorded and the distilled DI water extracted from the cell which was then cleaned and dried using compressed air before the introduction of the sample liquid. The sample liquids were introduced after allowing the sensor to stabilise thermally for about 10 minutes. The measurements were repeated by randomly introducing the samples to the sensors. The sensing surface was cleaned and dried after every measurement using a wash cycle of distilled DI water, and the sensors allowed to stabilise thermally before the next measurement. The baseline signal (without a liquid loading) between the measurements at the stabilised temperature was examined and it was almost constant, hence indicating good repeatability in the replicate measurements.

Five replicate measurements on each sample were randomly performed with DI water as the reference liquid and the output signals analysed using principal components analysis (PCA) technique, a linear, supervised, non-parametric pattern analysis method. The output signals (phase difference and attenuation ratio) from each of the sensor's delay line were used as the input data for the principal component analysis. The principal component analysis was performed by Matlab® software in which a small program was written (see Appendix A) to perform the analysis. Figure 5.4 shows the PCA plot for the classification of the basic taste solutions.

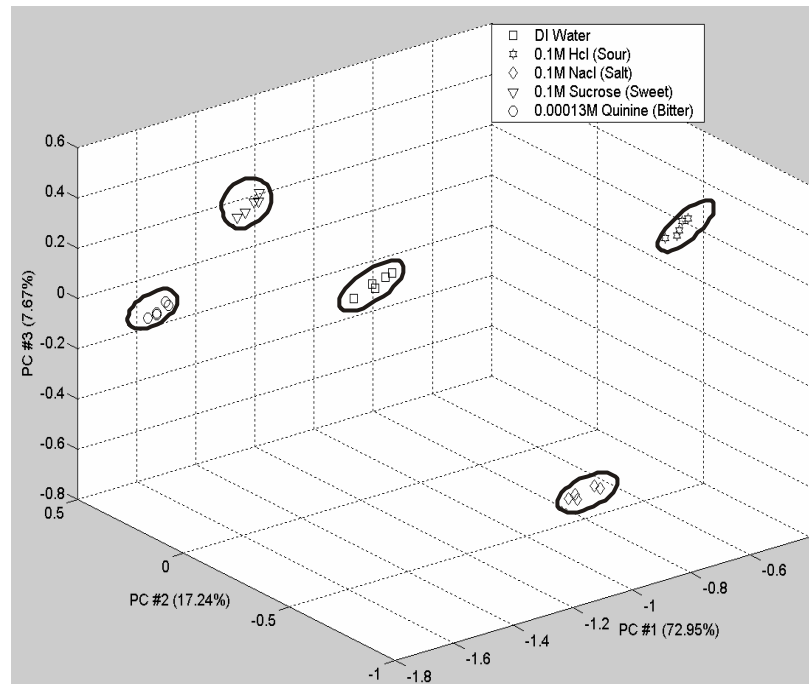


Figure 5.4 3D PCA plot for the four basic taste solutions and DI water as the reference

The plot shows that excellent separation was achieved and the sensors were able to classify all the solutions according to their taste. However, the concentration of the solutions used for this experiment was relatively high and thus further experiments were performed by diluting the solutions to determine the detection limit of the sensors.

5.3.2 Dilution of the taste solutions to determined the limit of detection

The aim of this experiment was to determine the effect of diluting the different taste solutions using DI water and determine the detection limit of the sensors in terms of its basic taste. The four solutions were diluted by a factor of 2^n with the exponent n varied from 1 to 5. Each time the volume of DI water was increased by a factor of 2^n and added to a fixed volume of the original solutions used in the experiment above. The measurements were repeated randomly as before with a cleaning and drying cycle between every measurement. The concentrations were reduced from 0.1M to 5.9×10^{-3} M for the NaCl, HCl and sucrose solutions and from 1.3×10^{-4} M to 7.6×10^{-6} M for the Quinine solution.

Figure 5.5 shows the PCA plot for the classification of the lowest concentration solutions in the dilution test. Again from this plot clear separation of the different taste

solutions can be seen. Knowing the diluted concentrations of the solutions we can approximate the detection limit of below 0.1%.

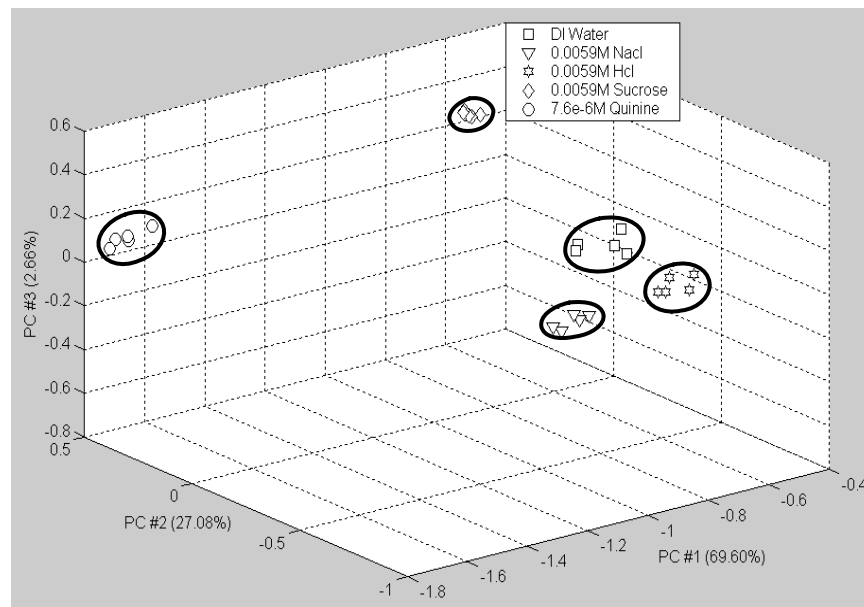


Figure 5.5 3D PCA plot for the lowest concentrations of the diluted sample solutions

Figure 5.6 shows a 2D PCA plot for all the concentrations of the different taste solutions and DI water as the reference. From the plot a trend can be noticed; as the concentration of the solutions was reduced by dilution the individual clusters of the different tastes tended towards that of the DI water.

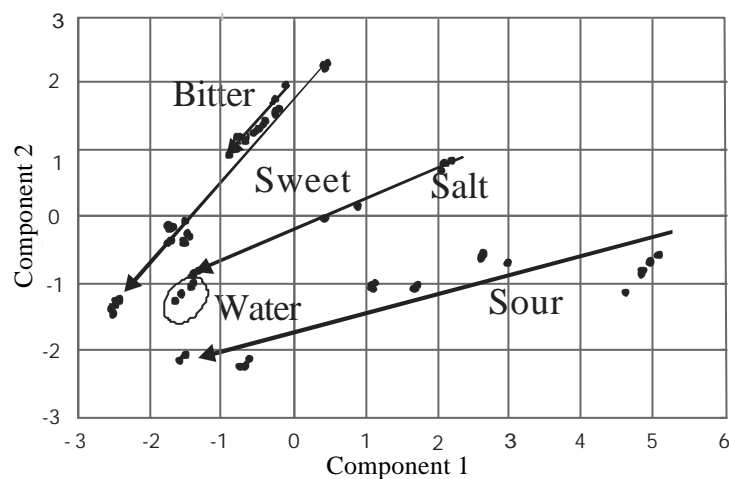


Figure 5.6 2D PCA plot for the dilution testing of the four different taste liquids

From the results the limit of detection of the different tastes was typically less than 1 mM of sweet, salty and sour and 1 μ M of bitter. Further dilution would be required to precisely locate the LOD as there was still separation between the samples.

5.3.3 Determination of the electrical properties of the taste samples

Using the same setup and following the same experimental procedure as for the experiments above the amplitude ratio and phase difference between the two delay lines of the sensor were measured using the vector voltmeter. DI water was used as the reference liquid. The velocity shift and attenuation change were determined from the phase difference and amplitude ratio between the two delay lines, respectively, in accordance to equations (5.3) and (5.4).

By applying equations (3.91) and (3.92) of acoustoelectric perturbation (see section 3.5.2 in chapter 3 for details) and the permittivity-conductivity chart (Figure 3.14 chapter 3) to the measured velocity shift and amplitude ratio, the conductivity and permittivity of the samples was determined. Figure 5.7 shows specifically the results for the sour (HCl) and salty (NaCl) solutions plotted on the permittivity-conductivity chart. It was determined as expected, that as the concentration of the solutions decreases the conductivity decreases with a small increase in permittivity. The electrical conductivity of the HCl solutions varied approximately from 1.4 to 3.7 S/m and the electrical permittivity between 76 and 74, with increasing concentration. The conductivity of NaCl increased from 0.08 to 1.1 S/m with increasing analyte concentration. The sweet (sucrose) and bitter (quinine) samples are very weak electrolytic solutions with conductivities close to that of DI water (i.e. practically zero) and so almost no change in conductivity with a change in concentration was noticed. So the major parameter here is the change in conductivity as expected, but conductivity alone cannot separate out the samples as a x % of bitter would equal y % of salty etc. Hence a conductivity sensor cannot solve the taste problem.

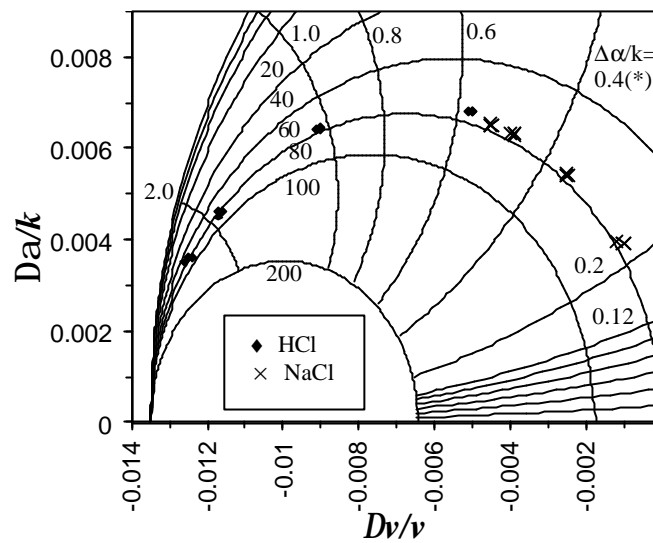


Figure 5.7 Experimental results for salty (NaCl) and sour (HCl) solutions of different concentrations on the permittivity-conductivity chart

5.4 Use of the SH-SAW sensors with real samples

The experiments already performed have used synthetically prepared samples, so next step was to use the sensors to discriminate between real samples, such as juices and milk, to confirm that our generic fingerprint approach in which the need for biochemical selective layers, normally used in liquid sensors, is removed. This section covers the experiments performed starting with the sensors applied to very different analytes such as orange juice and milk followed by concentrating the measurements into the different kinds of milk and the bacterial growth in fresh milk.

5.4.1 Experiment to discriminate between orange juice and fresh milk

The same setup was used as with the taste experiments. Fresh samples of orange juice and full fat milk (Tesco brand) were thermally stabilised to room temperature before performing the experiments. The sensor setup was placed in the heater as before and temperature controlled to $30 \pm 0.1^\circ\text{C}$ and DI water used as the reference liquid. Replicate measurements were taken at random with the sensors and liquid chambers cleaned and dried between every measurement. Results showing the discrimination of different liquid samples using principal components analysis (PCA) are presented in Figure 5.8. The principal components are derived using the four variables (sensor

responses) measured using the vector voltmeter, which are the attenuation ratio and phase difference on the shorted and free delay lines.

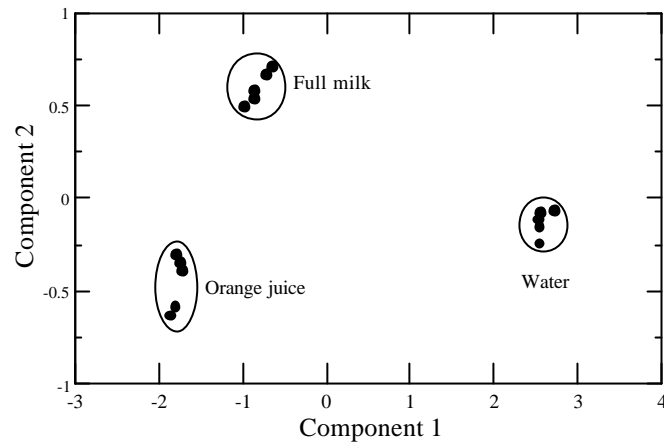


Figure 5.8 PCA plot of different liquids showing clear linear separation

The plot shows that excellent linear separation of the liquids was achieved proving the principle of the generic approach of liquid sensing without the presence of a selective layer. To determine the discrimination power of the sensors further experiments were performed with milk samples of different fat content as detailed below.

5.4.2 Discrimination between full-fat, semi-skimmed and skimmed milk

Commercial milk samples (Tesco brand) of different fat content (i.e. full-fat, semi-skimmed and skimmed milk) were purchased and tested using the SH-SAW sensor. The fat content in the milks is typically 4% in full-fat milk, 2% in semi-skimmed and virtually no fat in skimmed. 60 μ l of each of the milk samples was randomly dispensed into the liquid cell using the micro-pipette and five replicate measurements for each sample performed. The sensing surface and liquid cell were washed using warm ($\approx 30^\circ\text{C}$) DI water between each measurement. A PCA plot of the different milk samples with 100% linear separation is presented in Figure 5.9. In this case most of the variance is accounted for in the first principal component.

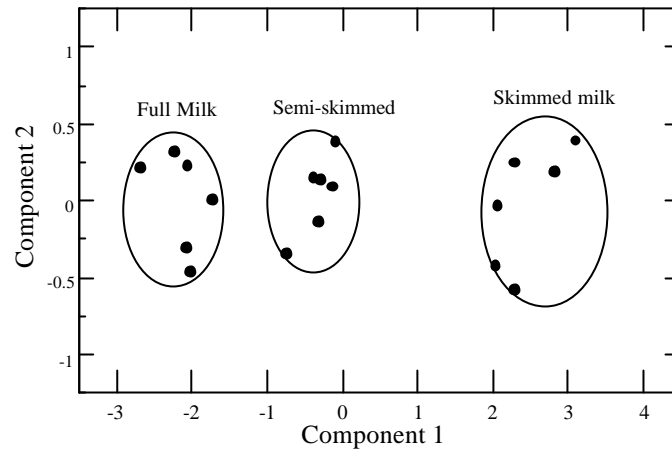


Figure 5.9 PCA of different milks showing good discrimination

An attempt to pre-process the data to improve the separation between the different milk samples is made, by taking both the difference and ratio of the attenuations and phase differences on each of the delay lines, which also reduces the number of parameters involved to simply two. Then a Fisher t-test is performed on the sample means of two populations at a time (e.g. skimmed and semi-skimmed milk), for testing the equality of the two population means based on the independent samples from the two populations. The test statistic is given by

$$t = \frac{(\bar{x}_1 - \bar{x}_2)}{S_p \sqrt{\frac{1}{n_1} + \frac{1}{n_2}}} \quad (5.5)$$

where \bar{x}_1 and \bar{x}_2 are the sample means, n_1 and n_2 the sample numbers and S_p^2 is the pooled estimate of the population standard deviation of the Fisher t-test and is given by

$$S_p^2 = \frac{(n_1 - 1)S_1^2 + (n_2 - 1)S_2^2}{(n_1 + n_2 - 2)} \quad (5.6)$$

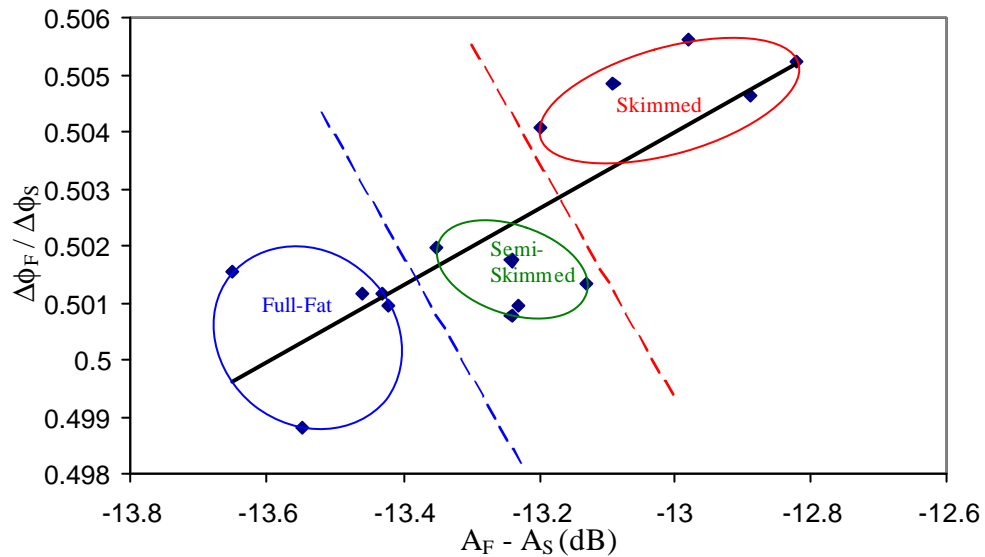
where S is the adjusted standard deviation (uses $(n - 1)$ rather than n).

The tests were performed on the different milk data and the results are displayed in Table 5.1 as Fisher t values for each of the variables (attenuation and phase on delay lines) for the pre-processed data, where ‘s’ denotes skimmed milk, ‘ss’ – semi-skimmed milk and ‘ff’ – full fat milk. The confidence level is found from standard statistical tables and for the eight degrees of freedom ($n_1 + n_2 - 2$) here, is better than 99.5% ($t = 4.5$) in several cases. Thus, having computed all the t values, the highest value of **10.23** indicates the best separation between the different samples and the associated pre-processing parameter was chosen to plot the data.

Table 5.1 Fisher t values on pre-processed milk data to determine the best separation combination

Pre-processing parameter				
Fisher t values	AF-AS	PF-PS	AF / AS	PF / PS
s - ss	3.16	4.31	-0.11	10.23
ss - ff	4.74	-1.19	-1.89	1.16
s - ff	6.25	1.53	-1.56	7.47

This corresponds to a plot of the phase difference ratio ($\Delta\phi_F / \Delta\phi_S$) versus the amplitude difference ($A_F - A_S$) in dB shown in Figure 5.10. The solid line represent a least squares regression through the data points whilst the two dashed lines are orthogonal to the regression line and represents two hyper-planes that can be used to classify the milk samples with a simple parametric test.

**Figure 5.10** Discrimination of different milks using the best combination of pre-processed data

As stated above the best combination for separation is the difference ratio ($\Delta\phi_F / \Delta\phi_S$) versus amplitude difference ($A_F - A_S$) in dB, where the amplitude difference in decibels is essentially the log of the ratio of the two signals. This was presented in chapter 3 where it was suggested that by taking the ratio of the two signals removes the common external effects hence giving the best separation as seen above.

5.4.3 Dilution of full-fat milk using DI water to determine the detection limit

In this experiment full-fat milk (4% fat) was diluted by adding DI water it. The concentration of the milk was diluted in stages by a factor of 2^n where n varied from 1

to 6. Each time the volume of DI water was increased by a factor of 2^n and added to a fixed volume of whole milk. Equal volumes of the mixtures ($60 \mu\text{l}$) were dispensed into the liquid cell using a micro-litre syringe and the device and cell cleaned and dried after each sample was tested using warm DI-water. The measurements were repeated randomly and 5 replicate measurements were conducted on each sample. Results are shown in Figure 5.11 for the most sensitive parameter that is the attenuation of the free delay line, where the dilution step has been converted to the approximate percentage of fat in the milk where full cream milk is 4% and pure DI is 0%. From the graph, the limit of detection of the free delay line loss was estimated to be ca. 0.1% of fat content.

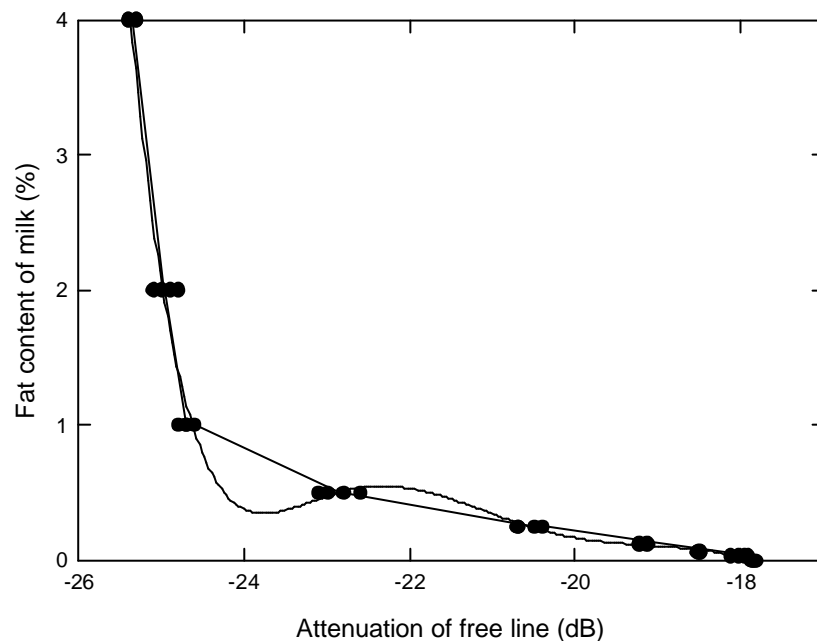


Figure 5.11 Effect of milk fat content on attenuation loss of 36YX.LT free delay line

5.4.4 Investigation of the freshness of full-fat milk samples

Here the experiment was conducted to investigate the freshness of whole milk samples. Fresh full milk was bought from the same supplier (Tesco) on five consecutive days and stored at $23.8 \pm 0.1^\circ\text{C}$ in glass-covered containers (removed from original packaging). They were stored at a higher temperature than normal (refrigerated) in order to accelerate the growth of bacteria and hence the process of the milk curdling. The measurements were then performed on the 5th day on all of the 5 samples. Again the samples were tested at random to obtain 5 replicate measurements of each sample for every day. The sensor and cell were washed out using warm DI water and dried

after each measurement. Amount of 60 μl of milk samples was dispensed onto the devices each time. Figure 5.12 shows five distinct clusters one for each day that the milk was tested.

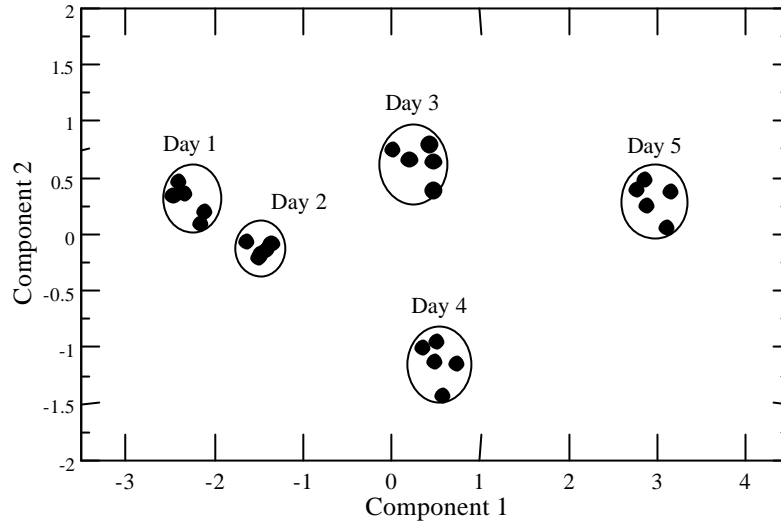


Figure 5.12 PCA of milk samples showing the effect of accelerated ageing

From the PCA plot above a clear discrimination in the milk samples as the bacteria growth enhanced over the days can be seen, however there is no information as to how much bacterial growth has occurred over this period and growth detection limit of the sensors. Thus, further experiments were performed using milk samples with known amounts of bacterial cells to determine the bacterial detecting limit of the sensing system.

5.4.5 Discrimination of fresh, bulling and bacterial loaded milk

Initial experiments were performed to detect the ability of the SH-SAW sensors to discriminate between a set of fresh, bulling and two other milk samples with different amounts of bacterial loads. These samples of milk were obtained from the Biological sciences department at Warwick and were prepared by a final year undergraduate student Mr. Peter Newton. The bulling milk sample can be explained in terms of the amount of hormone progesterone present in the milk. Progesterone is a hormone produced by the cow during ovulation and can be detected from samples of milk. Progesterone rises and falls during different periods of the cow's reproductive cycle. A typical cycle is around 21 days in duration. For the majority of the cycle progesterone is at higher levels and will drop a few days before the cow comes in to oestrus and starts

bulling. The progesterone level is at its lowest when the cow is actually bulling and remains low for around 4 to 6 days after when it will start rising again. The progesterone will rise to a peak before falling sharply a couple of days before the next oestrus. Since progesterone follows a known pattern it is possible to take samples from a cow and predict when the next oestrus is likely and thus when it is best to inseminate. This test would be very useful and economical to dairy farmers.

Three samples each of fresh milk, bulling milk (the samples are named as fresh and bulling milk however they are samples from the same cow at different points in the oestrus cycle) and one sample each of the two different bacteria (*S. uberis* 10 001) loaded milk (10^5 colony forming units per ml (cfu/ml)) and (10^7 cfu/ml), were run through the sensors at random as with the other experiments performing five replicate measurements on each sample. Figure 5.13 shows a PCA plot of the results obtained from this experiment and tight distinct clusters of the 4 common groups (fresh, bulling, lower bacterial load and higher bacterial load) with three samples in each were obtained with good separation between them. It also highlights changes in milk composition (in this case due to the oestrus cycle) affects the data from the sensors. It would be useful to examine samples from many cows in different herds which would provide a wide range of milk compositions due to factors such as genetic variation and varying diets, as well as different stages in the oestrus cycle. Thus the effect of the bacterial load on the data of the sensors has been shown however the colony forming units per ml (cfu/ml) were relatively high and did not determine the true detection limit of the sensors. As a result another experiment which is detailed in the next section was setup.

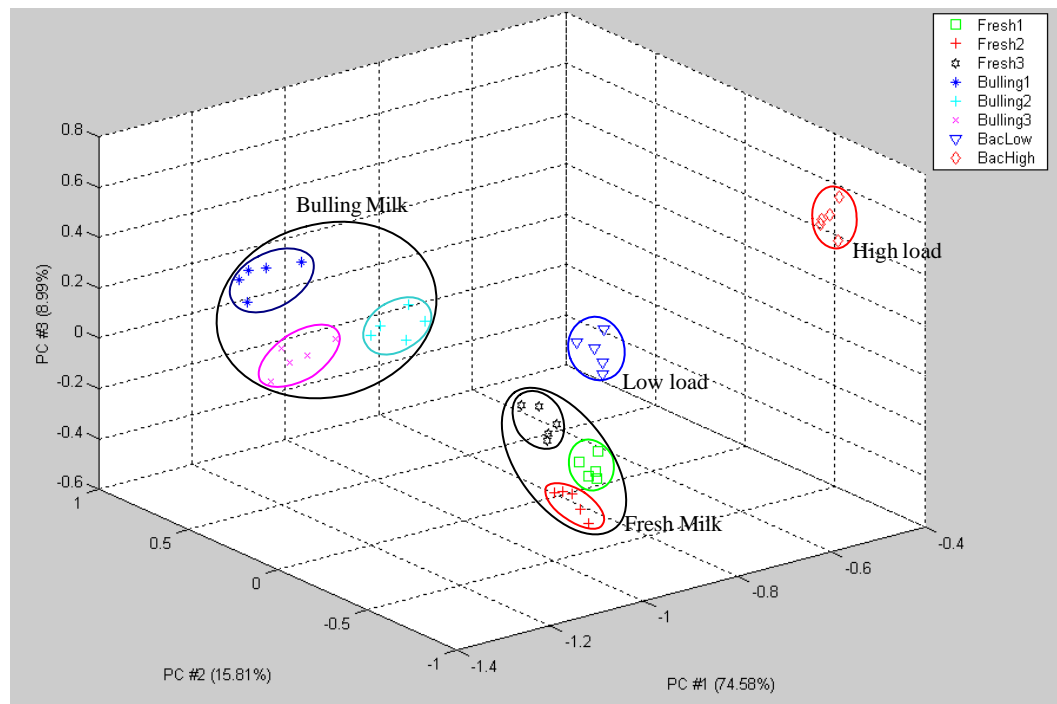


Figure 5.13 PCA plot showing the effects of milk from different points in the oestrus cycle and containing different bacterial loads on the SH-SAW sensors.

The samples used here (fresh, bulling, lower load and higher load) were frozen (-80°C) and the experiments repeated to see any effect in the samples due to freezing. The results were treated along with the data for the freshly prepared samples. The results are presented in Figure 5.14.

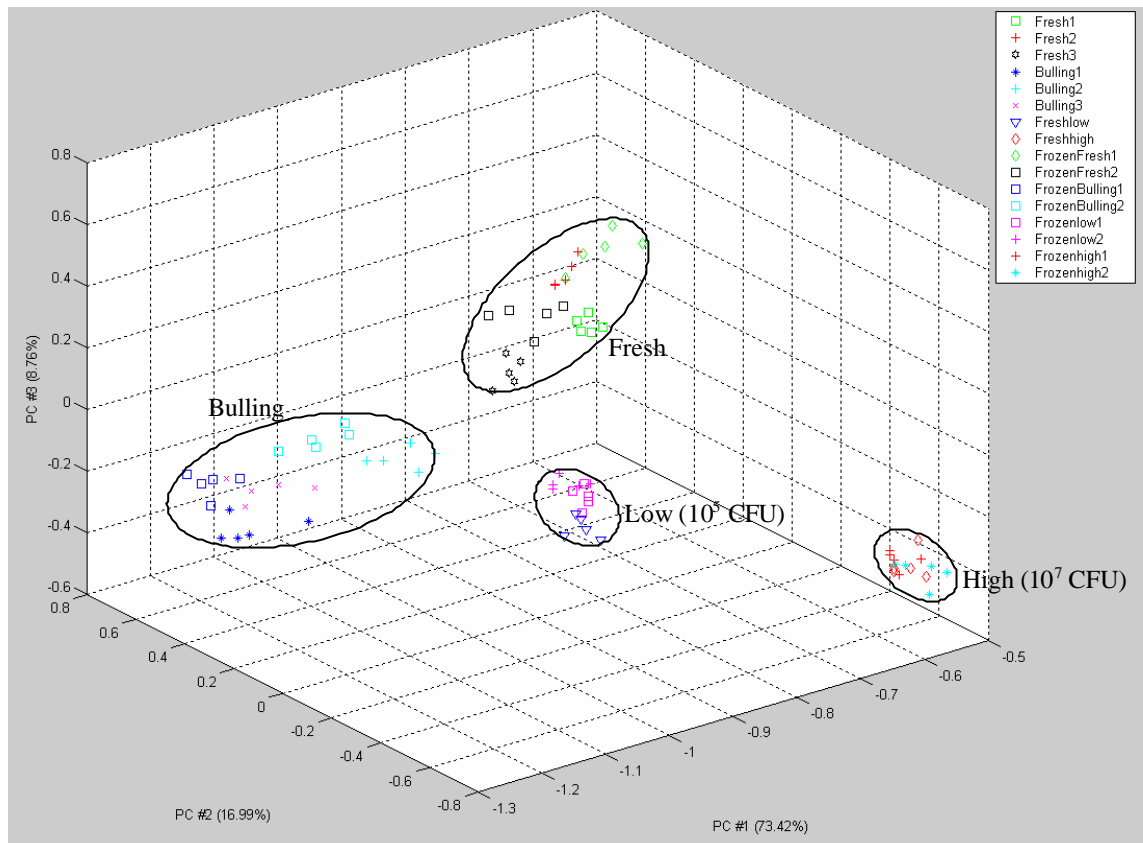


Figure 5.14 PCA plot showing the effects of milk from different points in the oestrus cycle and containing different bacterial loads on the SH-SAW sensors (both freshly prepared samples and frozen samples).

The plot shows that frozen samples are acceptable for use with the sensors, as the frozen samples cluster with the comparable fresh samples, albeit not as tightly as when the samples remain unfrozen.

5.4.6 Analysis of milk samples with a range of bacterial loading

To test the sensitivity of the electronic tongue, dilution series were set up to dilute stocks of *S. uberis* 10 001 and *S. aureus* 072 to obtain a count of about 10 cfu/ml. These were then used to inoculate milk, and a samples were taken every hour (starting from 2 hours (to avoid the lag phase) to 9 hours) to get a wide range of cell counts to be analysed by the SH-SAW electronic tongue. The negative control had phosphate buffered saline (PBS) added (since the dilution series was made in PBS). The approximate cell concentrations obtained are given in table 5.2. Also, to see if the presence of cells (without any physiological effects) has an effect, a dilution series was made up in milk, and then frozen immediately. The dilution series gave a range of cell

concentrations, ranging from approximately 10^7 cfu/ml to 10^2 cfu/ml. All these samples were stored before analysis at -80°C .

Table 5.2 Approximate cell concentrations obtained for testing the sensitivity of the electronic tongue.

Time (hours)	<i>S. aureus</i> (cfu/ml)	<i>S. uberis</i> (cfu/ml)
2	5	2
3	40	8
4	80	53
5	800	350
6	4.85×10^3	3.7×10^4
7	4.7×10^4	7×10^4
8	2.27×10^5	3.73×10^5
9	2×10^6	3.03×10^6

Overnight cultures were grown up in uninfected frozen milk as standards to provide a controlled test. The strains used were *S. uberis* (10 000 & 10 001) and *S. aureus* (072 & 073) and after growing them the cultures were frozen to -20°C .

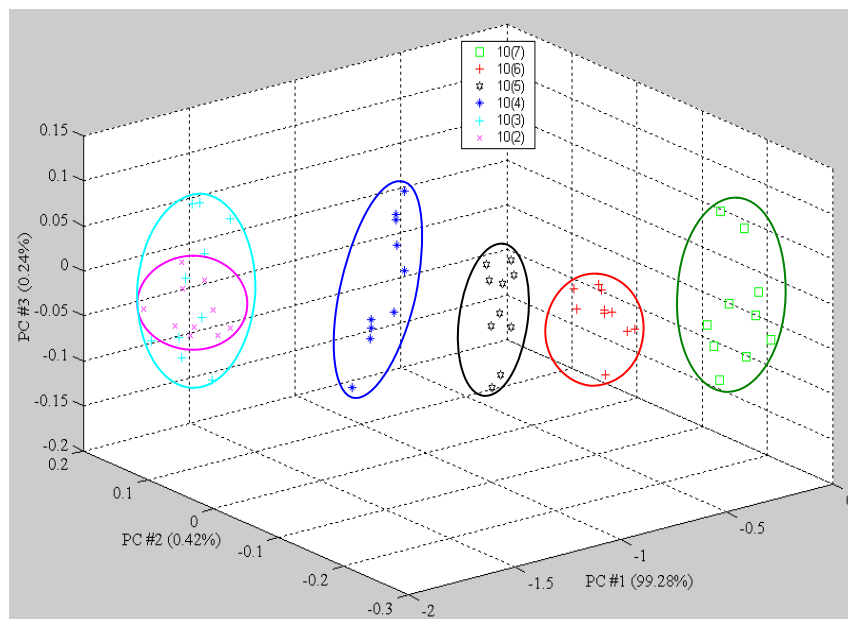


Figure 5.15 PCA plot showing the effect of bacterial (*S. uberis*) loading in milk on the sensor and its detection limit

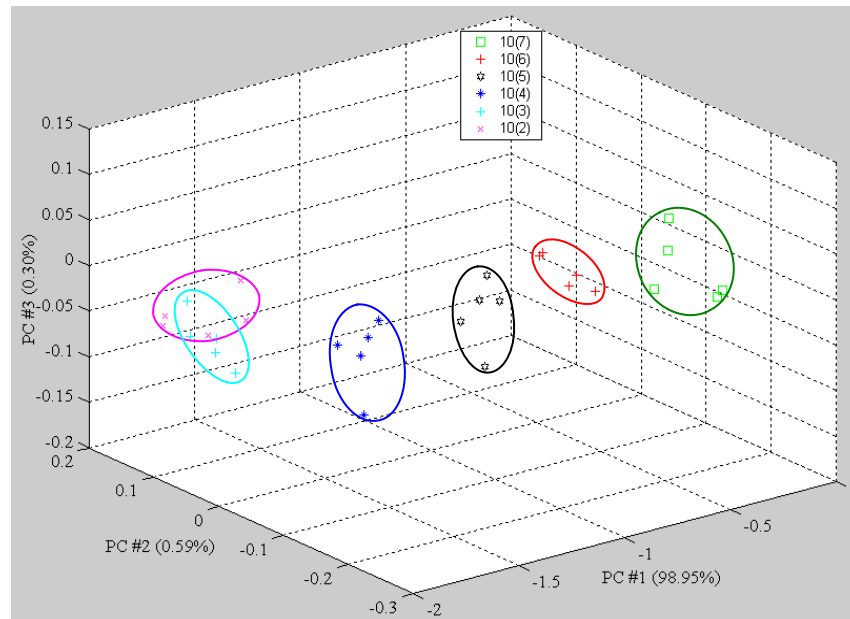


Figure 5.16 PCA plot showing the effect of bacterial (*S. aureus*) loading in milk on the sensor and its detection limit

It can be seen from both the PCA plots above (Figures 5.15 and 5.16) that the sensors were able to detect and distinguish between different levels *cfu/ml* of the different strains of bacteria down to 10^3 *cfu/ml*. The 10^2 *cfu/ml* and 10^3 *cfu/ml* clusters overlap and hence we can conclude that the limit of detect of the sensors to the bacteria is approximately 10^3 *cfu/ml*. In the case of biological applications lower levels of detection of the order of 10^2 *cfu/ml* and below are normally desired suggesting that the sensors would need to be coated to enhance the limit of detection, sensitivity and specificity to certain strains. The use of these sensors as a bio-sensor is attractive and this is discussed in chapter 8 as further work.

5.5.7 Testing of mastitic milk samples

Nine mastitic milk samples were also tested using the SH-SAW electronic tongue. All nine samples were from different cows, three contained coagulase-negative staphylococci, five contained *S. aureus*, and one contained *S. aureus* and streptococci. Three blanks were used. They were milk samples, frozen at -20°C , from two cows (from a different herd to the mastitic samples) and also a frozen sample from the bulk milk tank.

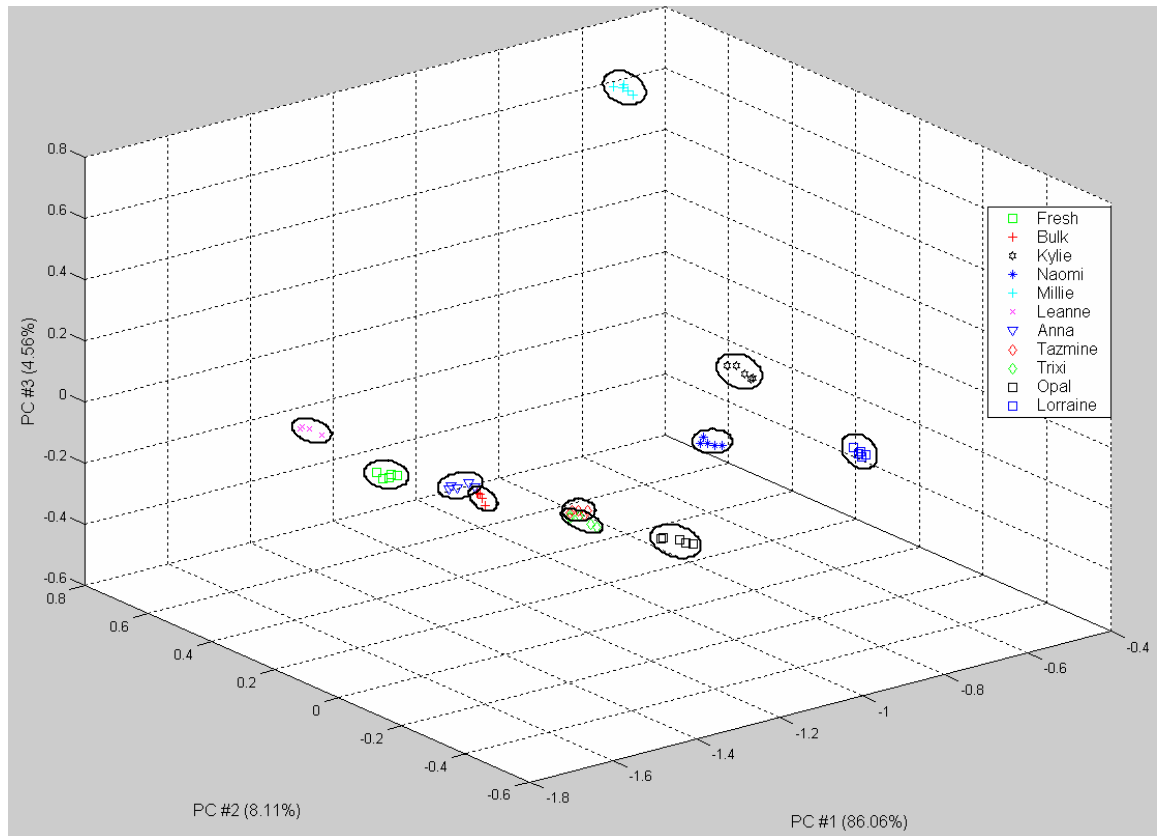


Figure 5.17 PCA plot for the different mastitic milk samples

It seems that there is no clustering of species in the data from the SH-SAW electronic tongue, although the replicates of each sample clustered very tightly. This could be an artefact of the data analysis – since, all the samples contained either *S. aureus* or coagulase-negative staphylococci, it could be that the PCA plot has ‘stretched’ data which is, in fact, much closer together. It would be very useful to obtain mastitic samples that contain a wide variety of species to give a clearer picture as to whether or not different species can be detected using the electronic tongue. Another important factor that must be addressed by future research is the number of bacteria present in the mastitic samples. This could be more difficult than just a straightforward viable count, since there will most likely be different species present, because of the normal bacterial flora of the udder. This may require more complex enumeration procedures, such as quantitative polymerase chain reaction (PCR). This is important, as it has already been shown that the bacterial load of a sample affects the output data from the SH-SAW electronic tongue.

It is difficult to draw conclusions from such a small data set and as mentioned before it would be useful to obtain a wide selection of mastitic samples from many

different herds, as it is clear that changes in milk composition (such as the oestrus cycle) affects the data. The output signals from the sensors are affected by conductivity of the milk samples (conductivity is greatly affected by bacterial loadings in milk etc. and conductivity tests are used for milk testing [5.2] and [5.3]). However, in a complex liquid such as milk there are many other potential sources of variation that could also affect the signal. This could equally be either a positive or a negative influence. It could be that this will allow the detection of other changes induced by a mastitic infection, and so improve diagnosis – this could be particularly important in the detection of sub-clinical mastitis, since measuring electrical conductivity alone has been shown to have only successfully detected 50% of sub-clinical cases [5.4]. Equally, it could be a negative influence, as the changes in the data due to the mastitis could be obscured by the detection of all sorts of other natural variation in the milk composition.

5.7 Conclusions

The S parameter characterisation results with the network analyser in chapter 4 were then used here to perform measurements using the vector voltmeter/signal generator setup to characterise the sensors using liquid samples. The principle of operation and ability to detect a variety of different liquids without a selective coating over the sensing area of the sensors has been proven. The use of the dual delay line setup to eliminate common mode effects such as the affect of temperature has been proven experimentally and through pre-processing of the data from the sensors.

The ability of the sensing system to discriminate between four basic tastes without the use of either electrochemical sensors or selective membranes has been demonstrated with the sensor responding to various physical parameters of the liquid, and so in an indirect rather than direct measure of taste. A detection limit of about 0.1% has been achieved. The theory of the electro-acoustic interactions has been used to relate the experimental results to electrical properties of the liquids under test and promising results have been achieved. Two physical parameters, conductivity or pH, were studied and cannot be used to classify uniquely both the type of taste and its concentration – whereas the four acoustic parameters can do so.

Furthermore, apart from using single synthetic samples each related to a single basic taste, the sensing system has also been used to analyse complex samples, such as cow's milk. The sensors have been used to discriminate between milks of different fat

content (skimmed, semi-skimmed and full-fat) as well as in a dilution test of full-fat milk where a very encouraging sensitivity figure of about 0.1% fat content was achieved. Promising results were obtained from the milk freshness test showing the possible application of the sensors as milk freshness indicators.

The ability to discriminate between different levels of sourness (indirectly measured through the bacterial growth) in milk samples, have been presented with a limit of detection of about 10^3 cfu/ml . The results imply that relatively subtle changes in taste can be measured as this is related to significant cellular damage due to the growth of bacteria. The sensors were also used to classify fresh milk samples and bulling milk samples from the same cow at different points in the oestrus cycle and encouraging results were achieved however this requires further work. Similarly in the experiment where mastitic milk samples from nine cows were run through the electronic tongue, although tight clustering and discrimination was achieved, further work is required to conclude meaningful results. All the data have been treated using principal components analysis showing that the sample vectors are simply linearly separable – demonstrating a basic pattern recognition problem. Thus there is scope to improve the discrimination power through the use of pre-processing (i.e. feature selection) and non-linear pattern recognition classifiers (e.g. support vector mapping). The next chapter covers the combination of the SH-SAW electronic tongue devices with electronic nose devices to realise an artificial flavour sensing system.

5.8 References

- [5.1] D. Dobos, *Electrochemical data, a handbook for electrochemists in industry and universities*, Elsevier Scientific Publishing Company Amsterdam-Oxford-New York (1975), pp. 105-132.
- [5.2] De Mol, R.M and W. Ouweltjes, Detection model for mastitis in cows milked in an automatic milking system, *Preventive Veterinary Medicine* 49 (2001), pp.71-82.
- [5.3] J. M. Musser, K. L. Anderson, M. Caballero, D. Amaya, and J. Maroto-puga, Evaluation of a hand-held electrical conductivity meter for detection of subclinical mastitis in cattle, *American Journal of Veterinary Research* 59 (1998), pp.1087-1091.
- [5.4] G. F. W. Haenlein, Advances in electronics are helping dairy farmers, Dairy management column, URL:
<http://ag.udel.edu/extension/information/dairycol/dmc2-99.htm>

CHAPTER 6

Combination of the electronic tongue and electronic nose

6.1 Introduction

A challenging problem in the food and beverage processing industries is the maintenance of the quality of food products, and consequently much time and effort are spent on developing methods for this. Panels of trained experts evaluating quality parameters are often used, which, however, entail some drawbacks. Discrepancy can occur due to human fatigue or stress, sensory panels are time consuming, expensive, and cannot be used for online measurements. The development of alternative methods to panels for the objective measurements of food products in a consistent and cost-effective manner is thus highly desirable. In chapter 1 the perception of flavour was introduced and how it is related to the senses of taste and smell. In this respect, the combination of artificial senses (taste and smell) has great potential to partly replace flavour panels, since the outcome will resemble a human-based sensory experience. This chapter details the design and characterisation of an artificial flavour sensing system comprising of SH-SAW devices (so called electronic tongue devices) and an array of chemFET (so called electronic nose devices). The aim of the study in this chapter is to demonstrate the ability of the combined system to discriminate different liquid samples that cannot easily be identified by the electronic nose or tongue individually. The design and operating principle of the chemFET devices is detailed followed by the description of the combined tongue/nose system setup used for the artificial flavour sensing.

6.2 MOS ChemFET sensors

There are, at present, several types of gas sensor technologies based upon a number of different operating principles, as discussed in chapter 1. A limitation of these sensors is the difficulty in amalgamating the gas sensitive materials within monolithic CMOS design. There are a number of sensor technologies that could be integrated with the control electronics inheriting many of the advantages of modern CMOS, such as low cost and high device reproducibility. An example of such devices are room temperature ($T < 100\text{ }^{\circ}\text{C}$) bulk CMOS chemFET sensors that could employ a conducting polymer film as the active (gate) material.

The use of FET sensors with polymer layers as chemicals sensors was first reported by Josowicz and Janata in 1986 [6.1]. The basic configuration of these sensors involves the metal (or polysilicon) gate of the FET being replaced with a conducting polymer gas sensitive layer. This layer is deposited directly on top of the gate oxide and the sensor response is related to a change in the work function between the polymer and the semiconductor. This in turn modulates the threshold voltage of the MOSFET. It is believed that the change of work function within the polymer is due to either a swelling effect where the polymer expands or contracts thus altering the average work function or due to an a change in the band structure of the polymer by the interactions between the polymer and the test vapour. These sensors are useful for electronic nose systems because of their ability to operate at room temperature hence their low power operation, and compatibility with CMOS processing that reduces the cost of fabrication.

6.2.1 Design considerations of ChemFET sensors

The sensors used here were designed by Dr. J. A. Covington for a doctoral research project at the University of Warwick 2001 [6.2]. The principle parameters considered in the development of these chemFET sensing structures were the operational mode, device dimension and the sensor electrode material.

6.2.1.1 Mode of operation

Many conventional sensors are operated at either constant voltage or constant current. The FET has a non-linear forward IV characteristic and can be operated in three different regimes, sub-threshold ($V_{GS} < V_T$), linear ($V_{DS} < V_{GS} - V_T$) or saturated ($V_{DS} > V_{GS} - V_T$). Typically, the linear or saturated regimes are used due to the larger signals

and simpler operation. The linear regime is where the drain current (I_{DS}) varies approximately linearly with the gate (V_{GS}) and drain voltages (V_{DS}) [6.3, 6.4]. The linear regime of an n -channel FET is given by: (the quadratic term is small and usually ignored ($V_{DS}^2 \ll V_{GS}V_{DS}$))

$$I_{DS} = \frac{W}{L} m_h C_O \left[(V_{GS} - V_T) V_{DS} - \frac{V_{DS}^2}{2} \right] \quad 0 < V_{DS} < V_{GS} - V_T \quad (6.1)$$

where m_h is the effective surface mobility of the electrons in the channel, C_O is the gate capacitance per unit area, V_T is the threshold voltage, W is the channel width and L is the channel length. The response of an n -channel chemFET sensor, to an active gas or vapour, has been shown to modulate the threshold voltage [6.5]. Considering the linear mode of operation, the change in drain current at constant V_{GS} and V_{DS} is given by:

$$\Delta I_{DS} = - \left(\frac{W}{L} m_h C_O V_{DS} \right) \Delta V_T \quad (6.2)$$

In the saturated region, where $V_{DS} > V_{GS} - V_T$ (after pinch off), the drain current stabilises and can be defined as

$$I_{DS} = \frac{W m_h C_O}{2L} (V_{GS} - V_T)^2 \quad (6.3)$$

Operating the chemFET at constant current and considering a change in the threshold voltage only, before and after exposure to gas/vapour, can be equated to

$$\Delta V_{GS} = \Delta V_T \quad (6.4)$$

Hence, any chemical interactions which affect the threshold voltage can be monitored directly. This has a number of advantages over operating in the constant voltage regime – (1) ΔV_{GS} is now independent of W/L , m_h , C_O and so no process variations; (2) Constant current circuits are easier to generate in CMOS and constant voltage circuits require external resistors; (3) The linear regime may give larger responses, but the sensitivity ($\Delta V_{GS}/V_{GS}$) is the same. Furthermore I_{DS} is independent of V_{DS} . However, this is only applicable at constant temperature, as an increase in temperature will modify the transconductance of the device. Constant voltage operation in the saturated region is possible though complex with no advantages.

Another configuration is to operate the devices in pairs with one sensing device and the other as a reference. Taking the differential output of the two devices allows the possibility to isolate some of the remaining fabrication and temperature effects. This is a common strategy for sensors of many types (as discussed with the SH-SAW devices).

A schematic of this configuration is shown in figure 6.1. Such a design is appealing as current sources, with the reference FET driven by a current mirror, and amplifiers are simple to design in CMOS.

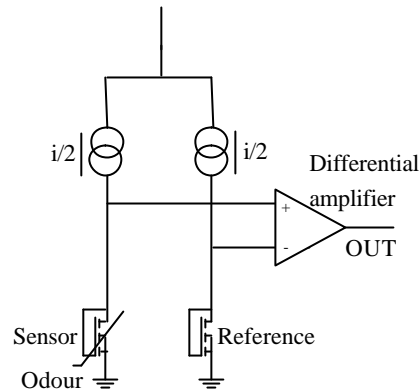


Figure 6.1 Schematic of a sensor and reference with integrated circuitry.

6.2.1.2 ChemFET sensor design

The chemFET sensor used here was designed and fabricated in collaboration between the Institute of Microtechnology, University of Neuchatel, Switzerland and the University of Warwick. These devices were originally designed on a joint European project and are being used in a number of research applications [6.6].

The overall device was designed as an array of four enhanced *n*-type MOSFET sensors. The individual devices were constructed within *p*-wells on an *n*-type lightly doped silicon substrate to minimise interference between adjacent sensors. The devices have a common gate and drain and operate in the saturated region. The devices were designed with two channel dimensions, $385\ \mu\text{m} \times 10\ \mu\text{m}$ (channel width/length (W/L) = 38.5) and $105\ \mu\text{m} \times 5\ \mu\text{m}$ ($W/L = 21$). The meandered channel was made to reduce the overall size of the sensor and to improve electrical connectivity to the active polymer materials. The overall area of the sensor array is $624\ \mu\text{m} \times 495\ \mu\text{m}$ for the $10\ \mu\text{m}$ channel length and $483\ \mu\text{m} \times 282\ \mu\text{m}$ for the $5\ \mu\text{m}$ channel length. A *pn*-diode was also included in the design to monitor the temperature of the substrate. Al tracks were used to contain the drain, source and gate, but Au was used as the sensing electrode (i.e. the gate of the FET sensor). Accessibility to the Au gate was achieved by etching through the silicon nitride passivation layer and subsequent oxide layers. In the sensing FETs the gold was also etched exposing the gate oxide. Figure 6.2 shows a cross-sectional

and top view of an individual sensor, showing particularly the common gate and drain and the active polymer material in contact with the gate oxide.

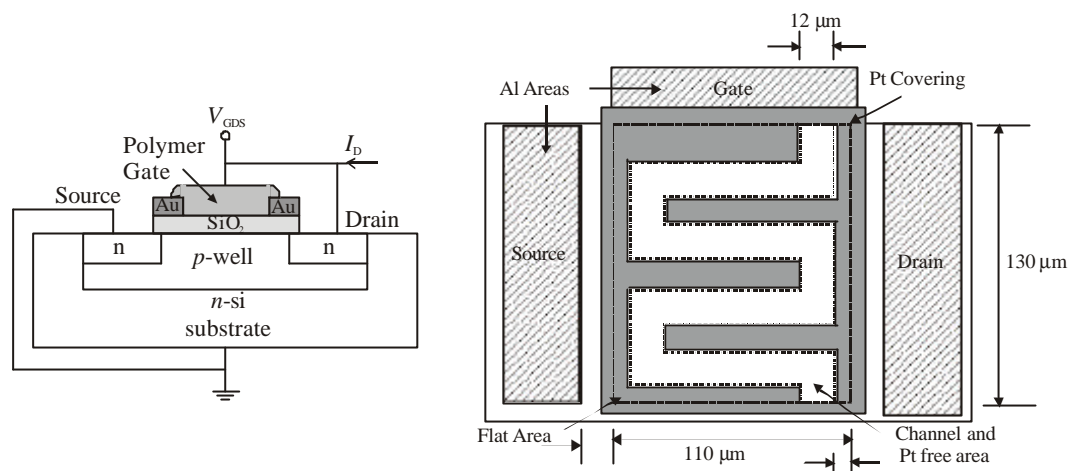


Figure 6.2 Schematic of a single chemFET device with channel dimensions of $385 \mu\text{m} \times 10 \mu\text{m}$. [6.2]

This opening is $2 \mu\text{m}$ larger than the channel to ensure that in fabrication any misalignment between the source/drain mask and the gold/gate etching mask does not result in the gold electrode covering any of the channel.

The final die size of the devices was 4 mm^2 with pads of $300 \mu\text{m}^2$ for electrical connection to the sensors. The array device was produced with 4 different combinations of solid gate (channel covered by gold) and open gate (channel oxide exposed), as detailed in Table 6.1. These combinations of open and closed gate produce chemFET arrays with references, with either one reference for the rest of the array or one reference per chemFET. By using these references, information regarding the FET itself can be gathered and gives the possibility of taking a differential output removing some of the fabrication variables. An added option is to have four open chemFET sensors giving the possibility of having multi-polymer arrays.

Though these sensors are not completely CMOS compatible, as gold is used as the gate, the remainder of the process is. This gold gate structure allows the evaluation of a range of conducting polymers. Furthermore, it can simply be replaced with polysilicon for a standard process. Figure 6.3 gives a detailed schematic of the array device with all the connection pads.

Table 6.1 ChemFET sensor different gate configurations [6.2]

Configuration	Description
4 Open gates	Used for multi-polymer arrays, for up to 4 different polymers
3 Open gates 1 Closed gate	Multi-polymer array of up to 3 different polymers, with 1 reference FET.
2 Open gates 2 Closed gates	Two chemFET sensors each with references.
4 Closed gates	Device testing

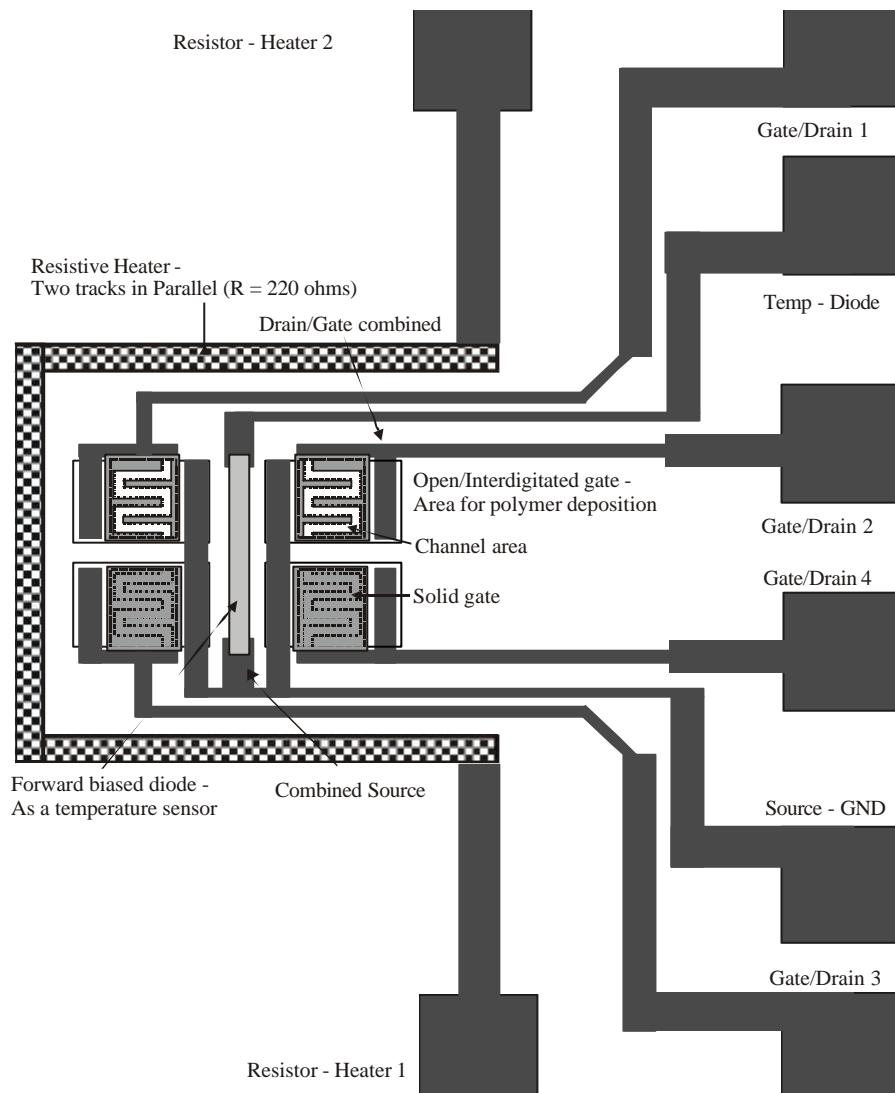


Figure 6.3 Schematic drawing of chemFET array device [6.2]

Figure 6.4 below shows a photograph of the final device before polymer deposition.

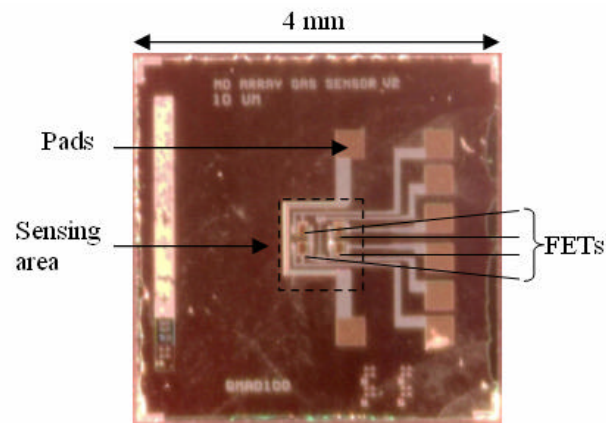


Figure 6.4 Photograph of fabricated 4-element ChemFET sensor [6.2]

A close up photograph of the sensing area is shown in Figure 6.5. The picture shows a standard device with 2 closed / solid gates and 2 open / exposed channels of $385 \mu\text{m} \times 10 \mu\text{m}$ where the gold electrode has been removed revealing the gate oxide. From the picture the included *pn*-thermodiode can be identified that can be used to monitor the temperature of the silicon substrate, however this was not required as the test equipment has accurate external temperature control ($\pm 0.1 \text{ }^\circ\text{C}$).

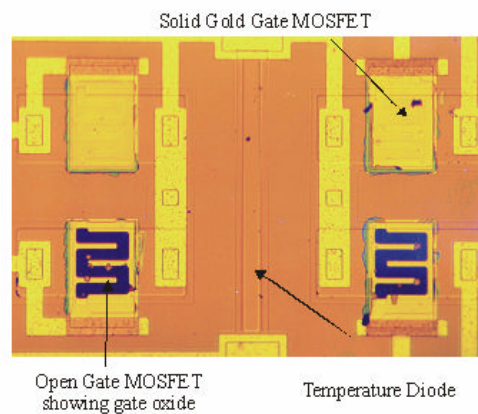


Figure 6.5 Close up picture on sensing area [6.2]. The black meandering line is the exposed gate oxide.

The device was mounted in a standard 14-pin DIL package (Spectrum Semiconductors, USA), as shown in Figure 6.6 below.

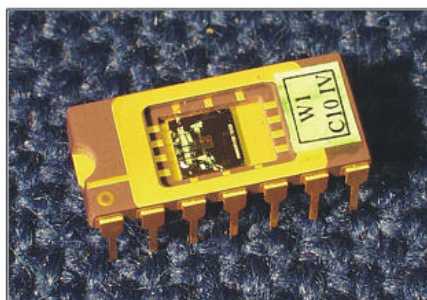


Figure 6.6 Photograph of packaged device [6.2]

6.2.1.3 Deposition of the polymer material

The room temperature chemFET sensors used here were coated with carbon black composite polymers. Carbon-black composite polymers are a combination of carbon black spheres and insulating polymer, where the carbon black provides electrical properties to the composite material. Three different types of composite polymer were used in these devices:

- Poly(ethylene-co-vinyl acetate) with 66:33 ethylene to vinyl acetate by % weight.
- Poly(styrene-co-butadiene) AB block copolymer with 30% of styrene.
- Poly(9-vinylcarbazole)

The deposition was performed using a system comprising of a standard liquid dispenser (RS Components, No. 552-179) with an airbrush (Student-plus ISB550, Revell, USA). The details of the deposition system and procedure are explained in [6.2].

6.3 Measurement setup for the combined nose/tongue system

6.3.1 Electronic interface for the chemFET sensors [6.2]

The FET sensor array is controlled using an instrument that consists of custom interface electronics, a National instruments card and a software control system written in LabVIEW™. The software control program is used to record the results from the instrument and to interface with measurement circuitry. The program interacts with the electronic instrument via the PC-DIO-24 National Instrument cards (these have 24 digital control lines that can be configured as either inputs or outputs in three banks of eight). The instrument is powered by a single linear PSU (Model Mp. LK 35, VERO-BICC Electronics), supplying ± 12 volts and + 5 volts.

The constant current card consists of constant current interface, filter and amplifier section and the measurement circuitry. The circuit operates by using the op-amp (quad OP470GP) as the constant current source. This is achieved by using a precision diode (LT1009CZ, $2.5\text{V} \pm 5\text{ mV}$) which restricts the voltage to 2.5 volts between one side of the scaling resistor (R_{SCALE}) and the non-inverting input of the op-amp. The magnitude of the constant current set by the scaling resistor is given by

$$V_{\text{Sensor}} = R_{\text{Sensor}} \times I_{\text{Sensor}} \quad (6.5)$$

$$V_{\text{Sensor}} = R_{\text{Sensor}} \times \frac{2.5}{R_{\text{SCALE}}} \quad (6.6)$$

where V_{Sensor} is the voltage drop over the sensor and R_{Sensor} is the resistance of the sensor (here the channel of the MOSFET). A default R_{SCALE} of $250\text{ k}\Omega$ ($\pm 0.1\%$) was connected to give a current of $10\text{ }\mu\text{A}$ to drive the sensors, although any value of resistance can be chosen to give a wide range in current values.

The second stage is a combination of a second order low pass filter and amplifier, using a simple resistor/capacitor/op-amp (Quad OP470GP) combination. Its purpose is to remove noise from the signal and to scale the output (V_{Sensor}) to 10 volts. The filter is set to a frequency of 160 Hz, and the amplification to a default value of two. A simplified circuit diagram is shown in Figure 6.7. The final part of the card is the measurement electronics. This is performed by a pair of on board analogue to digital converters (ADCs), the Burr-Brown ADS1211. This IC is a 24 bit ADC based on a sigma-delta converter and can be used to scan four channels. The output from the ADC's can be controlled via a simple three-wire interface, connected to the PC-DIO-24 and software control system.

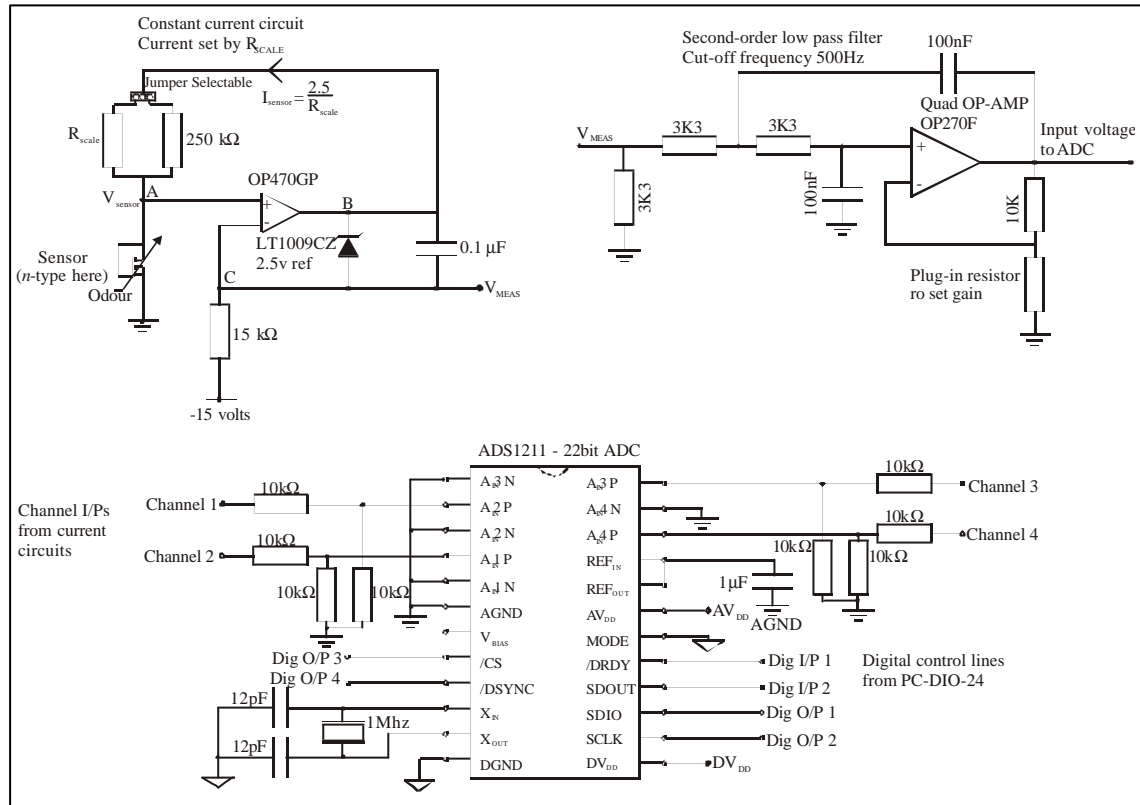


Figure 6.7 Simplified circuit diagram of constant current electronic hardware [6.2]

6.3.2 Measurement setup for the SH-SAW sensors

The vector voltmeter / signal generator setup was used with the SH-SAW devices as before (see chapter 4). The set-up includes a signal generator (HP 8648C), the dual SH-SAW sensor and a vector voltmeter (HP 8505A). The experimental procedure involved the measurement of both the phase velocity and attenuation of the SH-SAW signals propagating on the delay lines of the sensor. Using this setup, an electrical signal is fed from the signal generator to the input IDTs; the amplitude ratio ΔA and phase difference Δf between the input and output signals of each delay line and between the output signals of the sensing and reference delay lines were monitored by the vector voltmeter. The fractional velocity shift $\Delta v/v$ and attenuation change $\Delta a/k$ of the SH-SAW can be derived from the phase difference and the amplitude ratio, respectively (see chapter 4 for details).

6.3.3 Combined experimental setup

The combination of the both the FET and SH-SAW sensors was used to analyse the same sample, with the SH-SAW devices measuring the liquid phase while FET devices

were used to analyse the headspace above the sample liquid. The liquid chamber used previously for the SH-SAW devices was modified to accommodate the FET devices on the top side above the liquid (see Figure 4.6 (chapter 4)). The top of the liquid cell was machined with a depression to allow the 14 pin DIL package to fit in. The package is mounted face down to detect the sample headspace (pins point up to allow socket connection to control electronics interface see Figure 6.8). The device was clamped down using a brass fitting across the back of the 14 pin DIL package with screws on either end as shown in Figure 6.8. The cell was placed over the SH-SAW device in the same way as with the previously discussed experiments.

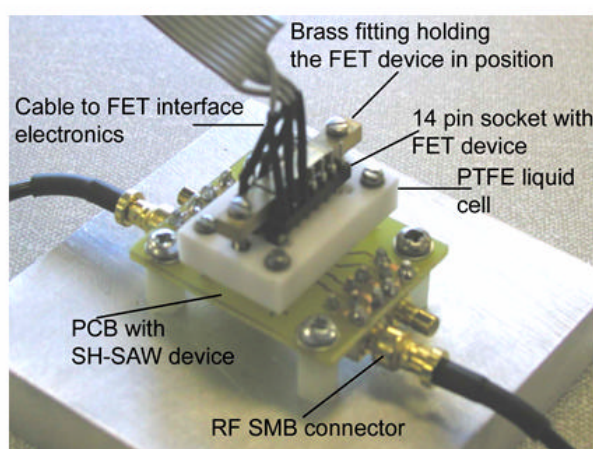


Figure 6.8 Photograph of the flavour sensing system with a PTFE sample cell [6.7]

Figure 6.9 below shows a photograph of the full experimental setup including the measurement instruments for the electronic nose and tongue.

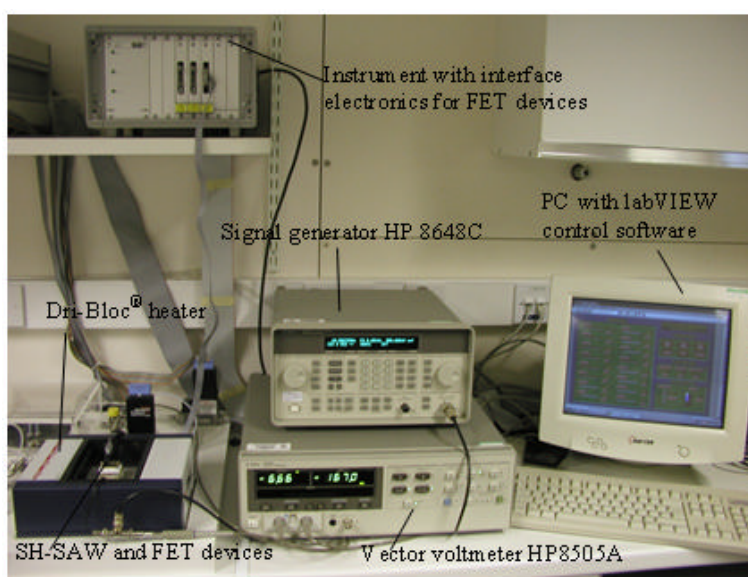


Figure 6.9 Photograph of the experimental setup for the combined electronic nose/tongue measurements

6.3.4 Control software

The control program for the FET devices which simply interfaces with the measurement circuitry and records values from the sensors was written in LabVIEWTM. The complete program including the front panel and pop-up menus can be found in [6.2]. The front panel has a number of slide bar indicators displaying the voltages across the sensors and the control parameters, specifically the present time, finish time and sample rate. A number of switches are also shown that allow the user to enter system parameters, including the gain for each sensor, save details (e.g. file name) and finish time. The front panel of the program is given in Appendix A

The control program for the SH-SAW devices is the same as that used for all the other measurements previously described. The instruments used in the measurement setup (i.e. vector voltmeter) were controlled via a GPIB cable and National Instruments GPIB card using a program again written in LabVIEWTM. The details of this simple control program were given in chapter 5 with the front panel and block diagrams given in Appendix A.

6.4 Experiments performed with the combined nose/tongue system

In order to investigate the contribution of the electronic nose devices to the overall performance of the flavour system, tests were initially performed on liquid samples that had previously been tested using only the electronic tongue. The chemFET devices used for these initial tests were coated with carbon black composite polymers employing poly(styrene-co-butadiene) and poly(9-vinylcarbazole). All the experiments were performed under a controlled temperature using a commercial Dri-BlocTM heater. The sensors were left for 60 minutes before testing at a constant temperature of $30 \pm 0.1^\circ\text{C}$ at 50% r.h. A sensor baseline for the FET devices was acquired before the injection of the liquid sample for reference purposes. After injection of the liquid (60 μl) into the micro-cell using a micro-pipette (Gilson Pipetman P200), the sensor signals were monitored for a period of 15 minutes. The response of the FET sensors was defined as the difference between the baseline and the value recorded after 15 minutes of exposure to the liquid. The liquid cell and the SH-SAW devices were cleaned and dried after each measurement using DI water and the sensors were allowed to stabilise to the control environment before conducting the next measurement. These experiments

were replicated 5 times for each sample and repeated for two different nose chips with each sensor chip having a single different polymer.

6.4.1 Experiment to discriminate between orange juice and fresh milk

Measurements were conducted to discriminate between different liquid samples (i.e. de-ionised (DI) water, orange juice and milk). Results showing the discrimination of different liquids using principal components analysis for the e-tongue are presented in Figure 6.10. The amplitude ratio and phase difference on each of the delay lines (electrical shorted and free) were used as the four parameters for the principal components analysis. The PCA plot in Figure 6.10 as expected, shows excellent separation of the three very low vapour pressure liquids.

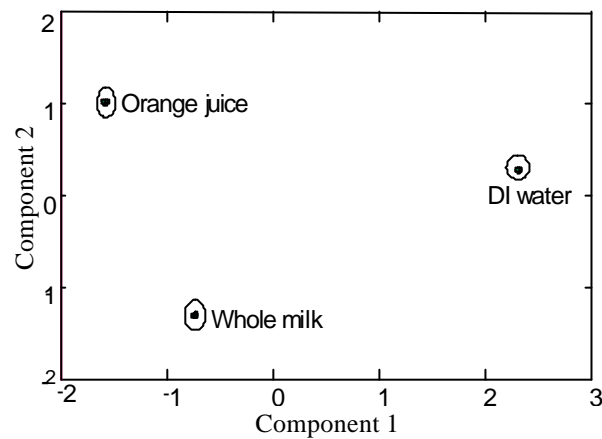


Figure 6.10 PCA of liquids with the e-tongue showing excellent linear discrimination

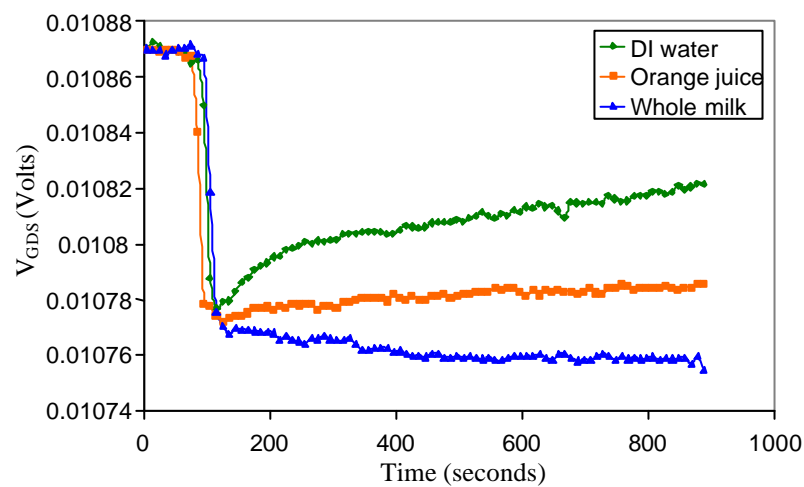


Figure 6.11 Response of the poly(9-vinylcarbazole) FET sensor to the different liquids

Figure 6.11 above shows the transient response of a FET sensor to the three liquids although a visual difference can be noticed in the responses in the plot, it is actually very small (order of 10^{-5} Volts). Clearly, from this it can be concluded that the electronic nose devices cannot easily discriminate between such liquids of low vapour pressure. This was as expected, however a combination of the results from nose and tongue was performed to see the effect on the separation, using principal components analysis. The components used were the change in gate/drain-source voltage (ΔV_{GDS}) of each of the four chemFETs along with the attenuation and phase data for each delay line of the SH-SAW devices, as mentioned earlier. The combined PCA plot is shown in Figure 6.12, again showing 100% separation. Good separation was achieved but the individual clusters were spread out compared to those for the tongue data alone, proving that the electronic nose does not respond well to low vapour pressure liquids such as DI water.

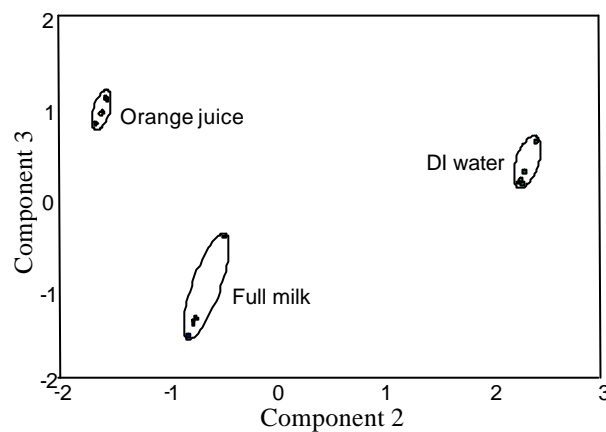


Figure 6.12 Combined PCA plot of different liquids using the e-tongue and e-nose together

6.4.2 Experiment to discriminate between milks of different fat content

Further experiments were performed on milk samples with different fat content, as was done with the electronic tongue (whole milk with 4% fat, semi-skimmed with 2% fat and skimmed milk with no fat). The same procedure was followed for these experiments as described earlier. Results showing the discrimination of different milks using principal components analysis for the SH-SAW device are presented in Figure 6.13. This plot again shows very good discrimination and tight clustering of the different milks samples. From the response of the FET sensors to the different milks, some discrimination can be observed but not as promising as the SH-SAW devices. The transient response of the one of the FET sensors is presented in Figure 6.14 overleaf.

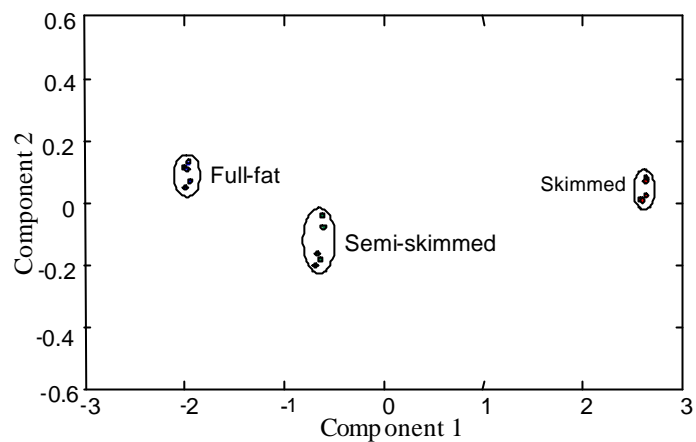


Figure 6.13 PCA plot of different milks with the e-tongue only

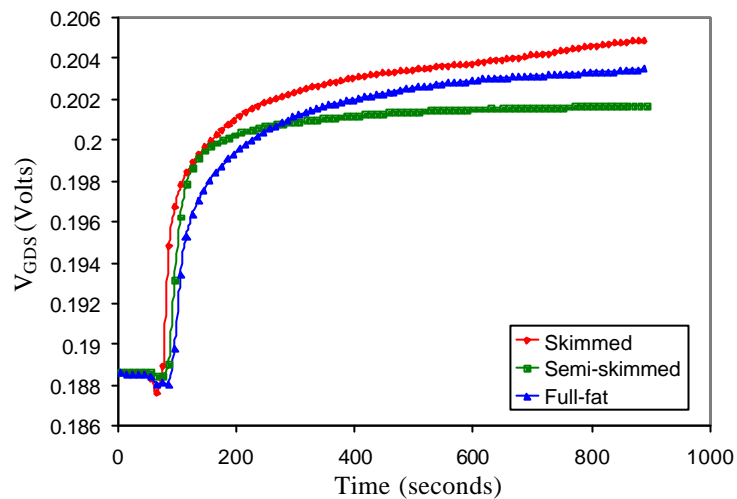


Figure 6.14 Transient response of the poly(styrene-co-butadiene)FET sensor to milks of different fat content

The FET and SH-SAW results were combined and a principal components analysis was performed on the data for the different milks. Figure 6.15 overleaf presents the combined principal components plot on the different milk data for the flavour system. The figure shows good separation of the different milks, however, again the clustering is not as tight compared to the SH-SAW devices alone - as was the case with the different liquids (water, orange juice and milk). Thus from the results of the two sets of experiments mentioned above, it can be concluded that the FET based electronic nose does not add much to the discrimination power of the system for these particular applications. This was expected as the liquids used in the experiments have a very low vapour pressure and not inductive for the composite polymers, therefore not easily

detected by the electronic nose. The small variations in the responses of the electronic nose devices could be due to the difference in water content in the different samples.

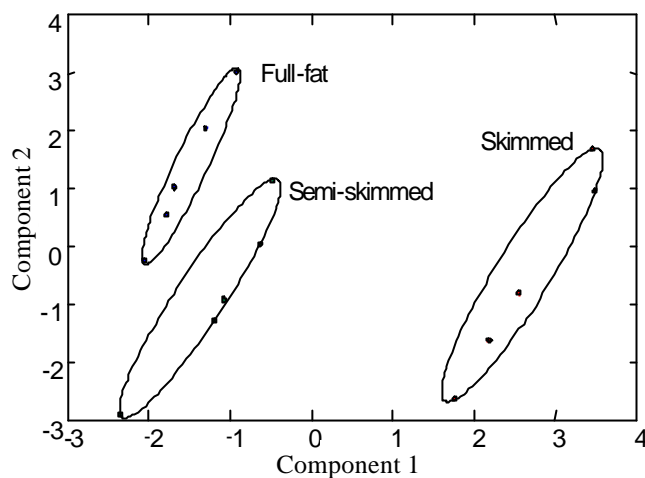


Figure 6.15 Combined PCA plot of different milks using the e-tongue and e-nose

Following the results gathered from the above experiments it was decided to perform experiments using a number of samples that are electronic tongue biased and a number that are electronic nose biased. It was anticipated that these experiments would give encouraging results to discriminate between complex solutions that contain substances that may not be detected by electronic tongue but would be picked up by the nose and vice versa. The details of the various synthetic analytes selected for these experiments and results obtained are discussed in the following section.

6.4.3 Experiments with nose/tongue biased analytes

Knowing that the SH-SAW electronic tongue devices respond well to the ionic solutions (very low vapour pressure) three of the different taste solutions used before were chosen along with two organic solutions (high vapour pressure) that are known to give good response from the FET nose devices. The solutions with their respective concentrations are given in Table 6.2 below.

Table 6.2 Electronic nose/tongue biased analytes

Solution	Concentration	Vapour pressure	E-Tongue	E-Nose
NaCl (0.1M)	0.1 M	Very low	✓	✗
Sucrose (0.1M)	0.1 M	Very low	✓	✗
Quinine	1 mg/mL	Very low	✓	✗
Ethanol (ethereal)	1000 ppm	High	✗	✓
Ethyl acetate (estery)	1000 ppm	High	✗	✓

Distilled DI water was used as the reference liquid and all the solutions were prepared or diluted (in the case of the organic samples) using the DI water. The same setup was used as for the other experiments and the same environmental conditions. Both the FET and SH-SAW sensors were controlled at $30 \pm 0.1^\circ\text{C}$ using a Dri-Bloc™ heater and at approximately 34% r.h. As before a sensor baseline for the FET devices was acquired before the injection of the liquid sample for reference purposes. The electronic nose device used for this experiment was coated with composite polymer - poly(ethylene-co-vinyl acetate). After injection of the liquid (60 μl) into the micro-cell using the micro-pipette (Gilson Pipetman P200) the measurements were recorded for 15 minutes. The liquid cell and the SH-SAW devices were cleaned and dried after each measurement using DI water and the sensors were allowed to stabilise to the control environment for approximately 15 minutes before conducting the next measurement.

Five replicate measurements were performed on each analyte and the results analysed as before using principal components analysis. As before the four components (amplitude ratio and phase difference data) from the electronic tongue were used for the analysis. For the electronic nose devices the voltage difference data for each of the four FETs was used for the analysis. The data for each of the sensors were normalised to a range of [0,1] using $R = (x - x_{\min}) / (x_{\max} - x_{\min})$ where x_{\min} and x_{\max} are across all samples for each sensor.

Figure 6.16 shows a 2-D principal components plot for the electronic tongue data on the five samples and DI water as the reference liquid. It can be seen from the plot that there is good separation and clustering of the salty, bitter, sweet and ethery samples however there is an overlap of the DI water and the estery cluster. It was expected for the tongue not to respond very well to the high vapour pressure organic solutions of relatively low concentrations (1000 ppm) and this explains the estery

clustering close to DI water. However, the tongue still shows good separation of the ethery compound.

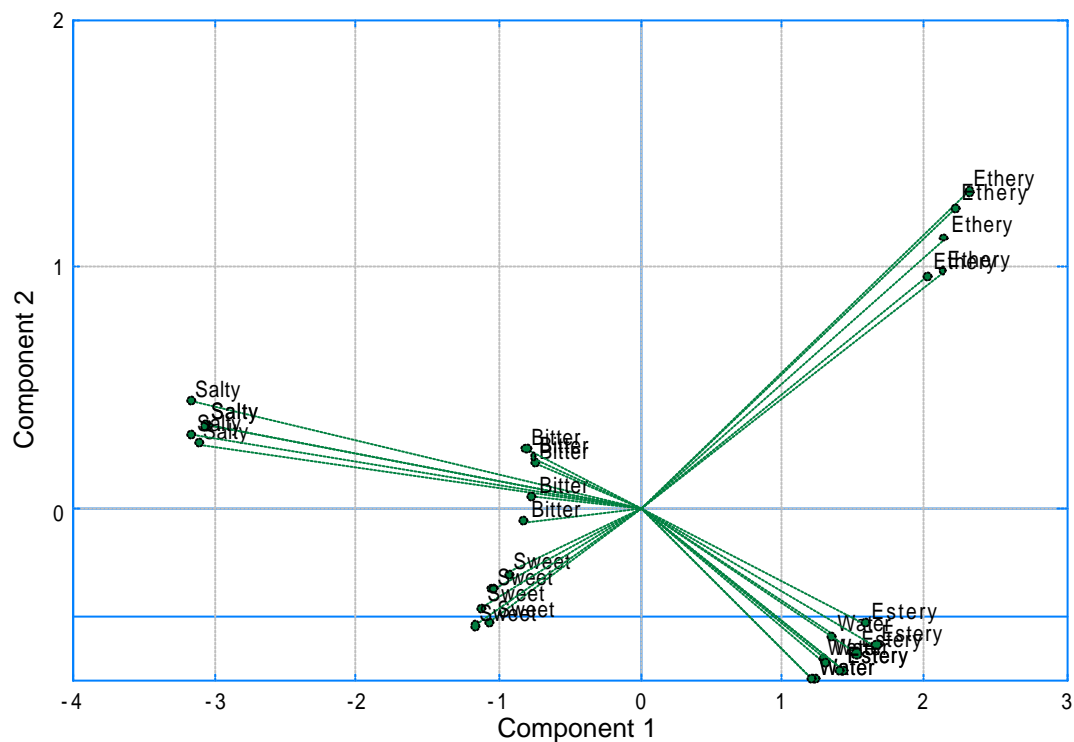


Figure 6.16 PCA plot for the E-tongue data only

As a result of overlap a third principal component was used to investigate its effect in improving the separation of the analyte clusters. Figure 6.17 overleaf shows a 3-D plot of the same electronic tongue data and shows full separation of all the samples with distinct clusters.

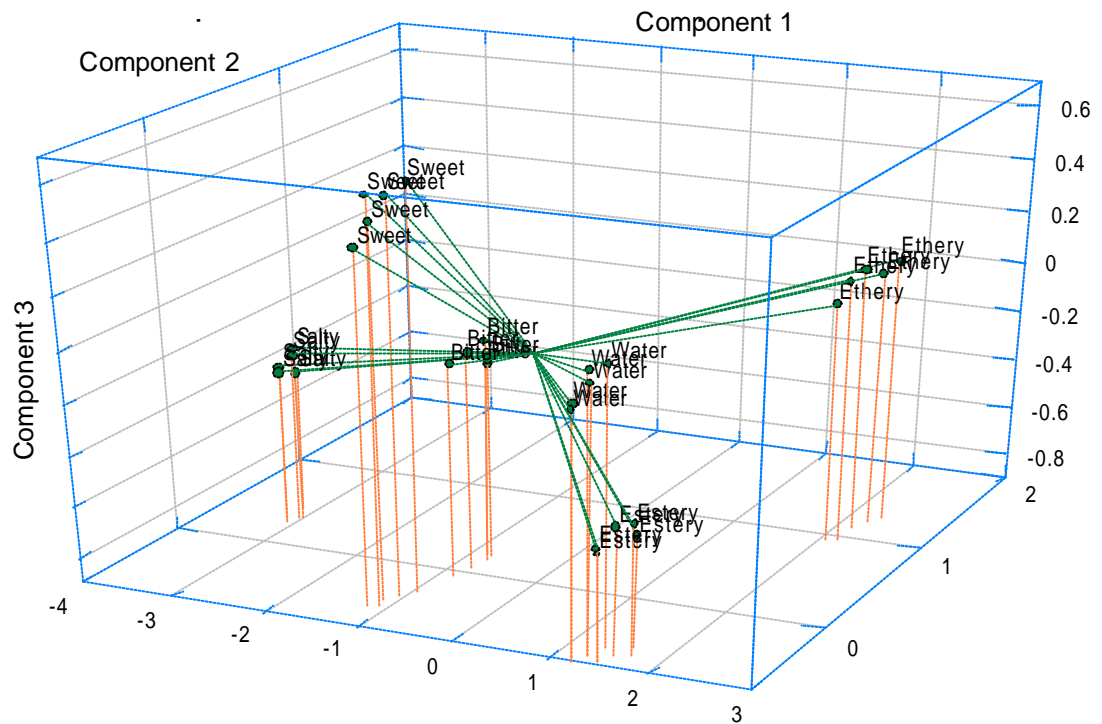


Figure 6.17 3-D PCA plot on the attenuation and phase data of the SH-SAW sensor

As before the change in the gate/drain-source voltage (ΔV_{GDS}) of each of the FETs, due to exposure to the samples, in the quad-FET electronic nose device were used for PCA analysis of the electronic nose results. Figure 6.18 gives four plots of the voltage (V_{GDS}) against time for the five analytes and DI water, for each of the four FETs in the electronic nose device. The plots for all four chemFETs show clear difference and large responses for both ethanol and ethyl acetate that have a high vapour pressure. Conversely, DI water, sucrose, NaCl and quinine responses were very small with small differences in the voltage change and hence almost no discrimination.

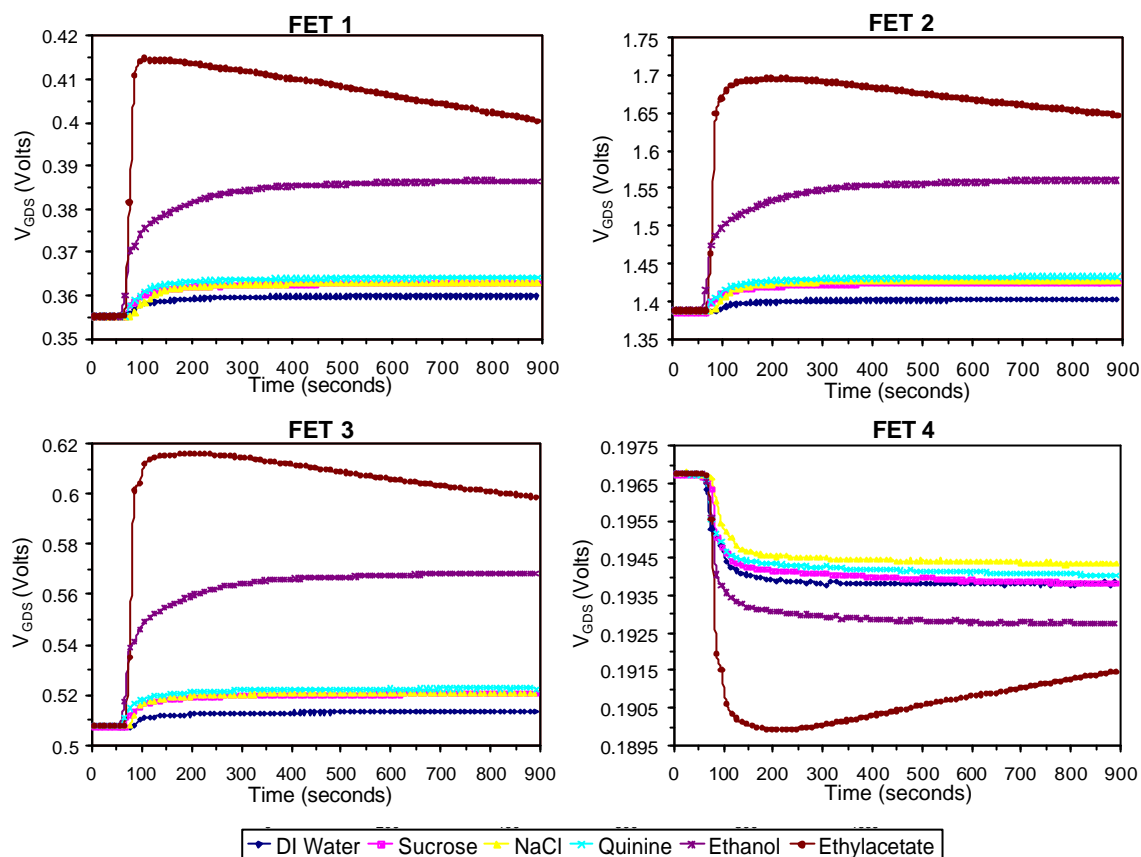


Figure 6.18 Transient responses of the 4 different ChemFETs in the array to the each of the samples

The transient sensor responses were as expected and the data were analysed using principal components analysis with the results presented in Figure 6.19. The 2-D PCA plot for the electronic nose voltage difference data could not separate all the analytes as demonstrated by the transient responses. Ethanol and ethyl acetate are clearly separated from the rest of the analytes as expected due to their high vapour pressure, hence easily sensed by the electronic nose. The effect of introducing a third principal component to improve the separation is demonstrated in a 3-D PCA plot (see Figure 6.20). It can be concluded that the electronic nose could not discriminate all the samples however it clearly separates the high vapour pressure ethereal and estery samples.

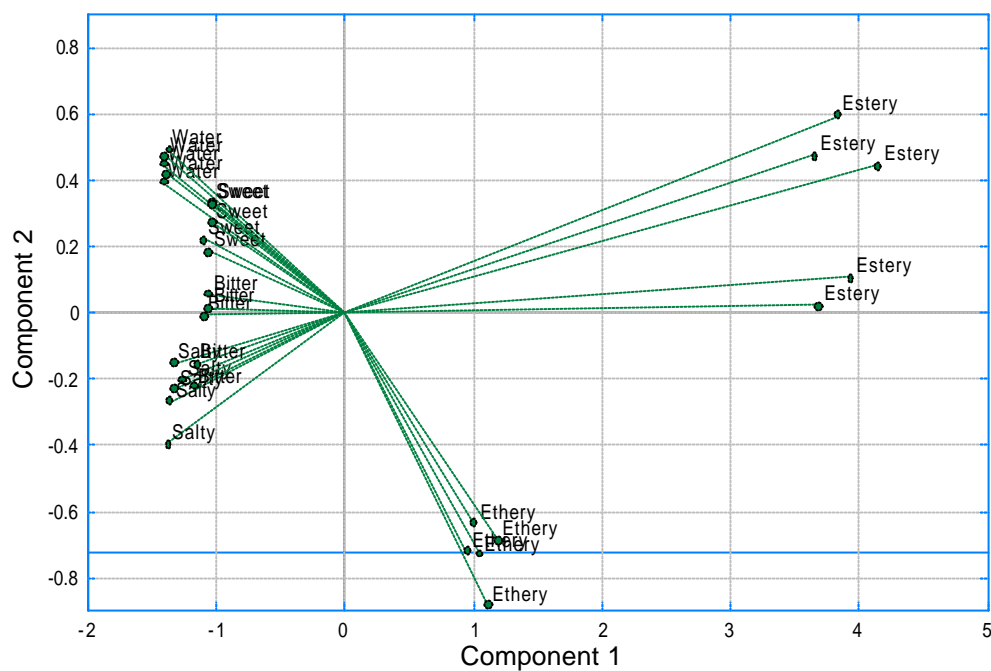


Figure 6.19 2-D PCA plot for the ΔV_{GDS} data from the 4 FETs

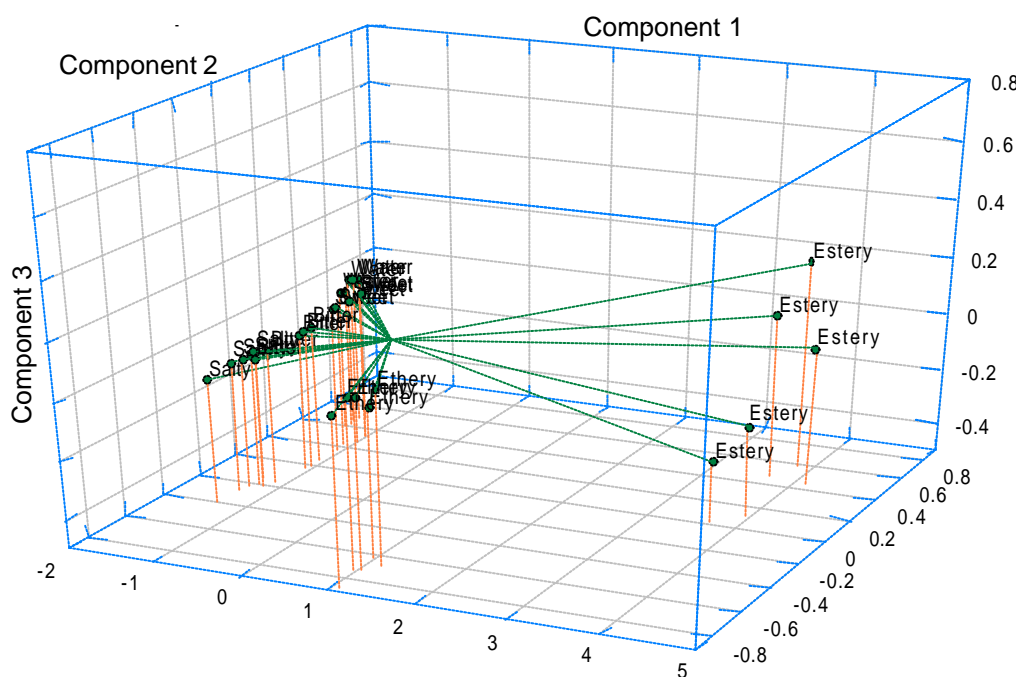


Figure 6.20 3-D PCA plot for the ΔV_{GDS} data from the 4 FETs

To determine the discriminating power of the combined system, PCA was performed on normalised electronic nose and tongue data together. Figures 6.21 and 6.22 give 2-D and 3-D PCA plots for the combined nose/tongue data. Through the individual analysis of the nose and tongue data, partial separation was shown in the 2-D PCA plot with

overlap of DI water and estery analyte for the tongue data. Good separation was however, achieved on using a third principal component. The electronic nose did not separate out the low vapour pressure analytes and water however gave very distinct responses to the high vapour pressure estery and ethereal compounds that separated out very well. Thus a combination of the data from both the nose and tongue was expected to give total separation of all the analytes.

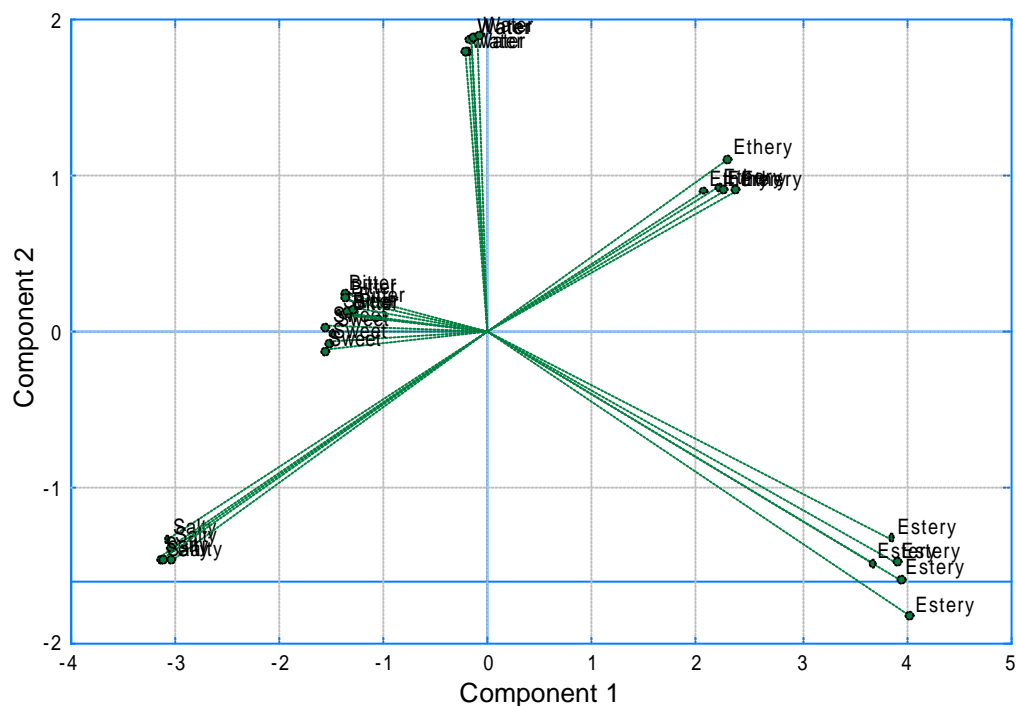


Figure 6.21 2-D PCA plot of the combined nose/tongue data

As anticipated the 2-D PCA plot, in Figure 6.21, shows 100% linear separation between all the samples. The 3-D plot in Figure 6.22 again illustrates full discrimination of all samples. In comparison to the 3-D plot of the electronic tongue data only (see Figure 6.17) which showed good separation of all samples the 3-D plot for the combined data gave stronger discrimination of the samples (note the change in scale in the 3rd principal component of Figure 6.22 (overleaf) to that of Figure 6.17), proving a definite contribution by the electronic nose.

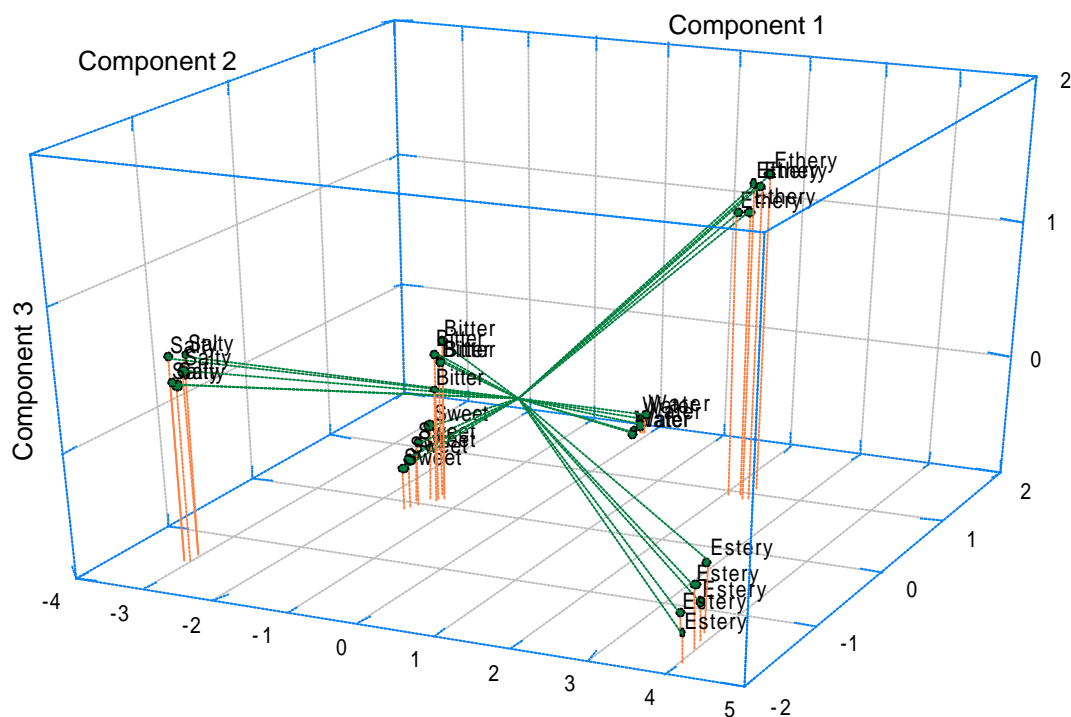


Figure 6.22 3-D PCA of the combined nose/tongue data showing 100% separation

6.5 Conclusions

The combined tongue/nose flavour system comprising of the SH-SAW liquid sensors and the chemFET gas sensors has been introduced. The design, operating principle and the measurement system for the electronic nose devices has been described together with the control program written in LabVIEWTM. The details of the combined flavour system setup have been covered along with the experimental procedures. Results from initial experiments performed using the combined flavour system on the complex samples (such as milks of different fat content) and different solutions (such as water and orange juice) showed little contribution from the electronic nose. However, the use of the combined nose/tongue system was justified with further experiments where three tongue biased solutions with low vapour pressure and two organic high vapour pressure nose biased solutions were tested with the system. The results of this investigation were as expected and concluded that the combination of the electronic nose and electronic tongue produced 100% discrimination between all the samples. These results are very encouraging and suggest the potential of the flavour system to analyse complex solutions in the food and beverage industries and in certain circumstances outperform the individual use of an electronic tongue or electronic nose.

6.6 References

- [6.1] M. Josowicz and J. Janata, Suspended gate field effect transistor modified with polypyrrole as an alcohol sensor, *Anal. Chem.*, 58, (1986), pp. 514-557.
- [6.2] J. A. Covington, *CMOS and SOI CMOS FET-based gas sensors*, PhD thesis, University of Warwick, School of Engineering, Coventry, UK (2001).
- [6.3] S. M. Sze, *Semiconductor Devices: Physics and Technology*, Wiley (1985), pp. 159-222.
- [6.4] E. S. Yang, *Microelectronic Devices*, McGraw-Hill (1988), pp. 229-253.
- [6.5] I. Lundström, M. Armgarth, A. Spetz, F. Winqvist, Gas sensors based on catalytic metal-gate field effect devices, *Sensors and Actuators*, 10 (1986), pp. 399-420.
- [6.6] D. Briand, B. van der Schoot, H. Sungren, I. Lundström, N. F. de Rooij, A low power micromachined MOSFET gas sensor, *Tech. Digest of Transducers*, Sendai, Japan (1999), pp. 938-941.
- [6.7] G. S. Sehra, J. A. Covington, M. Cole and J. W. Gardner, Combined electronic nose/tongue system for liquid analysis, *Proceeding of ISOEN'02*, Rome (2002), pp. 58-63.

CHAPTER 7

High frequency SH-SAW devices

7.1 Introduction

Further to the encouraging results obtained with the SH-SAW devices discussed in the previous chapters, new devices were designed to operate at higher frequencies with advantages of smaller size, higher sensitivity and ability of remote sensing through choice of industrial, scientific, medical ISM frequency. This chapter details the different designs of these devices, fabrication details and the measurement setups. The design and fabrication of the liquids cells to be used for testing of these devices are also given.

7.2 Design of the high frequency SH-SAW devices

The sensors were designed together with Irina Leonte (PhD student, Sensors Research Laboratory, Warwick University). The designs were based on the same basic principle as of the previous lower frequency devices discussed in chapter 3, having a dual delay line configuration with one metallised and electrically shorted delay line and one free electrically open line. The frequencies of operation were 433 MHz, 869 MHz, 2.45 GHz, and 10 GHz. The main reason to operate at these frequencies was to investigate the development of a wireless system, plus the advantage of smaller devices which would mean cheaper devices in terms of devices per wafer and also higher sensitivity. Both wired and wireless devices were designed at each frequency with the wireless devices now having reflective delay lines (output IDT replaced by reflectors). As

discussed in chapter 3, the main component on the sensor is the IDTs and in the case of the wireless sensors the reflectors, to effectively transform the RF signals into SAWs (and back into electrical signals) and efficiently reflect the waves. Two different types of IDTs and 3 different types of reflector designs were considered. The sensors were designed and fabricated on a 36° rotated Y cut X propagating lithium tantalate (36YXLT) piezoelectric substrate; the same as previous 61 MHz devices.

7.2.1 Wired and wireless sensor configurations

7.2.1.1 Wired configuration

This sensor arrangement follows from the previous 61 MHz devices, consisting of a dual delay line setup. It consists of transmitting and receiving IDTs of the associated frequency on each delay line. Two different types of IDTs were designed to be used with these devices, the uniform single electrode IDTs as employed for the 61 MHz devices and the double electrode IDTs which have the advantage of eliminating reflections from periodic electrodes. The design of the IDTs is discussed in the next section. Figure 7.1 below shows the dual delay line wired configuration to be used for the sensors at the various frequencies (up to 1 GHz).

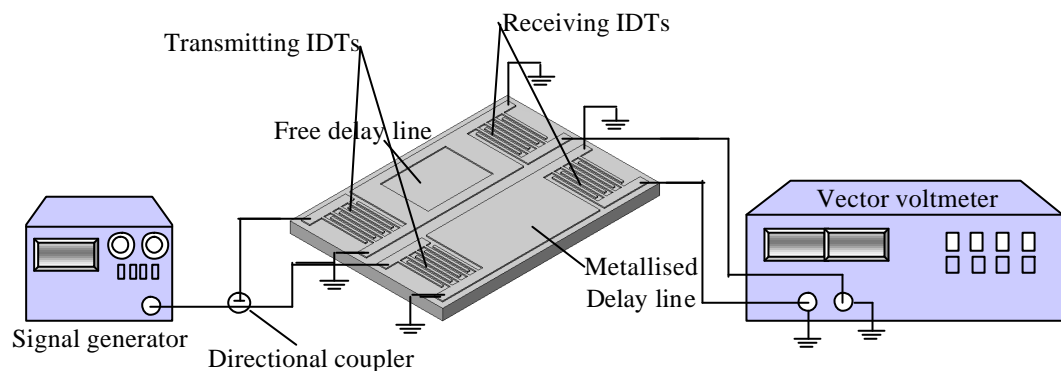


Figure 7.1 Wired setup for the high-frequency dual delay line sensors (same as 61 MHz)

As before with the lower 61 MHz devices, the dual delay line consists of a metallised line that is electrically shorted and a free line that is electrically active. This allows the measurement of both mechanical and electrical properties of analytes. These delay line device configurations can be used with any of the measurement setups discussed in chapter 4, i.e. network analyser, vector voltmeter or oscillator loop setup.

7.2.1.2 Wireless configuration

The measurement techniques for the wired sensors require electrical power supplied and cannot be operated in a wireless mode. For some sensor applications (e.g. on rotating machinery), a fixed wired connection between the sensor and the evaluation unit cannot be established. Usage of slip-rings and brushes is an alternative; however, these cause additional mechanical and electrical problems (i.e., interruptions, noise etc.), making these methods unusable in reliable systems [7.1]. Since the operating frequencies of the SAW devices is from tens of MHz to a few GHz, they directly match the frequency range of radios and radar. By connecting an IDT directly to an antenna SAWs can be excited remotely by electromagnetic waves. This fact suggests the possibility to realise passive, RF wireless, remotely operable SAW devices.

The wired delay line sensors have a transmitting IDT to which an RF signal is applied and due to the piezoelectric effect the IDT stimulates an acoustic wave that propagates along the surface of the elastic substrate, with its associated particle displacement in the vicinity of the surface [7.2]. Vice versa, a SAW generates an electric charge distribution at the receiving IDT and outputs an electrical RF signal [7.3]. In the case of making these two port delay line devices wireless, they have to be transformed into one port SAW devices with a single transducer electrically connected and all other being reflective. Thus there is still a transmitting IDT which can be connected to an antenna for wireless operation but the receiving IDT is replaced by a reflector. Figure 7.2 shows a schematic diagram of a sensor that can be operated as a passive wirelessly interpretable system [7.4].

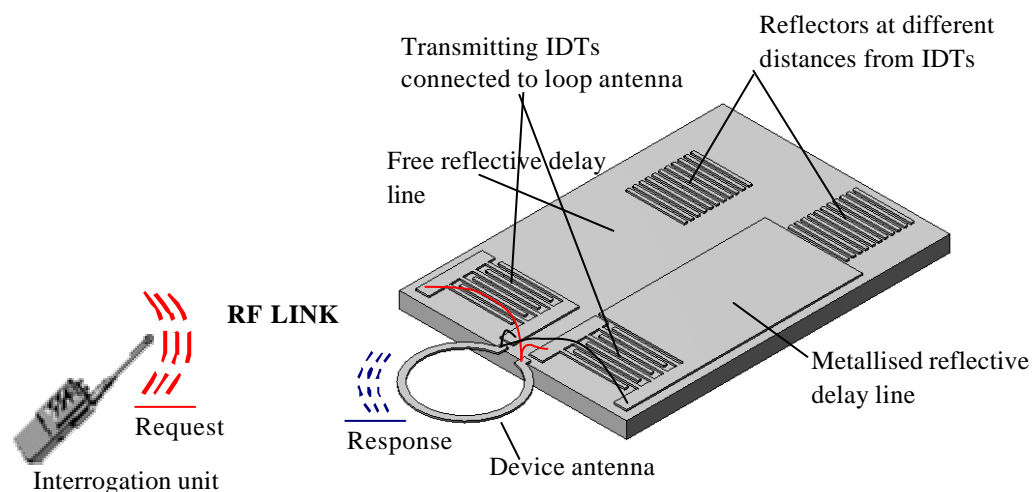


Figure 7.2 Setup for wireless operation of passive sensors (not to scale)

The diagram shows a dual reflective delay line sensor having an input IDT and a reflector for each reflective delay line. The IDT's are connected directly to a small antenna. The antenna-IDT configuration is able to convert the microwave signal from air to a SAW signal on the surface of the wafer and vice versa. The echoes from the reflectors (sensor responses) delayed in time, are picked up by the sensor antenna and retransmitted to the system antenna attached to an interrogation unit. The interrogation system evaluates the response signal and calculates the influence of the analytes, etc. to the sensor. The same dual line configuration is used for liquid properties discrimination, hence two reflected signals are retransmitted, separated in time due to the difference in the propagation velocity along the two paths (free and metallised) and due to the designs of the sensors which are discussed later.

7.2.2 IDT designs

Two different types of IDT designs were used for the high frequency SH-SAW sensors. Standard uniform IDTs with single electrodes were used as with the 60 MHz devices and double-electrode IDTs were also designed which are known to minimise reflections from the periodic electrodes. These reflections usually degrade the amplitude and phase response. In the double-electrode (split-electrode) geometries, with electrode widths and spacing of $a = L/8$ (see Figure 7.3) at the centre frequency, the differential path lengths are such that the SAW reflections from each split-electrode pair cancel out at the centre frequency, rather than add on as for single-electrode IDTs. One disadvantage of the split-electrode geometry is the increased lithographic resolution required for fabrication of the IDTs for the same centre frequency as of a single-electrode IDT.

7.2.2.1 Uniform single-electrode IDT design

The IDT design was performed following the same procedure as for the 60 MHz IDT described in chapter 3. The procedure and expressions used to calculate the various dimensions of the IDT structures for the different frequencies of operation are given here. In chapter 3 the expressions for the input, output admittances, phase, attenuation etc. were presented. It was seen that it is very important to keep the levels of spurious signals sufficiently low to obtain amplitude and phase responses without the presence of unwanted ripples; especially now that the devices are operating at significantly higher frequencies. The main sources of these spurious signals are acoustic reflections

of the SAWs from the edges of the piezoelectric substrate, feed-through and the triple transient signal (TTS). The acoustic reflections can be minimised using angled edges of the substrate and by using acoustic absorbers. The feed-through signals can be reduced by proper shielding and making the separation distance d between the input and output IDTs large enough. In the case of the ordinary bi-directional IDTs, the TTS can be lowered by making the TTS suppression S_{tt} high enough. Making S_{tt} results in higher insertion loss, meaning that the input and output IDTs are strongly unmatched, hence the input admittances y_{11} and y_{22} can be omitted in preliminary calculation of A_{tt} as given in equation (3.60) chapter 3.

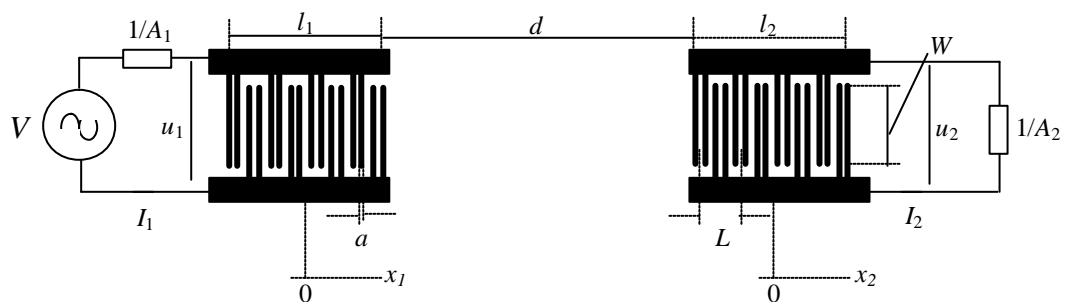
Using the equations from chapter 3 the IDTs for the four different operating frequencies were designed, for operation in a 50 Ω phase-measuring system. The amplitude and phase ripples were considered to lie under 1° , and since the output voltage of a delay line is the sum of the voltages of the main signal and the TTS, $|A_{tt}|$ can be estimated using the expression $|A_{tt}| < \tan(\Delta f)$ and having $\Delta f \leq 1^\circ$ gives $|A_{tt}| < 0.017$. During the design it was assumed that $|A_{tt}| = 0.015$ (which is equivalent to $S_{tt} = 40$ dB), giving $\Delta f = 0.6^\circ$. For 36° YX LiTaO₃ $v_f = 4161$ ms⁻¹, $v_m = 4110$ ms⁻¹, and $K^2 = 0.027$, $e_p^T = 51.7$. Using equation (3.42) $v_t = 4118$ ms⁻¹, and from equation (3.64) $G_p = 0.12$ μ S. Since the period is given by $I_t = v_t / f_0$, then $I_t = 9.6$ μ m and $a = 2.37$ μ m, for an operating frequency $f_0 = 433$ MHz. The aperture W was chosen to be 0.8 mm (greater than $20I_t$). The external measuring system is 50 Ω hence giving $y_1 = y_2 = 0.02$ S, then using equation (3.66) $N \approx 16$. The time delay t_0 for a separation distance d between the input IDT and output IDT/reflector of a free delay line can be calculating using equation (3.56) (for the metallised delay line the SAW velocity v_m for a metallised surface has to be used in (3.56)). Using the same procedure the various parameters, of the IDT delay line sensors at the different operating frequencies, were calculated. Table 7.1 gives the details of the uniform IDT design parameters for the SH-SAW devices at the four different frequencies.

Table 7.1 Design parameters for single-electrode IDT SH-SAW delay line sensors

Parameter	433 MHz	869 MHz	2.45 GHz	10 GHz
Free SAW velocity (v_f)	4161.5 ms ⁻¹	4161.5 ms ⁻¹	4161.5 ms ⁻¹	4161.5 ms ⁻¹
Metallised SAW velocity (v_m)	4110.8 ms ⁻¹	4110.8 ms ⁻¹	4110.8 ms ⁻¹	4110.8 ms ⁻¹
SAW velocity in IDT area (v_t)	4118.3 ms ⁻¹	4118.3 ms ⁻¹	4118.3 ms ⁻¹	4118.3 ms ⁻¹
Centre frequency (f_0)	433 MHz	869 MHz	2.45 GHz	10 GHz
Wavelength (λ_t)	9.6 μm	4.8 μm	1.6 μm	0.4 μm
Width of IDT fingers (a)	2.4 μm	1.2 μm	0.4 μm	0.1 μm
IDT length ($l_1 = l_2$)	235.2 μm	117.6 μm	39.2 μm	9.8 μm
Distance between IDTs (d)	4405.6 μm	4643.6 μm	2371.2 μm	2400.1 μm
Acoustic aperture (W)	800 μm	400 μm	200 μm	50 μm
Number of gaps ($N_1 = N_2$)	16	16	6	6
Time delay t_0 for distance d	$\approx 1.17 \mu\text{s}$	$\approx 1.17 \mu\text{s}$	$\approx 0.58 \mu\text{s}$	$\approx 0.58 \mu\text{s}$
Overall size of device ($l \times w$)	5.0 \times 2.5 mm ²	5.0 \times 2.5 mm ²	2.5 \times 2.0 mm ²	2.5 \times 2.0 mm ²

7.2.2.2 Double-electrode IDT design

The procedure followed in the design of the double-electrode finger IDTs is almost identical to that of the single-electrode IDTs with some variation to certain equations. Figure 7.3 below shows a delay line with double-electrode IDTs, with all the various corresponding parameters.

**Figure 7.3** Structure of delay line with double electrode IDTs

Looking back at the equations from chapter 3 under section 3.3.3, the expressions for the input conductance G_1 at the resonance frequency and the static capacitance C_0 were presented. The expression for G_1 was given by

$$G_1 = w_0 W (\mathbf{e}_0 + \mathbf{e}_p^T) F(s) K^2 N_s^2 \quad (7.1)$$

where

$$F(s) = \left[\frac{\sin ps}{P_{-s}(\cos \Delta)} \right]^2 R_s \quad (7.2)$$

here $s = 1/S_e$, where S_e is the number of electrodes per electrical period L . $\Delta = pa/L$, where a is the width of the electrodes and L is the period (see Figure 7.3). $P_{-s}(\cos \Delta)$ is a Legendre function of the first kind. K^2 is the electromechanical coupling coefficient for SAW, $w_0 = 2pf_0$, f_0 being the resonance frequency, W is the aperture length, \mathbf{e}_0 is the dielectric constant of vacuum, \mathbf{e}_p^T is the effective dielectric constant of the substrate, R_s is a constant coefficient which depends on s and N_s is the number of gaps for which $a_n \neq 0$. Previously for the single-electrode IDTs $s = 1/2$ with $R_s = 1/2$ and $N_s = N$, but now in the case of the double-electrode IDTs $s = 1/4$ as $S_e = 4$ (4 electrodes per period as shown in Figure 7.3), hence giving $R_s = 1/4$ and $N_s = N/2$.

Following the design procedure and employing equations (3.34) through to (3.40) of chapter 3, substituting $s = 1/4$ in all the relevant equations and assuming the IDTs have a constant period L ; the widths of gaps and of electrodes are equal to a ($a = L/8$) (see figure 7.3). An expression for the conductance G_0 was obtained as below

$$G_0 = 2.443 f_0 W (\mathbf{e}_0 + \mathbf{e}_p^T) K^2 \quad (7.3)$$

and the static capacitance C_0 of a single full-aperture overlap for a double-electrode IDT ($s = 1/4$) can be calculated from the expression

$$C_0 = 0.707 W (\mathbf{e}_0 + \mathbf{e}_p^T) \quad (7.4)$$

Then substituting G_0 and C_0 given by equations (7.3) and (7.4), respectively, in the corresponding expressions for the design procedure used for the single-electrode IDTs, the double-electrode IDT delay line was designed. Table 7.2 gives the design parameters for the double-electrode IDT delay line SH-SAW devices.

Table 7.2 Design parameters for double-electrode IDT SH-SAW delay line sensors

Parameter	433 MHz	869 MHz	2.45 GHz
Free SAW velocity (v_f)	4161.5 ms ⁻¹	4161.5 ms ⁻¹	4161.5 ms ⁻¹
Metallised SAW velocity (v_m)	4110.8 ms ⁻¹	4110.8 ms ⁻¹	4110.8 ms ⁻¹
SAW velocity in IDT area (v_t)	4118.3 ms ⁻¹	4118.3 ms ⁻¹	4118.3 ms ⁻¹
Centre frequency (f_0)	433 MHz	869 MHz	2.45 GHz
Wavelength (λ_t)	9.6 μm	4.8 μm	1.6 μm
Width of IDT fingers (a)	1.2 μm	0.6 μm	0.2 μm
IDT length ($l_1 = l_2$)	75.6 μm	37.8 μm	10.2 μm
Distance between IDTs (d)	4405.6 μm	4643.6 μm	2371.2 μm
Acoustic aperture (W)	800 μm	400 μm	200 μm
Number of gaps ($N_1 = N_2$)	15	15	12
Time delay t_0 for distance d	$\approx 1.17 \mu\text{s}$	$\approx 1.17 \mu\text{s}$	$\approx 0.58 \mu\text{s}$
Overall size of device ($l \times w$)	5.0 \times 2.5 mm ²	5.0 \times 2.5 mm ²	2.5 \times 2.0 mm ²

For the aid of comparison between the two types of IDTs and the effect of the number of gaps, double finger IDTs with the same number of gaps between electrodes as with the single-finger electrodes were also designed.

7.2.3 Reflector design

The use of metallic gratings causes electrical reflection in addition to mechanical reflection. The elements of SAW reflection gratings are composed of periodically spaced discontinuities. These can consist simply of open- or short-circuited thin metal strips (or a combination of the two), deposited on the surface of the piezoelectric substrate. Alternatively, they can be formed by etching shallow grooves (or pedestals) into the substrate surface. In each instance, the periodicity of the grating at the centre frequency yields a cumulative resultant reflection from the *front* edges of the discontinuities at the centre frequency f_0 . In addition, a metallisation ratio h is chosen so that SAW reflections from the *back* edges of these discontinuities also add constructively at f_0 .

The number of strips (or grooves) required for near-total reflectivity normally depends on the reflection mechanism involved. The reflection of the SAW waves from a reflection grating is maximum at the frequency (centre) for which all the individual reflections are additive, however there is a narrow frequency range over which the grating will reflect SAW waves with reduced efficiency. The width of the grating can be specified as the frequency range over which the grating reflection coefficient magnitude exceeds some minimum value. This specification depends on a number of design parameters including: the substrate type used; the type of reflection grating; the number of reflector elements; and diffraction and other losses in the grating structures.

7.2.3.1 Reflection mechanisms and behaviour in periodic structures

Four distinct types of reflection mechanisms contribute to the reflection process in a SAW grating. These are associated with: piezoelectric shorting; geometric discontinuities; electrical regeneration; and mass loading [7.5]. Important features of these mechanisms are described below:

Piezoelectric shorting: The electric field associated with the SAW propagation is short-circuited by the conductivity of the film and causes a perturbation to the SAW propagation. These reflection effects due to piezoelectric shorting are normally significant only for materials with large values of electromechanical coupling coefficient K^2 , such as LiTaO_3 and LiNbO_3 .

Geometric discontinuity: A geometric discontinuity occurs on the substrate surface when grooves are etched into it, or when metal strips are deposited. This discontinuity causes an impedance discontinuity resulting in SAW reflection. The effect of aluminium strips on substrates such as quartz and LiNbO_3 have very similar acoustic propagation properties. As a result the geometric reflection from an open-circuited Al strip of thickness h is similar to that for a groove of the same depth. For substrates with high electromechanical coupling coefficient, the case of having very thin metal strips results in a geometric effect that is usually smaller than the piezoelectric shorting or regeneration. This can be improved with thicker strips with film thickness ratio $h/l \gg 1\%$. Furthermore, in the case of substrates with a high value of K^2 the geometric effect of open ended metal strips, subtracts from the net piezoelectric and

regenerative effects. However, the geometric effect from shorting the strips adds to the piezoelectric one, hence making this construction a more efficient SAW reflector.

Electrical regeneration: Surface waves incident on a grating establish a time-varying electric potential between the adjacent strips. In turn, this potential causes regeneration of a surface acoustic wave in addition to the reflected component due to piezoelectric shorting.

Mass loading: The differences in both density and elastic properties between metal strips and the piezoelectric substrate present a mass-loading discontinuity. This effect results in reflections adding to the piezoelectric shorting and regeneration.

These effects play an important part in the determining the reflection characteristics of the structures and is highly influenced by effects such as electrical connection among the strips of the gratings. Furthermore, since more than one mechanism may be contributing at about the same level in a given grating, it is essential to determine whether or not their reflection coefficient phases have the same or opposite sign. Before looking at the individual types of gratings the fundamentals of reflection are presented.

For analysing the SAW propagation in grating structures, a typical equivalent circuit is considered, as shown in Figure 7.4. Here, k_i and R_i are the wavenumber and acoustic impedance, respectively, for the SAW in the region i . The SAW reflection occurs at the impedance discontinuity R_1/R_2 that is modelled to exist at each electrode edge [7.6].

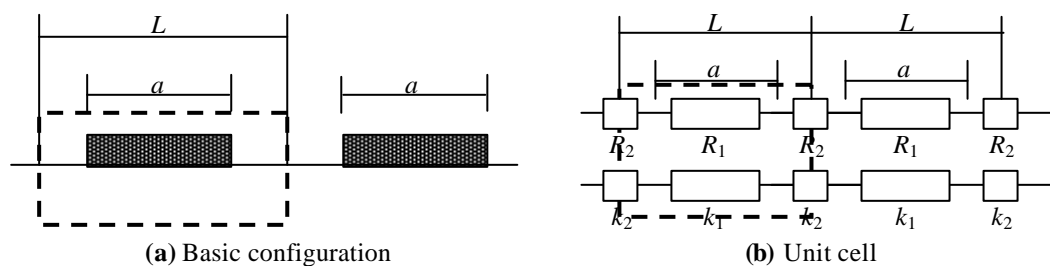


Figure 7.4 Equivalent circuit model for a grating structure

There is no physically clear definition of the acoustic impedance for the SAW and since the SAW devices are usually characterised by electrical quantities measurable at

electrical ports, there is no need to know the actual field strength. Thus the ratio R_1/R_2 is only required for the analysis. Along with the reflection caused by the mechanical discontinuity at the surface, reflection due to the electrical discontinuity at the surface also occurs as described above.

Consider a reflection from a strip as shown in Figure 7.5 below. A portion of the incident SAW with amplitude A_{in} is reflected due to the impedance mismatch at the strip ends. Using the equivalent circuit in Figure 7.5, the reflected SAW amplitudes from the left and right ends of the strip, respectively, are given by

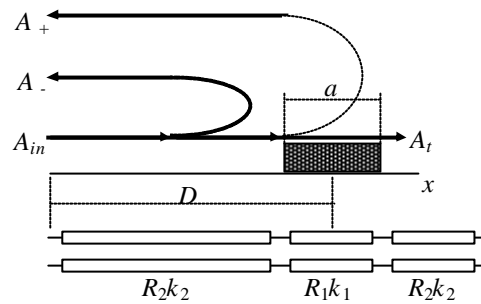


Figure 7.5 Incidence and reflection at a strip

$$A_- = r_- A_{in} \exp\{-j(2k_2 D - k_2 a)\} \quad (7.5)$$

$$A_+ \cong r_+ A_{in} \exp\{-j(2k_2 D + k_1 a)\}, \quad (7.6)$$

where r_- and r_+ are the reflection coefficients at the front (left) and back (right) ends of the discontinuities, given by $r_- = -r_+ = (R_1 - R_2)/(R_1 + R_2)$. For deriving purposes it is assumed that $|r_{\pm}| \ll 1$, then the reflection coefficient G_s per strip is given by

$$G_s = \frac{A_+ + A_-}{A_{in}} \cong 2j r_- \sin(k_1 a) \exp(-2jk_2 D). \quad (7.7)$$

This suggests that the reflection by the strip occurs from its middle and the equivalent reflection point is called the reflection centre. Furthermore, since $|G_s| = 2|r_- \sin(ka)|$, $|G_s|$ takes a maximum value when $a/l \cong 1/4$, noting that $\angle G_s = \pm p/2$ and the sign is determined by that of r_- .

Now consider the wave propagation in a periodic structure with periodicity L as shown in Figure 7.6.

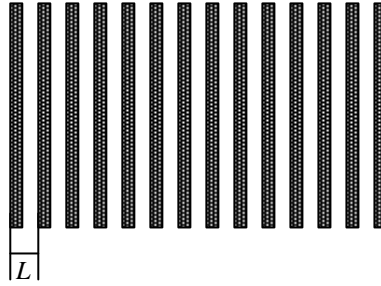


Figure 7.6 Periodic grating structure

Considering an infinitely long structure with equivalent periods, then eigenmodes called grating modes exist and their field distribution $u(x_1)$ for each period is similar to each other. This implies that, $u(x_1)$ must satisfy the following condition known as the Floquet theorem [7.7].

$$u(x_1 + L) = u(x_1)\exp(-jkL), \quad (7.8)$$

where k is the wave number of the grating modes, and grating period is L .

Define a function $U(x_1) = u(x_1)\exp(+jkx_1)$, the Floquet theorem suggests $U(x_1)$ must be a periodic function with periodicity of L . Hence $U(x_1)$ can be expressed in the Fourier expansion form of

$$U(x_1) = \sum_{n=-\infty}^{+\infty} A_n \exp(-2jn x_1 / L) \quad (7.9)$$

which gives

$$u(x_1) = \sum_{n=-\infty}^{+\infty} A_n \exp\{-j(k + 2n\mathbf{p} / L)x_1\} \quad (7.10)$$

the relation in (7.10) suggests that the field in the periodic structure with periodicity L is expressed as a sum of sinusoidal waves with discrete wavenumbers $k_n = 2\mathbf{p}n / L + k$. Alternatively, it can be considered that wave components with spatial frequency $k + 2n\mathbf{p} / L$ are produced by the spatial modulation of the incident wave with k and grating vector is given by $2\mathbf{p} / L$. The wave fields scattered at each period may interfere, and usually over a wide frequency band they cancel each other, resulting in a negligible effective reflected field. This case can be described using equation (7.10) by a single term with $n = 0$. However, in a certain frequency band, the scattered waves are in phase and they sum up resulting in very strong reflection. In this case multiple terms in equation (7.10) must be used for an accurate description of the wave field. This

phenomenon is called a Bragg reflection. If the SAW wavelength in the grating is I_t , then the phase matching condition is given by

$$2L = nI_t \text{ or } 4pL/I_t = 2np \quad (7.11)$$

this is known as the Bragg condition (see Figure 7.7) and can be rewritten in terms of the wavenumber $k_t = 2p/I_t$ as

$$k_t = np/L \text{ or } |k_t + 2np/L| = |k_t| \quad (7.12)$$

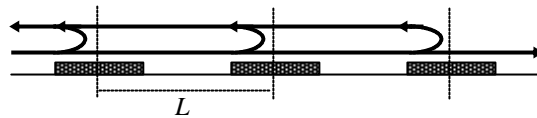


Figure 7.7 Bragg reflection

Various components with the wavenumbers $k_t + 2np/L$ are generated by spatial modulation of the incident SAW with the wavenumber k_t . Then Bragg reflection occurs, and a component with wavenumber $k_t - 2p/L$ will grow only when the component has the same phase velocity as that of the incident SAW as shown in Figure 7.8. By defining the equivalent SAW phase velocity v_t in the grating, the Bragg frequency can be written as in equation 7.13 below, satisfying the condition of equation (7.11)

$$f \cong npv_t/L \quad (7.13)$$

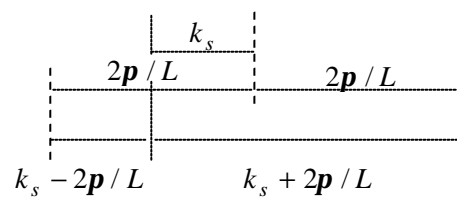


Figure 7.8 Bragg condition

7.2.3.2 Reflector grating designs

There are three typical configurations of the reflector grating as previously stated. Figure 7.9 shows these configurations, (a) shows an open-circuited (OC) grating where each of the strips is electrically isolated (b) shows a short-circuited (SC) grating where every strip is connected electrically in parallel and (c) is the combination of the OC and SC gratings called the positive and negative reflection (PNR) type grating [7.8].

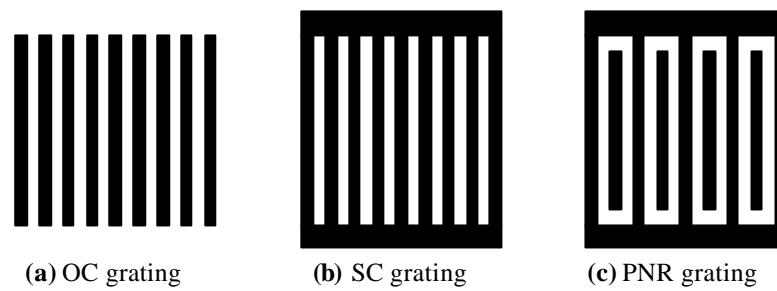


Figure 7.9 Basic reflector types

The PNR configuration offers a larger reflection coefficient compared to the OC and SC configuration of the gratings. Considering the above mentioned factors the different reflector gratings were designed and placed on the overall layout of the wireless devices, relative to the input IDTs (the overall device layouts are given in the next section). The different reflector configurations were designed to compare the effective reflection from each type. Table 7.3 below gives the details of various reflector gratings at the different operating frequencies of the SH-SAW devices.

Table 7.3 Design parameters of reflector gratings for the reflective delay line devices

Parameter	433 MHz	869 MHz	2.45 GHz
Free SAW velocity (v_f)	4161.5 ms ⁻¹	4161.5 ms ⁻¹	4161.5 ms ⁻¹
Metallised SAW velocity (v_m)	4110.8 ms ⁻¹	4110.8 ms ⁻¹	4110.8 ms ⁻¹
SAW velocity in IDT area (v_t)	4118.3 ms ⁻¹	4118.3 ms ⁻¹	4118.3 ms ⁻¹
Centre frequency (f_0)	433 MHz	869 MHz	2.45 GHz
Wavelength (λ_t)	9.6 μ m	4.8 μ m	1.6 μ m
Width of reflector fingers (a)	2.4 μ m	1.2 μ m	0.4 μ m
Acoustic aperture (W)	800 μ m	400 μ m	200 μ m
Number of strips	50	50	50
Reflector type*	OC/SC/PNR	OC/SC/PNR	PNR
Overall size of device ($l \times w$)	5.0×2.5 mm ²	5.0×2.5 mm ²	2.5×2.0 mm ²

* PNR reflectors were designed with 25 pairs of open- and short-circuited strips (total of 50 strips)

7.2.4 SH-SAW device layouts

The sensor layouts were done using the L-Edit package from Tanner Tools Inc. A number of different design configurations of the wired and wireless sensors were

considered. The subsections here give the basic layout details of the wired and wireless sensors (details of all the configurations designed are given in Appendix C).

7.2.4.1 Wired SH-SAW sensor layout

Figure 7.10 shows a schematic layout of a dual-delay line SH-SAW device, for an operating frequency of 433 MHz with the device dimensions. As before one delay line is electrically shorted while the other is electrically active to allow simultaneous measurements of electrical and mechanical properties.

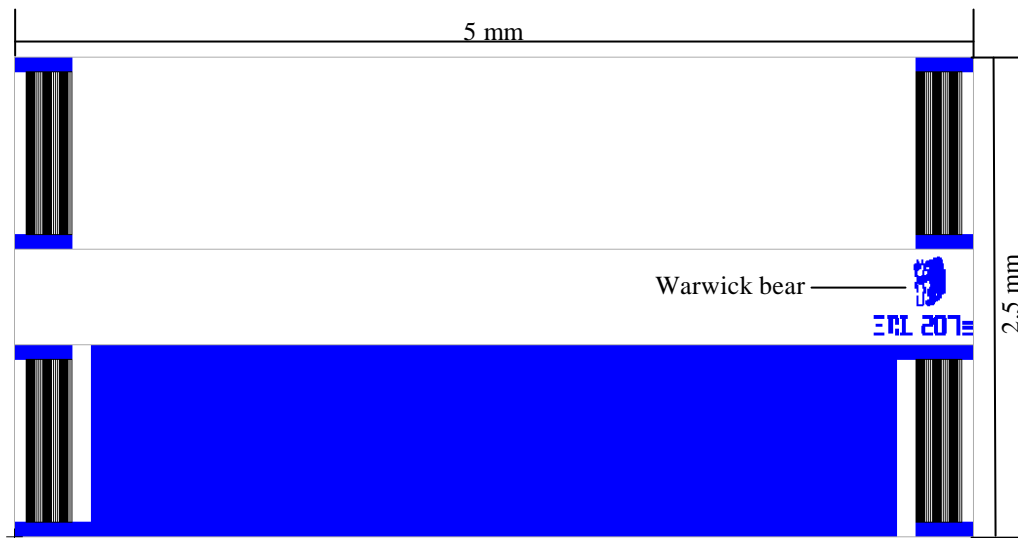


Figure 7.10 Layout of wired 433 MHz dual-delay line SH-SAW sensor

7.2.4.2 Wireless SH-SAW sensor layout

Figure 7.11 shows the typical layout of one of the 433 MHz wireless SH-SAW devices with the PNR type reflectors and all the dimensions. Again it is a dual delay line device with a shorted and free delay line, however the delay path on the free delay line is kept shorter (devices with 1mm and 2mm shorter delay paths designed) than the other so as to allow for a greater time difference between reflected signals from each line, hence making the measurement easier and avoiding overlap of the signal pulses.

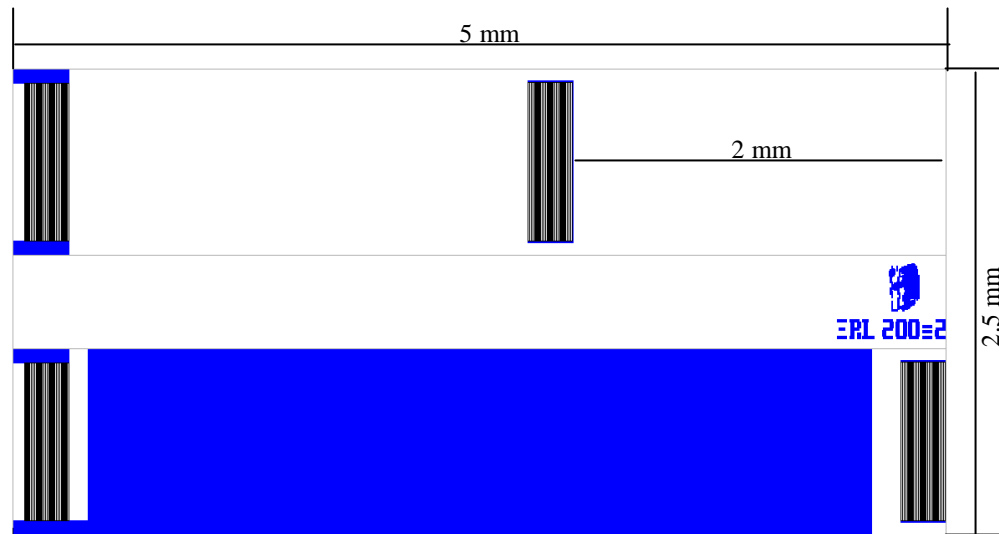


Figure 7.11 Layout of a wireless 433 MHz dual-delay line SH-SAW sensor with PNR reflectors and the free delay line 2mm shorter

7.3 Fabrication of the high frequency devices

Chapter 4 outlined the standard processes used for the SAW device fabrication and it also highlighted that the choice of photolithography technique depends mainly on the minimum feature size (resolution and accuracy) of the patterned structure required. Since the feature size is inversely proportional to the operating frequency of the SAW device, the resolution required for these new high frequency devices is much higher than the 61 MHz devices. Thus the fabrication was based on a high resolution process to develop structures as small as 100 nm. Features of this resolution are impractical to process using contact lithography (use of masks) therefore direct write on the wafer photoresist was employed via an electron beam writer. Furthermore, a lift-off process was chosen to develop the high resolution electrodes of the IDTs as it known to have its advantages over an etch process, with small features (see chapter 4). The following sections give a description of the fabrication process from pattern generation to the wafer dicing.

7.3.1 Pattern generation

The individual device layouts of the various configurations were arranged on a wafer level using L-Edit package from Tanner Tools Inc. The individual blocks were carefully arranged on the wafer space so as to maximise the use of the wafer area and get maximum number of devices from each wafer. Also considered was the distance

between each block to allow for the dicing. Devices of the same size were clustered together in areas of the wafer to make the dicing process simpler. The final wafer layout was exported as a GDS II file that can be converted and read by the electron beam writer either for a direct write or mask generation. Figure 7.12 below illustrates the final layout at wafer level.

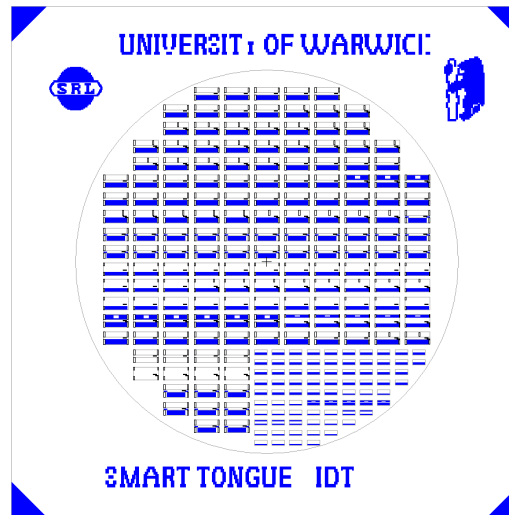


Figure 7.12 Final wafer layout for fabrication

7.3.2 Wafer cleaning

As mentioned in chapter 4 the cleaning of the wafers is important in order to achieve successful fabrication of the devices. The wafers have a high degree of cleanliness when received from the manufacturers however the wafers can gather many contaminants when exposed to the environment. All the processing is therefore performed under clean room conditions. The wafers were given a solvent clean to remove any surface contaminants, by immersing in an acetone bath at 60°C for 10 minutes followed by rinsing in IPA (iso-propanol) and then thoroughly rinsed in de-ionised water. Removal of stubborn contaminants was performed by immersing the wafers in a mixture of three parts of deionised water ($3\text{H}_2\text{O}$), one part ammonium hydroxide (NH_4OH) and one part of 30% unstabilised hydrogen peroxide (H_2O_2) at 75°C for 10 minutes (the solution must be handled carefully as it is harmful). The wafers were then thoroughly rinsed in DI water and dried using nitrogen.

7.3.3 Deposition of the grounding layer

As LiTaO_3 wafers are both piezoelectric and pyroelectric¹, the wafers were metallised on both sides and held in aluminium clamps to make a connection between the two sides of the wafer. This was essential to prevent electric sparking on the faces of the wafer as a result of the wafers being subjected to a temperature gradient (pyroelectric effect). The metallisation and short circuiting of the surfaces provides a path for even spread of the charge and prevents sparking from point to point. This metallisation layer has been referred to as grounding layer. Titanium was chosen for this metallisation rather the chromium because titanium is marginally better in terms of diffusing through the top metallisation layer (i.e. gold) which can cause adhesion problems. However, the main reason for the choice of titanium was that a dry etch of the grounding layer was needed and chrome cannot be dry etched. 30 nm of titanium were evaporated on both sides of the wafer using a Plassys electron beam evaporator.

7.3.4 Photoresist coating

The metallised wafer was then coated with a bi-layer of Polymethylmethacrylate (PMMA), which was used as the photoresist. A bi-layer of the photoresist was deposited to minimise the ‘wing-effect’ during the lift-off process. This is achieved by depositing two PMMA photo-resist layers of different molecular weights. Developing of this bi-layer of resist after writing using the electron beam writer or exposed to UV light through a mask, results in the top layer of photoresist producing an over hanging structure as shown in Figure 7.13 below. This is a due to the two layers developing at different rates and hence the first layer getting under cut. This procedure thus helps to achieve the desired film after the lift-off.

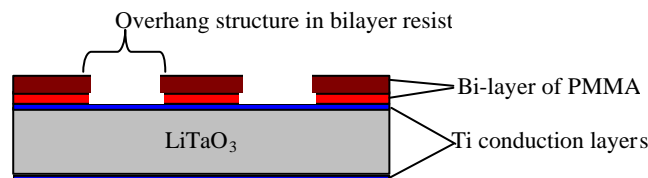


Figure 7.13 Developed bi-layer of photo-resist producing an ‘over-hang’

The layers of PMMA were deposited by spinning at 5000 rpm for 1 minute. The photoresist layers were then baked in an oven at 180°C for 45 minutes to remove all the

¹ Piezoelectric materials, such as LiTaO_3 also demonstrate a pyroelectric effect, whereby a temperature gradient induces a strain and so charge, and creates a voltage.

solvents from the photoresist. The wafer was clamped while heating and cooling, as mentioned before to ensure no pyroelectric sparking on the surfaces and the temperature was gradually ramped up.

7.3.5 Electron beam writing

After the baking of the photoresist the wafer was allowed to cool down to room temperature while still clamped. It was then written upon using a Leica EBPG 5 HR 100 electron beam writer. The GDS II pattern file is converted to a form that can be read by the beam writer and then sent to it. The respective resolutions, spot sizes and beam dosages used for the different feature sizes are given in Table 7.4.

Table 7.4 E-beam settings used for writing the different feature sizes

Feature size	Resolution	Spot size	Beam dosage
> 2 μm	300 nm	400 nm	250 $\mu\text{C}/\text{cm}^2$
2 μm	200 nm	300 nm	325 $\mu\text{C}/\text{cm}^2$
1 μm	100 nm	160 nm	400 $\mu\text{C}/\text{cm}^2$
400 nm	40 nm	56 nm	500 $\mu\text{C}/\text{cm}^2$
200 nm	20 nm	28 nm	500 $\mu\text{C}/\text{cm}^2$

7.3.6 Developing

After writing the photoresist was developed using a mixture of 2.5:1 of iso propanol (IPA) and methylisobutylketone (MiBK) for 45 seconds at 23°C. The wafer was then rinsed in IPA for 30 seconds and blow dried using nitrogen.

7.3.7 Metallisation and lift-off

The developed wafer was then metallised in the Plassys electron beam evaporator with 10 nm of titanium and 120 nm of gold. The metallisation process is computer controlled and performed in one step. The unwanted Ti and Au are then lifted off in an acetone bath at 45°C for 30 minutes. After the lift-off the wafer is rinsed in IPA and dried using nitrogen.

7.2.8 Removal of the grounding layer

The Ti charge conduction layer is removed by performing a selective etch on the Ti using reactive ion etching (RIE). The RIE was performed in the Oxford Instruments

S100 machine using SiCl_4 . The etch depth was monitored using reflectometry. Figure 7.14 illustrates the above described fabrication steps.

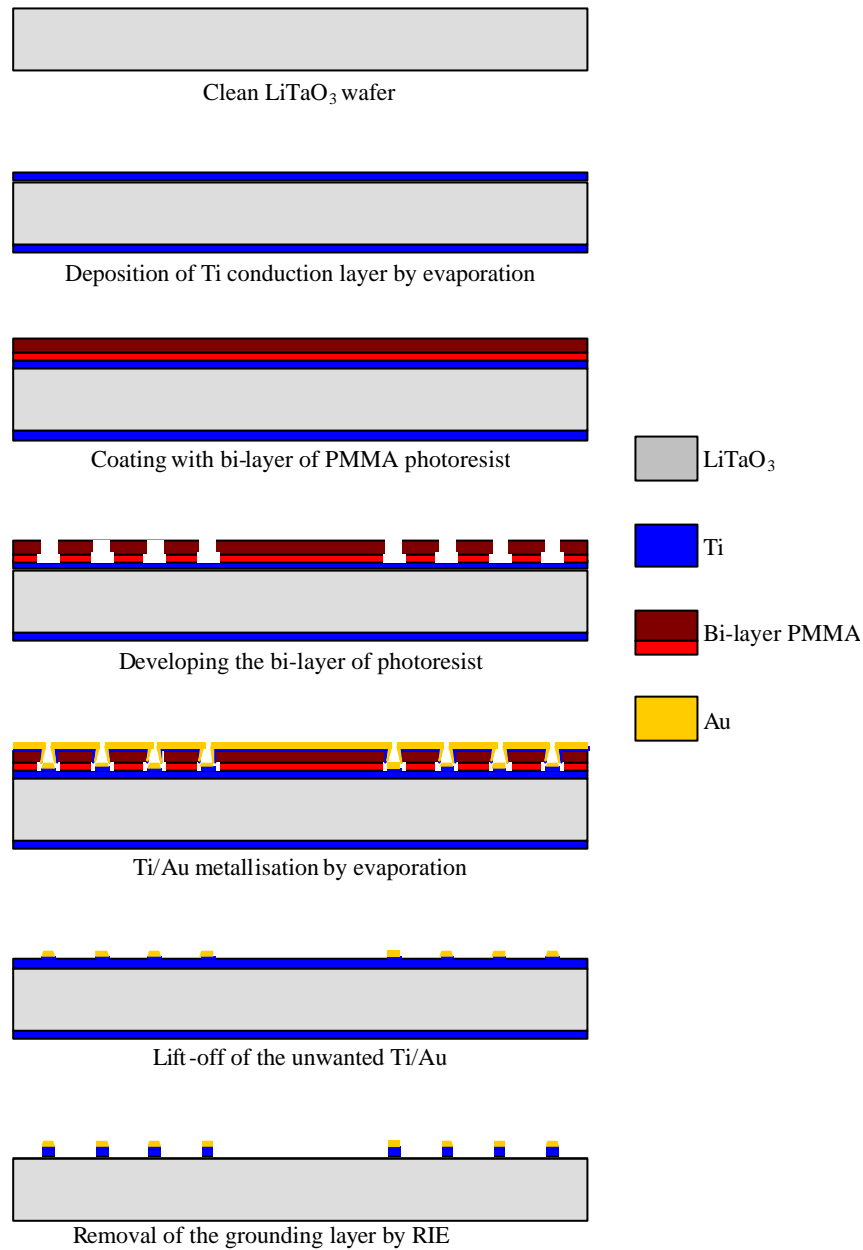


Figure 7.14 Fabrication process steps of high frequency SH-SAW devices

Pictures taken via a microscope during a test run of the fabrication while optimising the fabrication process, of the different feature sizes ($2\ \mu\text{m}$ to $200\ \text{nm}$) are shown in Figure 7.15 overleaf. All the pictures show very well defined features even at the smallest $200\ \text{nm}$ structures.

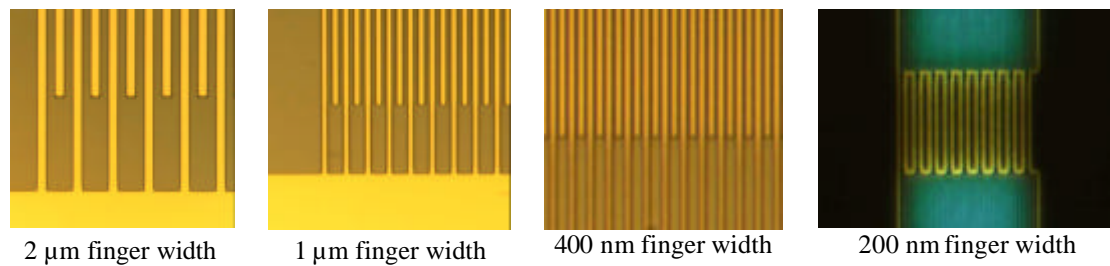


Figure 7.15 Photographs of IDT fingers (Test run)

7.4 Measurement systems

Measurements setups for both the wired and wireless configurations of the SH-SAW devices are described here. As with the 61 MHz devices these new high frequency devices will first be characterised using the HP8753ES vector network analyser. This gives a complete and unambiguous characterisation of device response from a complete frequency response spectrum, including all four S parameters as described in section 4.32. For the real time measurements the signal generator/vector voltmeter setup (see Figure 7.1) was chosen for the measurement of the wired SAW sensors. A measurement system for the wireless system has been proposed and is currently under construct in conjunction with Mr. Mark Hunt and Ms. Irina Leonte, research students at the University of Warwick.

7.4.1 Measurement setup for wired sensors

The same setup as that used for the 61 MHz SH-SAW devices was chosen for these new devices, however only the 433 MHz and 869 MHz can be measured using the HP 8505A vector voltmeter due to its frequency range limitation of 1 GHz. The 2.45 and 10 GHz wired devices can be measured using the vector network analyser setup. As previously described the experimental procedure involves the measurement of both the phase velocity and attenuation of the SH-SAW signals propagating on the delay lines of the sensor. Using this setup, an electrical signal is fed from the signal generator to the transmitting IDTs; the amplitude ratio ΔA and phase difference Δf between the input and output signals of each delay line and between the output signals of the sensing and reference delay lines are monitored by the vector voltmeter. The fractional velocity shift $\Delta v/v$ and attenuation change $\Delta a/k$ of the SH-SAW can be derived from the phase

difference and the amplitude ratio, respectively. Figure 7.1 shows a schematic drawing of the setup.

7.4.2 Proposed measurement setup for wireless sensors

A schematic representation of a wireless setup is shown in Figure 7.2. It comprises of the wireless SAW sensor, a device antenna and an interrogation unit with the system antenna. The wireless SH-SAW sensor layout details were covered in section 7.1.4 and to make these devices passive they have to be remotely excited by the aid of a RF signal received by a small device antenna. A small loop antenna has been built and proposed for this system and further detail can be found in [7.9].

The interrogation unit (IU) proposed, operates in a similar way to pulsed radar systems and is being designed to comply with UK regulations as specified in the Radio Interface Requirements EN 300 220-1 for short-range devices. During transmission a short burst of electromagnetic energy is transmitted to the surface acoustic wave sensor via the system antenna on the IU. These short pulses are produced by mixing the digital baseband signal with the 433 MHz carrier which translates the baseband signal to the required frequency range as specified in the legislation. The transmission is isolated from the return path by a SPDT GaAs FET switch which provides an isolation of approximately 80 dB, and a 1 dB insertion loss [7.10]

The receiving section of the transceiver is based on a simple homodyne architecture. After detection, the time delay (relating to phase) and the amplitude between the received signals from each reflective delay line is required to extract useful information about the measurand. An inter-pulse delay time measurement system has been proposed in [7.10] where more details can be found.

7.5 Micro-fluidic chambers

As previously covered, custom designed liquid chambers are required to hold the liquid over the sensors while under test. The relatively smaller size of the new high frequency devices pose a challenge to fabricate the new test chambers. Since the SH-SAW devices designed are of two different die sizes micro-fluidic chambers to match these sizes had to be designed and fabricated. Four different liquid chambers were designed and fabricated to fit over the SH-SAW sensors. The devices with the larger die size allowed the capability of machining the cells in stainless steel, but for the smaller

higher frequency devices the micro fluidic cells had to be fabricated using micro stereo lithography (MSL). These chambers were fabricated at Georgia Institute of Technology using the Viper system for the MSL process. The design and fabrication details are covered in the following sections.

7.5.1 Stainless steel chambers

This chamber was designed using AutoCAD[®] and machined in-house at the Engineering workshops at Warwick. The machining was done using the Bridgeport[®] Series I CNC machine by Textron Inc. Stainless steel was chosen as the chamber material as it has very high chemical stability and very easy to clean. The chamber was designed to allow the flow of the liquid in and out of the central reservoir that is in contact with the sensor. The volume of the central tank is $2.5 \times 1.5 \times 1.0 \text{ mm}^3$ and an overall dimension of $6 \times 9 \times 4 \text{ mm}$. The bore sizes were of 1.7 mm diameter into which the tubing is fit and chambers were designed to be fastened to the custom designed PCBs using bolts that act as guiding pins for location of the cell over the sensing area of the SH-SAW device that is mounted on the PCB. Figure 7.16 shows a photograph from underneath (side that rests on the sensor surface) of a stainless steel flow micro chamber with an inlet and outlet bore. Design schematics with all the dimensions are given in Appendix B.

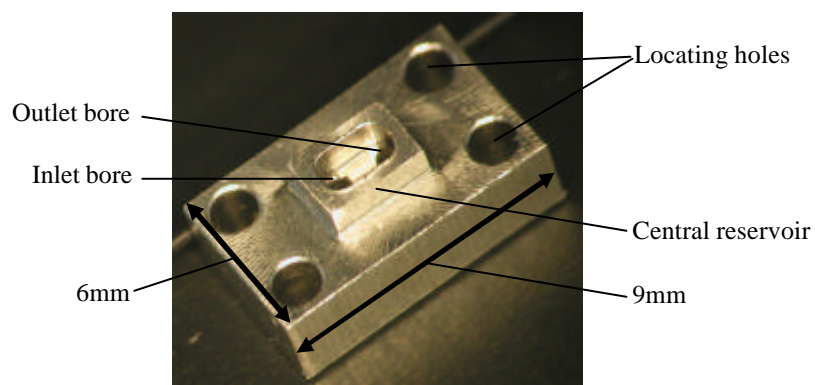


Figure 7.16 Stainless steel flow cell

These cells were also designed for static measurements. This cell has the same dimensions as the flow cell but without an inlet and outlet, instead has a simple central reservoir. These cells were successfully fabricated using the machining technique

however for the small die devices higher aspect ratio was required to develop smaller cells. Hence, other techniques such as Stereolithography were explored.

7.5.2 MSL micro-cells

7.5.2.1 Stereolithography

Stereolithography (SL) is an additive, layer-by-layer fabrication technique [7.11]. This technology can be used to fabricate components of many different shapes and hence commonly employed in customised packages for MEMS devices. A stereolithography apparatus (SLA) fabricates each layer based on computer-generated data points, such that any complex cross-sectional shapes can be generated and stacked to form a real 3-D structure. Microstructures with high aspect ratios can also be fabricated by superimposition of many layers (up to 2000 or more). Furthermore, SL can be used successfully to build structures around an insert [7.12], such as MEMS devices fabricated on silicon chips, so that many components can be integrated into the system with the packages built around them. SLA has the capability to fabricate many parts layer by layer simultaneously, allowing the capability of mass production and integrate many packages on the substrate.

The chambers required for the microsensors are small in size with small volumes to hold the sample liquid and it is necessary to maintain accurate dimensions and minimal dead volume in order to provide the correct sample injection volumes for the sensors. The SLA techniques have the capabilities to fabricate easily small and 3-D reaction chambers with customized designs of flow channels.

The SL systems is based on fabrication of 3-D parts using a layer-based additive fabrication process that traces the cross-sections of the parts on the top surface of a vat of liquid polymer [7.12]. The basic principle of SL involves using UV light as the energy to bond together 2-D cross-sectional layers of the structure to produce a 3-D object. In order to build real 3-D microstructures with SLA, 3-D CAD software, are used to design a 3-D model from which an STL file is generated. Using software such as the STL 3D Lightyear software (3D System, Valencia, CA), the STL file can be opened and the build parameters of the 3-D model specified. Another slice file is then generated that the SL system uses to perform the layer by layer build. After the machine receives the slice data from the CAD system, its UV system automatically traces out the cross-section of each layer.

A schematic diagram of the SLA is shown in Figure 7.17. The SL process can be summarized as follows. After the computer sends the information of a layer cross-section to the control system, two galvanometers direct the laser to scan that cross-section on the surface of the vat. Once the light hits the polymer, the resin starts to solidify through photopolymerisation. The platform then lowers by one layer thickness and the zephyr blade sweeps across the vat surface to recoat and smooth the surface for another layer. The zephyr blade functions similar to a doctor blade, which is a commonly used material coating mechanism. The zephyr blade pumps the resin from the vat and redeposits it on the top surface of the part to build each layer. After the recoat process, the machine is ready to scan and build another layer on top of the previous one.

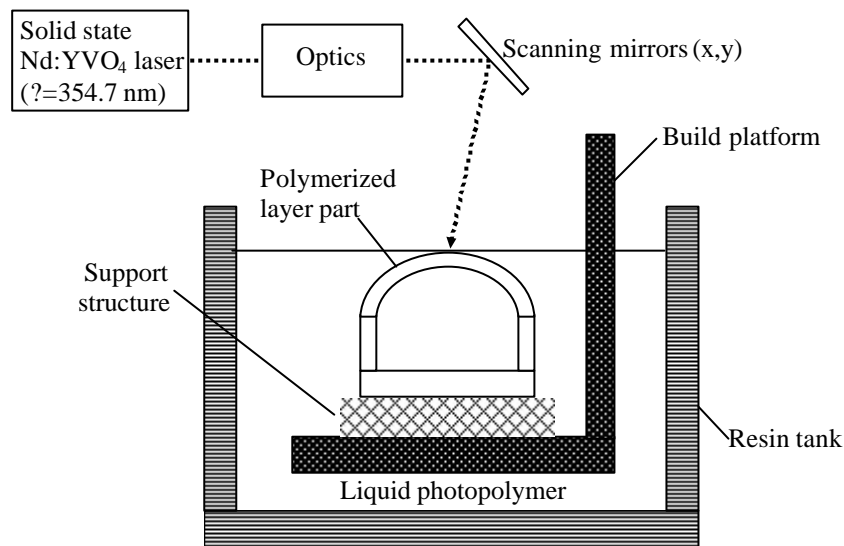


Figure 7.17 Schematic of typical SLA setup

7.5.2.2 Microstereolithography

The commercial SLA has a laser beam diameter of 200-300 μ m. The feature size of the finished structure is determined by the diameter or resolution of the laser beam, the reaction zone for polymerization in the resin, and the size of the monomer inside the resin. Micrometer-scale structures cannot be fabricated with the resolution of the SL apparatus such as the SLA-3500. In order to manufacture low-cost micro parts and microstructures, a great deal of interest has been devoted to develop micro-SL technology [7.13]. To improve the resolution of SL, the Bertsch and Ikuta groups developed two types of micro-SL technologies. Bertsch developed an “integral” process, which completes a layer in one exposure [7.14 – 7.17]. A schematic diagram

of the apparatus is shown in Figure 7.18. The micro-SLA uses a dynamic pattern generator in an open layer surface process, which does not depend on the shape of the pattern. This means that each radiation exposes the entire layer with no laser scanning necessary and the dynamic pattern generator automatically changes to the shape of the cross-section of that layer. The irradiated areas are polymerized selectively whereas the non-irradiated areas remain in liquid form. The liquid resin is irradiated for several seconds to allow the photo-transformation to occur.

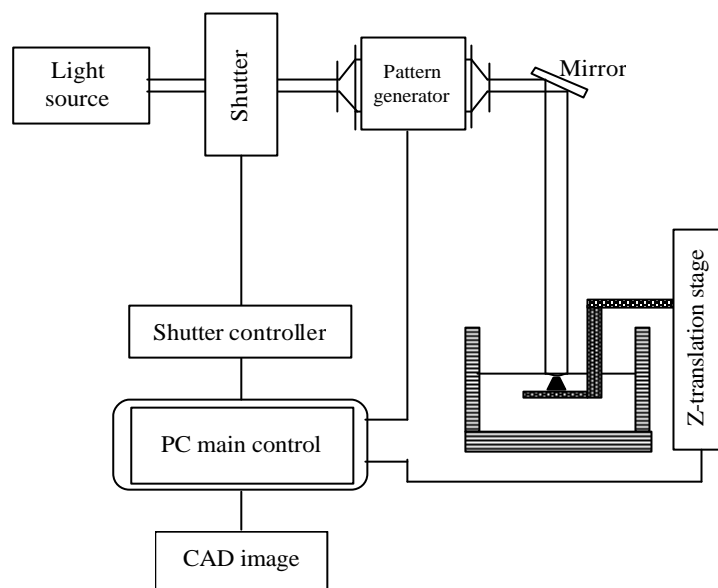


Figure 7.18 Dynamic mask projection MSL

Further developments such as by the Ikuta group include an “IH Process” (Integrated Harden Polymer Process) in the system that can fabricate 3-D microstructures [7.18]. The cross-sectional shape of the final product is patterned by a UV beam focused in the liquid UV polymer through the lenses, shutter, and transparent plate on the moveable build platform. The area under focus at a time is microscopic which allows a micron resolution. The process involves the solidifying of a thin layer of resin with UV light and stacking from bottom to top with the motion of a moveable build platform, to develop complicated 3-D structures. These two micro-SLA systems have been improved in resolution by using optical lenses or UV light sources with a pattern generator.

7.5.2.3 CAD design and MSL fabrication

The test structures were designed and drawn using AutoCAD[®]. The 3-D models were then sliced using AutoCAD[®] software to give cross-sectional layers of 50 μm along the direction of build of the test structures. The smallest thickness (50 μm in the SLA system used) of the individual slices was chosen to minimise the stair-stepping effect which results in rough side walls of the structures. Supports are used in the actual building of the test structures and these supports are later easily removed from the test structures without any major imperfections on the surfaces. The various support and build parameters, such as delay time between layers, recoat velocity or hatch patterns and spacing are specified using the machine software tools.

Prior to the build the machine begins with initialisation of the parameters such as the resin level and platform position. The material surface is prepared by sweeping the zephyr blade across the vat surface to make sure the vat surface is smooth for scanning the first layer. This also removes any objects that are blocking the laser light. Then, the two galvanometers start to direct the laser light across the top of the vat to trace out the cross-section of the part. The zephyr blade usually pauses a few seconds before it starts to recoat for the subsequent layer. This delay time permits the resin to polymerize after the area has been exposed to the UV laser. The next layer of resin is then applied by a deep-dip or a sweep with a zephyr blade. A deep-dip is the motion of the build platform as it dips into the vat of more than a layer thickness. A pause of a few seconds allows the resin to smoothen and to get ready for the laser scanning of the next layer. The layers are built up by repetition of this process until the structure is complete.

After the structures are built they were cleaned using an ultrasonic glycol ether-TPM (solvent) bath which removes any extra resin surrounding the structure giving an accurately shaped structure. The solvent is rinsed off using DI-water and isopropanol and then air dried ready for assembly. During the building process the resin does not fully solidify and this can be used as an attempt to integrate additional components to the structure such as external micro-tubing etc. The structure is then fully solidified using a post-cure step which cures the liquid resin between the surfaces producing a bond. This post cure is done using post-cure apparatus (PCA) and a thermal oven.

7.5.2.4 SLA system used

The Viper SI2™ SLA® system was used to fabricate the test chambers for the new high frequency devices. The Viper SI2 system is a solid imaging system that offers the capability of building standard and high-resolution structures. The system allows choice between a standard resolution mode, for the best balance of build speed and part resolution, and high resolution (HR) mode for ultra-detailed small structures and features. This is carefully controlled by a high speed scanning system using an integrated digital signal processor (DSP) and a single solid-state laser that delivers 100mW of available power. The laser wavelength is of 354.7 nm for use with the epoxy resins. The resin used was the RenShape™ SL 5510, which is a low viscosity, humidity resistant material and offers very high accuracy with excellent sidewall quality. The minimum thickness of a build layer on this system is 50µm. Further details of the Viper si12 system specifications and the RenShape SL 5510 resin are given in Appendix B.

7.5.2.5 Flow chamber design

The chamber was designed to be used with a flow system and the high frequency devices. The flow into the central reservoir (volume of $1 \times 1.2 \times 0.75 \text{ mm}^3$) is via bores (1.1 mm diameter) at approximately 60° angles to the bottom flat of the chamber. As with the micro-machined chambers four holes to aid guiding and location were included in the design. Figure 7.19 below shows a cross-sectional side view of the design flow chamber and a photograph of the MSL fabricated chamber.

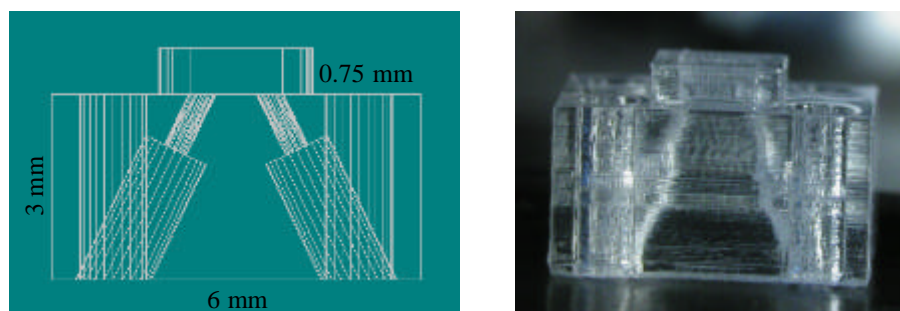


Figure 7.19 MSL cell for flow measurements

7.5.2.6 Disposable chamber

This design consists of a top reservoir into which the liquid is manually fed and the liquid flows freely onto the sensor surface and the measurements performed. As with

the other chambers it is clamped down to the PCB over the sensing area of the device and in the same way the locating holes for the guiding pins are also included in this design. A small a breather hole is created from the central tank above the sensor to the outside of the chamber. The top reservoir has a volume of 8 mm^3 with a liquid holding capacity of 1.2 mm^3 over the sensor surface. Figure 7.20 below shows a 3-D view of the design model and photograph of the fabricated MSL chamber.

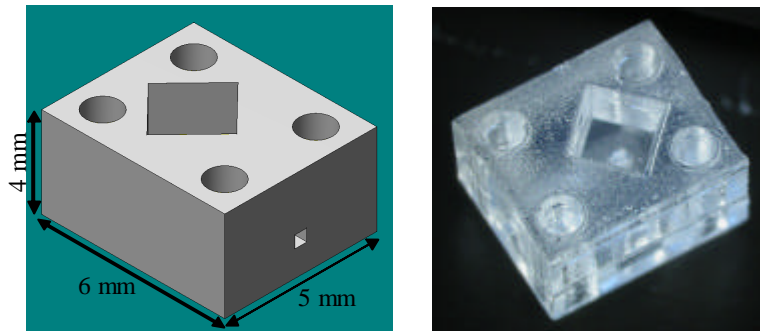


Figure 7.20 MSL disposable cell for static measurements

7.5.2.7 Parylene coating

The chambers were also covered with a $10 \mu\text{m}$ thick conformal coating of parylene of uniform thickness. This was achieved using a vapour deposition polymerisation process using the SCS/PDS 2010 Specialty Coating Systems, INC machine. The coating forms from a monomer vapour without an intermediate liquid stage. This results in very uniform coating on structures with sharp edges, points, flat surfaces, crevices or exposed internal surfaces. The parylene coating offers the advantages of chemical inertness, solvent resistance (most common solvents), outstanding barrier (very low permeability to moisture and gases), high resistance to bacteria (applicable to biochemical applications), a wide temperature range (-200°C to $+200^\circ\text{C}$) and it has a very high dielectric strength. Furthermore, it has very low coefficient of friction and hence reduces the liquids from adhering to the walls of the chambers.

7.6 Conclusions

The design details of the high frequency SH-SAW sensors have been covered in this chapter, for both the wired and wireless configurations. In the design of the wireless sensors the choice of three different types of reflectors has been made to determine the most efficient one. Various different sensor configurations at the different frequencies

were also designed. Also discussed is the fabrication process with as much as possible detail that could be disclosed by the fabricators (Kelvin Nanotechnology Ltd, Glasgow). The fabrication process is currently in progress and a processed wafer is expected within the next few weeks. The processing has taken longer than expected due to difficulties with optimising the fabrication particularly in overcoming the pyroelectric sparking on wafer surfaces. After optimising the process a test wafer was processed and very well defined features were achieved down to the 200nm size. Unfortunately due to time constraints for the submission of this research thesis, testing of the fabricated devices is not possible to be included.

The measurement setup for both the wired and proposed measurement setup for the wireless high frequency sensors have been described. The transmitting side of the interrogation unit for the wireless sensors has been built and is currently under test while the receiver end is being built. Various different antennas will be experimented for both the interrogation unit and the sensors, which is part of the further work. Liquid chambers for the new sensors have been designed, fabricated and will be tested on receiving the new devices as part of the future work.

7.7 References

- [7.1] A. Pohl, A review of wireless SAW sensors, *IEEE Transactions on Ultrasonics, Ferroelectrics, and Frequency Control*, Vol. 47, No. 2 (March 2000), pp. 317-332.
- [7.2] L. Reindel, A. Pohl, G. Scholl, T. Ostertag, and R. Weigel, SAW-Based radio sensor systems, *IEEE Sensors Journal*, vol. 1, no. 1(June 2001), pp. 69-78.
- [7.3] D. P. Morgan, *Surface-wave devices for signal processing*, Elsevier, Netherlands, (1985).
- [7.4] F.Seifert, W. E. Bulst, and C. Ruppel, Mechanical sensors based on surface acoustic waves, *Sensors and Actuators*, A44 (1994), pp. 231-239.
- [7.5] C. Dunnrowicz, F. Sandy, and T. Parker, Reflection of surface waves from periodic discontinuities, *Proceedings of the IEEE Ultrasonics Symposium*, (1976), pp. 386-390
- [7.6] K. Hashimoto, *Surface acoustic wave devices in telecommunications – modelling and simulation*, Springer-Verlag, Berlin, Heidelberg (2000), pp. 25-46.
- [7.7] R. E. Collin, *Field theory of guided waves*, McGraw-Hill, New York (1960), pp. 368-408
- [7.8] M. Takeuchi, and K. Yamanouchi, New type of SAW reflectors and resonators consisting of reflecting elements with positive and negative reflection coefficients, *IEEE Transactions of Ultrasonics, Ferroelectrics, and Frequency Control*, UFFC-33 (1986), pp. 369.
- [7.9] I. Leonte, M. Hunt, G. Sehra, M. Cole, J. W. Gardner, M. Noh, and P. Hesketh, A wireless microsystem for liquid analysis, *IEEE Sensors conference*, (October 2004), Vienna, Austria.
- [7.10] I. Leonte, M. Hunt, G. Sehra, M. Cole and J. W. Gardner, SAW bio-liquid sensors with RF interrogation, *Proceedings of the IEEE High Frequency Postgraduate Students Colloquium*, (September 2004) UMIST Manchester, UK, pp. 47-52.
- [7.11] P. F. Jacobs, Rapid prototyping and manufacturing, fundamental of stereolithography, *Society of manufacturing engineers*, (1992).
- [7.12] A. Kataria, and D. W. Rosen, Building around inserts: Methods for fabricating complex devices in stereolithography, *Proc. of Design Engineering Technical Conferences*, DETC00/MECH-14206, (September 2000).

- [7.13] K. Okuta, T. Ogata, M. Tsubio, and S. Kojima, Development of mass productive micro stereo lithography, *Proceedings of IEEE International Conference on Micro Electro Mechanical Systems* (1996), pp. 301-306,
- [7.14] A. Bertsch, P. Bernhard, C. Vogt, and P. Renaud, Rapid prototyping of small size objects, *Rapid Prototyping Journal*, Vol. 6, No.4 , (2000), pp. 259-266.
- [7.15] A. Bertsch, S. Zissi, J. Y. Jezeque, S. Corbel, and J. C. Andre, Microstereophotolithography using a liquid crystal display as dynamic mask-generator, *Micro. Technol.*, 3 (1997), pp. 42-47.
- [7.16] A. Bertsch, J. Y. Jezequel, and J. C. Andre, Study of the spatial resolution of a new 3D microfabrication process: the microstereo-photolithography using a dynamic mask generator technique, *Journal of Photochem. Photobiol. A: Chem.* Vol. 107 (1997), pp. 275-281.
- [7.17] L. Beluze, A. Bertsch, and P. Renaud, Microstereolithography: a new process to build complex 3D objects, Symposium on design, test and microfabrication of MEMs / MOEMs, *Proc. of SPIE*, Vol. 3680, No. 2, (1999), pp. 808-817.
- [7.18] K. Ikuta, and K. Hirowatari, Real three dimensional micro fabrication using stereo lithography and metal moulding, *Proceedings of the IEEE International Workshop on Micro Electro Mechanical Systems* (1993), pp. 42-47.

CHAPTER 8

Conclusions and further work

8.1 Aims and conclusions

In recent years there has been significant interest in the development of biomimetic devices so called “electronic tongue” and “electronic nose” devices for various applications including medical diagnostics. Many applications, such as environmental monitoring, identification and quality control in the food and beverage industries, require on-line or at-line monitoring so there is a large demand for electronic tongue/nose sensors at low cost with good reproducibility. The majority of the reported liquid sensors are based upon an electrochemical principle, the most common ones being potentiometric, conductimetric and amperometric (or voltammetric). These devices employ ion selective electrodes/membranes that make them more specific to only certain types of chemical species, so multiple sensor elements with different kinds of electrode materials (metals and/or coating materials) are required to identify different samples. Electrochemical sensors are extremely sensitive to the impedance between the electrode and liquid (a dipole layer) and thus very sensitive to trace level contamination or fouling.

The aim of this study has been the development and characterisation of new low cost, robust, micropower, durable SH-SAW liquid sensors. The approach adopted is based upon a generic fingerprint approach correlated to key physical parameters, i.e. the technique does not rely upon the use of inorganic, organic or biological layers. The approach is thus inherently superior to standard electrochemical techniques that are

more surface sensitive (nanolayers) and less robust when coated with biological membranes (e.g. glucose sensors). The study involved, firstly the design and development of SH-SAW devices employing a dual delay line configuration with no selective coatings; secondly the combination of the SH-SAW devices with bulk CMOS chemFET electronic nose devices to show the possibility of an artificial flavour sensing system; and finally the design and fabrication of high frequency SH-SAW devices for possible wireless sensing applications.

The SH-SAW devices have been employed to sense a number of different liquid analytes and provided very encouraging results. The dual delay line configuration makes it possible to attain acoustoelectric and mechanical properties of the sample liquids. The combined electronic tongue/nose system was able to discriminate certain solutions, which neither the tongue nor the nose alone, could discriminate separately.

8.1.1 Dual-delay line SH-SAW sensors

The design of the device itself was an important consideration, because this defines the operation of the sensor. The choice of the substrate was critical because it governs the acoustic wave propagation mode that is appropriate for liquid sensing. LiTaO_3 has a high piezoelectric constant and so was chosen for the SH-SAW devices upon which the dual delay line configuration was patterned to allow simultaneous measurements of both the acoustoelectric and mechanical properties of the liquid under test. A fully integrated version could use ZnO as the piezoelectric layer that is compatible with CMOS technology.

The main component in the sensor design was the transducers (IDTs) which were carefully designed to match the source and loads 50 Ω impedances, thus allowing maximum power transmission and low insertion losses. The wafers were processed at the Central Microstructures Facility (Rutherford Appleton Laboratories), Didcot, UK, by a standard photolithography process, and using gold as the metallisation layer due to its relative inertness and high conductivity.

The SAW sensors were mounted on custom built PCBs with a PTFE cell to accommodate the liquid under test. The sensors were characterised and used to analyse a number of different liquid samples using a signal generator/vector voltmeter setup in a controlled environment. The signal generator was used to feed a single RF frequency to drive the sensors and a vector voltmeter, controlled via a GPIB interface to a PC

using LabVIEWTM software, used to measure the amplitude ratio and phase difference between the input and output signals.

8.1.2 *S*-parameter characterisation of the SH-SAW devices

The *S*-parameter measurement of the devices was critical to attain useful information about the performance of the devices and parameters, such as the resonant frequency of the transducers and the transmission frequency for minimum insertion losses. The HP 8753ES vector network analyser setup was used to measure the *S*-parameters. The devices demonstrated a typical resonant frequency value of around (61 ± 2) MHz with a return loss of approximately -25 dB ($S_{11} \sim 0.05$ with 0 being perfectly matched). This showed that the input port of the device was not perfectly matched to the 50 Ω source but allowed the majority (95%) of the power through with 5% reflecting back or lost. The impedance of the input port was also measured using the Smith chart format of the network analyser and typical impedance values of around (50 ± 3) Ω were seen for the transducers, showing a close match to the 50 Ω source and load. Insertion losses of 10 to 15 dB were measured at the transmission frequencies, which compare to 15 dB for the theoretical value.

8.1.3 SH-SAW as liquid sensors (electronic tongue)

Having determined the key parameters from the network analyser, the signal generator/vector voltmeter setup was used to analyse a number of different liquid samples. Initial sensor characterisation consisted of measuring sensitivities to temperature, volume of liquid loadings and dielectric permittivity. A temperature coefficient of approximately -30 ppm/ $^{\circ}$ C was observed for a single line but the differential frequency shift of the dual delay line configuration, reduced this value by a factor of 150 to only -0.2 ppm/ $^{\circ}$ C. A very significant reduction in the temperature dependence of the baseline signal. The effect of liquid volume loading above the sensor surface was investigated and results showed negligible mass loading effect on the output of the sensors at loads above a value of 40 μ l of water, i.e. 40 mg.

The ability of the sensing system to discriminate between four basic tastes without the use of either electrochemical sensors or selective membranes has been demonstrated. The SAW sensor responds to physical rather than chemical or biological

properties at the liquid interface, and so in an indirect measure of taste. A detection limit of less than 1 mM of sweet, salty and sour, and 1 μ M of bitter was observed.

The theory of the electro-acoustic interactions has been used to relate the experimental results to electrical properties of the liquids under test and promising results have been achieved. Two basic physical parameters, conductivity or pH of the liquid, were studied and found that they cannot be used to classify uniquely both the type of taste and its concentration – whereas the four acoustic parameters proved to do so.

Apart from using simple compounds each related to a single basic taste, the sensing system was also used to analyse complex samples, such as cow's milk. The sensors have been used to discriminate between milks of different fat content (skimmed, semi-skimmed and full-fat) as well as in a dilution test of full-fat milk. A very encouraging sensitivity figure of about 0.1% fat content was achieved. Promising results were also obtained from the milk freshness test showing the possible application of the sensors as milk freshness indicators.

The ability to discriminate between different levels of sourness (indirectly measured through the bacterial growth) in milk samples, have been presented using milk samples with two different types of bacterial species (*S. uberis* and *S. aureus*). The sensors again achieved an encouraging figure for the limit of detection of about 10^3 cfu/ml . This value of sensitivity is not enough for some applications but it can be improved by coating the sensing surface of the devices with a bio-chemical selective coating. But that would defeat the purpose here to employ robust uncoated SAW devices.

The results imply that some relatively subtle changes in taste in milk can be measured because the growth of bacteria leads to the breakdown in cell membranes which in turn results in the release of high levels of calcium – and hence a significant change in the conductivity of the milk.

The sensors were also used to classify fresh milk samples and bulling milk samples from the same cow at different points in the oestrus cycle and encouraging results were achieved however this requires further work. Similarly in the experiment where mastitic milk samples from nine cows were run through the electronic tongue, although tight clustering and discrimination was achieved, further work is again required to conclude meaningful results. The main issue here is that the cow to cow

variation in milk quality is considerable and so this may explain some of the variation between milk samples.

All the data have been analysed using principal components analysis showing that the sample vectors are simply linearly separable – demonstrating a basic pattern recognition problem. Thus there is scope to improve the discrimination power through the use of more sophisticated pre-processing techniques (i.e. feature selection) and non-linear pattern recognition classifiers (e.g. support vector machines).

8.1.4 Combined electronic tongue/nose system

The combined nose/tongue flavour system employed both polymer coated chemFET sensors and dual SH-SAW sensors. The 4 element FET array was made using a bulk silicon CMOS process, with an active polymeric gate material, operating near ambient temperatures (< 100 °C), with channel lengths of either 10 μm or 5 μm . These room temperature devices were designed and fabricated for research carried out by Dr. J. A. Covington (School of Engineering, University of Warwick) in collaboration with the Institute of Microtechnology at the University of Neuchatel. The array device consisted of 4 *n*-channel enhanced MOSFETs with a meandering channel and a commoned gate and drain, and was operated in the saturated regime. The gold gate was etched to expose the gate oxide so the polymer is in contact with the gate oxide and form the conducting but porous gate. Though not normally used in a standard CMOS process, gold allows many different active sensing materials to be used. For standard CMOS, doped polysilicon can be used instead of gold, but there are limitations to the number of electro-active polymers that can be deposited on top of it.

Carbon black composite polymers comprising of, insulating polymer (usually used in gas chromatography) with carbon black nanospheres endowing electrical properties to the composite material, were used in the combined system. The three polymers used were, poly(ethylene-co-vinyl acetate), poly(styrene-co-butadiene) and poly(9-vinylcarbazole) mixed with a 20% carbon loading (by weight). These polymers can be spray coated on to the FET gates and so do not require gate materials suitable for electrochemistry. The chemFET devices were controlled and measured using custom instrumentation interfaced by LabVIEWTM software.

The combined system was then used to analyse samples previously studied with just the SH-SAW sensors (i.e. different milks, orange juice and water). Results from these initial experiments showed little contribution from the electronic nose, in

separating them. However, the use of the combined nose/tongue system was justified when further experiments were undertaken in which three solutions with inorganic low vapour pressures and two organic solutions with high vapour pressures were tested by the system. The results of the individual sensors showed that the tongue partially separated the samples and required a third principal component for full separation. Conversely, the nose could not separate all the samples; however it showed very good responses to the high vapour pressure sampled which were not very well separated by the tongue. The combination results were thus superior and it was concluded that the combination of the electronic nose and electronic tongue produced 100% discrimination between all of these samples. Overall the results are very encouraging and suggest the possible applications of the flavour system to analyse complex solutions in the food and beverage industry and for screening of clinical samples.

8.1.5 High frequency SH-SAW devices

New high frequency (433 MHz, 869 MHz, 2.45 GHz and 10 GHz) devices were designed for both wired and wireless configurations with ordinary and double finger electrodes that minimise reflections from periodic electrodes. Three different types of reflectors were designed for the wireless devices to determine the most efficient type. The devices are currently being fabricated by Kelvin Nanotechnology Ltd, Glasgow, UK.

The proposed measurement system for the wireless sensors is currently being investigated and is based on similar operational principles to pulsed radar systems to comply with UK regulations as specified in the Radio Interface Requirements EN 300 220-1 for Short-Range Devices. The measurement system requires careful design and further work is required to determine the resolution and accuracy of these high frequency sensors when operating in complex liquids. Also additional work is required on the antenna designs to develop miniature and highly efficient device antennas as the losses in the wireless system in the presence of a liquid on the sensing surface are relatively high (approximately 40 dB in the sensor). This work is being undertaken by Ms Irina Leonte another PhD student in the Sensors Research laboratory.

8.1.6 Project objectives

Many of the objectives of this study have been realised; these are summarised below:

- SH-SAW liquid sensors based on dual delay line configuration without selective coatings have been successfully designed and developed.
- The liquid sensors have been characterised and the principle of operation without the presence of any bio-chemical selective coatings has been proven.
- The ability of the dual SH-SAW devices to be used as taste sensors has been demonstrated by classifying basic synthetic solutions corresponding to the four basic tastes. Complex liquid samples have also been classified with very encouraging results.
- A combined electronic tongue/nose system has been realised and the flavour system's combined ability to discriminate solutions, better than the tongue or the nose individually, has been successfully demonstrated.
- Lastly, high frequency SH-SAW devices have been designed and are currently being fabricated; liquid test cells have been fabricated and an interrogation system is currently being developed for the wireless sensors.

8.2 Application of the dual SH-SAW sensors

Clearly, the outcome of this research is to create a possible commercial sensor for the electronic tongue industry. An instrument of this type could contain a single sensor or an array of these sensors for liquid sensing. The question is whether these sensors are superior in some way to present commercial sensors or give a significant advantage for an electronic tongue instrument. On the positive side, these sensors are miniature, low-cost, robust, durable, micropower devices based on physical rather than electrochemical principles (as are most current commercial system). Furthermore, the sensors have the ability to detect various properties of an adjacent liquid without any membrane, making the devices more durable with a longer life time in comparison to coated electrochemical sensors that are susceptible to trace level surface contamination/fouling. However, there is loss of specificity, and in some applications, selectivity, but the sensors can easily be adapted to a particular application by simply coating the sensing area improving the selectivity and sensitivity. The fabrication process is simple and controllable so repeatability of the devices is not a real issue, however the packaging of the devices is very critical and small variations can result to

devices with different acoustic losses. The differential approach does ameliorate this issue because the differential loss of the dual delays is critical and not the absolute attenuation or delay. Effects from the external environment (e.g. temperature) are minimised through having a dual delay line configuration, which again makes these devices very desirable for an electronic tongue instrument.

The sensitivity and selectivity limitation has already been addressed above. Another limitation is the measurement systems used (network analyser, signal generator/vector voltmeter), which are expensive, complex and not portable, making them impractical for field applications. Furthermore, the resolution and the time to take a measurement from the sensors may not be good enough for certain applications using these measurement systems. These limitations can be overcome by the design of SAW oscillator electronics which also improves the sensitivity of the sensing system. This has been discussed as further work.

The high frequency SH-SAW devices show promise to use in electronic tongue instruments, as not only that they have higher sensitivity they also offer the capability of wireless operation for example possible embedding of the sensors in the packaging of perishable drinks to monitor freshness.

8.3 Future work

In this study the work with the SH-SAW liquid sensors has been directed upon proving the fundamental principle of detecting different liquids acoustically without a selective coating on the sensing surface, but at the expense of selectivity and sensitivity in certain applications. Since the results from the study show great promise for the use of these sensors in electronic tongue instruments the next step would be to improve the sensitivity and resolution of the measurements by developing the SH-SAW delay lines in an oscillator loop to make real-time measurements. This will also result in a portable system and possibility for hand held systems. Furthermore, the use of these SH-SAW devices as biosensors is a possibility because they can easily be adapted by coating the sensing area with bio-chemical coating which will significantly enhance the selectivity and sensitivity to particular species – at the cost of repeatability and life-time.

The combination of the SH-SAW electronic tongue devices and the chemFET electronic nose devices also gave promising results and is worth exploring further with possible integration of two, especially having the SH-SAW delay line in an oscillator

loop. The FETs are made using a standard CMOS process and so integration of the MOSFETs and associated circuitry is not an issue. The most difficult part of the process is the opening up of the gate to the ultrathin gate oxide and the long term stability of the baseline signal (i.e. threshold voltage). The latter can be addressed again by the use of a differential measurement to remove the problem of drifting of the absolute value of the polymer work function.

The SH-SAW sensors in the study have intrinsically good reproducibility and stability they can be applied to a number of applications such as in identification and quality control of liquid sample. However the size of the devices in this study was relatively large and this means higher production costs therefore the developing the high frequency devices, is very desirable. Not only will this increase the sensitivity it will also reduce cost of production. (for example the number of 60 MHz devices per 3" wafer was ~ 40 and number of 433 MHz devices per 3" wafer is ~ 200) Operating at the higher frequencies also allows the possibility of wireless sensing as proposed and this is currently being studied as future work.

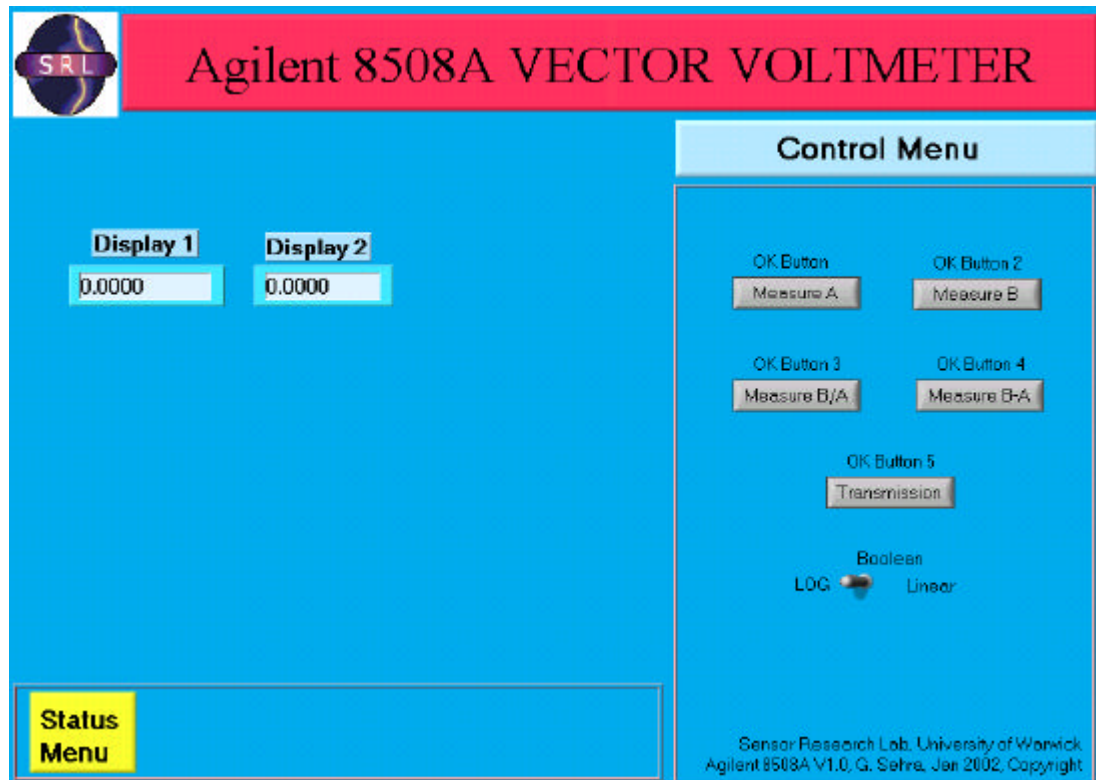
The results of this research have shown great promise with a large number of possible applications. This great potential provides the encouragement to embark on further development of these liquid/odour sensing devices, with the possibility of integrating the technologies into a commercial flavour sensing instrument.

Appendix A

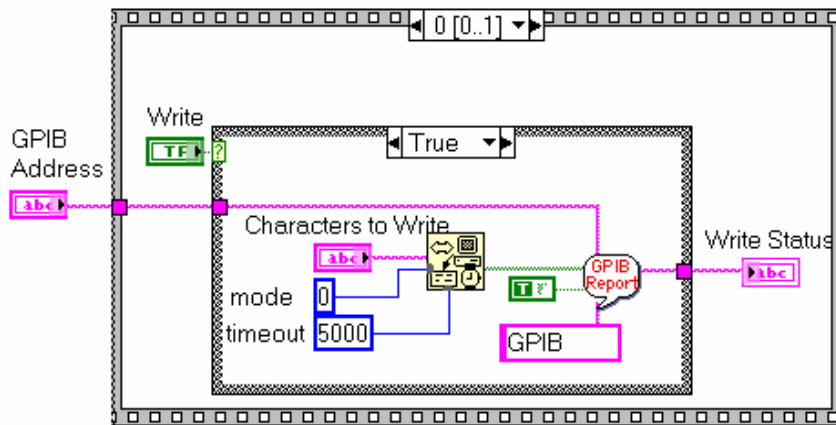
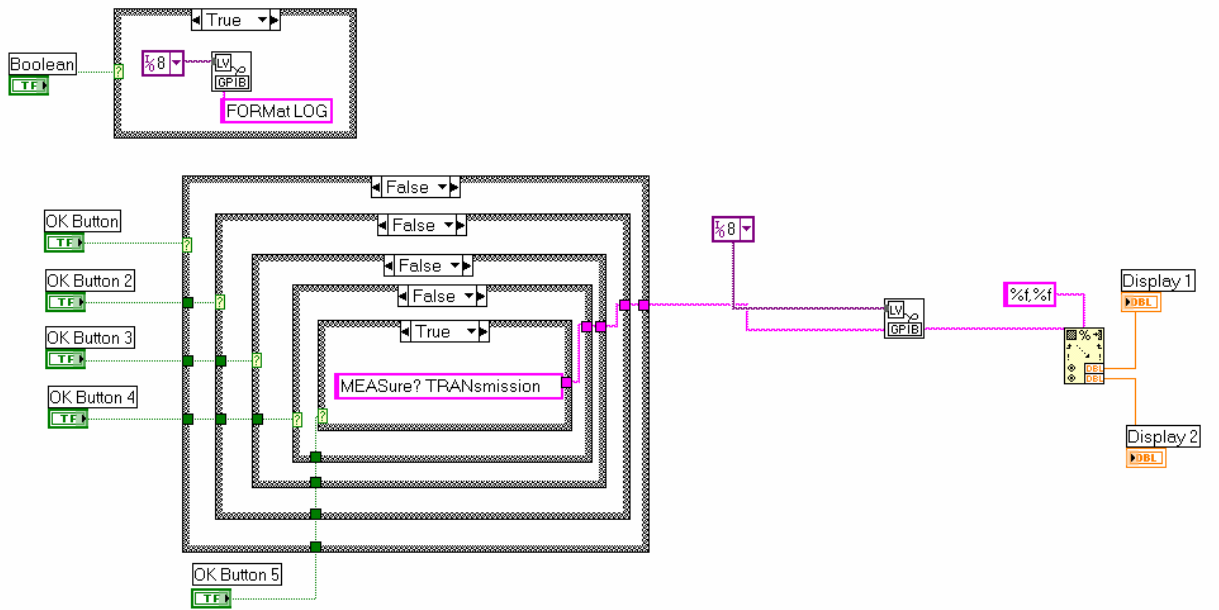
Software programs

This appendix contains the simple software for the top level routines for:

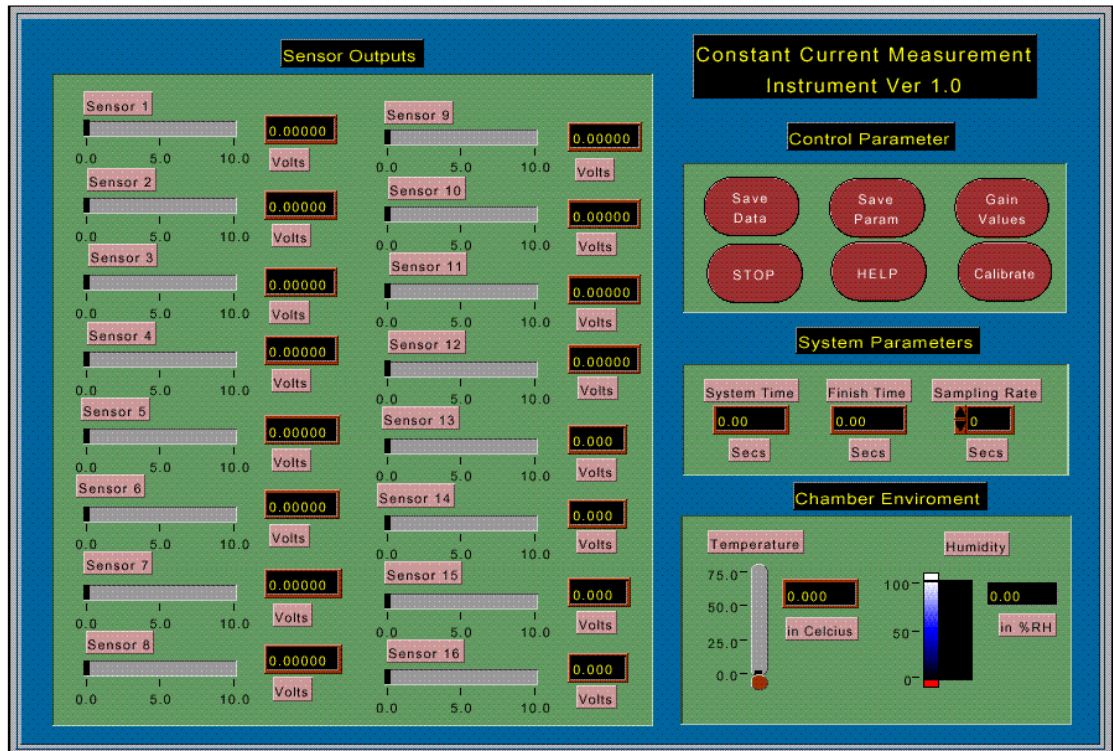
1. GPIB controller for vector voltmeter
2. MatlabTM program for PCA analysis

Front panel of GPIB Vector voltmeter controller

Block diagram of GPIB controller



Front panel of constant current characterisation instrument



Principal component analysis Matlab™ software

```

clear all;clc;
N1=load('Tastesdilution.txt');
rows=size(N1,1)
clus=25;
h1=(rows/clus);g=rows/clus;h=rows/clus;e=0;margin=h1;
min_N1=min(N1,[],1);max_N1=max(N1,[],1);
for i=1:rows,for j=1:4,X(i,j)=(N1(i,j)-min_N1(1,j))/(max_N1(1,j)-min_N1(1,j));end;end;
h1=rows/clus;g=rows/clus;h=rows/clus;e=0;g1=(rows/clus);
[center,U,obj_fcn] = fcm(X,clus);clc;
%-----
%Display for the programmer
%-----
disp('-----');
disp(' % Processing Smart -Tongue data %');
disp(' % Data processing program developed by %');
disp(' % Gurmukh Sehra %');
disp(' % %');
disp('-----');
disp('');
%-----
% FINDING most POSSIBLE MEMBERSHIP FOR EACH ELEMENT, finding the maximum membership from
% the n memberships for each data point.Maximum membership indicates the proper membership
% for that data point.
%-----
for i=1:rows,[q(i) qt(i)]=max(U(:,i));end;c=[];
%-----
AD=abs(corrcoef(X));[I,t]=sort(sum(AD,2));
Lcs1=X(:,t(1,1));Lcs2=X(:,t(2,1));Lcs3=X(:,t(3,1));
C1=center(:,t(1,1)); C2=center(:,t(2,1)); C3=center(:,t(3,1));
%-----
%PCA Plot%
%-----
[scores,loads,ssq] = pca(X,0,0,3);D1=scores(:,1);D2=scores(:,2);D3=scores(:,3);
if clus==2,
    a1=D1(1:g,1);a2=D2(1:g,1);a3=D3(1:g,1);e=g;
    b1=D1(e+1:2*g,1);b2=D2(e+1:2*g,1);b3=D3(e+1:2*g,1);
end;
if clus==3,
    a1=D1(1:g,1);a2=D2(1:g,1);a3=D3(1:g,1);e=g;
    b1=D1(e+1:2*g,1);b2=D2(e+1:2*g,1);b3=D3(e+1:2*g,1);e=2*g;
    c1=D1(e+1:3*g,1);c2=D2(e+1:3*g,1);c3=D3(e+1:3*g,1);
end;
if clus==4,
    a1=D1(1:g,1);a2=D2(1:g,1);a3=D3(1:g,1);e=g;
    b1=D1(e+1:2*g,1);b2=D2(e+1:2*g,1);b3=D3(e+1:2*g,1);e=2*g;
    c1=D1(e+1:3*g,1);c2=D2(e+1:3*g,1);c3=D3(e+1:3*g,1);e=3*g;
    d1=D1(e+1:4*g,1);d2=D2(e+1:4*g,1);d3=D3(e+1:4*g,1);
end;
if clus==5,
    a1=D1(1:g,1);a2=D2(1:g,1);a3=D3(1:g,1);e=g;
    b1=D1(e+1:2*g,1);b2=D2(e+1:2*g,1);b3=D3(e+1:2*g,1);e=2*g;
    c1=D1(e+1:3*g,1);c2=D2(e+1:3*g,1);c3=D3(e+1:3*g,1);e=3*g;
    d1=D1(e+1:4*g,1);d2=D2(e+1:4*g,1);d3=D3(e+1:4*g,1);e=4*g;
    e1=D1(e+1:5*g,1);e2=D2(e+1:5*g,1);e3=D3(e+1:5*g,1);
end;
if clus==6,
    a1=D1(1:g,1);a2=D2(1:g,1);a3=D3(1:g,1);e=g;
    b1=D1(e+1:2*g,1);b2=D2(e+1:2*g,1);b3=D3(e+1:2*g,1);e=2*g;
    c1=D1(e+1:3*g,1);c2=D2(e+1:3*g,1);c3=D3(e+1:3*g,1);e=3*g;
    d1=D1(e+1:4*g,1);d2=D2(e+1:4*g,1);d3=D3(e+1:4*g,1);e=4*g;
    e1=D1(e+1:5*g,1);e2=D2(e+1:5*g,1);e3=D3(e+1:5*g,1);e=5*g;
    f1=D1(e+1:6*g,1);f2=D2(e+1:6*g,1);f3=D3(e+1:6*g,1);
end;
if clus==7,
    a1=D1(1:g,1);a2=D2(1:g,1);a3=D3(1:g,1);e=g;
    b1=D1(e+1:2*g,1);b2=D2(e+1:2*g,1);b3=D3(e+1:2*g,1);e=2*g;
    c1=D1(e+1:3*g,1);c2=D2(e+1:3*g,1);c3=D3(e+1:3*g,1);e=3*g;
    d1=D1(e+1:4*g,1);d2=D2(e+1:4*g,1);d3=D3(e+1:4*g,1);e=4*g;
    e1=D1(e+1:5*g,1);e2=D2(e+1:5*g,1);e3=D3(e+1:5*g,1);e=5*g;
    f1=D1(e+1:6*g,1);f2=D2(e+1:6*g,1);f3=D3(e+1:6*g,1);e=6*g;
    g1=D1(e+1:7*g,1);g2=D2(e+1:7*g,1);g3=D3(e+1:7*g,1);
end;
if clus==8,

```



```

a1=D1(1:g,1);a2=D2(1:g,1);a3=D3(1:g,1);e=g;
b1=D1(e+1:2*g,1);b2=D2(e+1:2*g,1);b3=D3(e+1:2*g,1);e=2*g;
c1=D1(e+1:3*g,1);c2=D2(e+1:3*g,1);c3=D3(e+1:3*g,1);e=3*g;
d1=D1(e+1:4*g,1);d2=D2(e+1:4*g,1);d3=D3(e+1:4*g,1);e=4*g;
e1=D1(e+1:5*g,1);e2=D2(e+1:5*g,1);e3=D3(e+1:5*g,1);e=5*g;
f1=D1(e+1:6*g,1);f2=D2(e+1:6*g,1);f3=D3(e+1:6*g,1);e=6*g;
g1=D1(e+1:7*g,1);g2=D2(e+1:7*g,1);g3=D3(e+1:7*g,1);e=7*g;
h1=D1(e+1:8*g,1);h2=D2(e+1:8*g,1);h3=D3(e+1:8*g,1);e=8*g;
i1=D1(e+1:9*g,1);i2=D2(e+1:9*g,1);i3=D3(e+1:9*g,1);e=9*g;
j1=D1(e+1:10*g,1);j2=D2(e+1:10*g,1);j3=D3(e+1:10*g,1);e=10*g;
k1=D1(e+1:11*g,1);k2=D2(e+1:11*g,1);k3=D3(e+1:11*g,1);e=11*g;
l1=D1(e+1:12*g,1);l2=D2(e+1:12*g,1);l3=D3(e+1:12*g,1);e=12*g;
m1=D1(e+1:13*g,1);m2=D2(e+1:13*g,1);m3=D3(e+1:13*g,1);e=13*g;
n1=D1(e+1:14*g,1);n2=D2(e+1:14*g,1);n3=D3(e+1:14*g,1);
end;
if clus==15,
a1=D1(1:g,1);a2=D2(1:g,1);a3=D3(1:g,1);e=g;
b1=D1(e+1:2*g,1);b2=D2(e+1:2*g,1);b3=D3(e+1:2*g,1);e=2*g;
c1=D1(e+1:3*g,1);c2=D2(e+1:3*g,1);c3=D3(e+1:3*g,1);e=3*g;
d1=D1(e+1:4*g,1);d2=D2(e+1:4*g,1);d3=D3(e+1:4*g,1);e=4*g;
e1=D1(e+1:5*g,1);e2=D2(e+1:5*g,1);e3=D3(e+1:5*g,1);e=5*g;
f1=D1(e+1:6*g,1);f2=D2(e+1:6*g,1);f3=D3(e+1:6*g,1);e=6*g;
g1=D1(e+1:7*g,1);g2=D2(e+1:7*g,1);g3=D3(e+1:7*g,1);e=7*g;
h1=D1(e+1:8*g,1);h2=D2(e+1:8*g,1);h3=D3(e+1:8*g,1);e=8*g;
i1=D1(e+1:9*g,1);i2=D2(e+1:9*g,1);i3=D3(e+1:9*g,1);e=9*g;
j1=D1(e+1:10*g,1);j2=D2(e+1:10*g,1);j3=D3(e+1:10*g,1);e=10*g;
k1=D1(e+1:11*g,1);k2=D2(e+1:11*g,1);k3=D3(e+1:11*g,1);e=11*g;
l1=D1(e+1:12*g,1);l2=D2(e+1:12*g,1);l3=D3(e+1:12*g,1);e=12*g;
m1=D1(e+1:13*g,1);m2=D2(e+1:13*g,1);m3=D3(e+1:13*g,1);e=13*g;
n1=D1(e+1:14*g,1);n2=D2(e+1:14*g,1);n3=D3(e+1:14*g,1);e=14*g;
o1=D1(e+1:15*g,1);o2=D2(e+1:15*g,1);o3=D3(e+1:15*g,1);
end;
if clus==16,
a1=D1(1:g,1);a2=D2(1:g,1);a3=D3(1:g,1);e=g;
b1=D1(e+1:2*g,1);b2=D2(e+1:2*g,1);b3=D3(e+1:2*g,1);e=2*g;
c1=D1(e+1:3*g,1);c2=D2(e+1:3*g,1);c3=D3(e+1:3*g,1);e=3*g;
d1=D1(e+1:4*g,1);d2=D2(e+1:4*g,1);d3=D3(e+1:4*g,1);e=4*g;
e1=D1(e+1:5*g,1);e2=D2(e+1:5*g,1);e3=D3(e+1:5*g,1);e=5*g;
f1=D1(e+1:6*g,1);f2=D2(e+1:6*g,1);f3=D3(e+1:6*g,1);e=6*g;
g1=D1(e+1:7*g,1);g2=D2(e+1:7*g,1);g3=D3(e+1:7*g,1);e=7*g;
h1=D1(e+1:8*g,1);h2=D2(e+1:8*g,1);h3=D3(e+1:8*g,1);e=8*g;
i1=D1(e+1:9*g,1);i2=D2(e+1:9*g,1);i3=D3(e+1:9*g,1);e=9*g;
j1=D1(e+1:10*g,1);j2=D2(e+1:10*g,1);j3=D3(e+1:10*g,1);e=10*g;
k1=D1(e+1:11*g,1);k2=D2(e+1:11*g,1);k3=D3(e+1:11*g,1);e=11*g;
l1=D1(e+1:12*g,1);l2=D2(e+1:12*g,1);l3=D3(e+1:12*g,1);e=12*g;
m1=D1(e+1:13*g,1);m2=D2(e+1:13*g,1);m3=D3(e+1:13*g,1);e=13*g;
n1=D1(e+1:14*g,1);n2=D2(e+1:14*g,1);n3=D3(e+1:14*g,1);e=14*g;
o1=D1(e+1:15*g,1);o2=D2(e+1:15*g,1);o3=D3(e+1:15*g,1);
p1=D1(e+1:16*g,1);p2=D2(e+1:16*g,1);p3=D3(e+1:16*g,1);
end;

figure(2);view(3);grid on ;hold on;

if clus==2, plot3(a1,a2,a3,'gs');plot3(b1,b2,b3,'r+');
    q=num2str(round(g));q1=num2str((round(g)+1));q2=num2str(2*round(g));
end;

if clus==3,plot3(a1,a2,a3,'gs');plot3(b1,b2,b3,'r+');plot3(c1,c2,c3,'kh');
    q=num2str(round(g));q1=num2str((round(g)+1));q2=num2str(2*round(g));
    q3=num2str(2*round(g)+1);q4=num2str(3*round(g));
end;

if clus==4, plot3(a1,a2,a3,'gs');plot3(b1,b2,b3,'r+');plot3(c1,c2,c3,'kh');plot3(d1,d2,d3,'b*');
    q=num2str(round(g));q1=num2str((round(g)+1));q2=num2str(2*round(g));
    q3=num2str(2*round(g)+1);q4=num2str(3*round(g));q5=num2str(3*round(g)+1);q6=num2str(4*round(g));
end;

if clus==5,plot3(a1,a2,a3,'ks');plot3(b1,b2,b3,'k+');plot3(c1,c2,c3,'kh');plot3(d1,d2,d3,'k*');
    plot3(e1,e2,e3,'ko');
    q=num2str(round(g));q1=num2str((round(g)+1));q2=num2str(2*round(g));
    q3=num2str(2*round(g)+1);q4=num2str(3*round(g));q5=num2str(3*round(g)+1);
    q6=num2str(4*round(g));q7=num2str(4*round(g)+1);q8=num2str(5*round(g));
end;

if clus==6, plot3(a1,a2,a3,'gs');plot3(b1,b2,b3,'r+');plot3(c1,c2,c3,'kh');
    plot3(d1,d2,d3,'b*');plot3(e1,e2,e3,'c+');plot3(f1,f2,f3,'mx');

```



```

q=num2str(round(g));q1=num2str((round(g)+1));q2=num2str(2*round(g));
q3=num2str(2*round(g)+1);q4=num2str(3*round(g));q5=num2str(3*round(g)+1);
q6=num2str(4*round(g));q7=num2str(4*round(g)+1);q8=num2str(5*round(g));
q9=num2str(5*round(g)+1);q10=num2str(6*round(g));
end;

if clus==7, plot3(a1,a2,a3,'gs');plot3(b1,b2,b3,'r+');plot3(c1,c2,c3,'kh');
plot3(d1,d2,d3,'b*');plot3(e1,e2,e3,'c+');plot3(f1,f2,f3,'mx');plot3(g1,g2,g3,'mv');
q=num2str(round(g));q1=num2str((round(g)+1));q2=num2str(2*round(g));
q3=num2str(2*round(g)+1);q4=num2str(3*round(g));q5=num2str(3*round(g)+1);
q6=num2str(4*round(g));q7=num2str(4*round(g)+1);q8=num2str(5*round(g));
q9=num2str(5*round(g)+1);q10=num2str(6*round(g));q11=num2str(6*round(g)+1);q12=num2str(7*round(g));
end;

if clus==8, plot3(a1,a2,a3,'gs');plot3(b1,b2,b3,'r+');plot3(c1,c2,c3,'kh');
plot3(d1,d2,d3,'b*');plot3(e1,e2,e3,'c+');plot3(f1,f2,f3,'mx');plot3(g1,g2,g3,'bv');plot3(h1,h2,h3,'rd');
q=num2str(round(g));q1=num2str((round(g)+1));q2=num2str(2*round(g));
q3=num2str(2*round(g)+1);q4=num2str(3*round(g));q5=num2str(3*round(g)+1);
q6=num2str(4*round(g));q7=num2str(4*round(g)+1);q8=num2str(5*round(g));
q9=num2str(5*round(g)+1);q10=num2str(6*round(g));q11=num2str(6*round(g)+1);q12=num2str(7*round(g));
q13=num2str(7*round(g)+1);q14=num2str(8*round(g));
%legend('Fresh1','Fresh2','Bulling1','Bulling2','low1','low2','high1','high2');
end;

if clus==9, plot3(a1,a2,a3,'gs');plot3(b1,b2,b3,'r+');plot3(c1,c2,c3,'kh');
plot3(d1,d2,d3,'b*');plot3(e1,e2,e3,'c+');plot3(f1,f2,f3,'mx');plot3(g1,g2,g3,'bv');plot3(h1,h2,h3,'rd');plot3(I1,I2,I3,'gd');
q=num2str(round(g));q1=num2str((round(g)+1));q2=num2str(2*round(g));
q3=num2str(2*round(g)+1);q4=num2str(3*round(g));q5=num2str(3*round(g)+1);
q6=num2str(4*round(g));q7=num2str(4*round(g)+1);q8=num2str(5*round(g));
q9=num2str(5*round(g)+1);q10=num2str(6*round(g));q11=num2str(6*round(g)+1);q12=num2str(7*round(g));
q13=num2str(7*round(g)+1);q14=num2str(8*round(g));q15=num2str(8*round(g)+1);q16=num2str(9*round(g));
end;

if clus==10, plot3(a1,a2,a3,'gs');plot3(b1,b2,b3,'r+');plot3(c1,c2,c3,'kh');
plot3(d1,d2,d3,'b*');plot3(e1,e2,e3,'c+');plot3(f1,f2,f3,'mx');plot3(g1,g2,g3,'bv');plot3(h1,h2,h3,'rd');plot3(i1,i2,i3,'gd');plot3(J1,J2,J3,'ks');
q=num2str(round(g));q1=num2str((round(g)+1));q2=num2str(2*round(g));
q3=num2str(2*round(g)+1);q4=num2str(3*round(g));q5=num2str(3*round(g)+1);
q6=num2str(4*round(g));q7=num2str(4*round(g)+1);q8=num2str(5*round(g));
q9=num2str(5*round(g)+1);q10=num2str(6*round(g));q11=num2str(6*round(g)+1);q12=num2str(7*round(g));
q13=num2str(7*round(g)+1);q14=num2str(8*round(g));q15=num2str(8*round(g)+1);q16=num2str(9*round(g));
q17=num2str(9*round(g)+1);q18=num2str(10*round(g));
end;

if clus==11, plot3(a1,a2,a3,'gs');plot3(b1,b2,b3,'r+');plot3(c1,c2,c3,'kh');
plot3(d1,d2,d3,'b*');plot3(e1,e2,e3,'c+');plot3(f1,f2,f3,'mx');plot3(g1,g2,g3,'bv');plot3(h1,h2,h3,'rd');plot3(i1,i2,i3,'gd');plot3(j1,j2,j3,'ks');
plot3(k1,k2,k3,'bs');
q=num2str(round(g));q1=num2str((round(g)+1));q2=num2str(2*round(g));
q3=num2str(2*round(g)+1);q4=num2str(3*round(g));q5=num2str(3*round(g)+1);
q6=num2str(4*round(g));q7=num2str(4*round(g)+1);q8=num2str(5*round(g));
q9=num2str(5*round(g)+1);q10=num2str(6*round(g));q11=num2str(6*round(g)+1);q12=num2str(7*round(g));
q13=num2str(7*round(g)+1);q14=num2str(8*round(g));q15=num2str(8*round(g)+1);q16=num2str(9*round(g));
q17=num2str(9*round(g)+1);q18=num2str(10*round(g));q19=num2str(10*round(g)+1);q20=num2str(11*round(g));
legend('Fresh','Bulk','Kylie','Naomi','Millie','Leanne','Anna','Tazmine','Trixi','Opal','Lorraine');
end;

if clus==12, plot3(a1,a2,a3,'gs');plot3(b1,b2,b3,'r+');plot3(c1,c2,c3,'kh');
plot3(d1,d2,d3,'b*');plot3(e1,e2,e3,'c+');plot3(f1,f2,f3,'mx');plot3(g1,g2,g3,'bv');plot3(h1,h2,h3,'rd');plot3(i1,i2,i3,'gd');plot3(j1,j2,j3,'ks');
plot3(k1,k2,k3,'bs');plot3(l1,l2,l3,'cs');
q=num2str(round(g));q1=num2str((round(g)+1));q2=num2str(2*round(g));
q3=num2str(2*round(g)+1);q4=num2str(3*round(g));q5=num2str(3*round(g)+1);
q6=num2str(4*round(g));q7=num2str(4*round(g)+1);q8=num2str(5*round(g));
q9=num2str(5*round(g)+1);q10=num2str(6*round(g));q11=num2str(6*round(g)+1);q12=num2str(7*round(g));
q13=num2str(7*round(g)+1);q14=num2str(8*round(g));q15=num2str(8*round(g)+1);q16=num2str(9*round(g));
q17=num2str(9*round(g)+1);q18=num2str(10*round(g));q19=num2str(10*round(g)+1);q20=num2str(11*round(g));
q21=num2str(11*round(g)+1);q22=num2str(12*round(g));
end;

if clus==13, plot3(a1,a2,a3,'gs');plot3(b1,b2,b3,'r+');plot3(c1,c2,c3,'kh');

plot3(d1,d2,d3,'b*');plot3(e1,e2,e3,'c+');plot3(f1,f2,f3,'mx');plot3(g1,g2,g3,'bv');plot3(h1,h2,h3,'rd');plot3(i1,i2,i3,'gd');plot3(j1,j2,j3,'ks');
plot3(k1,k2,k3,'bs');plot3(l1,l2,l3,'cs');plot3(m1,m2,m3,'ms');

```

```

q=num2str(round(g));q1=num2str((round(g)+1));q2=num2str(2*round(g));
q3=num2str(2*round(g)+1);q4=num2str(3*round(g));q5=num2str(3*round(g)+1);
q6=num2str(4*round(g));q7=num2str(4*round(g)+1);q8=num2str(5*round(g));
q9=num2str(5*round(g)+1);q10=num2str(6*round(g));q11=num2str(6*round(g)+1);q12=num2str(7*round(g));
q13=num2str(7*round(g)+1);q14=num2str(8*round(g));q15=num2str(8*round(g)+1);q16=num2str(9*round(g));
q17=num2str(9*round(g)+1);q18=num2str(10*round(g));q19=num2str(10*round(g)+1);q20=num2str(11*round(g));
q21=num2str(11*round(g)+1);q22=num2str(12*round(g));q23=num2str(12*round(g)+1);q24=num2str(13*round(g));
end;

if clus==14, plot3(a1,a2,a3,'gs');plot3(b1,b2,b3,'r+');plot3(c1,c2,c3,'kh');
plot3(d1,d2,d3,'b*');plot3(e1,e2,e3,'c+');plot3(f1,f2,f3,'mx');plot3(g1,g2,g3,'bv');plot3(h1,h2,h3,'rd');plot3(i1,i2,i3,'gd');plot3(j1,j2,j3
,'ks');
plot3(k1,k2,k3,'bs');plot3(l1,l2,l3,'cs');plot3(m1,m2,m3,'ms');plot3(n1,n2,n3,'m+');
q=num2str(round(g));q1=num2str((round(g)+1));q2=num2str(2*round(g));
q3=num2str(2*round(g)+1);q4=num2str(3*round(g));q5=num2str(3*round(g)+1);
q6=num2str(4*round(g));q7=num2str(4*round(g)+1);q8=num2str(5*round(g));
q9=num2str(5*round(g)+1);q10=num2str(6*round(g));q11=num2str(6*round(g)+1);q12=num2str(7*round(g));
q13=num2str(7*round(g)+1);q14=num2str(8*round(g));q15=num2str(8*round(g)+1);q16=num2str(9*round(g));
q17=num2str(9*round(g)+1);q18=num2str(10*round(g));q19=num2str(10*round(g)+1);q20=num2str(11*round(g));
q21=num2str(11*round(g)+1);q22=num2str(12*round(g));q23=num2str(12*round(g)+1);q24=num2str(13*round(g));
q25=num2str(13*round(g)+1);q26=num2str(14*round(g));
end;

if clus==15, plot3(a1,a2,a3,'gs');plot3(b1,b2,b3,'r+');plot3(c1,c2,c3,'kh');
plot3(d1,d2,d3,'b*');plot3(e1,e2,e3,'c+');plot3(f1,f2,f3,'mx');plot3(g1,g2,g3,'bv');plot3(h1,h2,h3,'rd');plot3(i1,i2,i3,'gd');plot3(j1,j2,j3
,'ks');
plot3(k1,k2,k3,'bs');plot3(l1,l2,l3,'cs');plot3(m1,m2,m3,'ms');plot3(n1,n2,n3,'m+');plot3(o1,o2,o3,'r+');
q=num2str(round(g));q1=num2str((round(g)+1));q2=num2str(2*round(g));
q3=num2str(2*round(g)+1);q4=num2str(3*round(g));q5=num2str(3*round(g)+1);
q6=num2str(4*round(g));q7=num2str(4*round(g)+1);q8=num2str(5*round(g));
q9=num2str(5*round(g)+1);q10=num2str(6*round(g));q11=num2str(6*round(g)+1);q12=num2str(7*round(g));
q13=num2str(7*round(g)+1);q14=num2str(8*round(g));q15=num2str(8*round(g)+1);q16=num2str(9*round(g));
q17=num2str(9*round(g)+1);q18=num2str(10*round(g));q19=num2str(10*round(g)+1);q20=num2str(11*round(g));
q21=num2str(11*round(g)+1);q22=num2str(12*round(g));q23=num2str(12*round(g)+1);q24=num2str(13*round(g));
q25=num2str(13*round(g)+1);q26=num2str(14*round(g));q27=num2str(14*round(g)+1);q28=num2str(15*round(g));
end;

if clus==16, plot3(a1,a2,a3,'gs');plot3(b1,b2,b3,'r+');plot3(c1,c2,c3,'kh');
plot3(d1,d2,d3,'b*');plot3(e1,e2,e3,'c+');plot3(f1,f2,f3,'mx');plot3(g1,g2,g3,'bv');plot3(h1,h2,h3,'rd');plot3(i1,i2,i3,'gd');plot3(j1,j2,j3
,'ks');
plot3(k1,k2,k3,'bs');plot3(l1,l2,l3,'cs');plot3(m1,m2,m3,'ms');plot3(n1,n2,n3,'m+');plot3(o1,o2,o3,'r+');plot3(p1,p2,p3,'c*');
q=num2str(round(g));q1=num2str((round(g)+1));q2=num2str(2*round(g));
q3=num2str(2*round(g)+1);q4=num2str(3*round(g));q5=num2str(3*round(g)+1);
q6=num2str(4*round(g));q7=num2str(4*round(g)+1);q8=num2str(5*round(g));
q9=num2str(5*round(g)+1);q10=num2str(6*round(g));q11=num2str(6*round(g)+1);q12=num2str(7*round(g));
q13=num2str(7*round(g)+1);q14=num2str(8*round(g));q15=num2str(8*round(g)+1);q16=num2str(9*round(g));
q17=num2str(9*round(g)+1);q18=num2str(10*round(g));q19=num2str(10*round(g)+1);q20=num2str(11*round(g));
q21=num2str(11*round(g)+1);q22=num2str(12*round(g));q23=num2str(12*round(g)+1);q24=num2str(13*round(g));
q25=num2str(13*round(g)+1);q26=num2str(14*round(g));q27=num2str(14*round(g)+1);q28=num2str(15*round(g));
q29=num2str(15*round(g)+1);q30=num2str(16*round(g));
legend('Fresh1','Fresh2','Fresh3','Bulling1','Bulling2','Bulling3','Freshlow','Freshhigh','FrozenFresh1','FrozenFresh2','FrozenBulling
1','FrozenBulling2','Frozenlow1','Frozenlow2','Frozenhigh1','Frozenhigh2');
end;

title('PCA plot of different milk samples');
xlabel(strcat('PC #1 (',num2str(ssq(1,3),'%2.2f'),'%')'));
ylabel(strcat('PC #2 (',num2str(ssq(2,3),'%2.2f'),'%')'));
zlabel(strcat('PC #3 (',num2str(ssq(3,3),'%2.2f'),'%')'));

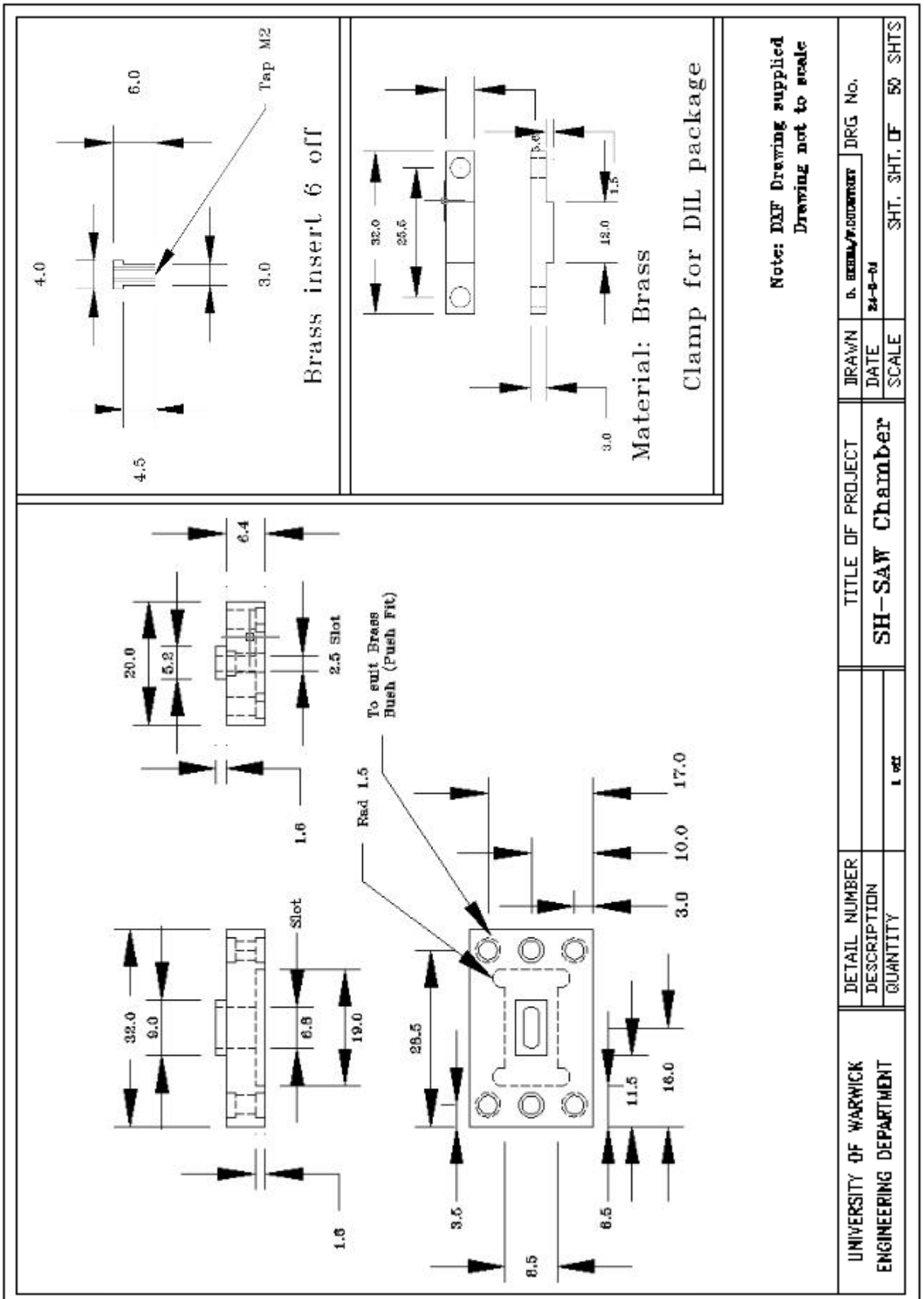
```

Appendix B

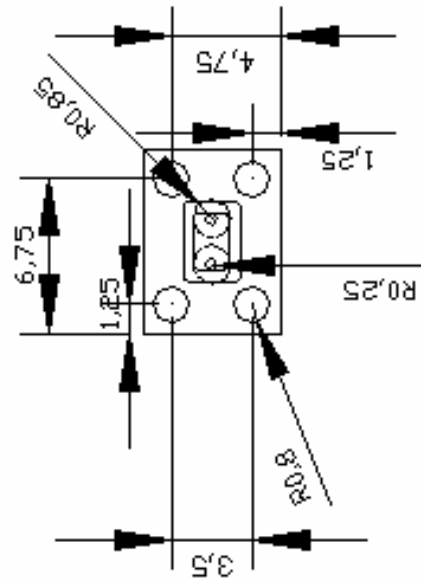
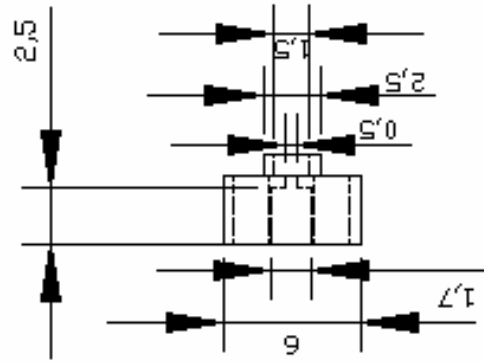
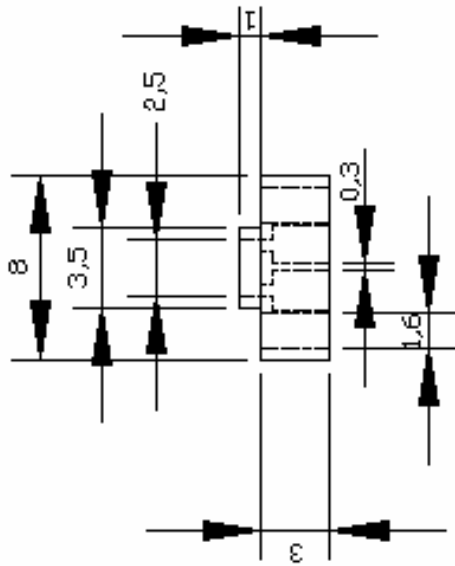
Cell design details

This appendix contains the design details of the liquid cells for:

1. 61 MHz devices
2. 433 MHz stainless steel flow and static measurement chambers
3. Details of resin used for the development of MSL chambers

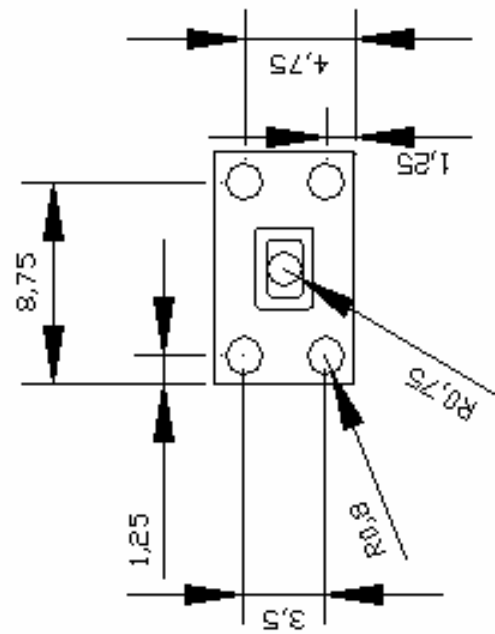
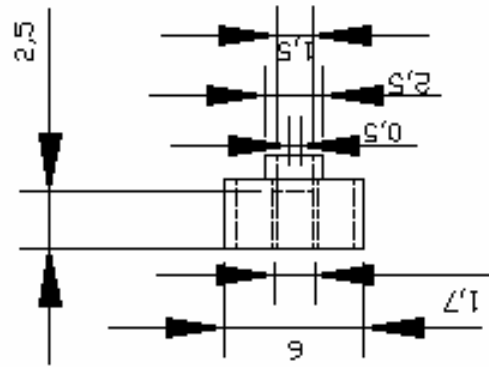
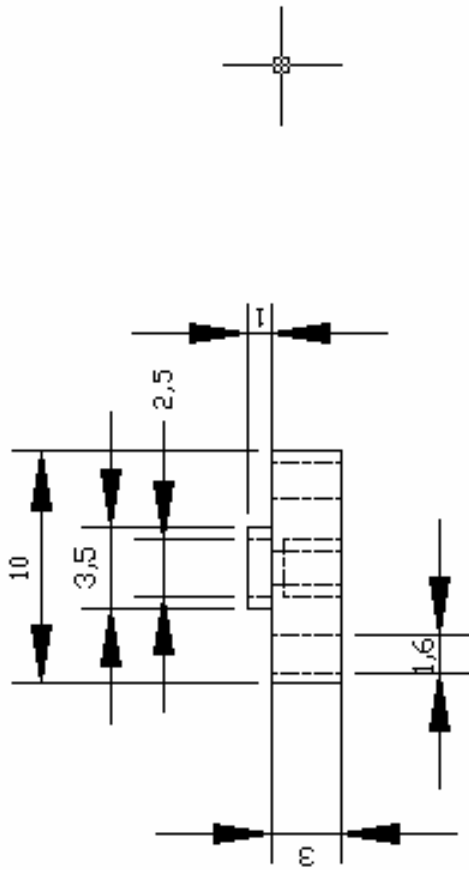


Material:- S/Steel
12 OFF
Not to scale



UNIVERSITY OF WARWICK ENGINEERING DEPARTMENT	DETAIL NUMBER	TITLE OF PROJECT	DRAWN BY	DRG. No.	FTC21
	DESCRIPTION		DATE		
	QUANTITY		SCALE	SHT. OF	50 SHTS

Material:- S/Steel
6 OFF
Not to scale


















UNIVERSITY OF WARWICK ENGINEERING DEPARTMENT	DETAIL NUMBER	TITLE OF PROJECT	DRAWN	DRG. No.	FTC21
	DESCRIPTION		DATE		
	QUANTITY		SCALE	SHT. SHT. OF	50 SHTS









Appendix C









High frequency SH-SAW device configurations








This appendix contains the details of the high frequency wired and wireless (433 MHz, 869 MHz, 2.45 GHz and 10 GHz) device configurations

SRL NUMBER	FREQUENCY /MHz	WIRELESS / WIRED	IDT FINGER TYPE	REFLECTOR TYPE	CONFIGURATION	CODE	PICTURE	No. of devices /wafer
196	433	Wireless	Solid	Open circuit	Dual delay line same length	WLSOF433DDLOCR		4
197	433	Wireless	Solid	Short circuit	Dual delay line same length	WLSOF433DDLSCR		4
198	433	Wireless	Solid	Positive & negative	Dual delay line same length	WLSOF433DDLPNR		3
199a1	433	Wireless	Solid	Open circuit	Dual delay line one shorter by 1 mm	WLSOF433DDLS1OCR		3
199a2	433	Wireless	Solid	Open circuit	Dual delay line one shorter by 2 mm	WLSOF433DDLS2OCR		5
200a1	433	Wireless	Solid	Short circuit	Dual delay line one shorter by 1 mm	WLSOF433DDLS1SCR		4
200a2	433	Wireless	Solid	Short circuit	Dual delay line one shorter by 2 mm	WLSOF433DDLS2SCR		6

201a1	433	Wireless	Solid	Positive & negative	Dual delay line one shorter by 1 mm	WLSOF433DDL1PNR		3
201a2	433	Wireless	Solid	Positive & negative	Dual delay line one shorter by 2 mm	WLSOF433DDL2PNR		5
207a	433	Wired	Solid		Dual delay line same length	WISOF433DDL		12
207	433	Wired	Split		Dual delay line same length	WISPF433DDL		7
207a1	433	Wired	Solid		Dual delay line same length free line with window	WISOF433DDLFW		9
207b	433	Wired	Split		Dual delay line same length	WISPF433DDL		6
207c	433	Wired	Solid		Dual delay line same length same finger pairs as split finger IDTs (6 finger pairs)	WISPF433DDL6FP		5
208a1	433	Wired	Solid		Dual delay line one shorter by 1 mm	WISOF433DDL1S		5

208a2	433	Wired	Solid		Dual delay line one shorter by 2 mm	WISOF433DDL2S		5
273	433	Wired	Solid		Dual delay line same length with voltage modulated electrode	WISOF433DDLVM		30
245a	869	Wired	Solid		Dual delay line same length	WISOF869DDL		5
245a1	869	Wired	Solid		Dual delay line same length free line with window	WISOF869DDLFW		5
245b	869	Wired	Split		Dual delay line same length	WISPF869DDL		5
246a1	869	Wired	Solid		Dual delay line one shorter by 1 mm	WISOF869DDL1S		4
246a2	869	Wired	Solid		Dual delay line one shorter by 2 mm	WISOF869DDL2S		4
274	869	Wireless	Solid	Open circuit	Dual delay line same length	WLSOF869DDLOCR		3

275	869	Wireless	Solid	Short circuit	Dual delay line same length	WLSOF869DDLSCR		4
276	869	Wireless	Solid	Positive & Negative	Dual delay line same length	WLSOF869DDLPNR		4
254	2450	Wireless	Solid	Positive & negative	Dual delay line same length	WLSOF2450DDLPNR		5
255a1	2450	Wireless	Solid	Positive & negative	Dual delay line one shorter by 1 mm	WLSOF2450DDL1SPNR		5
255a2	2450	Wireless	Solid	Positive & negative	Dual delay line one shorter by 2 mm	WLSOF2450DDL2SPNR		5
258a	2450	Wired	Solid		Dual delay line same length	WISOF2450DDL		8
258a1	2450	Wired	Solid		Dual delay line same length free line with window	WISOF2450DDLFW		5
258b	2450	Wired	Split		Dual delay line same length	WISPF2450DDL		6

259a1	2450	Wired	Solid		Dual delay line one shorter by 1 mm	WISOF2450DDL1S		7
259a2	2450	Wired	Solid		Dual delay line one shorter by 2 mm	WISOF2450DDL2S		7
262	2450	Wired	Split		Dual delay line same length	WISPF2450DDL		6
266	10000	Wired	Solid		Dual delay line same length	WISOF10DDL		5
266a	10000	Wired	Solid		Dual delay line same length free line with window	WISOF10DDLFW		5
267a1	10000	Wired	Solid		Dual delay line one shorter by 1 mm	WISOF10DDL1S		6
267a2	10000	Wired	Solid		Dual delay line one shorter by 2 mm	WISOF10DDL2S		6

Appendix D

Published Papers

This appendix contains papers that have been published in international journals and conference proceedings.